

Dissertation

Atomic-to-Nanoscale Modeling of Diborides via Machine Learning Interatomic Potentials

carried out for the purpose of obtaining the degree of Doctor technicae (Dr.techn.) submitted at TU Wien

Faculty of Mechanical and Industrial Engineering

by

Shuyao LIN (林舒瑶), MSc

Matr.Nr.: 12229963

under the supervision of

Asst.Prof. Dr.techn. Nikola Koutná

Institute of Materials Science, E308

Assoc.Prof. Dr. Davide Sangiovanni

Institute of Physics, Chemistry, and Biology (IFM), Linköping University, Sweden

Univ.Prof. Dipl.-Ing. Dr.mont. Paul Heinz Mayrhofer

Institute of Materials Science, E308

reviewed by

Assoc.Prof. Poulumi Dey Technische Universiteit Delft Delft, Netherland

Prof. Denis Music Malmö University Malmö, Sweden



I confirm, that the printing of this thesis requires the approval of the examination board.

Affidavit:

I declare in lieu of oath, that I wrote this thesis and carried out the associated research myself, using only the literature cited in this volume. If text passages from sources are used literally, they are marked as such.

I confirm that this work is original and has not been submitted for examination elsewhere, nor is it currently under consideration for a thesis elsewhere. I acknowledge that the submitted work will be checked electronically-technically using suitable and state-of-the-art means (plagiarism detection software). On the one hand, this ensures that the submitted work was prepared according to the high-quality standards within the applicable rules to ensure good scientific practice "Code of Conduct" at the TU Wien. On the other hand, a comparison with other student theses avoids violations of my personal copyright.



" Du bist eine freie Seele."



Acknowledgement

Contents will come with printed version.



Table of Contents

At	bstract	I										
Κι	urzfassung	П										
1	Introduction 1.1 Evaluation of mechanical properties in experiments	1 1 3 4 5 5 8 10 11 12										
2	Materials selection2.1 Transition metal diborides	15 15 17										
3	Computational methodology 3.1 Ab initio calculations 3.2 Training workflow for machine-learning interatomic potentials 3.3 Molecular dynamics simulation	21 21 23 25										
4	Data processing and analysis4.1 Structural stability4.2 Mechanical properties4.3 Phase identification	28 30 32										
5	Contribution to the field	44										
	Machine-learning potentials for nanoscale simulations of tensile deformation and fracture in ceramics											
Shear-activated phase transformations of diborides via machine-learning potent molecular dynamics												
	Machine-learning potentials predict orientation- and mode-dependent fracture in refractory diborides	110										
6	Summary and outlook	139										

Abstract

Ceramic materials exhibit exceptional hardness, thermal stability, and wear resistance, making them highly suitable for cutting tool coatings and a wide range of engineering applications. However, brittleness significantly limits the usage, and observing crack mechanisms during experiments can be challenging. Furthermore, ceramics that exhibit multiple stabilizable phases – susceptible to slight variations in stoichiometry or external forces – can experience considerable diminishment in their mechanical properties. For example, transition metal diborides (TMB₂), commonly used as hard coatings, can crystallize in three distinct structural polymorphs (P6/mmm: α , P6₃/mmc: ω and γ). Although phase-dependent properties have been observed experimentally, no comprehensive study yet explores the relationship between these phases and their behavior under real-world conditions – an understanding essential for future applications.

This work provides modeling insights into the relationships between the stability, structural, elastic, and fracture properties of Group-IV-VII TMB₂ ceramics. The primary methodologies applied include ab initio molecular dynamics (AIMD) and machinelearning-potential-assisted classical molecular dynamics (ML-MD). AIMD is employed to evaluate phase stability and intrinsic properties in an unbiased manner, while also generating training and validation sets for machine learning interatomic potentials (MLIP) within the moment tensor potential (MTP) framework. Using the developed MLIPs, ML-MD enables simulations at the nanoscale, providing additional insights into size-dependent behavior and phenomena that are not observable at the atomic scale. The model materials are TiB₂ (Group-IV, favor α phase), TaB₂ (Group V, favor α phase), WB₂ (Group-VI, favor ω phase, the rest TMB₂:s in this Group favor α phase), and ReB₂ (Group-VII, favor γ phase as TcB₂, while MnB₂ favors α phase).

My contribution to the field is presented through 3 core publications. The workflow and dataset generation protocols provide a general framework for developing robust, transferable MLIPs for ML-MD simulations of ceramics under diverse strains, temperatures, and loading conditions—beyond the reach of ab initio methods. The exceptional mechanical properties of mono-crystalline TMB₂ under both ambient equilibrium and extreme loading, and/or temperature conditions are also confirmed. Focusing on the three primary phase structures, this work reveals phase transition behaviors under ambient conditions and external forces, showing that such transformations can be activated by minor shear deformation when metastable phases are present. The transformation between the α and ω phases are highlighted in Group-IV, V, and VI TMB₂. This suggests that in real synthesis processes, phase transformations might be induced by the strain field modulations from the substrate material, particularly as additional forces along the growth direction can accelerate the process. Moreover, since the fracture toughness K_{Ic} is also essential for assessing ceramic's performance yet challenging to measure with atomistic precision, here-developed MLIPs are utilized to examine Mode-I crack responses in TMB_2 :s at nanoscale, validated against experimental K_{Ic} values.



Kurzfassung

Keramische Werkstoffe zeichnen sich durch außergewöhnliche Härte, thermische Stabilität und Verschleißfestigkeit aus, was sie besonders geeignet für Schneidwerkzeugbeschichtungen und zahlreiche technische Anwendungen macht. Allerdings schränkt ihre Sprödigkeit die Einsatzmöglichkeiten erheblich ein, und die experimentelle Beobachtung von Rissmechanismen gestaltet sich schwierig. Zudem können keramische Materialien mit mehreren stabilisierbaren Phasen – empfindlich gegenüber geringen Änderungen in der Stöchiometrie oder äußeren Einflüssen deutliche Einbußen ihrer Eigenschaften erfahren. Ein Beispiel sind Übergangsmetall-Diboride (TMB₂), die häufig als Hartstoffbeschichtungen verwendet werden und in drei unterschiedlichen Polymorphen kristallisieren können (P6/mmm: α , P6₃/mmc: ω und γ). Obwohl phasenabhängige Eigenschaften experimentell beobachtet wurden, existiert bislang keine umfassende Studie, die den Zusammenhang zwischen diesen Phasen und ihrem Verhalten unter realen Anwendungsbedingungen untersucht – ein Verständnis, das für zukünftige Anwendungen entscheidend ist.

Diese Arbeit bietet modellbasierte Einblicke in die Zusammenhänge zwischen der Stabilität sowie den strukturellen, elastischen und bruchmechanischen Eigenschaften von TMB₂-Keramiken der Gruppen IV bis VII. Die Hauptmethoden umfassen ab initio Molekulardynamik (AIMD) und klassische molekulardynamische Simulationen mit maschinell gelernten Potentialen (ML-MD). AIMD wird eingesetzt, um die Phasenstabilität und intrinsische Eigenschaften unbeeinflusst zu bewerten sowie Trainings- und Validierungsdatensätze für maschinell gelernte interatomare Potentiale (MLIP) im Rahmen des Momententensor-Potentials (MTP) zu generieren. Basierend auf den entwickelten MLIPs ermöglichen ML-MD-Simulationen Untersuchungen im Nanomaßstab und liefern zusätzliche Erkenntnisse über größenabhängige Effekte und Phänomene, die auf atomarer Ebene nicht beobachtbar sind. Die untersuchten Modellmaterialien sind TiB₂ (Gruppe IV, bevorzugt α -Phase), TaB₂ (Gruppe V, bevorzugt α -Phase), WB₂ (Gruppe VI, bevorzugt ω -Phase; andere TMB₂ dieser Gruppe bevorzugen die α -Phase) und ReB₂ (Gruppe VII, bevorzugt wie TcB₂ die γ -Phase, während MnB₂ die α -Phase bevorzugt).

Mein Beitrag auf diesem Forschungsgebiet wird durch drei zentrale Publikationen dargestellt. Der entwickelte Workflow sowie die Protokolle zur Datensatzgenerierung bilden ein allgemeines Rahmenkonzept zur Entwicklung robuster und übertragbarer MLIPs für ML-MD-Simulationen von Keramiken unter verschiedenen Dehnungen, Temperaturen und Belastungsbedingungen über den Anwendungsbereich von ab initio-Methoden hinaus. Die außergewöhnlichen mechanischen Eigenschaften von einkristallinem TMB₂ unter Gleichgewichtsbedingungen sowie unter extremen Belastungen und/oder hohen Temperaturen werden ebenfalls bestätigt. Mit Fokus auf die drei primären Phasenstrukturen zeigt diese Arbeit Phasenumwandlungen unter Umgebungsbedingungen und externen Kräften auf und belegt, dass solche Transformationen bereits durch geringe Scherbelastungen ausgelöst werden können, sofern metastabile Phasen vorhanden sind. Besonders hervorgehoben wird die Umwandlung zwischen der α - und der ω -Phase bei TMB₂ der Gruppen IV, V und VI. Dies legt nahe, dass Phasenumwandlungen in realen Syntheseprozessen durch Spannungsmodulationen des Substrats induziert werden können, besonders wenn Kräfte entlang der Wachstumsrichtung den Prozess beschleunigen. Da die Bruchzähigkeit $K_{\rm Ic}$ ein entscheidender, aber schwer messbarer Parameter für Keramiken ist, werden die entwickelten MLIPs zur Untersuchung von Mode-I-Rissreaktionen in TMB2 im Nanomaßstab eingesetzt und mit experimentellen Werten validiert.

Chapter 1

Introduction

1.1 Evaluation of mechanical properties in experiments

Ultra-high temperature ceramics exhibit exceptional properties, including superior hardness, wear resistance, and thermal stability, making them indispensable for demanding engineering applications. These attributes enable their widespread use in industrial settings, such as cutting tools, protective coatings, and aerospace components [1, 2]. The mechanical properties of these ceramics play a critical role in determining their performance and reliability across a wide range of applications. This section explores the experimental evaluation of these properties, as well as relevant difficulties. The discussion begins with an overview of essential parameters such as hardness, Young's modulus, and fracture toughness. Subsequently, the phase-dependent nature of these properties is examined, emphasizing how phase-dependence affects their synthesis process and mechanical behavior. Finally, the section addresses the challenges associated with understanding failure mechanisms, shedding light on the complexities of crack initiation, propagation, and ultimate failure in these brittle yet indispensable materials.

1.1.1 Key mechanical parameters of ceramics

The mechanical behavior of ceramics is characterized by a set of key parameters, each of which provides critical insights into their performance under specific loading and environmental conditions. Understanding these attributes helps to optimize ceramics for specific uses, while advancements such as high-entropy ceramics and superlattice aim to address their limitations, expanding their applicability [1, 3].

Mechanical properties such as strength, toughness, and ductility are critical parameters in understanding materials' behavior under stress, are commonly evaluated using stressstrain curves. The curve begins with the elastic region, where the slope represents the elastic modulus – a measure of stiffness and resistance to deformation under small strains. Strength, particularly, can be derived from larger strains while reaching the maximum stress. **Ductility**, on the other hand, is defined as the area under the stress-strain curve from the strain at the first maximum (i.e., strength) to the fracture point. For brittle materials, these two points are very close or may even overlap. As a result, their plastic deformation is negligible, leading to very low ductility. Finally, toughness is the total area under the stress-strain curve, encompassing both elastic and plastic deformation regions.

Experimentally, elastic modulus, which defines a material's stiffness, is often measured through ultrasonic testing or nanoindentation. For ceramics like aluminum nitride (AlN) [4], the elastic modulus is typically high, indicating significant resistance to elastic deformation under applied loads. The results generally show minimal deformation before the material reaches its elastic limit, contributing to their role in load-bearing applications. While for ceramics it is more common to provide indications of "compressive strength" rather than "tensile strength" (which is contrary to computational tests), compressive strength tests [5, 6], usually conducted using uniaxial compression. As shown in Fig. 1.1, materials like carbon-alloyed TaN show exceptional compressive strength, while providing typical crack pattern after failure. Similarly, hardness can be measured using techniques such as Vickers or Knoop hardness testing [7, 8]. These methods involve indenting the material with a diamond tip under a controlled force, and the hardness is determined by the depth indentation. Ceramics often exhibit high hardness, indicating they can endure significant contact stresses without undergoing deformation, underscoring their applicability in harsh environments [9, 10]. Further, ductility is often quantified by the total elongation or reduction in cross-sectional area, which reflects the material's capacity to deform plastically before fracture.

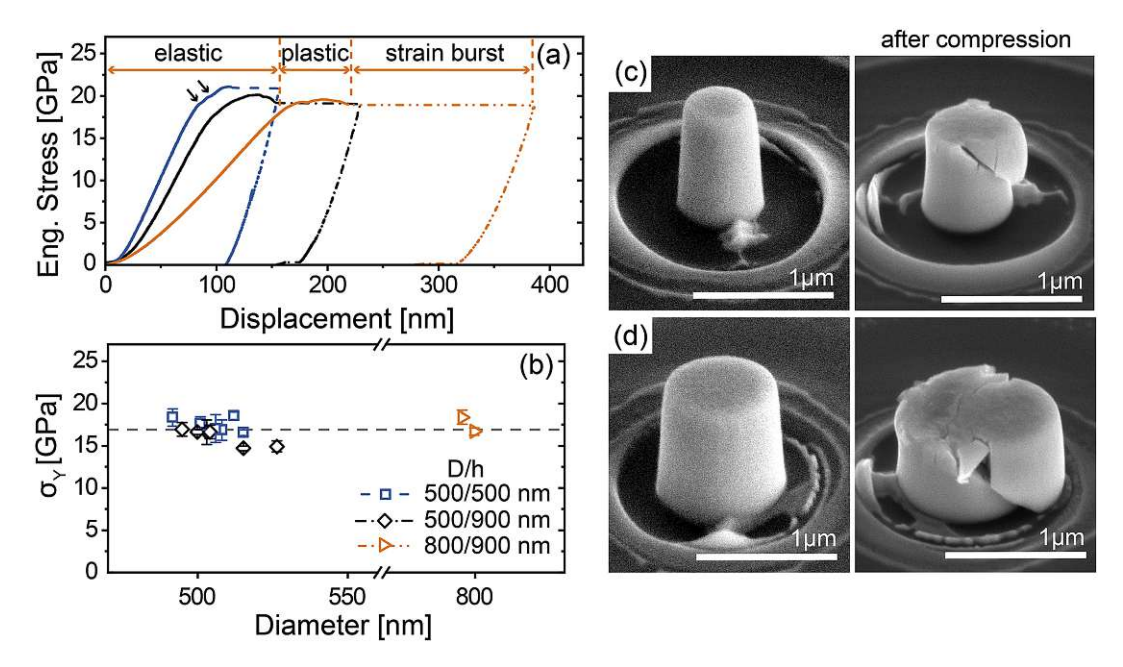


Fig. 1.1: Typical mechanical response of ceramics, as illustreated with micro-pillar compression tests from Ref. [5] . (a) Engineering stress-displacement curves acquired during the compression tests conducted in situ in a SEM. (b) Yield stress $\sigma_{\rm Y}$ plotted as a function of pillar diameter D. The dashed horizontal line corresponds to the average $\sigma_{\rm Y}$. (c,d) Representative SEM images of two pillars with D = (c) 500 nm and (d) 800 nm before and after compression, respectively. For full resolution of the SEM images, see the original publication (Ref. [5]).

In contrast, toughness, often measured by techniques such as the fracture toughness test or notched beam bending, provides insight into a material's ability to resist crack propagation [11]. Ceramics typically exhibit brittle failure, meaning they fracture suddenly with little to no plastic deformation before failure. When tested, materials like silicon carbide (SiC) [12, 13] display a sharp, catastrophic break once the critical

stress intensity factor is reached. This brittleness is a hallmark of ceramics, where cracks initiate at microstructural flaws and propagate rapidly. Hence, evaluating their ability to resist crack propagation under stress through critical stress intensity factor (K_{Ic}) is essential.

Crack propagation can occur under three distinct modes of loading: mode-I (opening mode), mode-II (sliding or in-plane shear mode), and mode-III (tearing or out-of-plane shear mode) [14, 15]. Among these, mode-I is considered the most critical for brittle materials, as it typically represents the weakest fracture resistance. K_{Ic} is determined experimentally using methods such as single-edge notched bending (SENB) and chevronnotch techniques, by introducing a pre-crack or notch into the specimen, applying a controlled load, and measuring the critical load at which crack propagation occurs. High hardness ceramics like transition metal nitrides (TMN) presents normally low K_{Ic} of around 1-5 MPa·m $^{1/2}$ [5].

1.1.2 Phase-dependent mechanical properties

For ceramics such as silicon nitride (Si₃N₄), transition metal carbides like tungsten carbide (WC), and transition metal diborides (TMB₂), the presence of multiple stable phases is affected by slight variations in stoichiometry or external forces can significantly affect their mechanical properties [16–18]. Fig. 2.1 shows the theoretically stabilizable phases of TMB₂ compounds (where TM=Ti, Ta, W, Re).

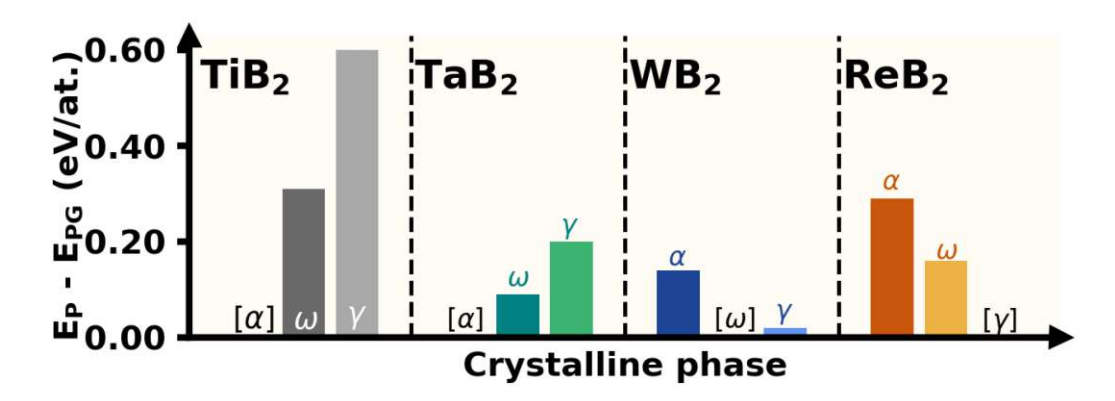


Fig. 1.2: Phase stability comparison in ab initio calculations, as illustrated with **potential energy**, E_P , difference between each polymorph (α, ω, γ) and the lowestenergy (ground-state) polymorph from room-temperature ML-MD equlibration (720atom supercells). The zero E_P difference shows that TiB_2 and TaB_2 favor the α phase, WB₂ favors the ω phase, and ReB₂ favors the γ phase. All the data are derived from this study, for computational details see the Section 3.

In Si₃N₄, for example, there are two primary phases: the α -phase (s.g. P $3\overline{m}1$) and β -phase (s.g. P6₃/mmc). While both phases exhibit excellent high-temperature stability and wear resistance, the β -phase typically offers better toughness and strength [16, 19]. Sintering can kinetically transform α phase to the ideal β -phase, but incomplete conversion leads to mixed phases, reducing mechanical performance. WC, known for its inherent stability, can experience a shift toward the cubic W₂C phase with slight

deviations in stoichiometry from hexagonal phase, leading to a notable reduction in mechanical performance and wear resistance [17, 20]. Fig. 1.3 shows the shear plasticity strength of TMB₂ compounds in different phases, highlighting how phase transitions can significantly impact mechanical behavior, as detailed discussed in [Publication II] together with phase transition behavior.

Defects and imperfect stoichiometry create discrepancies between theoretical predictions and real-world mechanical performance. Formation of un-preferred phases can lead to earlier failure or reduced operational performance, making it essential to account for these variations when designing for high-stress environments. Understanding and predicting these behaviors through modeling, alongside experimental validation, is crucial for optimizing the performance and reliability in applications.

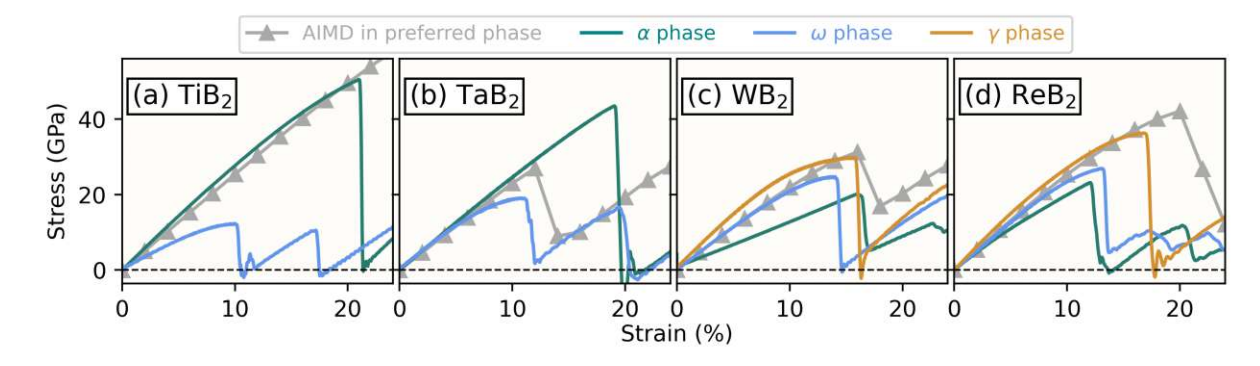


Fig. 1.3: Phase-dependent shear strength comparison with stress-strain curves during shear deformation along $(0001)[\overline{1}2\overline{1}0]$ at the nanoscale ($\approx 15{,}000$ atoms) of (a) TiB₂, (b) TaB₂, (c) WB₂, and (d) ReB₂ in all three phases (α in teal, ω in blue, γ in orange), as the gray triangular-line exhibit AIMD result in preferred phase (TiB₂ and TaB_2 favor the α phase, WB_2 favors the ω phase, and ReB_2 favors the γ phase.). All the data are derived from this study, for computational details see the Section 3.

1.1.3 Challenges in understanding failure mechanisms

Deformation and mechanical failure in ceramics are heavily influenced by the structural composition and crystallographic defects, with microstructural flaws playing a crucial role in determining overall strength and reliability. These effects arise not only at the nanoscale in single-crystal regions but also in more complex structures where phase transformations can occur between stable and metastable phases, either throughout the material or in localized areas under ambient operation conditions. This interplay between defects, microstructure, and phase behavior is central to understanding and predicting the mechanical performance of ceramics.

Ceramics often exhibit complex failure mechanisms before reaching their ideal fracture point, even in single-crystal forms - which are already challenging to synthesize - and these mechanisms become even more complex in polycrystalline samples containing numerous defects. Under deformation, instead of breaking along a clear cleavage plane, multiple defect sites typically form, leading to intricate stress concentrations and ultimately catastrophic failure when the highest strength is reached [21]. Consequently, the

fracture stress observed in experimental conditions is often much lower than predicted by atomistic simulations. Furthermore, localized phase transformations also adds to the challenge of accurate detection and evaluation in experiment. Nanoscale simulations, therefore, provide a critical tool for tracking these transformations and understanding how they influence mechanical performance under stress.

Experimental techniques used to characterize ceramic materials often fall short in resolving phase-dependent properties, making it difficult to fully understand how different phases contribute to the material's behavior under stress. On the top of that, this limitation is worsened by the complex microstructural features inherent in ceramics, which can include variations in grain size, porosity, and the presence of secondary phases, all of which play a crucial role in determining their mechanical properties. Furthermore, challenges in the experimental characterization of ceramic properties stem even for the most cutting edge modern experimental methods (e.g., SEM and AFM), in accurately capturing phase transitions, such as crystalline-to-amorphous transformations or polymorphism [22, 23]. These transitions, which can affect material properties like strength and toughness, are often subtle and difficult to detect in real time, complicating the correlation between structure and performance. Consequently, there is a pressing need for predictive modeling to complement experimental approaches, enabling a more comprehensive understanding of the relationships between microstructure, defects, and mechanical performance. Such modeling enables the isolation of individual defect effects, which is challenging in experiments where multiple factors are intertwined, thereby preventing clear identification of the dominant influences on material behavior.

1.2 Conventional modeling approaches: Foundations and limitations

Modeling material performance across different scales has been essential for understanding and predicting material properties. From the atomistic scale to the mesoscale, this section presents a comprehensive overview of current simulation methods for ceramic materials, highlighting their typical outputs and limitations.

1.2.1 Atomistic simulations

The first-principles method calculates a system's electronic states by solving Schrödinger equation [24] without empirical parameters, based solely on fundamental physics ¹. The properties of condensed matter are primarily determined by the interactions of valence electrons with each other and with ions, which define the electronic structure. Understanding material's properties through this approach involves using Hamiltonian operators to solve interacting quantum many-body problems. The expression for the interacting many-body Hamiltonian [25] is as follows

$$H_{tot} = \sum_{j} \frac{P_j^2}{2M_j} + \sum_{i} \frac{P_i^2}{2m} + \sum_{j < j} \frac{Z_j Z_j e^2}{|R_j - R_j|} + \sum_{i < i} \frac{e^2}{|r_i - r_i|} + \sum_{i,j} \frac{-Z_j e^2}{|R_j - r_i|}, \quad (1.1)$$

^{1*} General time-dependent Schrödinger equation: $i\hbar \frac{d}{dt} |\Psi(t)\rangle = \hat{H} |\Psi(t)\rangle$, where t is time, $|\Psi(t)\rangle$ is the state vector of the quantum, and \hat{H} is the Hamiltonian operator, an observable.

^{**} For a system of N electrons and M nuclei in a materials: $\hat{H}\Psi(\mathbf{r}_1,\mathbf{r}_2,\ldots,\mathbf{r}_N) = E\Psi(\mathbf{r}_1,\mathbf{r}_2,\ldots,\mathbf{r}_N)$, where E is the total energy.

where the first term on the left is the kinetic energy of the nucleus, the second term is the kinetic energy of the valence electron, the third term represents the Coulomb interaction between nuclei, the fourth term represents the Coulomb interaction between electrons and the fifth term represents the interaction between the nucleus and the electron. Here we have disregarded the spin and relativistic effects for the sake of simplicity.

Exact solutions to quantum many-body problems are practically impossible due to the complexity of the wave function, which scales exponentially with the number of particles. A key challenge is accurately treating electron-electron interactions. For ground-state properties, many-body problems can be effectively reduced using Density Functional Theory (DFT), which solves self-consistent single-particle equations and provides an approximation for analyzing electronic ground-state properties. Rather than solving for the many-body wave function Ψ , DFT focuses on the electron density $\rho(\mathbf{r})$, which is a function of only three spatial coordinates, irrespective of the number of electrons. Initially, the Hohenberg-Kohn theorem [26] established that a system's ground-state properties are uniquely determined by its electron density, providing the foundation for DFT. However, it does not provide a practical way to calculate the electron density directly. To overcome this limitation, the Kohn-Sham equation [27] was introduced, reformulating the problem into a set of self-consistent single-particle equations, making the calculations more accessible while retaining accuracy

$$\left[-\frac{\hbar^2}{2m} \nabla^2 + V(r) + V_H(r) + V_{XC}(r) \right] \psi_i(r) = \varepsilon_i \psi_i(r) , \qquad (1.2)$$

This expression is similar to the Schrödinger equation for a system containing multiple electrons and multiple nuclei interacting with each other, but differs from it for a multi-electron system. The left-hand side of the Kohn-Sham equation contains three potentials: V, V_H and V_{XC} . The first potential, V, represents the Coulomb interaction between the electron and nucleus. The second, V_H , is the Hartree potential, accounting for the classical electron-electron repulsion. And the third, V_{XC} , captures the exchangecorrelation contribution, including quantum mechanical electron-electron interactions that are beyond simple Coulomb forces. The iteration of self-consistent process follows:

- First define an initial guess for electron density $\rho(r)$.
- Take the initial electron density as a known quantity, the Kohn-Sham equation is solved for the single-particle wave function $\psi_i(r)$.
- Use the single-particle wave function obtained in the second step to get the electron density $\rho_{KS}(r) = 2 \sum_i \psi_i^*(r) \psi_i(r)$.
- Compare the calculated electron density $\rho_{KS}(r)$ with the initial electron density $\rho(r)$. If $\rho_{KS}(r)$ and $\rho(r)$ agree, then $\rho(r)$ is the ground state electron density of the system and can be used to calculate the total energy of the system. If different, the previous calculated ρ must be updated. The cycle then continues from step 2.

By iteratively solving these self-consistent equations, DFT enables the accurate and efficient calculation of electronic structure and material properties, bridging the gap between fundamental quantum mechanics and practical material science applications.

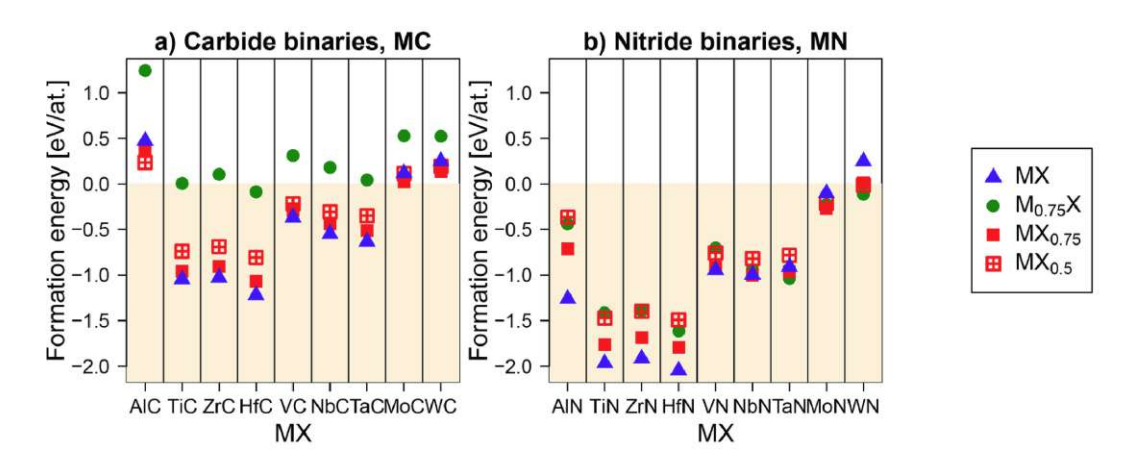


Fig. 1.4: Stability tests in DFT calculations, as illustrated with formation energy of MX binaries from Ref. [28] for (a) carbides, X=C, and (b) nitrides, X=N, in the cubic rocksalt phase with fully occupied lattice sites (MX) or containing vacancies (M_{0.75}X, MX_{0.75}, MX_{0.50}), M=Al, Ti, Zr, Hf, Nb, V, Ta, Mo, W.

Today, DFT is a widely used first-principles method for studying the ground-state properties of molecules and solids, including ceramics such as nitrides and carbides. DFT helps explore various properties, such as phase stability (e.g., E_f of nitrides and carbides ceramic with/without vacancies as shown in Fig. 1.4), electronic structure, mechanical strength, and defect behavior in these materials. For example, in nitrides and carbides, DFT can predict elastic-constants-based descriptors of mechanical properties, thermal stability, and thermoelectric parameters, making it valuable for designing high-performance ceramics [28–32]. However, DFT has limitations, including high computational costs, especially for large or complex structures, and difficulty accurately modeling electron correlations and long-range interactions. To overcome some of these limitations, ab initio molecular dynamics (AIMD) is often used in conjunction with DFT. AIMD simulates the dynamic behavior of atoms and molecules over time, allowing for more accurate studies of temperature-dependent properties and phase transitions in ceramic materials.

AIMD is grounded in quantum mechanics, to compute forces between atoms during simulations. Unlike classical molecular dynamics (MD), where force fields are predefined and will be discussed later, AIMD dynamically calculates forces based on electronic structure at each step, offering a more accurate description of atomic interactions. This allows for the simulation under real-world conditions, such as temperature and pressure, providing insights into time-dependent properties that static DFT calculations cannot capture. AIMD offers several advantages, including the ability to account for temperature effects, which is essential for studying thermal expansion, phase transitions, and diffusion processes. For example, AIMD can explore how nitrides or carbides behave under high temperatures, predicting properties like melting points or thermal stability [34–36]. It can also handle larger and more complex systems than DFT, overcoming phonon-related limitations by considering larger supercells. This flexibility makes AIMD useful for designing and optimizing ceramic materials with intricate structures, such as multiphase, disordered systems, and superlattice structure, as shown in Fig. 1.5.

However, due to its computational intensity, AIMD simulations are often restricted to short timescales (typically units of picoseconds) and relatively small system sizes (a few

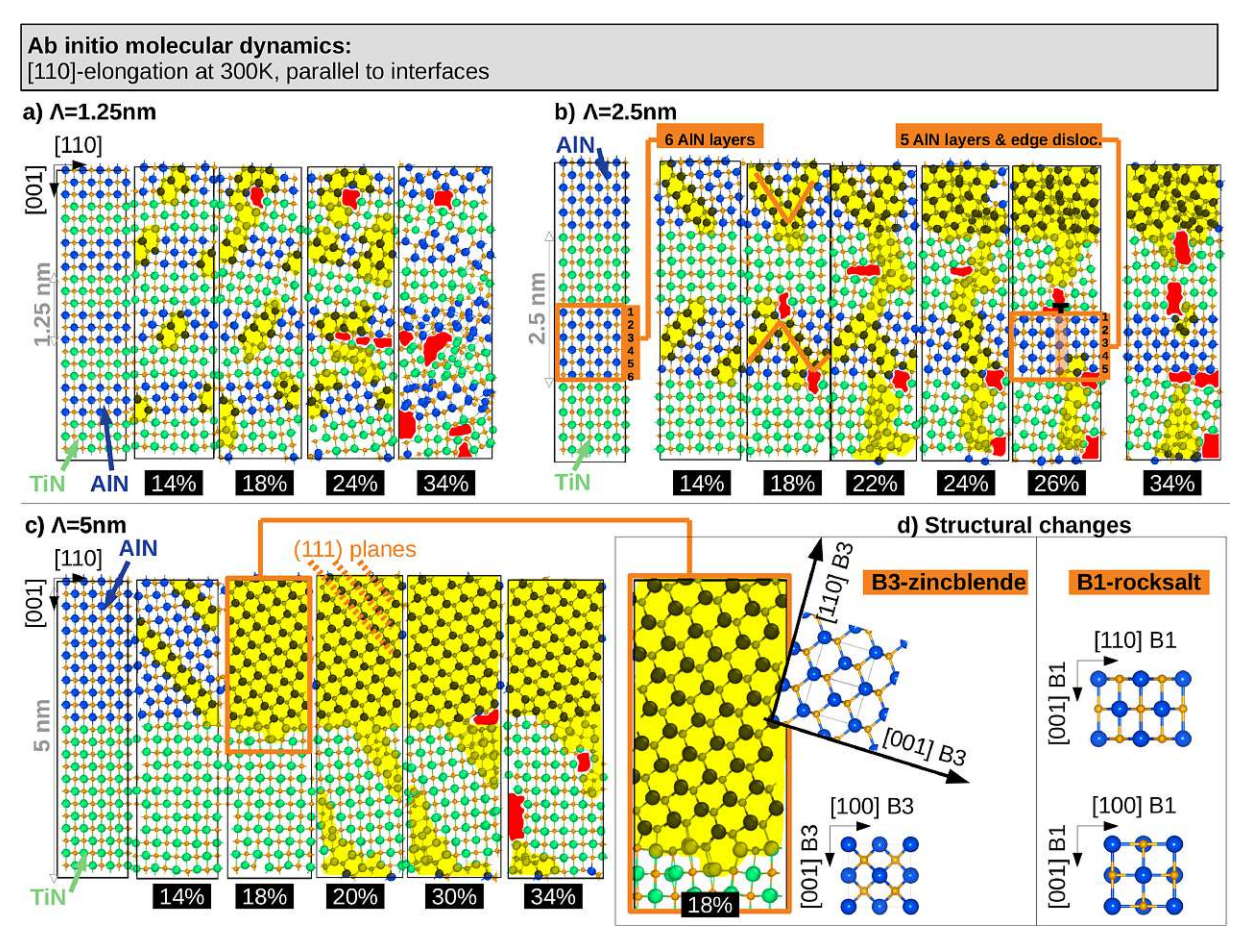


Fig. 1.5: Finite-temperature AIMD calculations, as exemplified with snapshots of AlN/TiN SLs from Ref. [33] with of (a) 1.25 nm, (b) 2.5 nm, and (c) 5 nm, strained in the [110] direction (parallel to interfaces), corresponding to selected strain steps. Snapshots at 14% (a,b,c) correspond to a stress drop one step beyond the yield point. Snapshots at 18% (a), 26% (b), and 20% (c) correspond to the deepest stress minimum during the stage of plastic deformation, while snapshots at 34% (a,b,c) show the fracture point. The yellow colouring highlights structural changes and interface incoherency, while the red colouring marks initiating voids/cracks. Panel (d) illustrates the B1-to-B3 phase transformation in AlN.

hundred atoms). This limits its ability to capture long-term behavior, large-scale defect evolution, or phenomena that require extended simulations, such as creep in ceramics or very slow diffusion processes [21]. Despite these constraints, AIMD remains a powerful tool for exploring dynamic and temperature-dependent properties at the atomic level.

1.2.2 Nanoscale simulations

Classical molecular dynamics (MD) simulates atomic interactions using predefined force fields, allowing detailed insights into atomic-scale phenomena, for systems with thousands to millions of atoms. It is computationally efficient for simulating short timescales (up to units of nanoseconds) but becomes costly for large systems or long-term behavior.



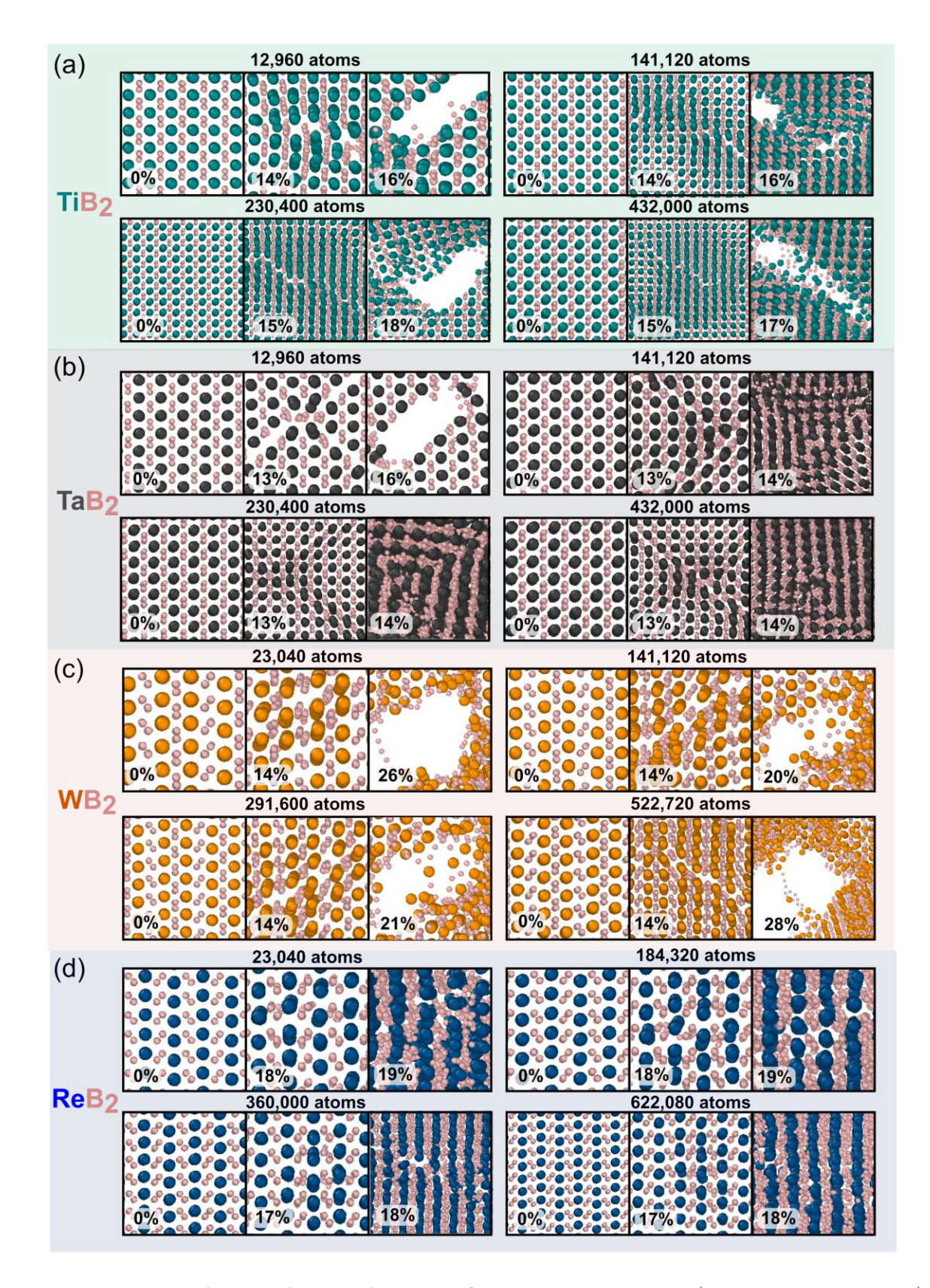


Fig. 1.6: Nanoscale tensile simulations of TMB₂ in ML-MD (TM = Ti, Ta, W, Re) along the $[10\overline{1}0]$ direction, performed using MD with MLIP. (a) TiB₂ and (b) TaB₂ in the α phase, (c) WB₂ in the ω phase, and (d) ReB₂ in the γ phase, which are their preferred phases. Simulation sizes range from 10^4 to 10^6 atoms for each material. All the data are derived from this study, for computational details see the Section 3.

For ceramics, MD has proven useful in studying mechanical properties, diffusion, defect dynamics, and thermal behavior. For example, MD simulations of ceramics like silicon carbide (SiC) or titanium nitride (TiN) often involve system sizes ranging from tens of thousands to millions of atoms [37–39]. This enables the study of fracture mechanics (e.g., tensile tests for TMB₂ as shown in Fig. 1.6 and discussed comprehensively in [Publication I]), crack propagation, or grain boundary behavior under various stress and temperature conditions, offering a detailed understanding of atomic-level processes in ceramics. MD's flexibility lies in its ability to simulate different environmental conditions, such as high temperature, pressure, or strain, making it suitable for diverse applications. It can model complex scenarios, including interactions with impurities or defects, providing a versatile tool for materials design and analysis. Researchers can also define specific environments, like mechanical loading or thermal gradients, to study how ceramics behave under real-world conditions.

However, MD has limitations. Its accuracy heavily depends on the quality of the interatomic potentials, which define how atoms interact. Developing accurate potentials for specific materials can be challenging, requiring deep knowledge of the material system. Moreover, MD simulations require expertise to properly set up and interpret, especially for complex ceramics with multiple phases or defects [40–42]. While MD is powerful for short timescales and small to moderate system sizes, it struggles with long-term processes or large-scale behaviors, limiting its applications.

1.2.3 Continuum modelling

Finite-element phase-field simulations, in contrast, operate on a mesoscale, modeling the evolution of microstructures such as grain growth, phase transitions, and domain patterns. It handles much larger systems (up to millimeters) over longer timescales (up to seconds or more) at a reduced computational cost compared to MD, as it focuses on continuous fields rather than individual atoms. This makes it valuable for predicting the long-term durability of ceramics used in high-temperature applications, such as coatings or refractory materials.

In ceramics studies, phase-field models can simulate grain growth or phase transformations across domains ranging from micrometers to millimeters, involving millions of grains. One typical example is the study of tetragonal-to-monoclinic phase transformations in zirconia (ZrO₂)-based ceramics [44, 45]. In these systems, phase-field simulations have been used to model how microcracks initiate and propagate due to this transformation, especially in thermal barrier coatings exposed to extreme temperature fluctuations. Another example is the observation of grain growth in traditional alloys |43, 46, 47], as shown in Fig. 1.7. Here, the evolution of grain boundaries is tracked over time, providing insights into how microstructures coarsen with real-time processing, effectively capturing the migration and interaction of grain boundaries, allowing for predictions of grain size distributions and growth kinetics.

One major limitation of phase-field modelling is the high computational cost, especially when simulating large systems or long-term processes, making it time-consuming and resource-intensive. Additionally, the method relies on accurate material parameters, such as grain boundary energies and mobility, which are often difficult to obtain or

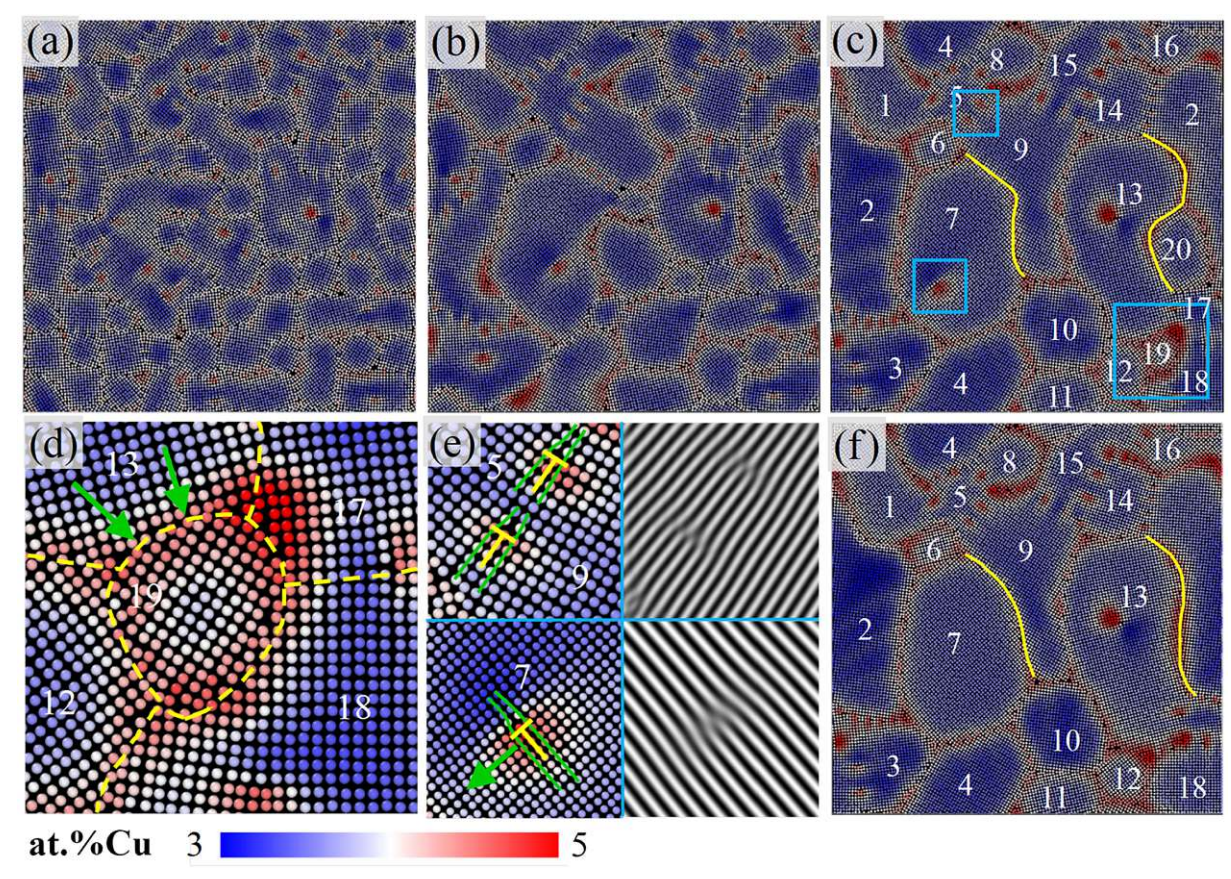


Fig. 1.7: Finite-element phase-field simulations, as exemplified with atomic evolution in traditional alloys from Ref. [43] for the different time: (a) 15 s, (b) 2 min, (c-e) 18 min, and (f) 60 min. (d) and (e) are enlarged of the blue frames in (c). (d) The process of the grain "19" is engulfed by surrounding grains. (e) The edge dislocations inside the grain "7" and grain "9", and the selected area Bragg fringe pattern.

measure for complex ceramic systems. Another limitation is that phase-field models, while effective at capturing mesoscale phenomena, lack the atomic-level detail required to fully understand nanoscale interactions [48, 49]. This makes the method less suitable for studying phenomena where atomic-scale precision is critical, such as defect interactions or small-scale phase transformations.

1.3 ML potentials: Bridging atomic and nanoscale

In MD simulations, interatomic potentials play a crucial role, as they define the forces between atoms, governing material behavior at the atomic level. Empirical potentials are applicable to traditional materials like metals, enabling simulations at scales that are beyond the reach of DFT and AIMD. However, these empirical potentials are often structure-specific and limited in their flexibility. They tend to work well for systems with simple compositions and typical physical settings (like annealing or moderate deformation) but are less effective for more complex materials or simulations requiring magnetic properties or other specialized conditions.

In recent years, machine learning interatomic potentials (MLIP) have emerged as a promising alternative [50]. By leveraging large datasets and sophisticated algorithms, MLIPs can capture a much wider range of atomic interactions, bridging the gap between atomic-scale precision and nanoscale simulation capabilities [51, 52]. This has opened new opportunities for exploring complex materials, such as multicomponent alloys or ceramics, at unprecedented scales. MLIPs offer greater freedom in material selection and enable more flexible simulation environments, such as handling diverse magnetic and mechanical properties. However, the development of MLIPs remains in its early stages, and a systematic strategy for generating and validating these potentials across different materials systems is still lacking, posing challenges for their broader application.

1.3.1 Empirical potentials

Empirical interatomic potentials provide approximate mathematical descriptions of atomic forces, allowing for efficient simulations of large systems. They are typically derived from a combination of experimental data, such as lattice constants, elastic constants, or cohesive energies, and quantum mechanical calculations. The fitting process involves adjusting the potential parameters to reproduce these key properties for specific materials. Common types of empirical potentials include the Lennard-Jones potential, the Embedded Atom Model (EAM), and the Tersoff potential.

For simple and typical ceramics like cubic TiN and BN, which often exhibit ionic or covalent bonding, potentials like the Tersoff potential are frequently used [53]. The Buckingham potential is particularly effective for ionic materials, as it accounts for both repulsive and attractive interactions between ions, making it suitable for ceramics like ZrO₂ [54, 55], while being less commonly used for metals. The Tersoff potential, on the other hand, is often used for covalently bonded ceramics such as BN [56], as it includes angular-dependent terms that better represent directional bonding in covalent systems. For alloys, the EAM is one of the most commonly applied potentials. EAM is particularly well-suited for metallic alloys, as it accounts for the many-body interactions characteristic of metallic bonding. It has been used to model alloys like copper-aluminum or nickeltitanium [57, 58], where the metallic nature of the bonding is critical to understanding properties such as dislocation behavior and phase transformations.

The key advantage of empirical potentials is their computational efficiency, enabling simulations of systems with millions of atoms over timescales of nanoseconds to microseconds. This makes them ideal for large-scale simulations of grain boundaries, defects, diffusion, and mechanical deformation in ceramics and alloys. Additionally, empirical potentials are easy to implement and are widely available for many common materials, providing a straightforward way to simulate a broad range of materials systems. However, empirical potentials come with significant limitations. Their accuracy is confined to the specific material systems for which they were designed, and they often struggle to capture the full complexity of bonding in more diverse or complex materials. For example, empirical potentials typically struggle to model systems with mixed bonding (e.g., ionic-covalent or metallic-ionic), and they lack the flexibility to handle materials with magnetic properties or highly anisotropic interactions. Moreover, empirical potentials are typically fitted to specific experimental or theoretical material's parameters (e.g., lattice constants, cohesive energies, or elastic moduli), and their transferability to new materials or conditions is often poor. This restricts their use in studying novel materials or complex phenomena, such as phase transitions or extreme environments.

1.3.2 ML-Based potentials

Machine-learning potentials represent a transformative approach for modeling interatomic interactions, providing a significant advancement over traditional empirical potentials by being data-driven and highly flexible. Unlike empirical potentials, MLIPs are trained on quantum mechanical data – often derived from DFT or AIMD – to capture a broader and more accurate range of atomic interactions ². This makes them particularly valuable for complex materials, where traditional models may struggle to describe the diversity of bonding environments and atomic-scale phenomena. Fig. 1.8 summarizes the comparison of present typical MLIPs [59].

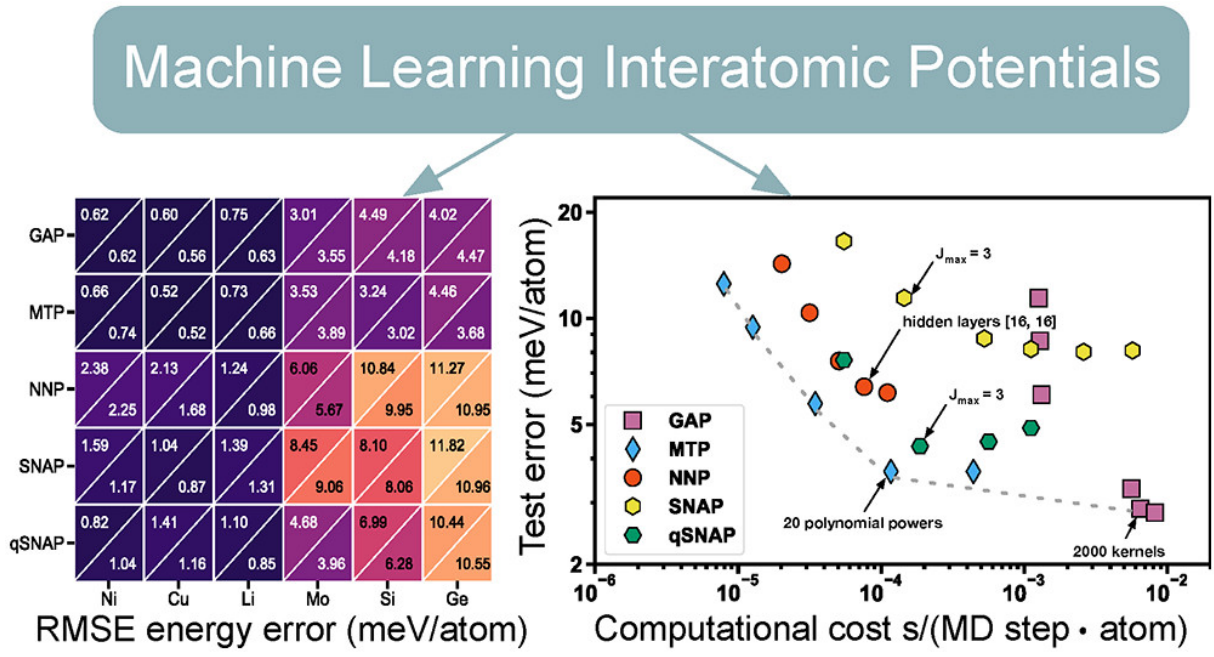


Fig. 1.8: Comparison of MLIPs for Mo system trained using various formalisms and their implementation from Ref. [59]. (right) Test error versus computational cost. The gray dashed line indicates an approximate Pareto frontier formed by the convex hull of points lying on the bottom left of the chart. Timings were performed by LAMMPS calculations on a single CPU core. Black arrows denote the "optimal" configuration for each MLIP that was used in subsequent comparisons. (left) Rootmean-square errors in predicted energies for the selected MLIPs. The upper left and lower right triangles within each cell represent training and test errors, respectively.

Several types of MLIPs have emerged in recent years, each offering unique methodologies and strengths, could be classifed into three different models: artificial neural network (NN) models, kernel-based models, and linear models [60]:

As a representative example of the first category, Neural Network Potentials
 (NNP) are among the most widely used, employing deep learning techniques

^{2*} In the case of **MLIP**, the process involves fitting the energy, forces, or stresses of a specific configuration. These configurations need to be encoded using descriptors of the local atomic environment in a mathematical form for training, as discussed in the following paragraphs.

^{**} This approach contrasts with training **empirical potentials**, where raw or direct data, such as lattice constants or surface energy, are used directly without the need for encoding the atomic environment in such a detailed manner [50].

to predict potential energy surfaces (PES) based on atomic configurations. This approach, used in frameworks like ANI [61], has been applied to oxide ceramics, accurately modeling phase transitions and defect behavior.

- A well-known example of second type, which employs a kernel function to map atomic configurations into a higher-dimensional space where linear relationships can be more easily identified, is Gaussian Approximation Potentials (GAP). GAP utilized Gaussian process regression to interpolate PES [62]. GAP, as implemented in the QUIP package [62], has been particularly effective for simulating complex systems like tungsten alloys [63, 64], where both short-range covalent and longrange Van der Waals interactions are significant.
- Finally, linear models typically use descriptors of atomic environments (e.g., radial distribution functions, bond angles) as input features and fit a linear model to predict the energy or forces. For instance, Atomic Cluster Expansion (ACE) is designed to provide a systematic and hierarchical representation of interatomic potentials as a sum of contributions from clusters of atoms [65]. ACE is implemented in, e.g., the PACE software [66], which is optimized for large-scale simulations of multicomponent systems. The ACE formalism allows for systematic improvements in accuracy by expanding atomic cluster functions, offering a balance between computational efficiency and precision. This makes ACE especially suited for a wide range of materials systems, including where traditional potentials may fall short. Compared to other MLIPs, ACE requires fewer fitting parameters, making it more computationally manageable for large systems. Moment Tensor Potentials (MTP), utilized in the MLIP package [67, 68], provide a middle ground between accuracy and efficiency, employing moment tensor descriptors to capture local atomic environments. Here the PES is represented as a linear combination of moment tensor descriptors \mathcal{M} , as $E_{\text{total}} = \sum_{i} \sum_{\alpha} C_{\alpha} \mathcal{M}_{\alpha} (\mathbf{R}_{i})$, where C_{α} are the coefficients to be fitted, \mathbf{R}_i is the local environment of atom i. MTPs have been successfully used in large-scale simulations of ceramics like silica [69], demonstrating their ability to case-dependent properties but still face limitations in terms of transferability across different phases without extensive retraining.

However, the accuracy of these models is highly dependent on the quality and diversity of the training data, and generating comprehensive datasets – especially for multicomponent or highly anisotropic materials – remains computationally expensive. Furthermore, while MLIPs like NNP, GAP, MTP, and ACE excel within the chemical space they are trained on, their transferability to novel phases or extreme conditions is often limited. A systematic strategy for training MLIPs that covers a broad range of material properties, phases, and defect configurations is still lacking. Additionally, while they offer near quantum-level accuracy for large-scale simulations, the computational cost of training and the expertise required to implement them are significant challenges.

Furthermore, in recent years, a number of universal foundation models have been developed [70–72]. These models are designed to be applicable to a wide range of compounds and are typically trained on large databases, such as the Materials Project [73], complemented by additional DFT-generated datasets. They demonstrate promising scalability in some complex environments, such as aqueous systems and cubic alloys. While generally consistent with DFT, these models require caution under dynamic conditions or in less stable, low-symmetry systems like orthorhombic phases and interfaces. Nonetheless, their baseline representations greatly speed up training of specialized models.

Chapter 2

Materials selection

Group-IV-VII transition metal diborides (TMB₂) are a significant class of materials known for their remarkable properties, including high hardness, excellent transport properties (both thermal and electrical), and unique structural characteristics, offering a suitable basis for further optimization motivated by specific industrial needs [74]. Phase and stoichiometry control in TMB₂ compounds have garnered significant interest in engineering fields, highlighting the need for large-scale simulations to predict and optimize their behavior, thereby enhancing material performance and reliability in practical applications. Fig. 2.1 illustrates the most typical three phase prototypes of Group-IV-VII transition metal diborides, highlighting the α (space group(s.g.), P6/mmm), ω (s.g. $P6_3/mmc$), and γ phases (s.g. $P6_3/mmc$). The α phase is favored by all Group-IV and -V TMB₂:s, Group-VI TMB₂:s prefer to stabilize in α (CrB₂ and MoB₂) and ω (WB₂) phase, while the γ phase is characteristic of Group-VII TMB₂:s [75, 76].

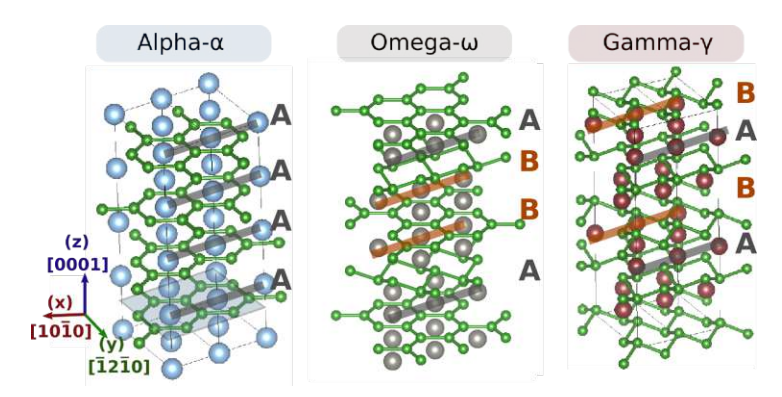


Fig. 2.1: Structural representations of the most typical phases in Group-IV-VII transition metal diborides: (left) α phase, (middle) ω phase, and (right) γ phase. Green atoms represent boron, while metal atoms are displayed in larger sized and distinguishable colors. The stackings marked here are according to the metallic sublattice.

2.1 Transition metal diborides

Group-IV (TiB₂, ZrB₂, HfB₂) and Group-V (VB₂, NbB₂, TaB₂) transition metal diborides (TMB₂:s) belong to a class of ultra-high temperature ceramics (UHTCs) known for their excellent physical and chemical properties. These TMB₂:s compounds share several key characteristics, such as crystallizing in the same hexagonal AlB₂-type

structure (under/near ideal stoichiometry), exhibiting excellent thermal stability, and having high hardness, wear resistance, and good electrical and thermal conductivity [77, 78. However, Group-IV and -V diborides, generally exhibit higher melting points (above 3000°C) compared to Group-VI diborides, which have melting points around 2100°C as summarized in Ref. [79]. Additionally, Group-IV diborides tend to show superior oxidation resistance, forming protective oxide layers at high temperatures [80]. Regarding commonly applied temperatures, their similar mechanical response under tensile and shear deformation between 300 to 1200 K is discussed in [Publication I] and [Publication II], with example of TiB_2 and TaB_2 , respectively.

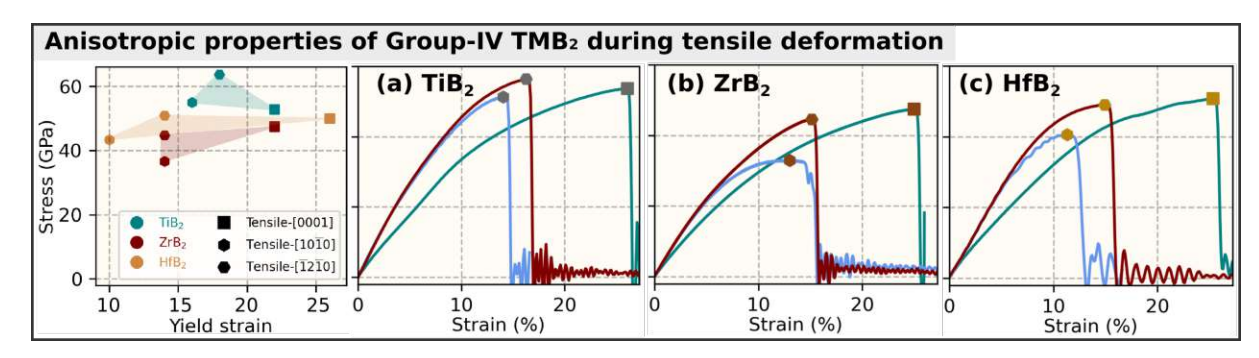


Fig. 2.2: Anisotropic properties of Group-IV TMB₂:s during tensile deformation along three main orientations. (Left) Stress-strain scatter pattern during tensile deformation along [0001] (square), $[10\overline{1}0]$ (hexagonal), and $[\overline{1}2\overline{1}0]$ (rotated hexagonal) for TiB₂ (gray), ZrB₂ (brown), and HfB₂ (yellow). The shaded area represents isotropy, with smaller areas indicating greater isotropy. Stress-strain curves of (a) TiB₂, (b) ZrB_2 , and (c) HfB_2 along [0001] (teal), [10 $\overline{1}0$] (red), and [$\overline{1}2\overline{1}0$] (blue), respectively. All the data are derived from this study, for computational details see the Section 3.

Group-VI TMB₂:s, including CrB₂, MoB₂, and WB₂, exhibit slightly different phase preferences and properties. While WB₂ tends to favor the ω phase, in contrast to the α phase preferred by the others. However, it can also be stabilized in the α phase, which will be discussed further in the next chapter. In terms of applications, CrB₂ is commonly used for wear-resistant coatings and holds potential in tribological applications [81]. MoB₂ and WB₂ are often utilized as hard coatings, high-temperature structural materials, and have emerging potential in electronic applications due to their conductivity and durability [82]. However, these materials tend to exhibit less structural stability at extreme temperatures, with a tendency toward phase separation. Research has shown that forming solid solutions between MoB₂ and WB₂ can enhance their stability; however, this approach tends to reduce the material's toughness [83–85]. In addition to previous researches, this work presents a direct comparison between Group-IV to -VI TMB₂ compounds, Tab. 1 summarizes the collected data on these materials, highlighting their preferred crystallographic phases.

Group-VII TMB₂:s are less frequently studied due to the high costs of synthesis and the need for precise equipment and controlled conditions. These materials exhibit unique bonding characteristics, with a tendency toward more complex phase behavior compared to Group-IV-VI TMB₂:s, primarily stabilizing in the γ phase. ReB₂ stands out with exceptional mechanical properties, achieving hardness around 54 GPa in experiments, rivaling diamond [86]. ReB₂ also has a high melting point (≈ 3000 °C) and metallic

thek	
Siblio Your knowledge	

Group	TMB_2	a	c	C_{11}	C_{33}	C_{44}	C_{12}	C_{13}	E	B	G	ν
	TiB_2	3.036	3.218	588	430	252	79	111	547	244	243	0.126
Group-IV	${\rm ZrB_2}$	3.176	3.536	531	381	263	68	129	511	232	226	0.132
	HfB_2	3.139	3.478	502	401	271	74	114	508	223	227	0.120
	TaB_2	3.094	3.327	510	392	252	72	125	486	221	214	0.134
Group-V	VB_2	2.998	3.030	652	496	224	136	125	572	283	246	0.164
	NbB_2	3.124	3.297	397	324	123	54	139	332	198	136	0.220
	WB_2	3.014	14.035	531	383	72	195	232	316	305	119	0.327
Group-VI	CrB_2	2.978	2.963	536	367	102	165	173	370	269	146	0.270
	MoB_2	3.031	3.328	508	413	126	127	187	392	270	156	0.257

Tab. 2.1: Room-temperature lattice parameters and elastic constants of Group-IV,V,VI TMB₂:s derived from *ab initio* MD simulations. Lattice parameters (a, c in Å) and elastic constants $(C_{ij}, \text{ in GPa})$ at the temperature 300 K, presented together with the polycrystalline bulk modulus, B (in GPa), shear modulus, G (in GPa), Young's modulus, E (in GPa), and Poisson's ratio, ν . WB₂ is in the ω phase, while all the others in α phase. All the data are derived from this study, for computational details see the Section 3.

conductivity, making it suitable for applications in extreme environments, such as wear-resistant coatings. In contrast, MnB₂ and TcB₂ have limited industrial applications due to their instability and lack of extensive research [87]. Also, magnetism is a characteristic of Group-VII TMB₂:s, which affect directly their electronic and mechanical behavior, particularly in MnB₂ [88], making it suitable for specific applications in electronics or spintronics. However, it adds another layer of complexity for synthesis as well as modelling. Current research trends focus on further developing ReB₂ for ultra-hard materials in the field of engineering, while MnB₂ is considered as candidate for energy-related application.

2.2 Phase-dependent behavior of diborides

The typical polymorph structures of TMB₂ discussed here are the α , ω , and γ phases. However, other phases can also appear, sometimes deviating from the ideal TM/B = 1:2 stoichiometry, and forming structures with different atomic ratios or incorporating defects. Particularly for W-B system, which exhibits a wide range of stabilizable stoichiometries [89], as illustrated in Fig. 2.3.

For instance, orthorhombic and cubic phases have been observed in some TMB₂ compounds, such as MnB₂, where non-hexagonal polymorphs emerge. These phases, while often **metastable**, tend to revert to the hexagonal structure under standard conditions. Their similarity to other phases makes them challenging to detect, often leading to ambiguity in phase characterization. High-pressure phases are another possibility, where extreme pressures can induce structural changes in transition metal diborides. Theoreti-

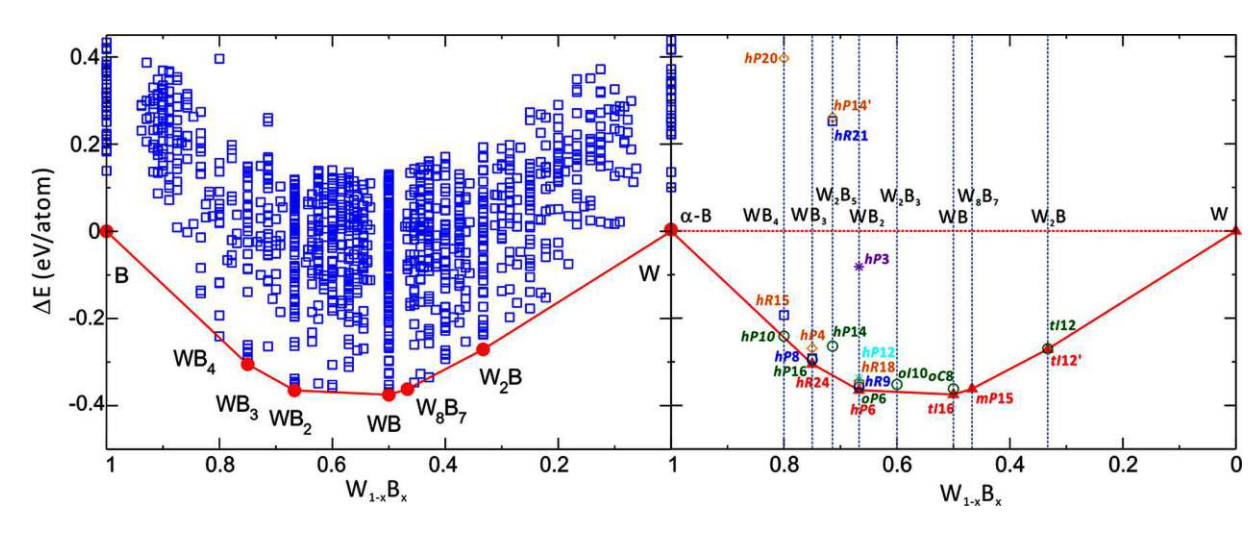


Fig. 2.3: Phase stability of W-B systems from Ref. [89], as predicted via 0 K DFT calculations of formation enthalpies: (Left) Enthalpies of formation for the W-B system, predicted using variable-composition evolutionary computations. Each square represents an individual structure, with the most stable ground-state phases (solid circles) connected to form the convex hull. (Right) A detailed convex hull plot, showing the formation enthalpy as a function of composition for selected tungsten borides. The plot includes all the lowest-enthalpy ground-state phases located on the convex hull, providing a clear visualization of the energetically favorable phases.

cal predictions for compounds like TiB₂ and ScB₂ suggest transitions into high-pressure polymorphs [90], though experimental validation remains elusive due to the complexities of high-pressure synthesis and detection. Many TMB₂ compounds, particularly those in Group-V and Group-VI, exhibit boron-deficient (substoichiometric) phases, often arising from the inherent difficulty in controlling stoichiometry during synthesis [91]. Boron vacancies within the crystal lattice introduce defects that significantly impact mechanical, electrical, and thermal properties. These vacancies disrupt the metallic and covalent bonding networks, influencing phase stability, electrical conductivity, and thermal behavior. In some cases, TMB₂ compounds may also form boron-rich (overstoichiometric) phases, especially during high-temperature processing [92–94]. Excess boron can precipitate as secondary phases, such as elemental boron or boron-rich compounds (e.g., B₆, B₁₂), which increase hardness but may reduce toughness. Additionally, overstoichiometric boron can complicate sintering processes, making it more difficult to achieve dense, defect-free materials. These phases can form thin amorphous layers at grain boundaries, which are typically undetectable by standard diffraction techniques [91, 95. However, it can be observed and quantified using neutron diffraction or transmission electron microscopy (TEM) [96], as demonstrated in Fig. 2.4, where the tissue phase in $TiB_{4.42}$ is identified using high-resolution TEM (HR-TEM).

The phase behavior and mechanical response of TMB₂ becomes increasingly complex when combined with other diborides or/and compounds, or subjected to extreme conditions. Group-IV TMB₂:s generally retain their α phase over a wide temperature range. However, under specific conditions—such as alloying—these materials can exhibit the formation of solid-solution or grain-boundary [97]. In contrast, Group-V and Group-VI display more complex phase behaviors at high temperatures. For example, at elevated

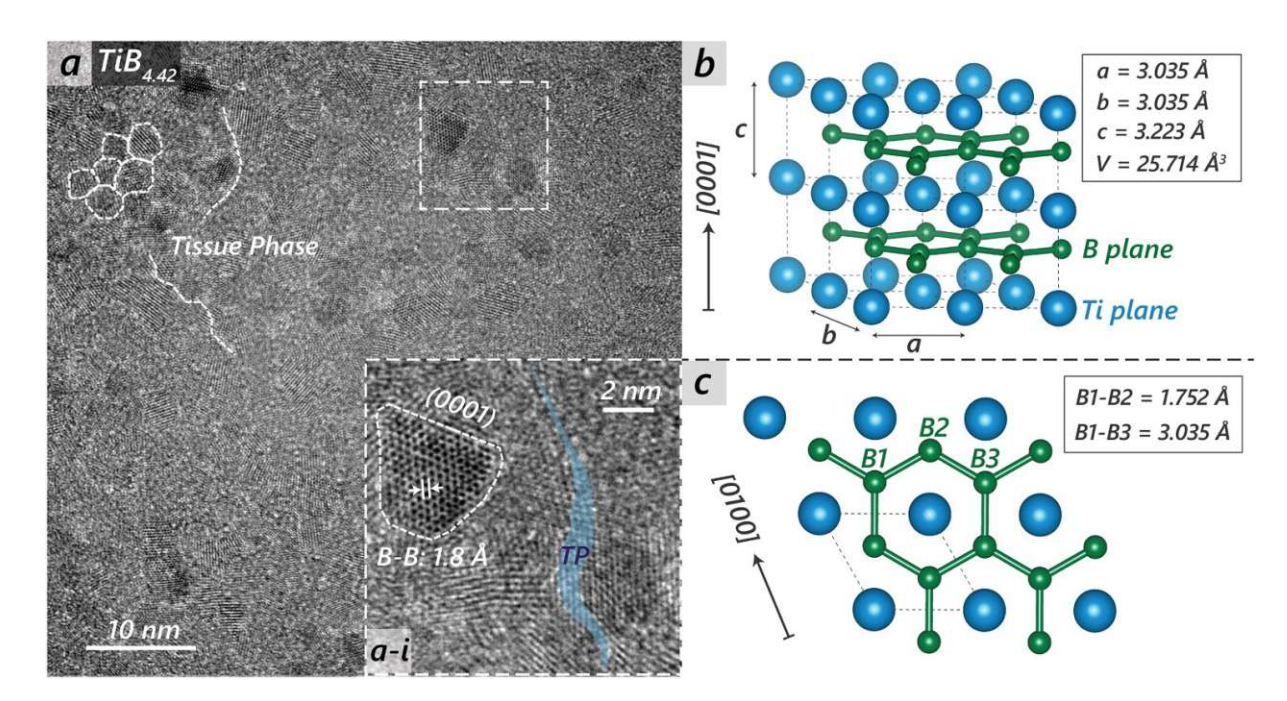


Fig. 2.4: High-resolution transmission electron microscopy (HR-TEM) top view analysis of a TiB_{4,42} thin film, revealing interatomic length scales from Ref. [96]. The dashed lines in panel (a) delineate specific nano-columns separated by boron-rich tissue phases. A magnified view of the selected area indicated by the dashed square in (a) is presented in (a-i), showcasing an ideally oriented [0001] column, with visible boron hexagons representing the basal B plane of the hexagonal TiB₂ crystal lattice (α phase). Measurements indicate an interatomic nearest B-B distance of 1.8 Å. The blue shaded area highlights an approximately 2 nm thick tissue phase (TP) separating the columns. Panel (b) depicts a α -TiB₂ atomic model while Ti in blue and B in green. Panel (c) presents the TiB₂ supercell with B-B distances delineated.

temperatures, WB₂ can undergo a transformation to another hexagonal phase, which reduced its hardness [98]. Additionally, phase transitions induced by temperature or pressure can also lead to drastic improvement in electrical behavior. For instance, certain materials like NbB₂ exhibit superconductivity at low temperatures [99, 100], with the transition to insulating or semiconducting states under specific conditions. Alloying diborides (e.g., ZrB₂-HfB₂ systems) can also facilitate the formation of solid solutions with enhanced properties [101]. These solid solutions are often thermodynamically stable at elevated temperatures, but they can undergo phase separation under specific conditions. For example, TaB₂ may decompose into various diborides or metal-rich phases, with the specific phase stability being influenced by the alloying elements and processing conditions, as disscused in [Publication V] with an example of AlB₂-TaB₂.

As discussed above, the synthesis and application of TMB₂ involve a complex interplay of chemistry and defects that significantly influence the resulting phase and properties of the material. However, traditional characterization methods often struggle to detect these variations in experiments and properly control the composition, making it challenging to observe comprehensive phase-dependent behavior. As such, a deeper investigation into the phase stability and transformation processes is essential for optimizing the design and performance of diboride materials. On this purpose, the impact of phase transitions

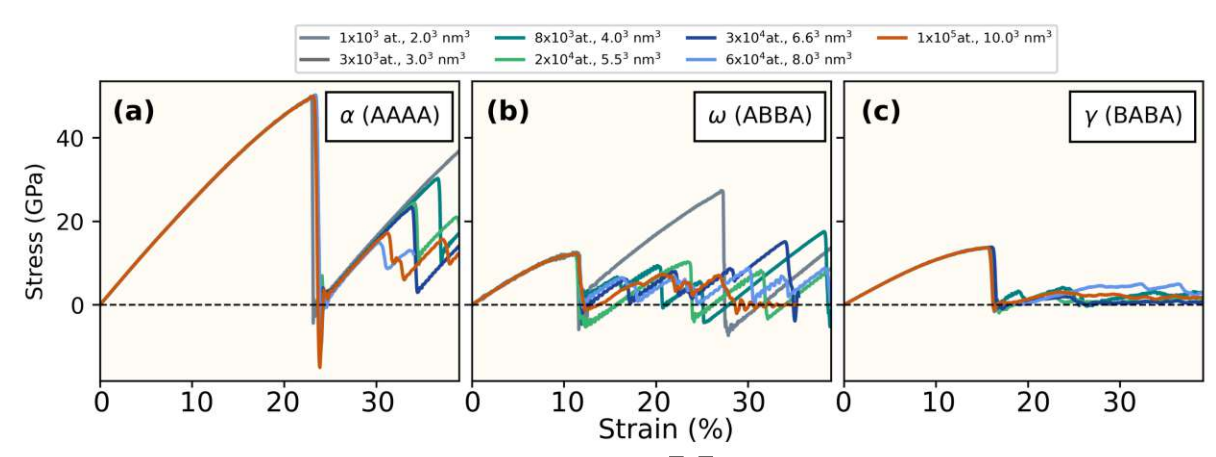


Fig. 2.5: Stress-strain curves during $(0001)[\overline{1}2\overline{1}0]$ shear deformation of TiB₂ are **presented for different phases:**(a) α , (b) ω , and (c) γ (recall Fig. 2.1, the stacking marked here are according to metallic sublattice, same for the next figure). The simulations conducted using different sizes of supercell at 300 K, and provide insight into the transition from atomic scale ($\approx 10^3$ atoms) to nanoscale ($\approx 10^5$ atoms). All the data are derived from this study, for computational details see the Section 3.

on mechanical properties is further discussed in [Publication II], which explores the relationship between phase stability, microstructural changes, and performance metrics, as illustrated in Fig. 2.5, the complete $\omega \to \alpha$ phase transition occurs during shear deformation in TiB₂. In contrast, Fig. 2.6 depicts a partial $\alpha \to \omega$ transition in WB₂ under similar conditions. These two examples highlight the significant impact of phase transitions on room-tenperature shear strength; specifically, the full transition in TiB₂ leads to a more pronounced reduction in mechanical performance compared to the partial transition observed in WB₂. Furthermore, while the decline in shear strength values does not exhibit significant changes with increasing size, the underlying phenomena associated with these properties do vary across atomic to nano scale.

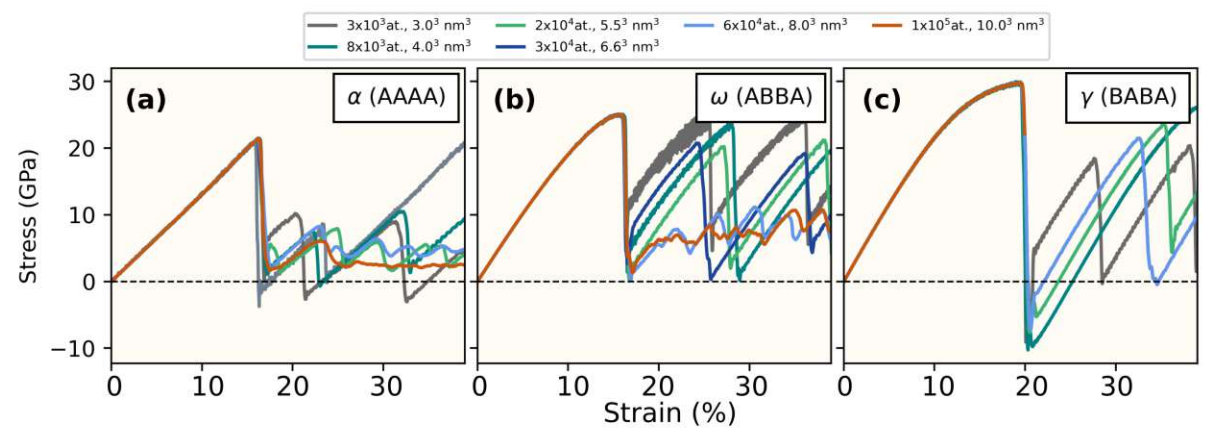


Fig. 2.6: Stress-strain curves during $(0001)[\overline{1}2\overline{1}0]$ shear deformation of WB₂ are presented for different phases:(a) α , (b) ω , and (c) γ (recall Fig. 2.1). The simulations conducted using different sizes of supercell at 300 K, and provide insight into the transition from atomic scale ($\approx 10^3$ atoms) to nanoscale ($\approx 10^5$ atoms). All the data are derived from this study, for computational details see the Section 3.

Chapter 3

Computational methodology

This section outlines the methodology for constructing accurate machine learning interatomic potentials (MLIPs) tailored to the selected materials. The process begins with equilibrium structure calculations at finite temperatures using ab initio molecular dynamics (AIMD), followed by training MLIPs within the moment tensor potential (MTP) formalism using the AIMD-generated data. The procedures for generating the training dataset, detailing the training workflow, and validating the developed MLIPs to ensure their reliability and applicability are presented.

3.1 *Ab initio* calculations

The ab initio calculations in this study serve as both the training data for developing MLIPs and the reference standard for their validation, playing a critical role in the overall process. The accuracy and precision of these calculations directly influence the performance of the target machine learning-assisted molecular dynamics simulations (ML-MD). Initially, equilibrium structures of the selected materials are determined through a two-step process combining isobaric-isothermal and canonical ensembles. Subsequently, step-wise deformation and extreme loading simulations are conducted using only the canonical ensemble. Finally, static calculations for surface energy and point defect energy are performed with the same level of accuracy, ensuring consistency and enabling the evaluation of the transferability of the developed MLIPs.

Finite-temperature Born-Oppenheimer ab initio molecular dynamics (AIMD) simulations and first-principles calculations were conducted using VASP [102], employing the projector augmented wave (PAW) [103] method and the Perdew-Burke-Ernzerhof exchange-correlation functional revised for solids (PBEsol) [104]. All simulations were performed with a plane-wave cut-off energy of 300 eV, as the AIMD simulations utilized Γ-point sampling of the reciprocal space, while a k-mesh of 60 in each direction for first-principles calculations. It is important to note that the pseudopotentials employed in this study use minimal valence electrons and show good agreement with prior theoretical studies (as exhibited in [Publication I]). However, for accurate calculations of electronic, phonon, or magnetic properties, the choice of pseudopotential requires careful testing to ensure accuracy and reliability.

For the equilibration of here-studied TMB₂, a two-step process was followed: (i) a 10 ps AIMD isobaric-isothermal (NpT) simulation using the Parrinello-Rahman barostat [105] and Langevin thermostat, and (ii) subsequent AIMD runs of 2 ps for

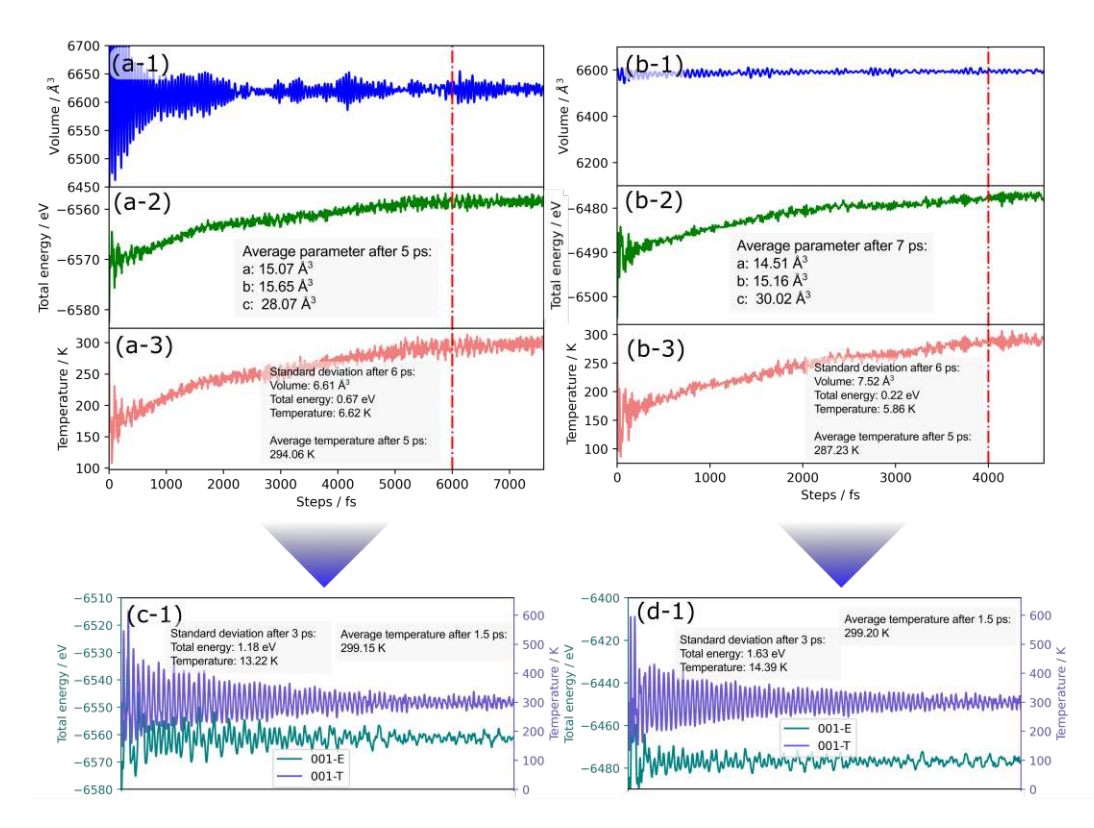


Fig. 3.1: Example of convergence evaluation during an AIMD simulation: The volume, total energy, and temperature evolution with an (a,b) NpT ensemble, using a 720-atom (left) WB₂ and (right) ReB₂ supercell and temperature of 300 K, respectively. Total energy variation during a (c,d) subsequent NVT simulation with time-averaged lattice parameters—calculated based on the NpT data after the red vertical line (converged). Specifically, equilibration is reached after 5 ps: steady trends in property vs. time. Thus, lattice parameter a is calculated as time-averages after 3 ps till the end of the simulation. All the data are derived from this study, for computational details see the text in this section.

300 K and 4 ps for 1200 K in the canonical (NVT) ensemble, using the time-averaged lattice parameters obtained from the NpT simulation (see Fig. 3.1 with example of ω -WB₂ and γ -ReB₂). For both tensile and shear deformation simulations, a 2% strain increment was applied, followed by a 2.7 ps NVT simulation at each strain step to ensure equilibration before proceeding to the next increment. The extreme load for tensile deformation corresponds to a 150% elongation along the deformation direction, while for shear deformation, it corresponds to a 60% displacement along the fixed direction. The purpose of conducting simulations under extreme load conditions is to generate additional atomic environments describing the onset of void formation and fracture. These representations are crucial for diborides capable of redistributing stress more plastically—such as WB₂, with a higher valence electron concentration than TiB₂—favoring bond rearrangements or local transformations to other polymorphs. For more ductile materials, these conditions may offer limited additional insight over step-wise tests, requiring adjusted load levels for effective training data. Static 0K calculations were performed using a smaller TMB₂ supercell (between 50-80 atoms). The supercell

was **fully relaxed** at 0 K (in terms of lattice constants and atomic positions) until forces on atoms were below 10^{-5} eV/Å and total energy was converged until 0.01 eV/supercell.

3.2 Training workflow for machine-learning interatomic potentials

This section presents a detailed strategy for training MLIPs tailored to ceramic systems, with a focus on binary diboride ceramics as an example. By outlining the key steps in the training process, it provides a comprehensive guide for developing accurate and transferable MLIPs that can be applied to a range of ceramic systems in case-dependent simulations. The developed training procedure is described below and depicted in Fig. 3.2.

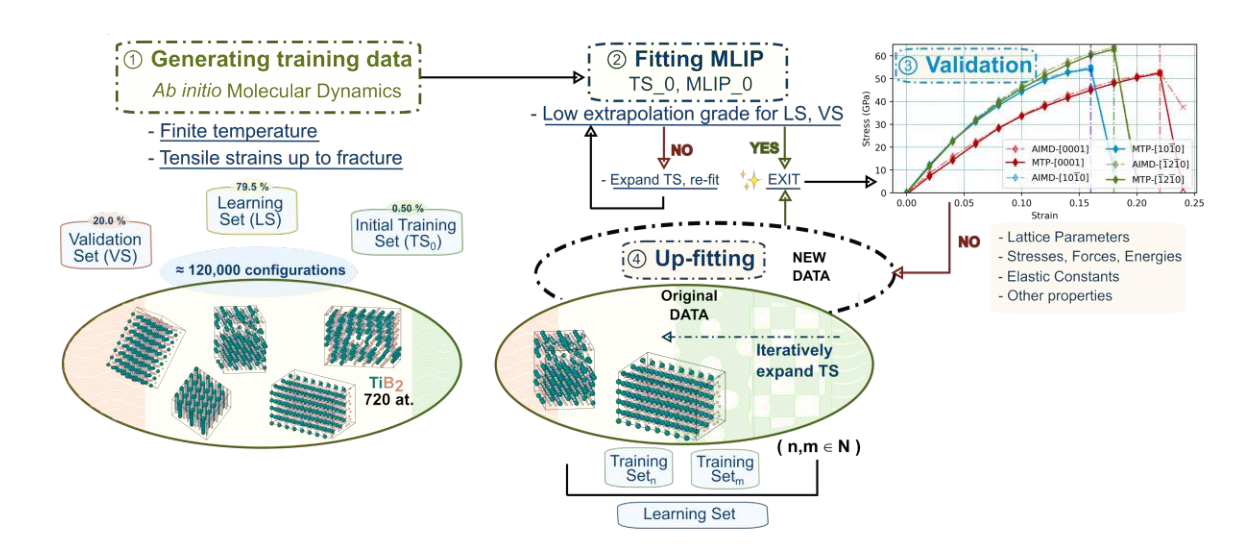


Fig. 3.2: Schematic visualization of general training procedure, validation, and upfitting. For the validation part, there's an example of stress/strain curves of TiB₂ while uniaxial step-wise tensile deformation, in which the results of AIMD and ML-MD exhibite excellent agreement. This result are derived from this study, for details see the text in this section.

In this study, ab initio training data are generated using finite-temperature AIMD simulations, which typically produce a large number of highly correlated configurations. Here, a configuration refers to a structure characterized by ab initio total energy, atomic forces, and the six components of the stress tensor. To prevent over-representation of similar configurations, the MLIP training process begins with a small subset of AIMD configurations and employs the MLIP's uncertainty estimation, quantified by the extrapolation/Maxvol grade [106] (γ) , to iteratively expand the training set. This process continues until all AIMD configurations are accurately represented. The Maxvol grade, mathematically formalized in Refs. [106–108], measures the degree of extrapolation in MLIP predictions for energy, forces, and stresses. Specifically, $\gamma \leq 1$ indicates interpolation, while $\gamma > 1$ reflects extrapolation. Building on the work of Shapeev and co-workers [68], who define $\gamma \leq 2$ as accurate extrapolation, a threshold value of $\gamma_{\text{thr}} = 2$ is adopted in this workflow as the criterion for concluding the training loop.

In greater detail, fitting/up-fitting process involves training the MTP to reproduce the high-fidelity reference data obtained from ab initio calculations, serves as critical bridges between an untrained or insufficiently trained MLIP and a fully developed, reliable MLIP. This is achieved by minimizing the errors between the MTP's predictions and the reference values for energies, atomic forces, and stress tensors. The initial training dataset (TS_i) , capturing configurations representative of the system's equilibrium and slightly perturbed states. The resulting potential is validated against an independently and randomly selected validation set (VS) to assess its accuracy within the interpolation domain of the sampled configuration space. Active learning complements this by iteratively improving the model's robustness. It begins with the MTP (IP_i) estimating an extrapolation grade (γ) for each configuration in LS, quantifying the degree to which a configuration lies outside the training data's interpolation region. Configurations with high γ values, indicative of extrapolation, are flagged for further exploration. For these configurations, will be incorporated into the next training dataset (TS_{i+1}). The MTP is then retrained as IP_{i+1} , gradually reducing its extrapolation errors.

A detailed example involving TiB₂ and other ceramics is thoroughly discussed in [Publication I].

Algorithm 1 MLIP training

- (1) Generate a pool of AIMD configurations.
- (2) Divide the pool into an initial training set (TS_0) , a learning set (LS), and a validation set (VS) by randomly selecting 0.5%, 79.5%, and 20% of non-overlapping configurations.
- (3) Fit an initial MLIP (MLIP₀, trained on TS₀). If γ of all configuration in the LS and VS is below $\gamma_{\rm thr}=2$, exit. Else, build TS₁ by adding (maximum 15) highly extrapolative configurations from the LS to TS_0 and fit a new MLIP (MLIP₁, trained on TS_1).
- (4) While γ of all configurations in the LS and VS is above $\gamma_{\text{thr}} = 2$, build TS_i by adding (maximum 15) highly extrapolative configurations from the LS to TS_{i-1} , and fit a new MLIP (MLIP_i, trained on TS_i).

Technical comments on above procedure:

- MLIP₀ in the step (3) is trained from an untrained MTP. MLIP_i in step (4) is fitted from $MLIP_{i-1}$ if maximum γ in the (i-1)th iteration is below 1000.
- The VS is not used for training but only as a reference.
- Besides γ , quality of the fit at each iteration i in (4) is monitored through errors of energies, forces and stresses (quantified by common regression model evaluation metrics, MAE, RMSE, R^2 , see e.g. Refs. [109–111]) for the TS_i (fitting errors) and the VS (validation errors) ¹.

As the core principles underlying the training process – including the systematic generation of high-quality training data, the iterative selection of configurations based on extrapolation uncertainties, and the progressive refinement of the model—are widely applicable across different formalisms, the training workflow outlined in this section. although developed using the MTP formalism, is expected to be transferable to other

¹One may use fitting and validation errors as additional criterion (besides $\gamma_{\rm thr}$) for exiting the training loop.

machine learning frameworks. In particular, those that incorporate a similar definition of extrapolation control, such as the Atomic Cluster Expansion (ACE) method, thereby broadening its applicability to different classes of materials and simulation conditions.

3.3 Molecular dynamics simulation

After developing MLIPs, the next step is to perform ML-MD simulations. Initially, the MLIP is validated by setting up a finite-temperature MD simulation that closely mirrors the conditions of the original AIMD calculations, essentially replicating the settings used in the training set. However, it is important to note that exact equivalence between MD and AIMD settings is not achievable, particularly in dynamic simulations. The relevant thresholds for acceptable differences between the two approaches are also provided. Once validated, the MLIP is scaled to nanoscale systems, and methodologies for evaluating the stability and feasibility of large-scale simulations are introduced to ensure model reliability throughout the simulations.

ML-MD calculations were carried out using the LAMMPS code [112], interfaced with the MLIP-2 package [113], which enables simulations with MTP-type potentials. The computational setup for the atomic-scale ML-MD simulations (validation tests) was made equivalent to the AIMD tests described previously, in terms of simulation duration and ensemble type. Specifically, the simulations were performed using the same supercell size and orientation as those in the AIMD calculations.

Fig. 3.3a-d shows stress/strain curves obtained from room-temperature AIMD and ML-MD tensile tests, where TMB₂ supercells (TM = Ti, Ta, W, Re, containing approximately 10^3 atoms and with dimensions around $\approx 1.5^3$ nm³) are loaded in the [0001] direction. The excellent quantitative agreement between the AIMD and ML-MD results confirms the reliability of the developed MLIPs, as deformation and mechanical failure phenomena match closely (Fig. 3.3-Snapshot). Specifically, the time-averaged stresses in ML-MD deviate from AIMD values by 0.07–1.94 GPa, resulting in a statistical error with RMSE ≈ 1.02 GPa and $R^2 \approx 0.9997$. It is important to note that a small difference (≤ 0.04) in the yield point between the two methods does not indicate a loss of agreement. As the applied stress approaches the material's strength, the system is near failure, and the dynamic nature of the simulation introduces randomness in this process. Repeated AIMD and ML-MD simulations would yield nearly overlapping average results for strength and yield point. The fracture point during [0001] deformation is excluded from the analysis, as the stress component in AIMD does not drop to zero due to long-range electrostatic effects that are not accounted for in the ML-MD simulations.

Nanoscale ML-MD tests were conducted using supercells containing over 10⁴ atoms. Before simulating mechanical deformation, the supercells were equilibrated for 5 ps at the targeted temperature using the isobaric-isothermal (NpT) ensemble coupled to the Nosé-Hoover thermostat, with a 1 fs time step. Tensile loading was applied by deforming the supercell at each time step with a constant strain rate of 0.5 m/s, while accounting for lateral contraction (Poisson's effect) through the NpT thermostat. Building on the atomistic validation results, Fig. 3.4 illustrates the size effect across both atomistic and nanoscale regimes, demonstrated with TiB₂ under continuous tensile deformation along the [0001] direction. At the nanoscale, the size effect continues to influence the

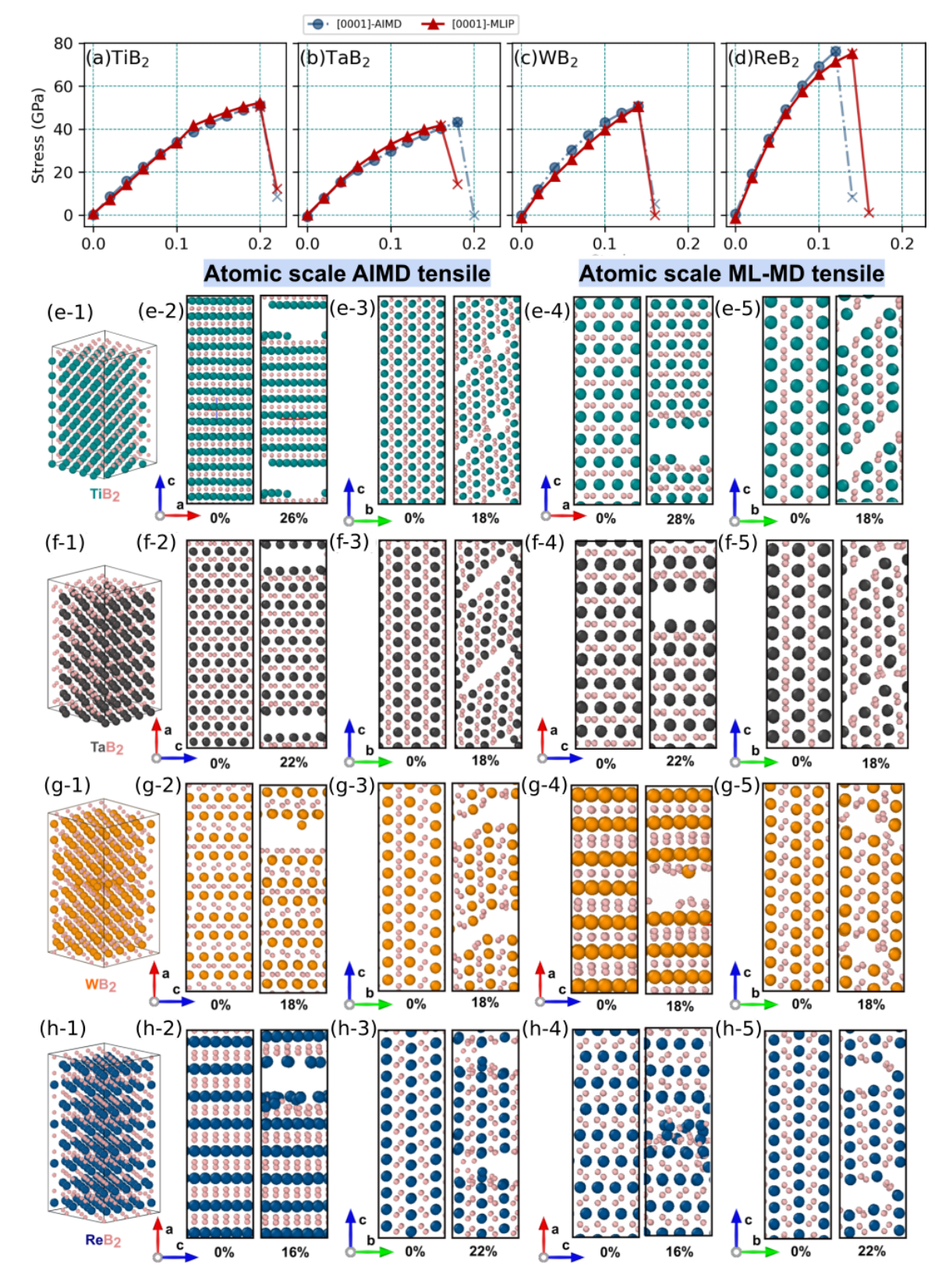


Fig. 3.3: Example of validating the developed MLIPs: Comparison of stress–strain responses (a–d), deformation mechanisms, and fracture initiation (e–h) during stepwise tensile test subject to [0001] per AIMD (blue) and ML-MD (red) of (a) α -TiB₂, (b) α -TaB₂, (c) ω -WB₂, and (d) γ -ReB₂, respectively. All the data are derived from this study, for computational details see the text in this section.

failure mechanism, although the maximum tensile strength shows only a slight variation. Additionally, not all developed MLIPs are capable of performing nanoscale simulations. MLIPs that produce stable configurations far beyond the yield point over extended timescales, along with reliable extrapolation grade values, are considered viable. In contrast, those that fail to progress beyond yielding are deemed unviable., as exhibited in **[Publication I]**. For cases involving phase transformations – such as those induced by shear deformation, as demonstrated in **[Publication II]** – which are inherently more complex to model and pose greater challenges for MLIP training, the current viability criteria may require re-evaluation. However, since tensile deformation is the most fundamental and straightforward deformation test, it is always preferable to first confirm the availability of the MLIP through tensile tests before proceeding with more complicated simulations. This offers a robust foundation for further investigations, such as the pre-cracked model used to simulate fracture toughness, as presented in **[Publication III]**.

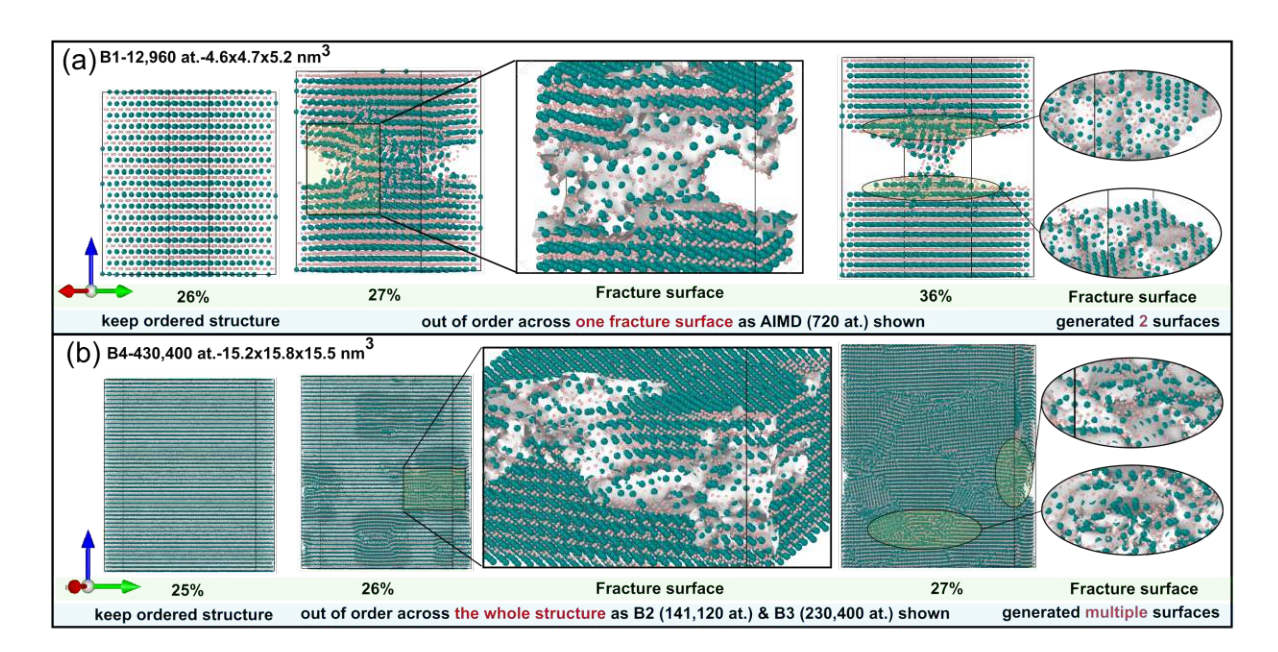


Fig. 3.4: Example of size effect in nanoscale via ML-MD in α-TiB₂ under [0001] tensile deformation, with Poisson's contraction applied on lateral sides. (a) At a 5 nm³ scale, failure occurs primarily along a single fracture surface; (b) At a 15 nm³ scale, failure extends across multiple sites throughout the structure, indicating a distributed fracture pattern. All the data are derived from this study, for computational details see the text in this section.

Chapter 4

Data processing and analysis

Using the ab initio and machine-learning-assisted molecular dynamics (ML-MD) simulations, this chapter deals with the data processing and analysis methodologies employed to extract key materials properties for Group-IV-VII diborides. The machine-learning interatomic potentials (MLIPs), developed and validated through the methods outlined in previous chapters, enable accurate calculations of lattice parameters and phase stability under deformation at finete-temperature. The focus here is to demonstrate the procedures for deriving relevant material properties, such as theoretical strength and elastic modulus, while also performing a quantitative structural analysis of nanoscale supercells, are crucial for understanding their mechanical response at atomic scale.

4.1 Structural stability

Structural stability can be assessed using both static and dynamic calculations. Each method offers distinct insights into the behavior of a material under different conditions, with the static calculations focusing on ground-state properties, and dynamic simulations capturing finite-temperature effects.

In static calculations, a material's structural stability is typically verified through phonon spectrum analysis. The absence of imaginary frequencies across the Brillouin zone is considered a key indicator that the structure is dynamically stable at zero Kelvin. This criterion ensures that the atomic arrangement does not spontaneously distort or collapse into a lower symmetry phase. Moreover, among the stable phases, the one with the lowest total energy is defined as the "ground-state" structure. This aspect of the results has been previously investigated, demonstrating the strong stability of both phases in the TMB₂ [114] compounds discussed here as shown in Fig. 4.1.

In finite-temperature AIMD calculation, the stability of a structure can be evaluated through three main criteria. First, after the simulation reaches equilibrium, the material must retain its crystallographic phase without any signs of distortion or amorphization. Simultaneously, the phonon spectrum should exhibit no negative frequencies. Second, both energy and force fluctuations during the simulation should converge to a stable pattern, indicating that the system has reached thermal equilibrium. An example of this stabilization is shown in Fig. 4.2, where fluctuations in energy and force flatten over time. Third, elastic constants can also be used as an additional measure of stability, by satisfying the Born stability criteria. For example, cubic crystals must satisfy conditions [115] such as $C_{11} > 0$, $C_{44} > 0$, and $C_{11} - C_{12} > 0$. These conditions

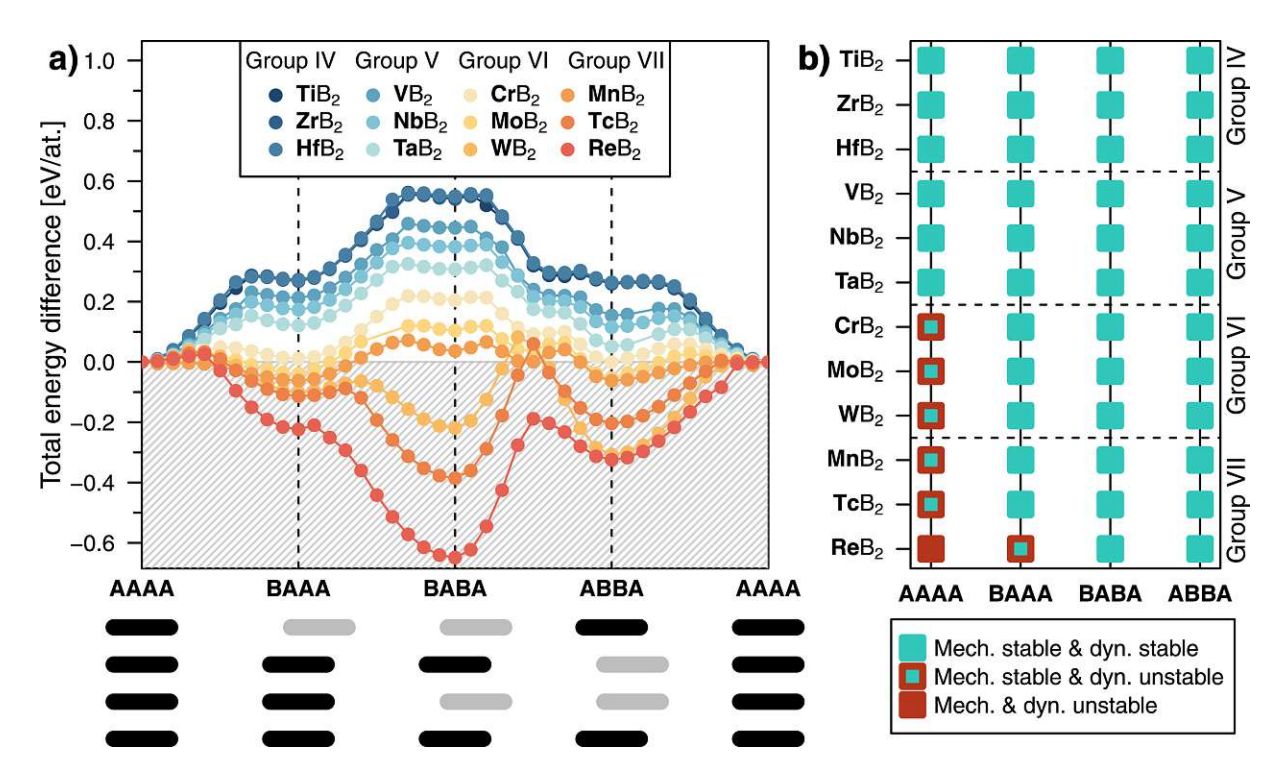


Fig. 4.1: Static stability tests from Ref. [114] for TMB₂ (TM are Group-IV-VII transition metals). (a) Total energy difference, with various stackings compared to the reference AAAA (α) stacking. The data points in-between stackings AAAA, BAAA, BABA (γ), and ABBA (ω) correspond to step-wise shifts of the respective metallic plane(s) as schematically shown below the x-axis. (b) Mechanical and dynamical stability of TMB structures with AAAA, BAAA, BABA, and ABBA stacking sequences, respectively.

ensure that the material is resistant to shearing and volume changes, thereby confirming its mechanical robustness.

For hexagonal phases, the evaluation of structural stability using elastic constants follows specific criteria tailored to the crystal symmetry, as it is characterized by a six-fold rotational axis, have a unique set of elastic constants due to their symmetry [116]. Hexagonal systems are described by five independent elastic constants: C_{11} , C_{12} , C_{13} , C_{33} , and C_{44} . Their mechanical stability conditions are expressed as [116, 117]:

- $C_{11} > 0$: The stability against longitudinal compression or extension along the a-axis.
- $C_{33} > 0$: The stability against longitudinal compression or extension along the c-axis.
- $C_{44} > 0$: The the material can resist shear deformation in the basal plane.
- $C_{11} C_{12} > 0$: To ensure stability against shear in the a-plane.
- $(C_{11} + C_{12})C_{33} > 2C_{13}^2$: To ensure mechanical stability against coupled deformations involving the a- and c-axis.

The full comparison of elastic constants for all here-studied materials are exhibited in [Publication II]. If any of these conditions are violated, the material is mechanically unstable and could undergo spontaneous deformation or collapse under stress.

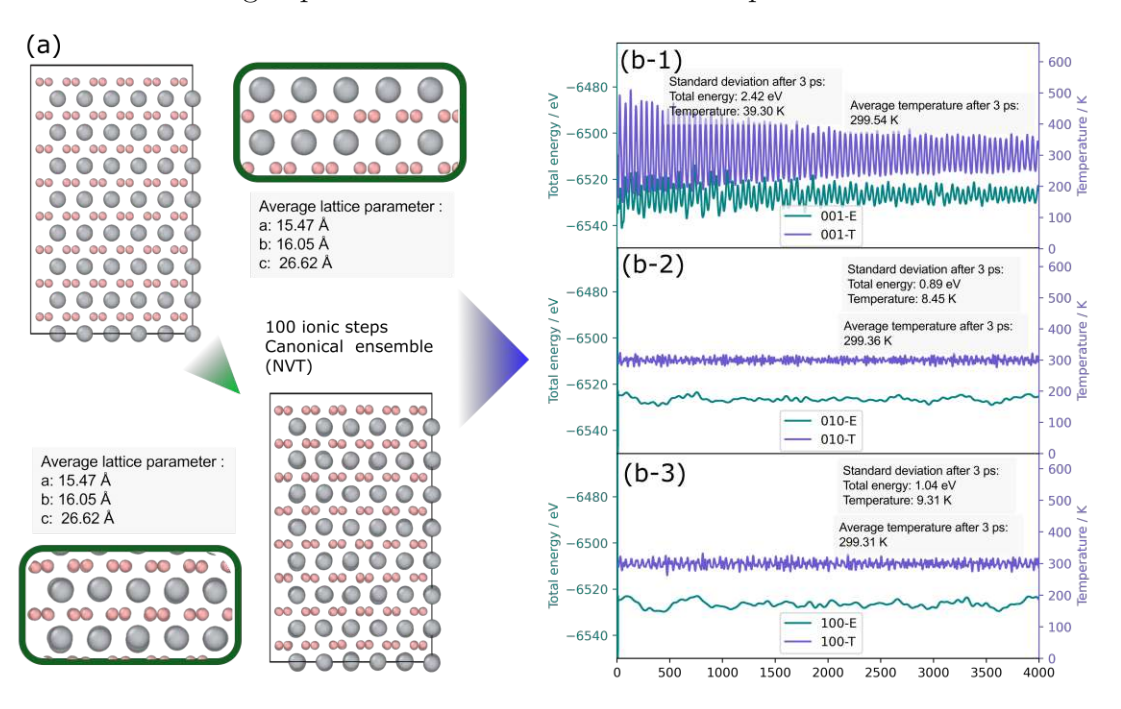


Fig. 4.2: Evaluation of structural stability in AIMD simulations, demonstrated by TaB₂. (a) Converged atomic stacking and lattice parameters (Å). (b) Convergence of temperature (K) and total energy (eV) as a function of simulation time (fs).

4.2 Mechanical properties

Calculating mechanical properties can be approached through two main methods: one based on elastic constants and another based on phenomenological models.

The mechanical properties are directly derived from the elastic constants, which can be used to calculate important mechanical properties such as bulk modulus, shear modulus, Young's modulus, and Poisson's ratio. For hexagonal systems, the Voigt and Reuss approximations are commonly used to estimate the average modulus. For bulk modulus B, the Voigt average assumes uniform compression, while the Reuss average assumes uniform stress. The Voigt bulk modulus B_V [118] for a hexagonal system is a measure of the material's resistance to uniform compression and is given by

$$B_V = \frac{2(C_{11} + C_{12}) + 4C_{13} + C_{33}}{9}, \qquad (4.1)$$

The Reuss average bulk modulus, B_R , is given by:

$$B_R = \frac{1}{2S_{11} + 2S_{12} + 4S_{13} + S_{33}} , (4.2)$$

where S_{ij} are the components of the elastic compliance matrix, which is the inverse of the stiffness matrix defined by the elastic constants. The polycrystalline bulk modulus (B) represents the effective modulus for the aggregate material. Since real materials often exhibit behavior between uniform strain and uniform stress conditions, B is typically calculated as the average of B_V and B_R :

$$B = \frac{B_V + B_R}{2} \,, \tag{4.3}$$

The shear modulus G reflects the material's resistance to shear deformation and can be calculated from the elastic constants. The Voigt average shear modulus, G_V , assumes uniform strain, is given by

$$G_V = \frac{1}{30} \left(7C_{11} - 5C_{12} + 12C_{44} + 2C_{33} - 4C_{13} \right) , \qquad (4.4)$$

The Reuss average shear modulus, G_R , assumes uniform stress, is given by

$$G_R = \left(\frac{4\left(S_{11} - S_{12}\right) + 3S_{33} + 4S_{44}}{5}\right)^{-1},\tag{4.5}$$

Similarly, the polycrystalline shear modulus (Hill shear modulus), G, is given by

$$G = \frac{G_V + G_R}{2} \,, \tag{4.6}$$

Young's modulus E and Poisson's ratio ν can also be derived from the elastic constants in similar forms ²

$$E = \frac{E_V + E_R}{2} \,, \tag{4.7}$$

$$\nu = \frac{\nu_V + \nu_R}{2} \,, \tag{4.8}$$

Furthermore, another common approach is using micro-mechanical testing or phenomenological models to estimate properties such as hardness, tensile strength, and fracture toughness, as we discussed in [Publication II], [Publication III] (with theoretical methods), and [Publication V] (with experimental methods). A detailed summary of the mechanical properties of TMB₂ compounds (where the transition metals (TM) belong to Group-IV-VI of the periodic table) is presented in Tab. 1.

At the end, by following Ref. [119], pre-cracked models are built and generated for calculating critical stress intensity under Mode-I (K_{IC}) by molecular statics calculation, in which the value based on empirical equation $K_I = \sigma_f \sqrt{a}$ – where σ_f is the applied stress required to propagate a crack and \sqrt{a} is the square root of the crack length, as presented in detail in [Publication III].

¹Since B_V represents the stiffest response and B_R the softest response, the ranking among these values should

^{2*} The Voigt Young's modulus: $E_V = \frac{9B_VG_V}{3B_V+G_V}$, the Reuss Young's modulus: $E_R = \frac{9B_RG_R}{3B_R+G_R}$ ** The Voigt Poisson's ratio: $\nu_V = \frac{3B_V-2G_V}{2(3B_V+G_V)}$, the Reuss Poisson's ratio: $\nu_R = \frac{3B_R-2G_R}{2(3B_R+G_R)}$.

4.3 Phase identification

For common phases, such as fcc, bcc, and hcp structures, phase identification is typically straightforward and can be efficiently performed using a combination of methods. Software packages like Ovito [120] and Atomman [121] are widely utilized in computational materials science for visualizing and analyzing atomic structures. They use techniques such as common neighbor analysis (CNA), Voronoi analysis, and polyhedral template matching to classify atoms based on their local environment, which works well for these standard crystal structures. For instance, as shown in Fig. 4.3, the original cubic zincblende (B3) phase is clearly identified with a specific quantitative ratio (highlighted in red). During tensile deformation, the emergence of the hexagonal wurtzite (B4) phase (marked in purple) can be directly detected, signifying a phase transformation under mechanical stress. This transition from the B3 to B4 phase highlights the material's structural response to deformation.

However, these methods have limitations when it comes to identifying more complex phases, especially those involving irregular stacking sequences, disordered structures, or multi-element systems with non-standard atomic arrangements. Such phases often deviate from the ideal atomic configurations that these algorithms are optimized to recognize. As a result, these tools may struggle to accurately differentiate between complex phases or capture fine structural details, e.g., the gray part in Fig. 4.3, which is marked as "unknown".

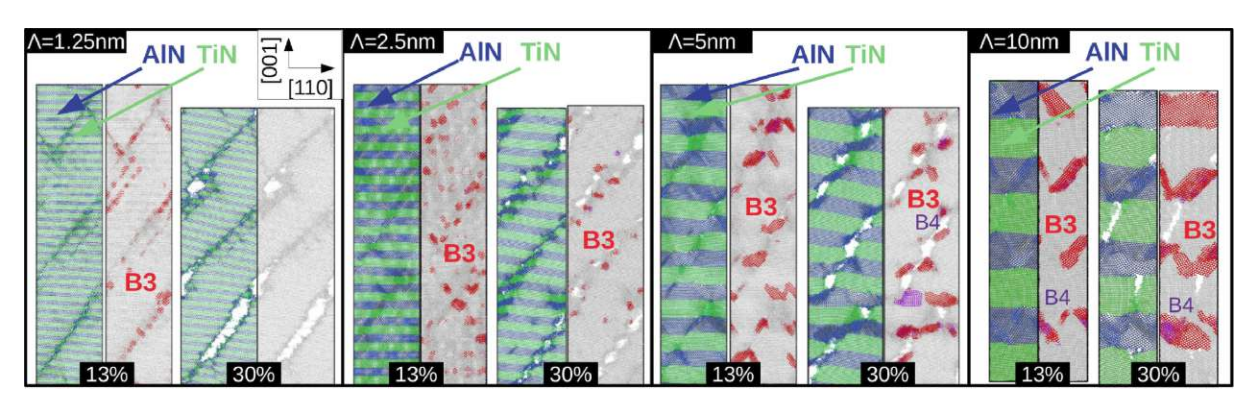


Fig. 4.3: Phase identification using standard tools in the OVITO package, as illustrated by AlN/TiN superlattices with MD snapshots, from Ref. [33] (SLs) with $\Lambda = \{1.25, 2.5, 5, 10\}$ nm under [110] tensile strain. The red-purple-grey color scheme represents regions where the B3 (red), B4 (purple), or other (grey) structural types are stabilized, as determined using the OVITO package.

To accurately study the phase transitions during deformation in the hexagonal phases under investigation, two methods were developed to detect these changes: bond analysis and Steinhardt parameter [122] calculations, as shown in [Publication II].

The bond length and angle evaluations (as shown in Fig. 4.4b with pie chart) focus on the nearest-neighbor B-B bonds within a 2 Å cutoff radius, chosen from the $[a/\sqrt{3}, a]$ interval to capture all the TMB₂ phases examined. This approach ensures that each boron atom is considered 3-coordinated. The analysis classifies boron layers as "flat" based on bond angles of $(120 \pm 5)^{\circ}$, a range determined from the standard deviation

 $(\approx 11^{\circ} \text{ for all TM elements})$ calculated from AIMD equilibration at room temperature under the NVT ensemble. For "puckered" layers, the bond angles differ depending on the specific TM element. Any angles falling outside these specified ranges were categorized as "other", indicating potential structural deviations.

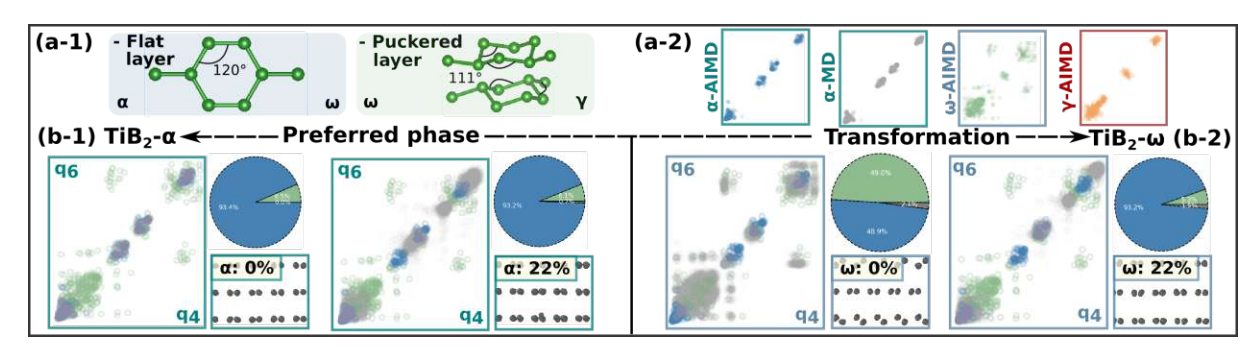


Fig. 4.4: Structural analysis and phase identification of nano-sized supercells (here $\approx 5^3$ nm³) using here-developed methods, as exemplified by TiB₂: both transforming to their energetically preferred phase upon shearing of the less favorable (ω resp. α) polymorph. (a) References for the α , ω and γ stackings (based on room-temperature equilibrated ab initio-scale supercells) using (a-1) angular descriptors (nearest-neighbor B–B atoms) and (a-2) Steinhardt parameters, namely, the q_4 vs. q_6 plots. The ranges of q_i s are always the same, (0.2, 0.8)). (b) Structural analysis of (b-1) α -TiB₂ and (b-2) ω -TiB₂ subject to room-temperature (0001)[$\overline{1210}$] shear deformation, in equilibrium and after yielding. All the data are derived from this study, for computational details see the Section 3.

For the Steinhardt parameter (as shown in Fig. 4.4b with scatter patterns) calculations, the PYSCAL [123] package was utilized. The Steinhardt parameters are particularly useful for distinguishing complex crystal structures, were averaged using Voronoi-weighted values, which provide more nuanced insights into the local environment [124]. Specifically, 10 Steinhardt parameters $(q_3, q_4, \ldots, q_{12})$ were calculated for each atom, with the focus on the boron sublattice. Although the individual parameter values (ranging from 0 to 0.6) did not clearly differentiate between the diboride polymorphs, pairwise combinations of the parameters $(q_i \text{ vs. } q_i, \text{ where } i, j \in [3, 12] \text{ and } i \neq j)$ revealed distinct patterns. Extensive testing showed that q_3 vs. q_4 plots were most effective [124] in estimating the phase composition of nanoscale supercells.

Bibliography

- [1] P. H. Mayrhofer, C. Mitterer, L. Hultman und H. Clemens. Microstructural design of hard coatings. *Prog. Mater. Sci.* 51.8 (2006), 1032–1114.
- P. H. Mayrhofer, H. Clemens und C. Mitterer. Interfaces in nanostructured thin films and their influence on hardness. Int. J. Mater. Res. 96.5 (2022), 468–480.
- D. W. Richerson und W. E. Lee. Modern ceramic engineering: properties, processing, and use in design. CRC press, 2018.
- D. Gerlich, S. Dole und G. Slack. Elastic properties of aluminum nitride. J. Phys. Chem. Solids 47.5 (1986), 437–441.
- T. Glechner, R. Hahn, T. Wojcik, D. Holec, S. Kolozsvári, H. Zaid, S. Kodambaka, P. H. Mayrhofer und H. Riedl. Assessment of ductile character in superhard Ta-CN thin films. Acta Mater. 179 (2019), 17–25.
- R. Rice. The compressive strength of ceramics. Ceramics in Severe Environments: Proceedings of the Sixth University Conference on Ceramic Science North Carolina State University at Raleigh December 7–9, 1970. Springer. 1971, 195–229.
- E. Broitman. Indentation hardness measurements at macro-, micro-, and nanoscale: a critical overview. Tribol. Lett. 65.1 (2017), 23.
- B. Jönsson und S. Hogmark. Hardness measurements of thin films. Thin solid films 114.3 (1984), 257–269.
- P. H. Mayrhofer, H. Clemens und F. D. Fischer. Materials science-based guidelines to develop robust hard thin film materials. Prog. Mater. Sci. (2024), 101323.
- W.-S. Oh, R. DeLong und K. J. Anusavice. Factors affecting enamel and ceramic wear: a literature review. J. Prosthet. Dent. 87.4 (2002), 451–459.
- G. A. Gogotsi. Fracture toughness of ceramics and ceramic composites. Ceram. Int. 29.7 (2003), 777–784.
- N. P. Padture und B. R. Lawn. Toughness properties of a silicon carbide with an in situ induced heterogeneous grain structure. J. Am. Ceram. Soc. 77.10 (1994), 2518-2522.
- W. N. Sharpe, O. Jadaan, G. M. Beheim, G. D. Quinn und N. N. Nemeth. Fracture strength of silicon carbide microspecimens. J. Microelectromechanical Syst. 14.5 (2005), 903–913.

- E. Tschegg. Mode III and mode I fatigue crack propagation behaviour under torsional loading. Journal of Materials Science 18 (1983), 1604–1614.
- S. Beden, S. Abdullah und A. Ariffin. Review of fatigue crack propagation models for metallic components. European Journal of Scientific Research 28.3 (2009), 364 - 397.
- [16]D. R. Messier, F. Riley und R. Brook. The α/β silicon nitride phase transformation. J. Mater. Sci. 13 (1978), 1199–1205.
- A. Kurlov und A. Gusev. Tungsten carbides and WC phase diagram. *Inorg. Mater.* |17|42 (2006), 121–127.
- F. Ling, K. Luo, L. Hao, Y. Gao, Z. Yuan, Q. Gao, Y. Zhang, Z. Zhao, J. He und D. Yu. Universal phase transitions of AlB₂-type transition-metal diborides. ACS omega 5.9 (2020), 4620–4625.
- L. Bowen, R. J. Weston, T. Carruthers und R. Brook. Hot-pressing and the α - β phase transformation in silicon nitride. J. Mater. Sci. 13 (1978), 341–350.
- A. S. Kurlov und A. I. Gusev. Phase equilibria in the W-C system and tungsten carbides. Russ. Chem. Rev. 75.7 (2006), 617.
- S. Lin, L. Casillas-Trujillo, F. Tasnádi, L. Hultman, P. H. Mayrhofer, D. G. [21]Sangiovanni und N. Koutná. Machine-learning potentials for nanoscale simulations of tensile deformation and fracture in ceramics. npj Comput. Mater. 10.1 (2024), 67.
- V. S. Puli, D. K. Pradhan, W. Pérez und R. Katiyar. Structure, dielectric [22]tunability, thermal stability and diffuse phase transition behavior of lead free BZT-BCT ceramic capacitors. J. Phys. Chem. Solids 74.3 (2013), 466-475.
- B. Wang, Z. Wu, A. Livingston und K. Li. A novel phase transition technique for fabrication of mesopore sized ceramic membranes. J. Membr. Sci. 339.1-2 (2009), 5-9.
- E. Schrödinger. An undulatory theory of the mechanics of atoms and molecules. |24|Physical review 28.6 (1926), 1049.
- A. K. Kerman und S. E. Koonin. Hamiltonian formulation of time-dependent variational principles for the many-body system. Ann. Phys. 100.1-2 (1976), 332-358.
- P. Hohenberg und W. Kohn. Inhomogeneous electron gas. Phys. Rev. 136 (3B) [26]Nov. 1964), B864–B871.
- W. Kohn und L. J. Sham. Self-consistent equations including exchange and [27]correlation effects. *Phys. Rev.* 140 (4A Nov. 1965), A1133–A1138.

- N. Koutná, A. Brenner, D. Holec und P. H. Mayrhofer. High-throughput firstprinciples search for ceramic superlattices with improved ductility and fracture resistance. Acta Mater. 206 (2021), 116615.
- J. Peng, E. Lara-Curzio und D. Shin. High-throughput thermodynamic screening of |29|carbide/refractory metal cermets for ultra-high temperature applications. Calphad 66 (2019), 101631.
- R. Khaledialidusti, M. Khazaei, S. Khazaei und K. Ohno. High-throughput com-[30]putational discovery of ternary-layered MAX phases and prediction of their exfoliation for formation of 2D MXenes. Nanoscale 13.15 (2021), 7294–7307.
- Z. Lou, S. Zhou, Y. Hou, H. G. Yang, H. Yuan und H. Wang. High-Throughput screening of metal nitrides for electrochemical nitrogen reduction. Appl. Surf. Sci. 665 (2024), 160289.
- K. F. Garrity. First-principles search for n-type oxide, nitride, and sulfide ther-[32]moelectrics. Phys. Rev. B Condens. Matter 94.4 (2016), 045122.
- N. Koutná, L. Löfler, D. Holec, Z. Chen, Z. Zhang, L. Hultman, P. H. Mayrhofer und D. G. Sangiovanni. Atomistic mechanisms underlying plasticity and crack growth in ceramics: a case study of AlN/TiN superlattices. Acta Mater. 229 (2022), 117809.
- D. G. Sangiovanni. Copper adatom, admolecule transport, and island nucleation |34|on TiN (0 0 1) via ab initio molecular dynamics. Applied Surface Science 450 (2018), 180-189.
- D. G. Sangiovanni, K. Kaufmann und K. Vecchio. Valence electron concentration [35]as key parameter to control the fracture resistance of refractory high-entropy carbides. Science Advances 9.37 (2023), eadi2960.
- D. Sangiovanni, F. Tasnadi, L. Johnson, M. Odén und I. Abrikosov. Strength, transformation toughening, and fracture dynamics of rocksalt-structure T i 1- x A lx N (0 x 0.75) alloys. Physical Review Materials 4.3 (2020), 033605.
- J.-P. Crocombette und L. Gelebart. Multiscale modeling of the thermal conductivity of polycrystalline silicon carbide. J. Appl. Phys. 106.8 (2009).
- C. R. Dandekar und Y. C. Shin. Molecular dynamics based cohesive zone law |38|for describing Al-SiC interface mechanics. Compos. - A: Appl. Sci. Manuf. 42.4 (2011), 355-363.
- [39]D. Sangiovanni, D. Edström, L. Hultman, I. Petrov, J. E. Greene und V. Chirita. Ab initio and classical molecular dynamics simulations of N₂ desorption from TiN (001) surfaces. Surf. Sci. 624 (2014), 25–31.
- S. Plimpton. Computational limits of classical molecular dynamics simulations. [40]Computational Materials Science 4.4 (1995), 361–364.

- P. Balbuena und J. M. Seminario. Molecular dynamics: from classical to quantum methods. Elsevier, 1999.
- W. H. Miller. The semiclassical initial value representation: A potentially practical way for adding quantum effects to classical molecular dynamics simulations. The Journal of Physical Chemistry A 105.13 (2001), 2942–2955.
- J. Li, X. Yi, B. Liu, Q. Fang und P. K. Liaw. A phase field crystal model for [43]real-time grain boundary formation and motion in complex concentration alloy. Acta Mater. (2024), 120425.
- M. Mamivand, M. A. Zaeem, H. El Kadiri und L.-Q. Chen. Phase field modeling [44]of the tetragonal-to-monoclinic phase transformation in zirconia. Acta Mater. 61.14 (2013), 5223–5235.
- M. Mamivand, M. A. Zaeem und H. El Kadiri. Phase field modeling of stress-|45|induced tetragonal-to-monoclinic transformation in zirconia and its effect on transformation toughening. Acta Mater. 64 (2014), 208–219.
- L.-Q. Chen. Phase-field models for microstructure evolution. Annu. Rev. Mater. Res. 32.1 (2002), 113–140.
- M. A. Miodownik. A review of microstructural computer models used to simulate [47]grain growth and recrystallisation in aluminium alloys. J. Light Met. 2.3 (2002), 125-135.
- [48]H. Henry. Limitations of the modelling of crack propagating through heterogeneous material using a phase field approach. Theoretical and Applied Fracture Mechanics 104 (2019), 102384.
- I. Steinbach. Phase-field models in materials science. Modelling and simulation in materials science and engineering 17.7 (2009), 073001.
- J. Behler. Perspective: Machine learning potentials for atomistic simulations. The Journal of chemical physics 145.17 (2016).
- J. Byggmästar, K. Nordlund und F. Djurabekova. Simple machine-learned interatomic potentials for complex alloys. Physical Review Materials 6.8 (2022), 083801.
- S. Urata, M. Bertani und A. Pedone. Applications of machine-learning interatomic potentials for modeling ceramics, glass, and electrolytes: A review. Journal of the American Ceramic Society (2024).
- [53]J. Los, J. Kroes, K. Albe, R. Gordillo, M. Katsnelson und A. Fasolino. Extended Tersoff potential for boron nitride: Energetics and elastic properties of pristine and defective h-BN. Phys. Rev. B Condens. Matter 96.18 (2017), 184108.
- J. Houska. Force field for realistic molecular dynamics simulations of ZrO₂ growth. |54|Comput. Mater. Sci. 111 (2016), 209–217.

- P. K. Schelling und S. R. Phillpot. Mechanism of thermal transport in zirconia and yttria-stabilized zirconia by molecular-dynamics simulation. J. Am. Ceram. Soc. 84.12 (2001), 2997–3007.
- E.-S. Oh. Elastic properties of various boron-nitride structures. Met. Mater. Int. |56|17 (2011), 21–27.
- J. Dziedzic, S. Winczewski und J. Rybicki. Structure and properties of liquid [57]Al-Cu alloys: Empirical potentials compared. Comput. Mater. Sci. 114 (2016), 219-232.
- K.-i. Saitoh, K. Kubota und T. Sato. Atomic-level structural change in Ni-Ti [58]alloys under martensite and amorphous transformations. Technische Mechanik-European Journal of Engineering Mechanics 30.1-3 (2010), 269–279.
- Y. Zuo, C. Chen, X. Li, Z. Deng, Y. Chen, J. Behler, G. Csányi, A. V. Shapeev, |59|A. P. Thompson, M. A. Wood u.a. Performance and cost assessment of machine learning interatomic potentials. J. Phys. Chem. A 124.4 (2020), 731–745.
- J. D. Morrow, J. L. Gardner und V. L. Deringer. How to validate machine-learned interatomic potentials. The Journal of chemical physics 158.12 (2023).
- J. S. Smith, O. Isayev und A. E. Roitberg. ANI-1: an extensible neural network potential with DFT accuracy at force field computational cost. Chem. Sci. 8.4 (2017), 3192-3203.
- [62]S. Klawohn, J. P. Darby, J. R. Kermode, G. Csányi, M. A. Caro und A. P. Bartók. Gaussian approximation potentials: Theory, software implementation and application examples. J. Chem. Phys. 159.17 (2023).
- G. Nikoulis, J. Byggmästar, J. Kioseoglou, K. Nordlund und F. Djurabekova. |63|Machine-learning interatomic potential for W-Mo alloys. J. Phys. Condens. Matter. 33.31 (2021), 315403.
- |64|M. Koskenniemi, J. Byggmästar, K. Nordlund und F. Djurabekova. Efficient atomistic simulations of radiation damage in W and W-Mo using machinelearning potentials. J. Nucl. Mater. 577 (2023), 154325.
- [65]Y. Lysogorskiy, C. v. d. Oord, A. Bochkarev, S. Menon, M. Rinaldi, T. Hammerschmidt, M. Mrovec, A. Thompson, G. Csányi, C. Ortner u.a. Performant implementation of the atomic cluster expansion (PACE) and application to copper and silicon. npj Comput. Mater. 7.1 (2021), 97.
- A. Bochkarev, Y. Lysogorskiy, S. Menon, M. Qamar, M. Mrovec und R. Drautz. |66|Efficient parametrization of the atomic cluster expansion. Phys. Rev. Mater. 6.1 (2022), 013804.
- I. S. Novikov, K. Gubaev, E. V. Podryabinkin und A. V. Shapeev. The MLIP package: moment tensor potentials with MPI and active learning. Mach. Learn.: Sci. Technol. 2.2 (2020), 025002.

- E. Podryabinkin, K. Garifullin, A. Shapeev und I. Novikov. MLIP-3: Active learning on atomic environments with Moment Tensor Potentials. arXiv preprint arXiv:2304.13144 (2023).
- L. C. Erhard, J. Rohrer, K. Albe und V. L. Deringer. Modelling atomic and |69|nanoscale structure in the silicon-oxygen system through active machine learning. Nat. Commun. 15.1 (2024), 1927.
- C. Chen und S. P. Ong. A universal graph deep learning interatomic potential for the periodic table. Nature Computational Science 2.11 (2022), 718–728.
- I. Batatia, P. Benner, Y. Chiang, A. M. Elena, D. P. Kovács, J. Riebesell, X. R. Advincula, M. Asta, M. Avaylon, W. J. Baldwin u.a. A foundation model for atomistic materials chemistry. arXiv preprint arXiv:2401.00096 (2023).
- A. Bochkarev, Y. Lysogorskiy und R. Drautz. Graph atomic cluster expansion for semilocal interactions beyond equivariant message passing. Physical Review X 14.2 (2024), 021036.
- A. Jain, S. P. Ong, G. Hautier, W. Chen, W. D. Richards, S. Dacek, S. Cholia, D. Gunter, D. Skinner, G. Ceder u.a. Commentary: The Materials Project: A materials genome approach to accelerating materials innovation. APL materials 1.1 (2013).
- M. Magnuson, L. Hultman und H. Högberg. Review of transition-metal diboride |74|thin films. Vacuum 196 (2022), 110567.
- S. Aydin und M. Simsek. First-principles calculations of MnB 2, TcB 2, and ReB 2 within the ReB 2-type structure. Physical Review B—Condensed Matter and Materials Physics 80.13 (2009), 134107.
- Y. Zhou, H. Xiang, Z. Feng und Z. Li. General trends in electronic structure, stability, chemical bonding and mechanical properties of ultrahigh temperature ceramics TMB₂ (TM= transition metal). J. Mater. Sci. Technol. 31.3 (2015), 285-294.
- P. Vajeeston, P. Ravindran, C. Ravi und R. Asokamani. Electronic structure, bonding, and ground-state properties of AlB₂-type transition-metal diborides. Phys. Rev. B Condens. Matter 63.4 (2001), 045115.
- A. Pereira, C. Perottoni, J. da Jornada, J. Leger und J. Haines. Compressibility of AlB₂-type transition metal diborides. J. Phys. Condens. Matter. 14.44 (2002), 10615.
- B. Post, F. W. Glaser und D. Moskowitz. Transition metal diborides. Acta Metall. |79|2.1 (1954), 20–25.
- L. Backman und E. J. Opila. Thermodynamic assessment of the group IV, V and VI oxides for the design of oxidation resistant multi-principal component materials. J. Eur. Ceram. 39.5 (2019), 1796–1802.

- M. Audronis, A. Leyland, P. Kelly und A. Matthews. The effect of pulsed magnetron sputtering on the structure and mechanical properties of CrB₂ coatings. Surf. Coat. Technol. 201.7 (2006), 3970–3976.
- S. Yin, D. He, C. Xu, W. Wang, H. Wang, L. Li, L. Zhang, F. Liu, P. Liu, Z. Wang u.a. Hardness and elastic moduli of high pressure synthesized MoB₂ and WB₂ compacts. High Press. Res. 33.2 (2013), 409–417.
- M. Dahlqvist und J. Rosen. Impact of vacancies on structure, stability and properties of hexagonal transition metal diborides, MB₂ (M= Sc, Y, Ti, Zr, Hf, V, Nb, Ta, Cr, Mo, W, Mn, and Fe). Materialia 26 (2022), 101629.
- X.-H. Yang und G.-H. Zhang. Preparation of ultrafine (W, Mo) B₁(W, Mo) B_{2.5} and (Mo, W) AlB solid solution composite powders. Ceram. Int. 49.22 (2023), 36137–36154.
- S.-M. Lin, Y. Long, C. Chang, B. Liu und H.-T. Lin. In-situ solid solution of [85]Mo or Cr in WB₂: Densification, microstructure, and properties. Ceram. Int. 49.4 (2023), 6522-6530.
- W. Dong, S. Xin, S. Ding, B. Sun, L. Xu, X. Shen, Z. An, G. Liu, L. Ma, X. Cai u. a. Dense nanocrystalline ReB2 bulk with ultrahigh hardness. Mater. Sci. Enq. A 885 (2023), 145635.
- |87|P. Kumar Yadawa. Elastic and Acoustic Properties of Hexagonal MnB₂, TcB₂ and ReB₂ Compounds. J. Adv. Phys. 2.2 (2013), 111–115.
- R. Masrour, E. Hlil, M. Hamedoun, A. Benyoussef, O. Mounkachi und H. E. [88]MOUSSAOUI. Structural, electronic and magnetic properties of MnB ₂. Bull. Mater. Sci. 38 (2015), 1065–1068.
- X.-Y. Cheng, X.-Q. Chen, D.-Z. Li und Y.-Y. Li. Computational materials discovery: the case of the W-B system. Acta Crystallogr. C 70.2 (2014), 85–103.
- |90|M. Zhang, H. Wang, H. Wang, X. Zhang, T. Iitaka und Y. Ma. First-Principles prediction on the high-pressure structures of transition metal diborides (TMB₂, TM= Sc, Ti, Y, Zr). Inorg. Chem. 49.15 (2010), 6859–6864.
- J. Palisaitis, M. Dahlqvist, A. J. Hall, J. Thörnberg, I. Persson, N. Nedfors, L. Hultman, J. E. Greene, I. Petrov, J. Rosen u.a. Where is the unpaired transition metal in substoichiometric diboride line compounds? Acta Mater. 204 (2021), 116510.
- [92]T. Moscicki, R. Psiuk, H. Słomińska, N. Levintant-Zayonts, D. Garbiec, M. Pisarek, P. Bazarnik, S. Nosewicz und J. Chrzanowska-Giżyńska. Influence of overstoichiometric boron and titanium addition on the properties of RF magnetron sputtered tungsten borides. Surf. Coat. Technol. 390 (2020), 125689.
- J. Thörnberg. Synthesis and Characterization of Transition Metal Diborides. |93|Bd. 2117. Linköping University Electronic Press, 2021.

- G. Giunchi, L. Malpezzi und N. Masciocchi. A new crystalline phase of the boron-rich metal-boride family: the Mg₂B₂₅ species. Solid State Sci. 8.10 (2006), 1202-1208.
- A. Bazhin, A. Goncharov, A. Pogrebnyak, V. Stupak und S. Goncharova. Superhardness effect in transition-metal diborides films. The Physics of Metals and Metallography 117 (2016), 594–601.
- C. Fuger, R. Hahn, A. Hirle, T. Wojcik, P. Kutrowatz, F. Bohrn, O. Hunold, [96]P. Polcik und H. Riedl. Tissue phase affected fracture toughness of nano-columnar TiB_{2+z} thin films. Mater. Res. Lett. 11.8 (2023), 613–622.
- [97]A. Khadimallah, X. Li und K. White. Solubility of tungsten in zirconium diboride solid solution. J. Eur. Ceram. 37.4 (2017), 1195–1203.
- H.-Y. Zhang, F. Xi, Z.-Y. Zeng, X.-R. Chen und L.-C. Cai. First-Principles |98| predictions of phase transition and mechanical properties of tungsten diboride under pressure. J. Phys. Chem. C 121.13 (2017), 7397–7403.
- C. A. Nunes, D. Kaczorowski, P. Rogl, M. R. Baldissera, P. A. Suzuki, G. C. Coelho, A. Grytsiv, G. André, F. Boureé und S. Okada. The NbB₂-phase revisited: Homogeneity range, defect structure, superconductivity. Acta Mater. 53.13 (2005), 3679-3687.
- [100]S. T. Renosto, R. Lang, E. Diez, L. E. Corrêa, M. da Luz, Z. Fisk und A. J. d. S. Machado. Evidence of unconventional superconductivity in the Ni-doped NbB₂ system. J. Alloys Compd. 787 (2019), 414–422.
- L. Scatteia, D. Alfano, F. Monteverde, J.-L. Sans und M. Balat-Pichelin. Effect |101|of the machining method on the catalycity and emissivity of ZrB₂ and ZrB₂-HfB₂-based ceramics. J. Am. Ceram. Soc. 91.5 (2008), 1461–1468.
- G. Kresse und J. Furthmüller. Efficient iterative schemes for ab initio total-energy [102]calculations using a plane-wave basis set. Phys. Rev. B 54.16 (1996), 11169.
- G. Kresse und D. Joubert. From ultrasoft pseudopotentials to the projector augmented-wave method. Phys. Rev. B 59 (3 Jan. 1999), 1758–1775.
- J. P. Perdew, A. Ruzsinszky, G. I. Csonka, O. A. Vydrov, G. E. Scuseria, L. A. Constantin, X. Zhou und K. Burke. Restoring the density-gradient expansion for exchange in solids and surfaces. Phys. Rev. Lett. 100 (13 Apr. 2008), 136406.
- M. Parrinello und A. Rahman. Polymorphic transitions in single crystals: A new [105]molecular dynamics method. J. Appl. Phys. 52.12 (1981), 7182–7190.
- E. V. Podryabinkin und A. V. Shapeev. Active learning of linearly parametrized |106|interatomic potentials. Comput. Mater. Sci. 140 (2017), 171–180.

- K. Gubaev, E. V. Podryabinkin und A. V. Shapeev. Machine learning of molecular properties: Locality and active learning. The Journal of chemical physics 148.24 (2018), 241727.
- Y. Lysogorskiy, A. Bochkarev, M. Mrovec und R. Drautz. Active learning strategies for atomic cluster expansion models. Phys. Rev. Mater. 7.4 (2023), 043801.
- D. Chicco, M. J. Warrens und G. Jurman. The coefficient of determination [109]R-squared is more informative than SMAPE, MAE, MAPE, MSE and RMSE in regression analysis evaluation. Peer J Computer Science 7 (2021), e623.
- C. J. Willmott. Some comments on the evaluation of model performance. Bull. Am. Meteorol. Soc. 63.11 (1982), 1309–1313.
- D. B. Figueiredo Filho, J. A. S. Júnior und E. C. Rocha. What is R² all about? Leviathan (São Paulo) 3 (2011), 60–68.
- A. P. Thompson, H. M. Aktulga, R. Berger, D. S. Bolintineanu, W. M. Brown, P. S. Crozier, P. J. in 't Veld, A. Kohlmeyer, S. G. Moore, T. D. Nguyen, R. Shan, M. J. Stevens, J. Tranchida, C. Trott und S. J. Plimpton. LAMMPS - a flexible simulation tool for particle-based materials modeling at the atomic, meso, and continuum scales. Comp. Phys. Comm. 271 (2022), 108171.
- I. S. Novikov, K. Gubaev, E. V. Podryabinkin und A. V. Shapeev. The MLIP package: moment tensor potentials with MPI and active learning. Mach. learn.: sci. technol. 2.2 (2020), 025002.
- T. Leiner, N. Koutná, J. Janovec, M. Zeleny, P. H. Mayrhofer und D. Holec. On [114]energetics of allotrope transformations in transition-metal diborides via plane-byplane shearing. *Vacuum* 215 (2023), 112329.
- M. Jamal, S. J. Asadabadi, I. Ahmad und H. R. Aliabad. Elastic constants of cubic crystals. Comput. Mater. Sci. 95 (2014), 592–599.
- F. Mouhat und F.-X. Coudert. Necessary and sufficient elastic stability conditions in various crystal systems. Phys. Rev. B Condens. Matter 90.22 (2014), 224104.
- R. Hearmon. The elastic constants of anisotropic materials. Rev. Mod. Phys. 18.3 (1946), 409.
- L. Fast, J. Wills, B. Johansson und O. Eriksson. Elastic constants of hexagonal [118]transition metals: Theory. Phys. Rev. B Condens. Matter 51.24 (1995), 17431.
- D. G. Sangiovanni, A. Kraych, M. Mrovec, J. Salamania, M. Odén, F. Tasnádi und I. A. Abrikosov. Descriptor for slip-induced crack blunting in refractory ceramics. Physical Review Materials 7.10 (2023), 103601.
- A. Stukowski. Visualization and analysis of atomistic simulation data with OVITO the Open Visualization Tool. Model. Simul. Mat. Sci. Eng. 18.1 (2009), 015012.

- L. Hale, Z. Trautt und C. Becker. Interatomic Potentials Repository Project. 2018.
- P. J. Steinhardt, D. R. Nelson und M. Ronchetti. Bond-orientational order in liquids and glasses. Phys. Rev. B Condens. Matter 28.2 (1983), 784.
- [123]S. Menon, G. D. Leines und J. Rogal. pyscal: A python module for structural analysis of atomic environments. J. Open Source Softw. 4.43 (2019), 1824.
- R. Tranås, O. M. Løvvik und K. Berland. Lattice Thermal Conductivity from [124]First Principles and Active Learning with Gaussian Process Regression. arXiv preprint arXiv:2309.06786 (2023).

Chapter 5

Contribution to the field

Results of my doctoral research are presented in manuscripts published in international peer-reviewed journals. The list below includes all my publications in chronological order, while working on computational materials science and solid state physics. The most important studies—selected for this thesis, with me as first author or co-author are briefly summarised in the upcoming paragraphs. The first-author publications, representing my main contributions, will be discussed in detail in the remainder of this chapter.

- 1. S. Lin, C. Shen, H. Zhang. Electric-field-tunable thermal conductivity in antiferroelectric materials. *Materials Today Physics*, 32, 100998, 2023. https://doi.org/10.1016/j.mtphys.2023.100998
- 2. J. Yue, Y. Liu, W. Ren, S. Lin, C. Shen, H.K. Singh, T. Cui, T. Tadano, H. Zhang. Role of atypical temperature-responsive lattice thermal transport on the thermoelectric properties of antiperovskites Mg_3XN (X = P, As, Sb, Bi). Materials Today Physics, 41, 101340, 2023. https://doi.org/10.1016/j.mtphys.2024.101340
- 3. S. Lin, J. Yue, W. Ren, C. Shen, H. Zhang. Strong anharmonicity and mediumtemperature thermoelectric efficiency in antiperovskite Ca_3XN (X = P, As, Sb, Bi) compounds. Journal of Materials Chemistry A, 12 (30), 19567-19579, 2024. https://doi.org/10.1039/D4TA02118E
- 4. S. Lin, L. Casillas-Trujillo, F. Tasnádi, L. Hultman, P.H. Mayrhofer, D.G. Sangiovanni, N. Koutná. Machine-learning potentials for nanoscale simulations of tensile deformation and fracture in ceramics. npj. Computational Materials, 10, 67, 2024. [Selected: Publication I]

https://doi.org/10.1038/s41524-024-01252-3

- 5. T. Stasiak, S. Debnárová, S. Lin, N. Koutná, Z. Czigány, K. Balázsi, V. Buršíková, P.Vašina, P.Souček. Synthesis and characterization of ceramic high entropy carbide thin films from the Cr-Hf-Mo-Ta-W refractory metal system. Surface and Coatings Technology, 485, 130839, 2024. [Selected: Publication IV] https://doi.org/10.1016/j.surfcoat.2024.130839
- 6. C. Hu, S. Lin, M. Podsednik, S. Mráz, T. Wojcik, A. Limbeck, N. Koutná, P.H. Mayrhofer. Influence of co-sputtering AlB₂ to TaB₂ on stoichiometry of nonreactively sputtered boride thin films. Materials Research Letters, 12(8), 561-570, 2024.

[Selected: Publication V]

https://doi.org/10.1080/21663831.2024.2357700

7. N. Koutná, S. Lin, L. Hultman, D.G. Sangiovanni, P.H. Mayrhofer. Machinelearning potentials for structurally and chemically complex MAB phases: strain hardening and ripplocation-mediated plasticity. Materials & Design, 114307, 2025.

[Selected: Publication VI]

https://doi.org/10.1016/j.matdes.2025.114307

8. S. Lin, D. Holec, D.G. Sangiovanni, T. Leiner, L. Hultman, P.H. Mayrhofer, N. Koutná. Shear-activated phase transformations of diborides via machine-learning potential molecular dynamics. Under Review in Acta Materialia.

[Selected: Publication II]

https://doi.org/10.48550/arXiv.2503.18171

9. S. Lin, Z. Chen, R. Janknecht, Z. Zhang, L. Hultman, P.H. Mayrhofer, N. Koutná, D.G. Sangiovanni. Machine-learning potentials predict orientation- and modedependent fracture in refractory diborides. Under Review in Acta Materialia.

[Selected: Publication III]

https://doi.org/10.48550/arXiv.2503.18171

Here I briefly summarise main findings of the publications used for this thesis and give a comment on my own contribution.

Publication I - Main Contribution

S.Lin, L. Casillas-Trujillo, F. Tasnádi, L. Hultman, P. H. Mayrhofer, D. G. Sangiovanni, N. Koutná. npj. Computational Materials, 10, 67, 2024.

We studied machine-learning interatomic potentials (MLIPs) for simulating the mechanical response of TiB₂ monocrystals up to failure. Our MLIP accurately replicates ab initio stresses and fracture mechanisms during room-temperature uniaxial tensile deformation. For larger-scale tensile tests, we performed MLIP up-fitting with additional ab initio configurations to analyze trends in strength, toughness, and crack initiation under various loading conditions. While our MLIP has limitations in modeling different lattice structures and Ti/B stoichiometries, our training procedure is applicable to other ceramic systems, successfully developing MLIPs for TaB₂, WB₂, ReB₂, TiN, and Ti_2AlB_2 .

My contribution: Methodology, Investigation, Analysis, Visualization, Original Draft

Publication II - Main Contribution

S.Lin, D.Holec, D.G.Sangiovanni, T.Leiner, L.Hultman, P.H.Mayrhofer, N.Koutná. Under review in Acta Materialia.

We studied the layered transition metal diborides (TMB₂) and their three structural polymorphs to explore the potential for phase-transformation plasticity under mechanical shear strain, addressing their inherent brittleness. By training machine-learning interatomic potentials (MLIPs) for TMB₂, we validated their predictive capabilities against ab initio data, focusing on structural and elastic properties as well as phase transformations. Nanoscale molecular dynamics simulations helped evaluate theoretical

shear strengths and their temperature dependence. Our analysis revealed that specific shear directions activate transformations between metastable and preferred phases, with the preferred phase of ReB₂ demonstrating unique temperature response.

My contribution: Methodology, Investigation, Analysis, Visualization, Original Draft

Publication III - Main Contribution

S.Lin, Z.Chen, R.Janknecht, Z.Zhang, L.Hultman, P.H.Mayrhofer, N.Koutná, D.G.Sangiovanni. Under review in Acta Materialia.

We studied fracture toughness $(K_{\rm Ic})$ and strength $(\sigma_{\rm f})$ in ceramic diborides TMB₂ (TM = Ti, Zr, Hf) using machine-learning interatomic potentials (MLIPs) trained on ab initio fracture data. Simulations of pre-cracked single crystals under K-controlled loading revealed straight transgranular crack extension in Mode-I, with extrapolated properties of $K_{\rm Ic} \approx 1.7-2.9 \text{ MPa} \cdot \sqrt{\text{m}}$ and $\sigma_{\rm f} \approx 1.6-2.4 \text{ GPa}$. For TiB₂, mixed-mode loading of prismatic cracks led to deflection onto pyramidal planes, consistent with nanoindentation tests on $TiB_2(0001)$ thin films. These results highlight the predictive power of MLIP-based fracture simulations and their relevance to orientation- and modedependent failure in ceramics.

My contribution: Methodology, Investigation, Analysis, Visualization, Original Draft

Publication IV

T.Stasiak, S.Debnárová, S.Lin, N.Koutná, Z.Czigány, K.Balázsi, V.Buršíková, P.Vašina, P.Souček. Surface and Coatings Technology, 485, 130839, 2024.

We studied the synthesis of multicomponent carbides with a NaCl-type fcc structure in the Cr-Hf-Mo-Ta-W system using reactive DC magnetron sputtering. By varying deposition conditions, including acetylene flow and temperature, we controlled the formation of metallic and ceramic phases. Films without acetylene formed a bcc metallic phase, while higher acetylene flows resulted in an fcc carbide phase. Crystalline films exhibited columnar morphology, while amorphous ones were dense. We achieved promising mechanical properties, with hardness up to 25±1 GPa and indentation moduli of 319±6 GPa, supporting DFT predictions. Our study advances the preparation of Cr-Hf-Mo-Ta-W multicomponent carbides via magnetron sputtering.

My contribution: Calculation, (DFT-) Analysis, Visualization, Review & Editing

Publication V

C.Hu, S.Lin, M.Podsednik, S.Mráz, T.Wojcik, A.Limbeck, N.Koutná, P.H.Mayrhofer. Materials Research Letters, 12(8), 561-570, 2024.

We studied transition metal diboride thin films for their mechanical properties and thermal stability. By combining experiments and simulations, we analyzed sputtered species distribution, gas-phase scattering, re-sputtering, and evaporation affecting film composition. We investigated vacancy formation and competing phases that govern phase constitution. Using co-sputtering from two compound targets, we developed phase-pure crystalline (Ta,Al)B₂ solid solution thin films and correlated stoichiometry changes with microstructure, hardness, and elastic modulus. My contribution: Calculation, (DFT-) Analysis, Visualization, Review & Editing

Publication VI

N. Koutná, S. Lin, L. Hultman, D.G. Sangiovanni, P.H. Mayrhofer.. Materials & Design, 114307, 2025.

We studied the feasibility of training machine-learning interatomic potentials (MLIPs) for chemically and structurally complex materials, using MAB phases as a model system. Focusing on group IV-VI transition metal-based MABs with 222, 212, and 314 structures, we trained and validated three MLIPs for predicting structural and mechanical properties across a broad chemical and temperature space. Validation includes lattice and elastic constants, energy and force errors on AIMD snapshots, and extrapolation grades. Nanoscale tensile simulations reveal that in-plane loading leads to high strength and shear banding via $\{110\}\langle 001\rangle$ slip, while [001] loading induces soft response, work hardening, and failure by kinking and delamination. Notably, W₂AlB₂ resists fracture through ripplocations and twinning up to 1200 K.

My contribution: Data curation, Validation, Review & Editing



Main Contribution I

NPJ. COMPUTATIONAL MATERIALS, NATURE PORTFOLIO

Machine-learning potentials for nanoscale simulations of tensile deformation and fracture in ceramics

Authors:

Shuyao Lin

Luis Casillas-Trujillo Ferenc Tasnádi Lars Hultman Paul H. Mayrhofer Davide G. Sangiovanni Nikola Koutná

Published: 02 April 2024



Machine-learning potentials for nanoscale simulations of tensile deformation and fracture in ceramics

Keywords: Machine learning interatomic potentials, diborides, thin film materials

Abstract

Machine-learning interatomic potentials (MLIPs) offer a powerful avenue for simulations beyond length and timescales of ab initio methods. Their development for investigation of mechanical properties and fracture, however, is far from trivial since extended defectsgoverning plasticity and crack nucleation in most materials—are too large to be included in the training set. Using TiB₂ as a model ceramic material, we propose a training strategy for MLIPs suitable to simulate mechanical response of monocrystals until failure. Our MLIP accurately reproduces ab initio stresses and fracture mechanisms during room-temperature uniaxial tensile deformation of TiB₂ at the atomic scale ($\approx 10^3$ atoms). More realistic tensile tests (low strain rate, Poisson's contraction) at the nanoscale $(\approx 10^4-10^6 \text{ atoms})$ require MLIP up-fitting, i.e. learning from additional ab initio configurations. Consequently, we elucidate trends in theoretical strength, toughness, and crack initiation patterns under different loading directions. As our MLIP is specifically trained to modelling tensile deformation, we discuss its limitations for description of different loading conditions and lattice structures with various Ti/B stoichiometries. Finally, we show that our MLIP-training procedure is applicable to diverse ceramic systems. This is demonstrated by developing MLIPs which are subsequently validated by simulations of uniaxial strain and fracture in TaB₂, WB₂, ReB₂, TiN, and Ti₂AlB₂.

Introduction

Simulations of materials' mechanical response—including (i) intrinsic strength and toughness, (ii) nucleation of extended defects (e.g., dislocations, stacking faults, cracks) and their implications for (iii) plasticity and fracture mechanisms—require length and time scales beyond limits of ab initio methods ($\approx 10^3$ atoms, $\ll \text{ns}$)[1-4]. The go-to approach in most cases would be classical Molecular Dynamics (MD), allowing to access atomistic pathways for deformation and fracture in nanoscale systems ($\approx 10^6$ atoms) and "realistic" operation conditions (e.g., ultra-high temperatures, times up to μ s). However, a severe problem of MD is that the necessary interatomic potentials do not exist for most engineering materials or are limited in accuracy and transferability with respect to temperatures, phases, and defective structures (see e.g. Refs. [5–7]).

A powerful avenue for MD simulations on multiple time and length scales with near ab initio accuracy is the application of machine learning interatomic potentials [8, 9] (MLIPs), in case of no ambiguity just "potentials"). MLIPs learn the atomic energy (or other atomic properties like forces) from a descriptor that characterizes local atomic environments in an ab initio training set[10]. Compared to conventional ab initio calculations, MD with MLIPs can achieve a speed up of as much as 5 orders of magnitude[11, 12]. Previous studies showed examples of MLIPs' transferability with respect to defects (e.g., grain boundaries [13], dislocation structures [14, 15]) and phases [16, 17 (e.g., Ni-Mo phase diagram illustrating superior performance of a MLIP over a classical potential [18]). Recently, Tasnádi et al. [19] have demonstrated high accuracy of MLIP-predicted elastic constants for TiAlN ceramics, hence, have set the stage for MLIP development beyond linear elastic regime.

Based on the parametrization of local structural properties, MLIPs can be fitted employing different formalisms: spectral neighbor analysis potentials (SNAP) [20], neural networks potentials (NNP) [21], Gaussian approximation potentials (GAP) [22], moment tensor potentials (MTP) [23], linearized interatomic potentials [24], or atom cluster expansion (ACE) potentials [10]. Benchmarks for some of these parametrizations have been published in case of carbon [25] or graphene [26], but are missing for chemically complex materials.

Fundamental challenges related to MLIP developments include (i) efficient training dataset generation, (ii) training strategies for simulations beyond length scales feasible for ab initio methods, and (iii) assessing the MLIPs' reliability over different length scales. Point (ii) closely relates to successively improving the MLIP's predictive power by up-fitting/active learning[27]. Here an important concept is the extrapolation/Maxvol grade (γ [28]) expressing the extent of MLIP's extrapolation on any structure containing given chemical elements (irrespective of the phase and stoichiometry). Readily available in current ACE and MTP implementations [29–31], γ allows selecting sufficiently "new" environments to expand the training set. Besides γ , other methods used for selecting configurations are stratified sampling or random selection (for detailed discussion of pros and cons see Refs. [32–35]). Besides identifying new environments, γ can serve to indicate the MLIP's reliability during MD simulations. This is particularly advantageous at scales where the direct validation by ab initio calculations is not possible.

Our work pursues the development of MLIPs suitable to simulate atomic-to-nanoscale deformation of ceramics, providing both methodological and materials science discussion. The model material, TiB₂, is a widely studied system, representative of ultra-high temperature ceramics (UHTCs). Exhibiting high hardness and resistance to corrosion, abrasive and erosive wear [36, 37], UHTCs are suitable to protect tools and machining components under extreme operation conditions [38–41]. TiB₂, which crystallizes in the AlB₂-type phase [42-44] (α , P6/mmm), exemplifies outstanding mechanical properties [45,46 of UTHCs. It exhibits high hardness of 41–53 GPa[47–49], has a melting point of 3500 K [50] and mature synthesis technologies [51, 52]. Insights into mechanical behaviour of TiB₂ and other diborides have been offered by ab initio calculations [53–55] and recently also by molecular dynamics with classical empirical potentials ($TiB_2|56$, 57], ZrB₂[58], HfB₂[59]). To date, however, no MLIP capable of predicting mechanical response of UTHCs until fracture has been reported.

Using the MTP formalism, we propose a general training strategy for development of MLIPs targeted to model tensile deformation and fracture of single-crystal ceramics at finite temperatures. The extrapolation grade, γ , is exploited to iteratively improve our MLIP and also as a mean of validation. Specifically, γ values calculated during MD tensile tests are discussed alongside with statistical errors of relevant physical observables, such as time-averaged stresses derived from equivalent ab initio molecular dynamics (AIMD) simulations. The newly-developed MLIP allows to describe tensile deformation in TiB₂ supercells with $\approx 10^3$ – 10^6 atoms, thus also providing a basis for analyzing size effects on mechanical properties and fracture patterns. Furthermore, we



test transferability of our MLIP to other loading conditions and phases, as well as applicability of our general training strategy to other ceramics, exemplified by TaB₂, WB_2 , ReB_2 , TiN, and Ti_2AlB_2 .

Methods

Ab initio calculations

Zero Kelvin ab initio calculations as well as finite-temperature Born-Oppenheimer ab initio molecular dynamics (AIMD) were carried out using VASP [60] together with the projector augmented wave (PAW) [61] method and the Perdew-Burke-Ernzerhof exchange-correlation functional revised for solids (PBEsol) [62]. All AIMD calculations employed plane-wave cut-off energies of 300 eV and Γ-point sampling of the reciprocal space.

Supercells. The model of TiB_2 was based on the AlB_2 -type structure (P6/mmm). The 720-atom (240 Ti+480 B) supercell—used to generate the training/learning/validation dataset—had size of $\approx (1.5 \times 1.6 \times 2.6)$ nm³, with x, y, z axes chosen to satisfy the following crystallographic relationships: $x \parallel [10\overline{1}0], y \parallel [\overline{1}2\overline{1}0], z \parallel [0001]$. Similar supercells—with 720 atoms (240 M+480 B)—were used in Section 6 for TaB₂, WB₂, and ReB₂, where the latter two are in the ω and γ phase [63], respectively. Cubic (fcc, Fm $\overline{3}$ m) TiN[64] was modelled in a 360-atom (180 Ti+180 N) supercell, with x, y, and z axes aligned with the [100], [010], and [001] directions. The orthorhombic (Cmcm) Ti₂AlB₂[65] was modelled in a 720-atom supercell (288 Ti+144 Al+288 B), oriented in the same way as the TiN supercell.

Equilibration of TiB₂ at 300 and 1200 K was performed in 2 steps: (i) 10 ps AIMD isobaric-isothermal (NPT) simulation with Parrinello-Rahman barostat [66] and Langevin thermostat, and (ii) a 2 ps for 300 K, 4 ps for 1200 K AIMD run within the canonical (NVT) ensemble based on Nosé-Hoover thermostat, using time-averaged lattice parameters from the NPT simulation. TaB₂, WB₂, ReB₂, TiN, and Ti₂AlB₂ were equilibrated at 300 K using the same approach.

Computational setup for simulations of TiB_2 's [0001], [10 $\overline{1}0$], and [$\overline{1}2\overline{1}0$] tensile deformation and $(0001)[\overline{1}2\overline{1}0]$, $(10\overline{1}0)[\overline{1}2\overline{1}0]$, and $(10\overline{1}0)[0001]$ shear deformation (all with Γ point sampling) followed Refs. [64, 67, 68]. Specifically, the equilibrated supercell was elongated or sheared in the desired direction using strain increments of 2%. Poisson's contraction effects were not considered in AIMD simulations. The supercells are equilibrated for 3 ps at each deformation step. Stress tensor components were calculated as averages of the final 0.5 ps. The same approach was used to simulate tensile deformation in TaB₂, WB₂, ReB₂, TiN, and Ti₂AlB₂.

Room-temperature elastic constants, C_{ij} , of TiB₂ were evaluated following Ref. [69], based on a second-order polynomial fit of the [0001], $[10\overline{1}0]$, and $[\overline{1}2\overline{1}0]$ stress/strain data $(C_{11}, C_{12}, C_{13}, C_{33})$ and of the $(0001)[\overline{1}2\overline{1}0], (10\overline{1}0)[\overline{1}2\overline{1}0],$ and $(10\overline{1}0)[0001]$ shear stress/strain data (C_{44}) , considering strains between 0 and 4%.

Simulations of TiB₂'s room-temperature volumetric compression were carried out for a 720-atom TiB₂ supercell maintained at 300 K (for 2 ps) within the NVT ensemble.

The surface energies were calculated at **zero Kelvin** using a 60-atom TiB₂ supercell (with a $3 \times 3 \times 1$ k-mesh and cut-off energy of 300 eV) together with a 10 Å vacuum layer. The supercells were fully relaxed until forces on atoms were below 10^{-2} eV Å⁻¹ and the total energy was converged with accuracy of 10^{-5} eV per supercell. Other ground-state and higher-energy structures from the Ti-B phase diagram (Ti₂B, Ti₃B₄, TiB, TiB₁₂, etc.) were fully relaxed at 0 K starting from lattice parameters and atomic positions from the Materials Project [70].

Development of machine-learning interatomic potentials (MLIPs)

We used the moment tensor potential (MTP) formalism, as implemented in the mlip-2 package [71]. Training data generation and general workflow are detailed in the Section 1 and Fig.1. Training/learning/validation sets included only equilibrated configurations: the initial part (5%) of NVT runs was discarded.

MLIPs were fitted based on the 16g MTPs (referring to the highest degree of polynomial-like basis functions in the analytic description of the MTP [23]), using the Broyden-Fletcher-Goldfarb-Shanno method [72] with 1500 iterations and 1.0, 0.01 and 0.01 weights for total energy, stresses and forces in the loss functional. A cutoff radius of 5.5 Awas employed, similar to other recent MLIP studies [19, 73]. Tests using larger cutoffs, 7.4 and 10.0 Å did not show notable changes in accuracy. Expansion of a training set by selection of configurations from a learning set (LS), was done using the select add command of the mlip-2 package. Specifically, all configurations in the LS were ordered by their extrapolation grade ($\gamma[28]$) and maximum 15 from the upper 20% was selected to expand the training set.

Details of MLIPs developed in this work (summarized in Fig. 1c) are given below.

MLIP-[0001], (MLIP-[10 $\overline{1}0$], and MLIP-[$\overline{1}2\overline{1}0$]): trained on AIMD snapshots of TiB₂ subject to room-temperature tensile loading in the [0001] ($[10\overline{1}0]$, $[\overline{1}2\overline{1}0]$) direction. See Section 1 and 2. MLIP-[1]: up-fitting MLIP-[0001], learning from the final TSs of MLIP- $[10\overline{1}0]$ and MLIP- $[\overline{1}2\overline{1}0]$. See Section 3. MLIP-[2] and MLIP-[3]: up-fitting MLIP-[1], learning from AIMD snapshots of TiB₂ equilibrated at 1200 K (MLIP-[2]), and sequentially elongated in the [0001] direction until cleavage (MLIP-[3]). See Section 3. MLIP-[4]: up-fitting MLIP-[1], learning from AIMD snapshots of TiB_2 elongated by 150% in the [0001] direction, initializing atoms at ideal lattice sites and equilibrating at 300 and 1200 K under fixed volume and shape. See Section 3–5.

Molecular dynamics with MLIPs (ML-MD)

ML-MD calculations were performed with the LAMMPS code [74] interfaced with mlip-2 package [71], which allows using MTP-type MLIPs (specified in the pair style command). Additionally, the active learning state file (state.als, for details see the mlip-2 documentation¹) was used to output the extrapolation grade, γ , values during the simulations.

¹https://gitlab.com/ashapeev/mlip-2-paper-supp-info

Computational setup of atomic scale ML-MD tensile and shear tests (at 300 or 1200 K) was equivalent to AIMD. Stress tensor components and elastic constants were calculated in the same way as described above in case of AIMD.

Nanoscale ML-MD tensile tests at 300 or 1200 K used supercells with 12,960 atoms (S1); 141,120 atoms (S2); 230,400 atoms (S3); and 432,000 atoms (S4); with dimensions of about $(1.5 \times 1.6 \times 2.6)$ nm³, $(4.6 \times 4.7 \times 5.1)$ nm³, $(10.6 \times 11.0 \times 10.3)$ nm³, $(12.1 \times 12.6 \times 10.4)$ nm³, (12.9) nm³, and $(15.2 \times 15.8 \times 15.4)$ nm³, respectively. Prior to simulating mechanical deformation, the supercells were equilibrated for 5 ps at the target temperature using the isobaric-isothermal (NPT) ensemble coupled to the Nosé-Hoover thermostat with a 1 fs time step. Tensile loading was simulated by deforming the supercell with a constant strain rate (50 Ås⁻¹), accounting for lateral contraction (Poisson's effect) in the NPT ensemble.

Atomic scale volumetric compression simulations used supercell sizes and deformation approach equivalent to what described above for AIMD. Surface structures and other Ti-B phases were fully relaxed at 0 K using conjugate gradient energy minimization in molecular statics (MS).

Visualization and structural analysis

The OVITO package [75] allowed us to visualize and analyze selected AIMD and ML-MD trajectories. In particular, we looked at (i) Radial pair distribution functions (with a cut-off radius of 5.5 Å), (ii) Elastic strain maps and (iii) Atomic strain maps (with cut-off radius of \pm 0.1 Å). For details see the OVITO documentation.

Results and discussion

We aim to develop MLIPs targeted to simulations of tensile deformation in TiB₂. Although the mechanical properties of ceramics are typically assessed by nanoindenation. microcantilever bending, or micropillar compression experiments, MD simulations of tensile loading can be directly compared to results of ab initio calculations. We simulate deformation along low-index [0001], $[10\overline{1}0]$, and $[\overline{1}2\overline{1}0]$ directions that are parallel or normal to the typical growth direction of hexagonal transition metal diborides [36] and have been considered in previous ab initio studies of surface energies and mechanical properties[55].

1 Training procedure and fitting initial MLIPs

Our general training procedure is described below (Procedure 2) and schematically depicted in Fig. 1a (for further details, see the Methods). Throughout this work, training configurations (i.e., structures labelled by ab initio total energies, forces acting on each ion, and six stress tensor components) are generated by finite-temperature AIMD calculations. To avoid over-representation, a training set is initialized by a small fraction of randomly selected AIMD snapshots and iteratively expanded using the concept of the extrapolation grade |28|, γ .

The extrapolation grade $\gamma \in \mathbb{R}^+$ (see equations 9-1 in Ref. [28]) expresses the degree of extrapolation when MLIP predicts atomic properties of a certain configuration. Specifically, $\gamma \leq 1$ means interpolation and $\gamma > 1$ extrapolation. Hence, the higher the γ , the larger is the uncertainty on predicted energies, forces, and stresses [28]. In practice, one sets an extrapolation threshold $(\gamma_{\rm thr})$. Configurations with $\gamma > \gamma_{\rm thr}$ are added to the training set to improve transferability of the potential. Procedure 2 uses $\gamma_{\rm thr} = 2$, motivated by our tests² as well as by previous work by the MTP developers [77] and by one of us[12] showing that such value corresponds to accurate extrapolation[77] (near-interpolation[12]).

Algorithm 2 MLIP training

- (1) Generate a pool of AIMD configurations.
- (2) Divide the pool into an initial training set (TS_0) , a learning set (LS), and a validation set (VS) by randomly selecting 0.5%, 79.5%, and 20% of non-overlapping configurations.
- (3) Fit an initial MLIP (MLIP₀, trained on TS₀). If γ of all configurations in the LS and VS is below $\gamma_{\rm thr} = 2$, exit. Else, build TS₁ by adding maximum 10% of configurations from the LS to TS₀, selected by the Maxvol algorithm [28] based on their extrapolation grade. Fit a new MLIP (MLIP₁, trained on TS_1).
- (4) While γ of all configurations in the LS and VS is above $\gamma_{\text{thr}} = 2$, build TS_i by adding maximum 10% of configurations from the LS to TS_{i-1} , selected by the Maxvol algorithm based on their extrapolation grade. Fit a new MLIP (MLIP_i, trained on TS_i).

Employing Procedure 2 and the MTP formalism, we fit three MLIPs: MLIP-[0001], MLIP-[1010], and MLIP-[1210]. The training uses snapshots from room-temperature AIMD simulations for a 720-atom TiB₂ supercell, uniaxially elongated in the [0001], $[10\overline{10}]$, and $[\overline{1210}]$ crystallographic direction, respectively, with a strain step of 2\% (for details of AIMD simulations, see the Methods). The entire pool of AIMD data consists of $\approx 120,000$ configurations, where each loading condition ([0001], [10 $\overline{10}$], and [$\overline{12}\overline{10}$]) represents $\approx 1/3$.

The final training sets (the last TS_i in the step (4) of Procedure 2) of MLIP-[0001], MLIP- $[10\overline{1}0]$, and MLIP- $[\overline{1}2\overline{1}0]$ contain 181, 155, and 180 configurations, respectively. The fitting and validation errors, quantified through the residual mean square error (RMSE[76]), of total energies, forces, and stresses do not exceed 2.6 meV atom⁻¹. 0.11 eV Å^{-1} , and 0.30 GPa, respectively. As follows from Procedure 2, $\gamma < \gamma_{\text{thr}} = 2$ for all configurations in the learning set.

2 MLIPs' validation against atomic scale tensile tests

Following evaluation of the fitting and validation errors (Section 1), further validation steps consist in using the above developed MLIPs to run MD simulations (ML-MD) of TiB_2 subject to tensile deformation.

²In particular, during each iteration (i) in the step (4) of Procedure 2, the maximum γ is correlated with errors of energies, forces and stresses (quantified via common regression model evaluation metrics, MAE, RMSE, R² see e.g. Ref. [76]) for the TS_i (fitting errors) and the VS (validation errors). With $\gamma_{\rm thr}=2$, we are limited mainly by the accuracy of the underlying ab initio training data.

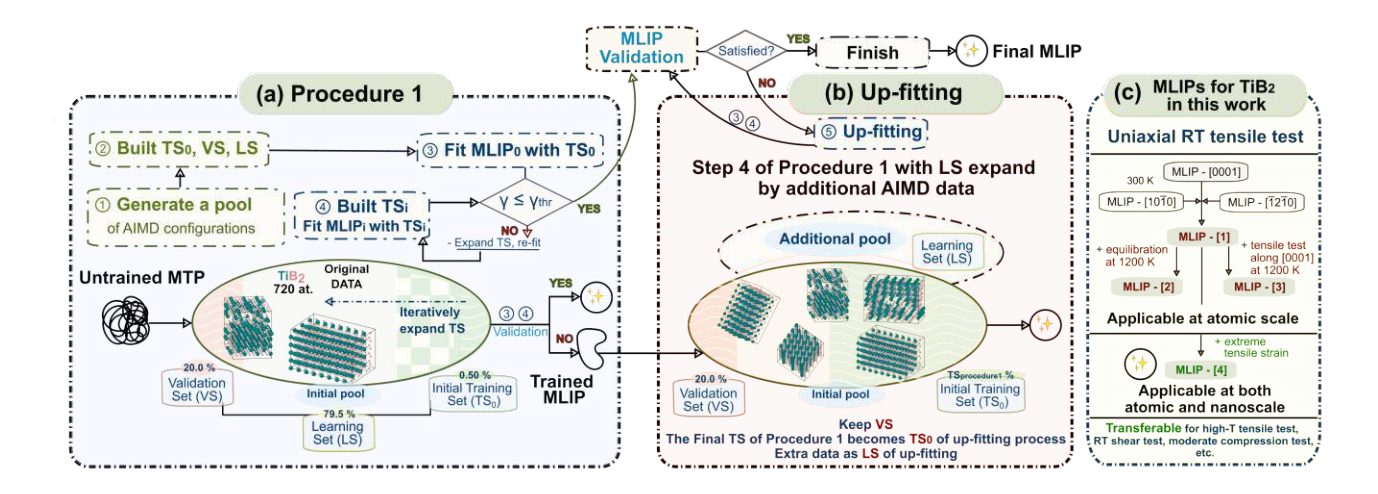


Fig. 1: Our MLIP training strategy. Schematic visualization of (a) our general training procedure (Procedure 2, Section 1), and (b) up-fitting (Section 2, 3), both applicable to any MLIP formalism with the extrapolation/Maxvol grade (γ) quantification, particularly MTP (used in this work) and ACE. (c) An overview of the here-developed MLIPs: MLIP-[0001], MLIP-[1010], MLIP-[1210] (applicable for atomic scale tensile loading, Sections 1 and 2); MLIP-[1], MLIP-[2], MLIP-[3] (intermediate MLIPs produced by up-fitting, Section 3); and MLIP-[4] (applicable for both atomic and nanoscale tensile loading, Section 3–5). Details of the training datasets are given in the corresponding sections and additionally summarized in the Methods under "Development of machine-learning interatomic potentials". both

During ML-MD, the MLIP's reliability is assessed via:

- (i) Comparison with AIMD predictions of physical, mechanical properties, and fracture mechanisms. In particular, we monitor time-averaged stresses, theoretical strength and toughness, and cleavage on different crystallographic planes.
- (ii) The extrapolation grade. At each ML-MD time step, we calculate γ of the corresponding configuration. Values exceeding *reliable* extrapolation signalise that the MLIP requires up-fitting (i.e., expanding the TS by additional configurations and going back to step (4) of Procedure 2; see Fig. 1b,c).

As suggested by MTP developers[77], we consider $\gamma_{\text{reliable}} \leq 10$ as reliable extrapolation. Such choice allows us to develop MLIPs with accuracy similar to the underlying ab initio training set.

Fig. 2a depicts stress/strain curves derived from room-temperature AIMD and ML-MD tensile tests, in which TiB₂ supercell ($\approx 10^3$ atoms, $\approx 1.5^3$ nm³) is loaded in the [0001], [10 $\overline{10}$], and [$\overline{12}$ 10] direction, respectively. Each deformation is simulated with a MLIP trained to the respective loading condition. Excellent quantitative agreement between AIMD and ML-MD results indicates reliability of our MLIPs. Specifically, time-averaged stresses in ML-MD differ from AIMD values by 0.07–1.94 GPa, yielding statistical errors RMSE ≈ 1.02 GPa, R² ≈ 0.9997 . Stresses normal to the loaded direction—not vanishing due to the omission of Poisson's effect in both AIMD and ML-MD simulations—are also used for assessing MLIPs' reliability. After fracture, the [0001] stress component recorded in AIMD does not drop to zero. The effect is due to long-range electrostatic effects, which are absent in ML-MD. The extrapolation grade during all ML-MD simulations remains low ($\gamma \leq 5 < \gamma_{\text{reliable}}$), thus suggesting reliable extrapolation.

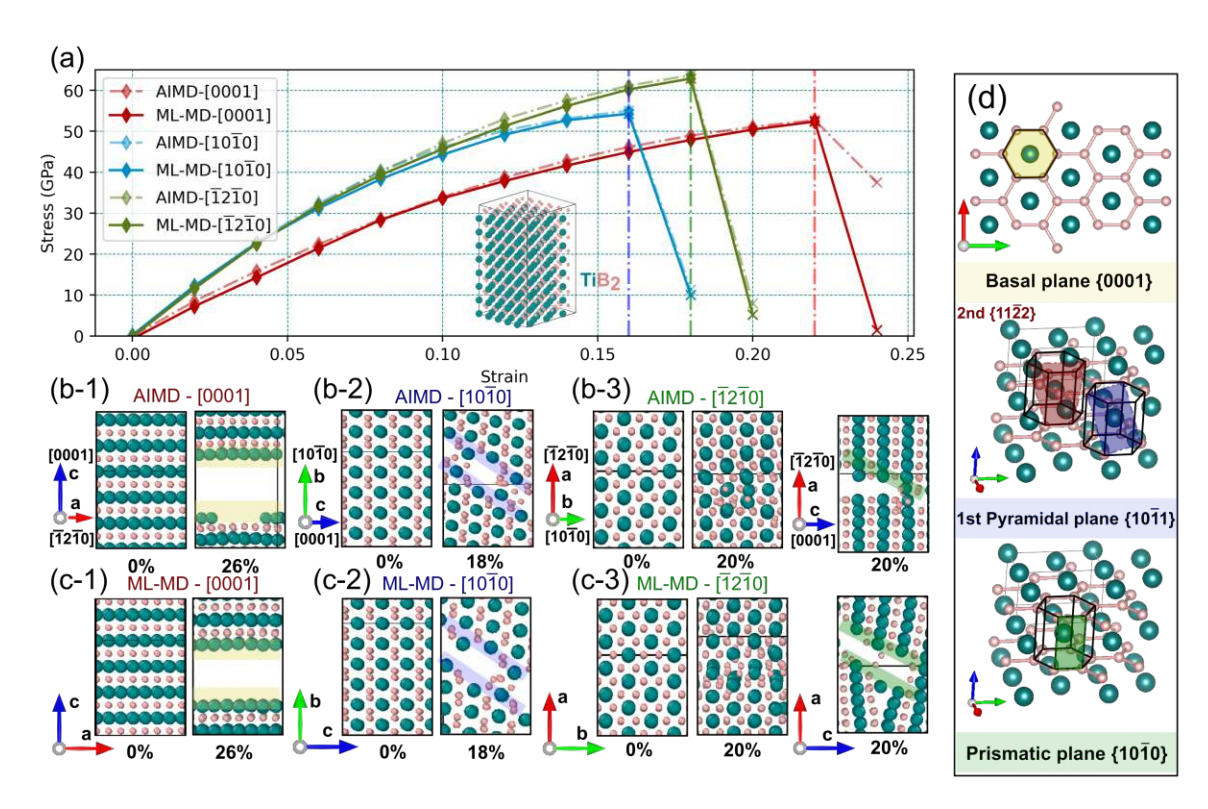


Fig. 2: Validation of the here-developed MLIPs (MLIP-[0001], MLIP-[1010], and MLIP-[1210]) against atomic scale room-temperature AIMD tensile tests. (a) Comparison of AIMD (dash-dotted line) and ML-MD (solid line) stress/strain curves for TiB₂ subject to [0001], [1010], and [1210] tensile deformation at 300 K, using a 720-atom supercell with dimensions of ≈ (1.52 × 1.58 × 2.57) nm³. Only the stress component in the loaded direction is plotted. (b, c) Snapshots of the fracture point in AIMD (b-1, b-2, b-3) and ML-MD (c-1, c-2, c-3). (d) Illustration of fracture surfaces (see alsoRef. [78]).

The calculated stress/strain curves allow us to evaluate TiB₂'s theoretical tensile strength and toughness along different crystal directions. We report results of the *ultimate* tensile strength, which corresponds to the global stress maximum during the tensile test [68]. We define the tensile toughness as the integrated stress/strain area. The property describes the ability of an initially defect-free material at absorbing mechanical energy until failure.

The theoretical tensile strengths of TiB_2 obtained by ML-MD are 63.7, 55.0, and 52.7 GPa for the $[\bar{1}2\bar{1}0]$, $[10\bar{1}0]$, and [0001] directions, respectively. These differ from AIMD values by maximum 0.8 GPa (0.99%). The ML-MD predicted toughness along $[\bar{1}2\bar{1}0]$, $[10\bar{1}0]$, and [0001] reaches 4.3, 3.1, and 4.3 GPa, respectively, differing from AIMD values by maximum 0.029 GPa (0.67%). Note, however, that theoretical tensile strength and toughness are affected by the supercell size. Strength and toughness values saturate over nm lengthscales (see following sections).

AIMD and ML-MD tensile-testing of TiB_2 reveal very similar fracture mechanisms (Fig. 2b–c). Specifically, the fracture surface formed during [0001] deformation almost perfectly aligns with (0001) basal planes (Fig. 2-(b-1),(c-1),d). Tensile loading along the [10 $\overline{1}0$] direction opens a void diagonally across Ti/B_2 layers (Fig. 2-(b-2),(c-2)). The fracture surface is parallel to the second order pyramidal planes of the $\{11\overline{2}2\}$ family (Fig. 2d). For the $[\overline{1}2\overline{1}0]$ loading condition, fracture planes are approximately

parallel to the $\{10\overline{1}0\}$ prismatic planes (Fig. 2-(b-3),(c-3),d). The TiB₂ fracture planes predicted in our simulations are consistent with experimentally-characterized slip planes in single-crystal TiB_2 [51, 79].

3 MLIPs' up-fitting for nanoscale tensile tests

As discussed in the previous section, MLIP-[0001], MLIP- $[10\overline{1}0]$, and MLIP- $[\overline{1}2\overline{1}0]$ provide reliable description of TiB₂'s response to uniaxial tensile loading at the atomic scale. This is indicated by low extrapolation grades ($\gamma \leq 5 < \gamma_{\text{reliable}}$) as well as stress/strain curves and fracture mechanisms in agreement with AIMD results.

As a next step, we carry out tensile tests at the nanoscale. Methodological differences between atomic and nanoscale simulations are listed below.

- Atomic scale tensile tests (presented in the previous section) employ 720-atom supercells with dimensions of $\approx (1.5 \times 1.6 \times 2.6) \text{ nm}^3$. Strain is incremented at steps of 2\% with fixed lattice vectors normal to the loaded direction.
- Nanoscale tensile tests employ supercells with four different sizes: S1 (12,960 at.), S2 (141,120 at.), S3 (230,400 at.), and S4 (432,000 at.), where $S1 \approx 5^3$ nm³ and $S4 \approx 15^3$ nm³. These simulations impose a continuous and homogeneous increase in strain (rate 50 Ås⁻¹) and account for Poisson's contraction.

Employing MLIP-[0001], MLIP- $[10\overline{1}0]$, and MLIP- $[\overline{1}2\overline{1}0]$ for room-temperature nanoscale tensile tests results in unphysical dynamics (losing atoms) and rapidly increasing extrapolation grades $(\gamma \gg 10^3 \gg \gamma_{\rm reliable})$ when approaching the fracture point. This indicates that deformation is controlled by formation of extended crystallographic defects, which are absent in atomic scale simulations. Thus, to enable description of TiB₂'s fracture at the nanoscale, our MLIPs require up-fitting (Fig. 1b). Generally, this is a non-trivial task[80, 81], since structures causing large γ cannot be directly treated by ab initio calculations.

Below, we describe up-fitting steps leading to MLIP-[4] (schematically depicted in Fig. 1c). We shall see that MLIP-[4] enables reliable simulations of TiB₂ tensile deformation at the nanoscale.

- We produce MLIP-[1] by up-fitting MLIP-[0001], where the LS is expanded by final TSs of MLIP- $[10\overline{1}0]$ and MLIP- $[\overline{1}2\overline{1}0]$. MLIP-[1] accurately simulates atomic scale tensile properties, but does not well describe nanoscale deformation and fracture in TiB₂ ($\gamma \gg \gamma_{\text{reliable}}$).
- We up-fit MLIP-[1] using three different LSs, producing MLIP-[2], MLIP-[3], and MLIP-[4]. MLIP-[2] and MLIP-[3] learn from AIMD snapshots of TiB₂ equilibrated at 1200 K (MLIP-[2]), and sequentially elongated in the [0001] direction until cleavage (MLIP-[3]). MLIP-[4] learns from AIMD snapshots of TiB₂ elongated by 150% in the [0001] direction, initializing atoms at ideal lattice sites and equilibrating at 300 and 1200 K under fixed volume and shape. Such large strain quickly induces fracture, thus providing additional information for training MLIP on highly deformed lattice environments and surface properties.

Tab. 1: Validation of the here-developed MLIP (MLIP-[1]) against theoretical and experimental (exp.) room-temperature elastic constants, C_{ij} . The C_{ij} values for TiB₂ (in GPa, at temperature T(K)) are shown together with the polycrystalline bulk modulus, B (in GPa), shear modulus, G(in GPa), Young's modulus, E (in GPa), and Poisson's ratio, ν , compared to reference ab initio and experimental (exp.) data. Ref. [82] and Ref. [83] is for TiB₂ single and polycrystal, respectively. AIMD and ML-MD elastic constants were evaluated following Ref. [69], based on a second-order polynomial fit of the [0001], [10 $\overline{1}$ 0], and [$\overline{1}$ 2 $\overline{1}$ 0] stress/strain data (C_{11} , C_{12} , C_{13} , C_{33}) and of the (0001)[$\overline{1}$ 2 $\overline{1}$ 0], $(10\overline{1}0)[\overline{1}2\overline{1}0]$, and $(10\overline{1}0)[0001]$ shear stress/strain data (C_{44}) , assuming strains up to 4%. For details see the Methodology section. Note that values from Ref. [84] were based on 0 K ab initio calculations coupled to phonon-theory assessments of thermal expansion.

	Nr. of atoms	T	C_{11}	C_{33}	C_{44}	C_{12}	C_{13}	E	В	G	ν	Source
DFT	192	300	640	446	251	62	91	574	244	260	0.106	Ref. [84]
AIMD	720	300	588	430	252	79	111	547	244	243	0.126	This work
ML-MD	720	300	588	409	261	85	98	554	236	246	0.113	This work
Exp.	-	300	660	432	260	48	93	565	244	266	0.099	Ref.[82]
Exp.	-	300	588	503	238	72	84	575	249	255	0.114	Ref. [83]

MLIP-[2], MLIP-[3], and MLIP-[4] all provide results in agreement with AIMD tensile tests at the atomic scale ($\gamma \leq 5 < \gamma_{\text{reliable}}$). Fracture mechanisms and elastic constants are also correctly reproduced. At the nanoscale, MLIP-[2] and MLIP-[3] exhibit lower γ than MLIP-[1]. However, the sought improvement ($\gamma \leq \gamma_{\text{reliable}}$) is achieved only by MLIP-[4], which will be used to carry out nanoscale ML-MD simulations of TiB₂ deformation.

The reliability of MLIP-[4] is indicated by low γ values, realistic description of structural changes during nanoscale tensile tests (see following section), and excellent agreement with ab initio and experimental values of TiB₂ lattice parameters (Tab. 2).

Tab. 2: Validation of the here-developed MLIP (MLIP-[4], equivalent results are produced by intermediate MLIP-[1-3]) against theoretical and experimental (exp.) lattice constants. The a and c values for TiB₂ (in Å) are shown at temperature T (K). Experimental values, Ref. [85] and Refs. [86, 87], are for TiB₂ powder and thin films, respectively.

	Nr. of atoms	T	a	c	Source
DFT	720	0	3.027	3.213	This work
ML-MD	720	0	3.027	3.213	This work
AIMD	720	300	3.035	3.218	This work
ML-MD	720	300	3.036	3.218	This work
ML-MD	$(13-430)\cdot 10^3$	300	3.036	3.217	This work
Exp.	-	300	3.032	3.229	Ref. [85]
Exp.	-	300	3.029	3.229	Ref. [86]
Exp.	-	300	3.021	3.230	Ref. [87]
AIMD	720	1200	3.056	3.249	This work
ML-MD	720	1200	3.056	3.249	This work
$\operatorname{ML-MD}$	$(13-430)\cdot 10^3$	1200	3.047	3.239	This work

To explain why MLIP-[4] enables nanoscale tensile tests, one needs to analyse the corresponding training set, TS(MLIP-[4]). In Fig.3, we visualize selected characteristics of TS(MLIP-[4]) in comparison to the training set of MLIP-[1], TS(MLIP-[1]), where the latter is not applicable to simulate TiB₂'s fracture at the nanoscale. The radial distribution function (RDF, Fig.3a) and bond angle distribution analysis suggest minor geometrical differences between structures contained in TS(MLIP-[1]) and TS(MLIP-[4]). Their total energy and stress distribution, however, differ significantly (Fig. 3b). In

particular, TS(MLIP-[4]) contains atomic configurations with higher total energy and higher total energy in combination with higher stress in principal crystallographic axes, which are missing in TS(MLIP-[1]). An illustration of structures from the two training sets is given in Fig.3c. The chosen snapshots indicate that TS(MLIP-[4]) provides a variety of atomic environments relevant for simulations of non-stoichiometry, locally amorphous regions, and surfaces, which are likely to be helpful also for nanoscale simulations.

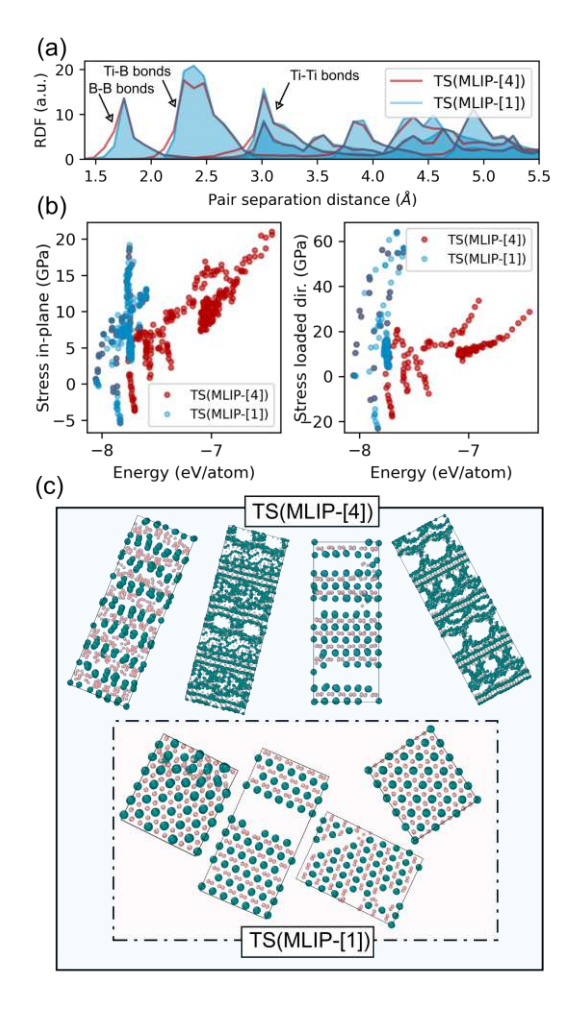


Fig. 3: Qualitative differences between configurations in the training sets (TSs) of the here-developed MLIPs suitable only for the atomic scale ML-MD tensile tests (MLIP-[1]) or for both atomic and nanoscale ML-MD tensile tests (MLIP-[4]). (a) Radial distribution function (RDF, with 5.5 Å cutoff) for B-B, Ti-B, and Ti-Ti bonds (integrated over all configurations). (b) Stress components (in-plane and in the loaded direction) vs. total energy of all configurations in the training set. (c) Snapshots of representative structures from the two training sets.

4 Size effects in tensile response of TiB₂

Equipped with the above developed MLIP-[4], in this section we discuss TiB₂'s response to room-temperature uniaxial tensile loading from atomic to nanoscale. Recall that an important difference between our atomic and nanoscale tensile tests is that the former disregard Poisson's contraction.

The stress/strain curves calculated by ML-MD at room temperature are depicted in Fig. 4. For strains below $\approx 10\%$, the tensile stresses computed for each loading direction remain unaltered by an increase in supercell sizes from $\approx 10^3$ to 10^6 atoms. Such overlap indicates consistency in elastic constants derived from atomic and nanoscale models. As already seen in atomic scale simulations, the basal plane is elastically isotropic, which is shown by the same initial slope of stress/strain curves for $[12\overline{1}0]$ and $[10\overline{1}0]$ elongation and in line with experimental reports for hexagonal crystals [88]. Due to Poisson's contraction, however, differences in stress/strain curves emerge beyond the linear-elastic regime. A shrinkage of the lattice parameters normal to the applied tensile strain yields Poisson's ratio ($\nu \approx 0.127^{-3}$) consistent with the value obtained from elastic constants ($\nu \approx 0.113$, see Tab. 1). Approaching the fracture point, differences between TiB₂'s tensile behavior at atomic and nanoscale become more apparent. For example, while atomic-scale simulations indicate that the [0001] direction is the softest, tensile tests at the nanoscale show that $[10\overline{10}]$ elongation returns the lowest strength value (Tab. 3). Even more pronounced size effects are expected for ceramics which exhibit plastic behavior upon tensile loading.

The TiB₂'s theoretical strength and toughness calculated during nanoscale simulations at room temperature remain essentially unchanged for supercell sizes increasing from $\approx 5^3$ nm³ to $\approx 15^3$ nm³ (see S1–S4 results in Tab. 3). Specifically, the $[\overline{1}2\overline{1}0]$ direction exhibits the highest tensile strength (≈ 56 GPa), followed by the [0001] direction $(\approx 54 \text{ GPa})$, and the [1010] direction ($\approx 51 \text{ GPa}$). The [0001] direction exhibits the highest toughness (≈ 4.80 GPa), followed by the $[\overline{1}2\overline{1}0]$ direction (≈ 3.37 GPa), and the [$10\overline{1}0$] direction (≈ 2.78 GPa).

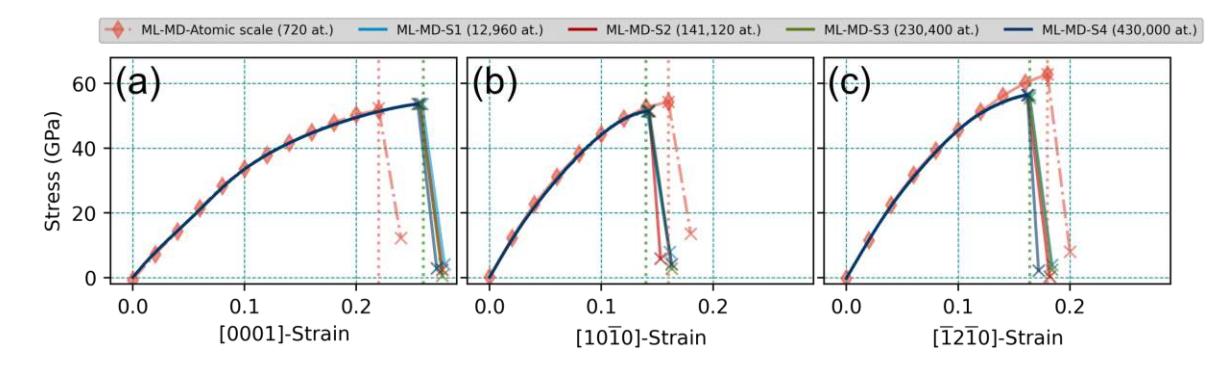


Fig. 4: Comparison of AIMD and ML-MD stress/strain curves calculated for TiB₂ at room temperature. The ML-MD tensile stresses, obtained using MLIP-[4], are plotted as a function of TiB₂ elongation parallel to (a) [0001], (b) $[10\overline{1}0]$, and (c) $[\overline{1}2\overline{1}0]$ directions. The orange diamonds correspond to atomic scale ML-MD simulations (720 at.), while the solid lines correspond to nanoscale ML-MD simulations (12,960–430,000 at.), as defined at the beginning of this section. Note that the theoretical strength of defect-free crystal models represents an ideal upper bound of strength attainable in actual ceramics. Much lower stresses are expectable in experiments due to, e.g., nanostructural defects.

Besides characterizing directional dependence of tensile strength and toughness in dislocation-free monocrystals, ML-MD nanoscale simulations also provide insights into crack nucleation and growth mechanisms. These are illustrated by Fig. 5, Fig. 6, and Fig. 7. Results of ML-MD atomic scale simulations are included for comparison.

³The Poisson's contraction was calculated as $\nu = -\frac{d\varepsilon_{\text{compressed}}}{d\varepsilon_{\text{elongated}}}$, where the $d\varepsilon_{\text{compressed}}$ ($d\varepsilon_{\text{elongated}}$) is the lattice parameter shrinkage (increment) orthogonal (parallel) to the loading direction. The presented value is an average of Poisson's ratios for both in-plane directions.

Tab. 3: Size and temperature effects on mechanical properties of TiB₂. The directional response to strain is assessed for supercells with sizes ranging from the atomic to the nanoscale. The mechanical properties of TiB₂ are extracted from ML-MD stress/strain data in Fig. 4.

Nr. of atoms	T (K)	Dimensions (nm)			Strength (GPa)			Toughness (GPa)			Fracture strain (%)		
		a	b	c	[0001]	$[10\overline{1}0]$	$[\overline{1}2\overline{1}0]$	[0001]	$[10\overline{1}0]$	$[\overline{1}2\overline{1}0]$	[0001]	$[10\overline{1}0]$	$[\overline{1}2\overline{1}0]$
720	300	1.51	1.58	2.57	52.72	55.01	63.69	4.33	3.11	4.32	22.0	16.0	18.0
12,960 (S1)	300	4.55	4.73	5.15	53.71	51.36	56.40	4.83	2.77	3.38	26.4	14.3	16.8
141,120 (S2)	300	10.63	11.05	10.30	53.69	51.44	56.41	4.81	2.78	3.37	26.4	14.3	16.8
230,400 (S3)	300	12.14	12.63	12.87	53.71	51.43	56.38	4.82	2.78	3.37	26.3	14.3	16.8
432,000 (S4)	300	15.18	15.79	15.45	53.67	51.47	56.42	4.80	2.78	3.37	26.2	14.2	16.8
720	1200	1.53	1.59	2.60	43.87	45.21	51.34	3.27	2.29	3.07	20.0	16.0	16.0
432,000 (S4)	1200	15.26	15.86	15.52	43.27	41.30	44.67	3.45	1.96	2.32	21.6	12.8	14.1

During atomic-scale simulations of [0001] elongation, all atoms in TiB₂ vibrate close to their ideal lattice sites until a sudden brittle cleavage induces formation of two surfaces almost perfectly parallel with (0001) basal planes (Fig. 5, row 1). At the nanoscale, fracture is initiated by opening of voids accompanied by local necking which produces lattice re-orientations (Fig. 5, row 2 and 3). Rapid void coalescence and fraying of ligaments results in corrugated fractured surfaces, predominantly with (0001) orientation. Following the stress release, inner parts of the crystal relax back to the ideal TiB₂ lattice sites.

The S1 supercell yields in only one region (Fig. 5, row 2). The larger S2, S3, and S4 supercells do not fracture in two pieces but nucleate cracks with size of few nm. For S4 supercells, the phenomenon is depicted in Fig. 5, row 3. The fractured surfaces do not align only with the basal planes but also with the {1011} first order pyramidal planes (see notation in Fig. 2d). Volumetric strain analysis (Fig. 5d,e) highlights locally increased tensile strain concentration surrounding small voids (see TiB₂ slice at $\approx 27\%$ strain) due to decreased interplanar spacings between Ti and B layers (predominantly due to |0001| compression) above and below the voids. The large size of S4 models allows cracks to propagate along different directions, thus offering a detailed view of fracture patterns.

For the $[10\overline{1}0]$ tensile test, size effects in fracture mechanisms are compared in Fig. 6. At the atomic scale, two voids open diagonally across Ti/B layers (Fig. 6, row 1). At the nanoscale, we observe nucleation of V-shaped cracks, as illustrated for the S1 and the S4 supercell (Fig. 6, row 2 and 3, and panels c, d), where S4 additionally reveals lattice rotation near the V-shaped defects. We infer that loading in the direction of strong covalent B-B bonds most often induces crack deflection and fracture at {1122} family of surfaces parallel to the second order pyramidal planes.

Changing to the $[\overline{1210}]$ tensile deformation, atomic scale simulations predict fracture along $\{10\overline{1}0\}$ prismatic planes (Fig. 7, row 1). This is underpinned also by nanoscale ML-MD (Fig. 7, row 2 and 3), suggesting that crack growth often occurs both orthogonally and diagonally across Ti/B layers (see the dashed line with arrow in Fig. 7e).

A direct comparison between experimental and ML-MD results of TiB₂ mechanical properties and preferred fracture planes would require synthesis and tensile testing of TiB₂ monocrystals. Unfortunately, TiB₂ ceramics are typically synthesized as thin films on substrates, which renders measurements of tensile strength essentially unfeasible. Nevertheless, as mentioned above, the fracture planes observed in ML-MD simulations

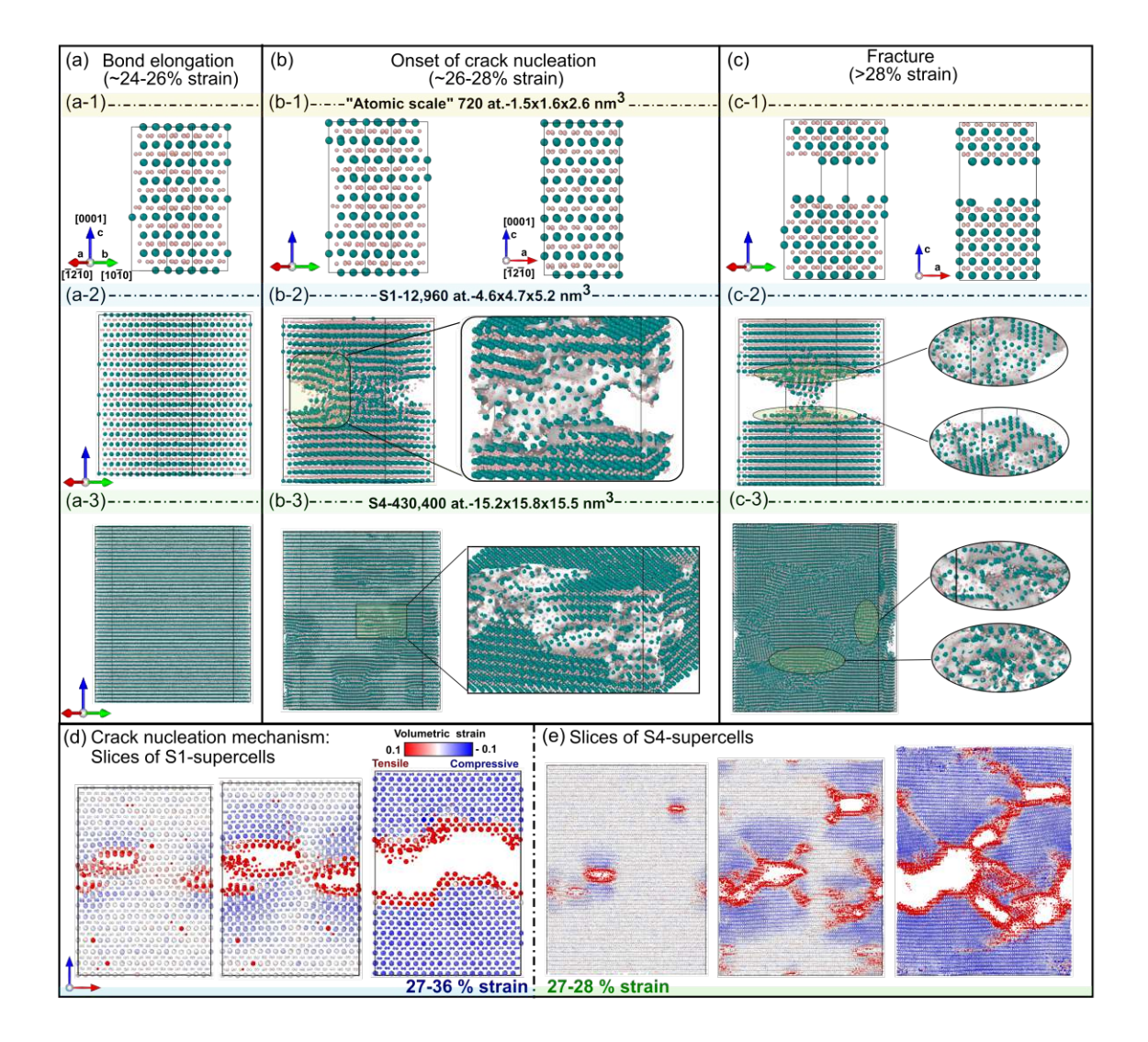


Fig. 5: Representative ML-MD snapshots of TiB₂ strained along [0001] at 300K. Upper (x-1), middle (x-2), and lower (x-3) panels show results of simulations over different lengthscales. Key deformation stages: (a) bond elongation in the loaded direction, (b) onset of crack nucleation, and (c) fracture. Thin slices of the nanoscale (d) S1 and (e) S4 supercells color-coded based on volumetric strain (using the corresponding equilibrium structure as reference). Red (blue) regions denote high tensile (compressive) strain.

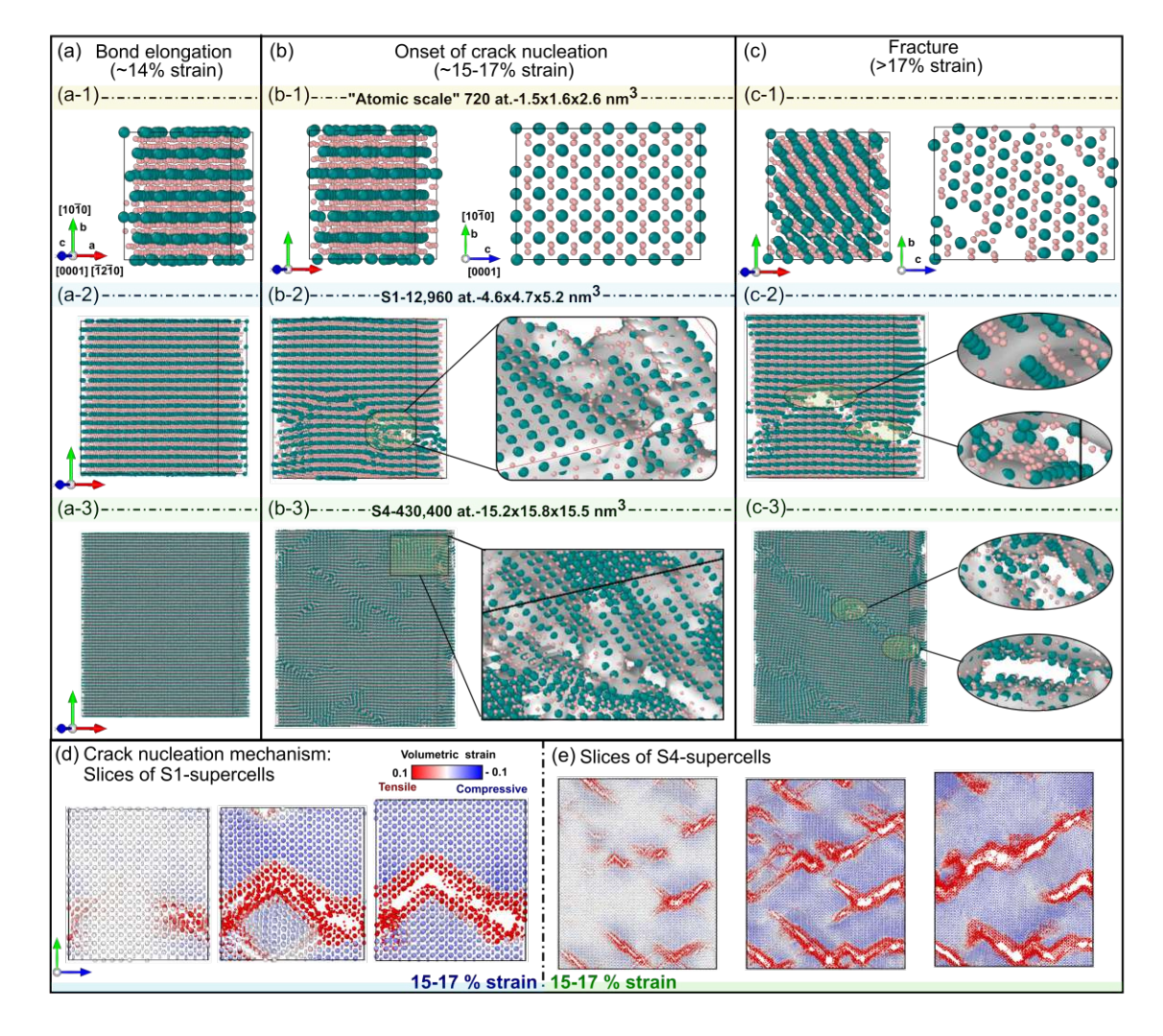


Fig. 6: Representative ML-MD snapshots of TiB₂ strained along [1010] at 300K. Upper (x-1), middle (x-2), and lower (x-3) panels show results of simulations over different lengthscales. Key deformation stages: (a) bond elongation in the loaded direction, (b) onset of crack nucleation, and (c) fracture. Thin slices of the nanoscale (d) S1 and (e) S4 supercells color-coded based on volumetric strain (using the corresponding equilibrium structure as reference). Red (blue) regions denote high tensile (compressive) strain.

are consistent with slip systems known to operate in TiB₂ at room temperature [51, 79. It is also worth noting that the high hardness measured for [0001]-textured TiB₂ thin films, 41–53 GPa [47–49], is consistent with large strength values predicted for TiB_2 by atomistic simulations.

In general, the fracture strength measured for hard ceramics is one-to-two orders of magnitude lower than the theoretical strength. The discrepancy is due to premature cracking initiated at native structural defects in actual materials. For example, microcantilever bending experiments conducted on hard polycrystalline Ti-Al-N evidence intergranular fracture, which severely limits the material strength to values below 10 GPa [89]; much smaller than corresponding theoretical strength results [64]. Nevertheless, prior to crack growth, the tensile stress accumulated at structural flaws of ceramics can locally reach several tens of GPa [90]. This reconciles stress states predicted by atomistic simulations with real mechanical-testing experiments. Likewise, the elongation withstood by defect-free ceramic models during tensile testing simulations is indicative of strain locally produced (nm lengthscale) in specimens subject to load (see fracture strains in Fig. 4).

5 Other loading conditions and MLIP's transferability

Our MLIP (MLIP-[4]) has been specifically developed and optimized to target atomic to nanoscale simulations of TiB₂ subject uniaxial tensile loading until fracture. Examination of the underlying training set (Fig. 3c) indicated a variety of atomic environments including, e.g., different Ti/B stoichiometries, locally amorphous regions, or surface structures. In this section, we discuss the MLIP's transferability to description of loading conditions, phases, and chemical environments for which it has not been explicitly trained on. In most cases, we conclude that up-fitting is necessary to guarantee quantitative agreement with ab initio results.

Accuracy of the predicted observables (e.g. shear strengths or surface energies) is presented in the context of extrapolations grades, allowing to identify types of configurations beneficial for further up-fitting, thus, broadening the MLIP's applicability.

- High-temperature tensile deformation of TiB₂. Since TiB₂ is an UHTC (see the Introduction), modelling its mechanical behaviour at elevated temperature is of high practical relevance. Here we choose 1200 K which is close to the highest anti-oxidation temperature of TiB and TiC reported experimentally [91].
 - Atomic scale [0001], $[10\overline{1}0]$, and $[\overline{1}2\overline{1}0]$ tensile tests at 1200 K show excellent quantitative agreement with AIMD simulations at the same temperature. Specifically, differences from AIMD-calculated stresses are 0.01–3.54 GPa, resulting in statistical errors RMSE ≈ 1.85 GPa, $R^2 \approx 0.9997$. Extrapolations grades indicate reliable extrapolation ($\gamma \leq 7 < \gamma_{\text{reliable}}$).
 - TiB₂'s theoretical tensile strength at 1200 K decreases by about 17–19% compared to 300 K. For tensile toughness, our simulations predict $\approx 25\%$ decrease. Fracture mechanisms remain qualitatively unchanged with respect to 300 K.
- Room-temperature shear deformation of TiB₂. Simulations of shear deformation provide useful insights for understanding of how dislocations nucleate and move

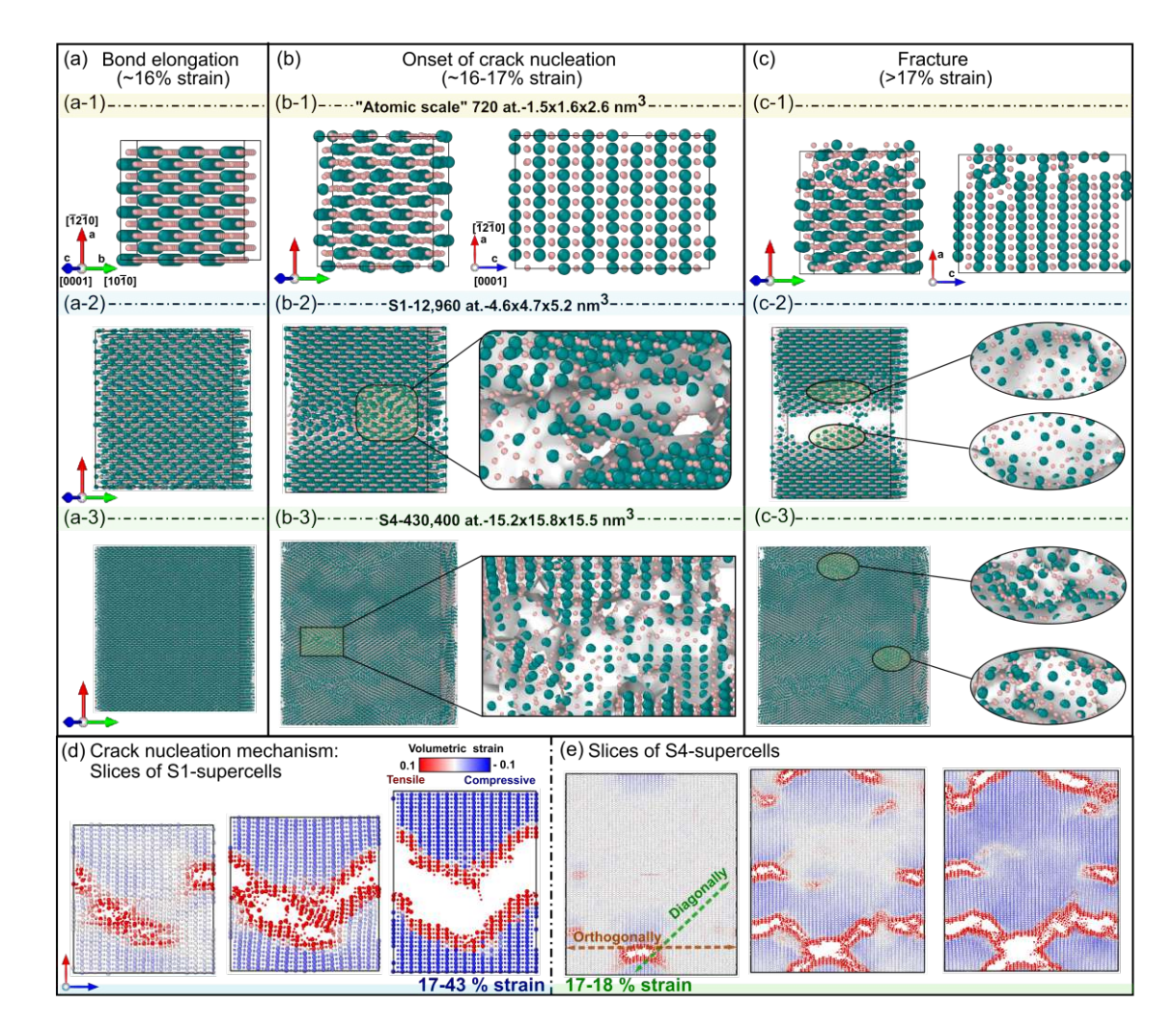


Fig. 7: Representative ML-MD snapshots of TiB₂ strained along [1210] at 300K. Upper (x-1), middle (x-2), and lower (x-3) panels show results of simulations over different lengthscales. Key deformation stages: (a) bond elongation in the loaded direction, (b) onset of crack nucleation, and (c) fracture. Thin slices of the nanoscale (d) S1 and (e) S4 supercells color-coded based on volumetric strain (using the corresponding equilibrium structure as reference). Red (blue) regions denote high tensile (compressive) strain.

in generally brittle UHTCs[92, 93]. Furthermore, as diborides typically crystallize in layered structures (α, γ, ω) , which correspond to different stacking of transition metal planes, shear deformation may induce plastic deformation via faulting, twinning, and phase transformation [63]. Based on experimental characterization of room-temperature slip in single-crystal TiB₂ [51, 79], we simulate shear deformation along $(0001)[\overline{1}2\overline{1}0]$, $(10\overline{1}0)[\overline{1}2\overline{1}0]$, and $(10\overline{1}0)[0001]$ slip systems.

Stress evolution during atomic scale ML-MD shear deformation (Fig. 8a) agrees well with equivalent AIMD simulations. This is particularly the case for strains below $\approx 20\%$, where stresses differ from AIMD values by 0.01–5.08 GPa (yielding statistical errors RMSE ≈ 3.72 GPa, $R^2 \approx 0.9993$) and γ is close to reliable extrapolation ($\gamma < 14$). This is a good result, if one considers that the training set did not contain sheared configurations. Shear strains above $\approx 20\%$ induce notably larger discrepancies in stresses (differing from AIMD by 5.4–8.5 GPa) and increased γ ($\gamma \leq 26$). The main reason is that lattice slip—responsible for a partial stress release during shearing—does not occur at the same strain step.

The shear strengths predicted by ML-MD for $(0001)[\overline{1210}]$, $(10\overline{10})[\overline{1210}]$, and $(10\overline{1}0)[0001]$ deformation, (49, 57, and 51 GPa), are $\approx 8\%$ lower than AIMD values (58, 72, and 68 GPa). Nevertheless, shear-induced structural changes observed during ML-MD correctly reproduce AIMD results (Fig. 8b,c,d).

When subject to $(0001)[\overline{1}2\overline{1}0]$ shearing, TiB₂ undergoes slip on the basal plane. The mechanism – activated for $(0001)[\overline{1210}]$ shear strain of $\approx 24\%$ – restores atoms to their ideal lattice sites (Fig. 8b). $(10\overline{1}0)[\overline{1}2\overline{1}0]$ shearing induces plastic flow on both $(\overline{1210})[10\overline{10}]$ and $(10\overline{10})[\overline{1210}]$ slip systems. The mechanisms are activated at strains near 30% and 50% (Fig. 8c). Both are accompanied by displacements of Ti and B atoms from ideal TiB₂ lattice sites. Similar to the results in (Fig. 8c), shearing along $(10\overline{1}0)[0001]$ activates different slip systems (Fig. 8d). TiB₂(0001) lattice layers glide along [10 $\overline{1}$ 0] at $\approx 30\%$ strain. A further increase in strain to $\approx 50\%$ induces glide of (1010) planes along the [0001] direction. The latter process results in significant displacements of B atoms and formation of stacking faults, as indicated by horizontal green lines in Fig. 8d (panels on the right).

The excellent agreement between ML-MD and AIMD stress/strain curves within the elastic shear response, accompanied by reasonably good agreement near TiB₂ yielding, suggests that up-fitting our MLIP[4] to accurately model shear deformation would benefit from adding configurations near TiB₂'s shear instabilities to the training set.

Room-temperature volumetric compression of TiB₂. Training on snapshots of compressed structures may be important not only for simulations of e.g. uniaxial compression or nanoindentation, but also in order to correctly account for Poisson's contraction during tensile deformation. For TiB₂, the relatively low Poisson's ratio (Tab. 1) is manifested by a rather small lateral shrinkage of the supercell during nanoscale tensile testing simulations. Here we simulate severe volumetric compression of TiB₂ at room temperature. All lattice vectors are compressed by up to 12% to show rapidly growing γ values and suggest how to improve MLIP reliability by up-fitting.

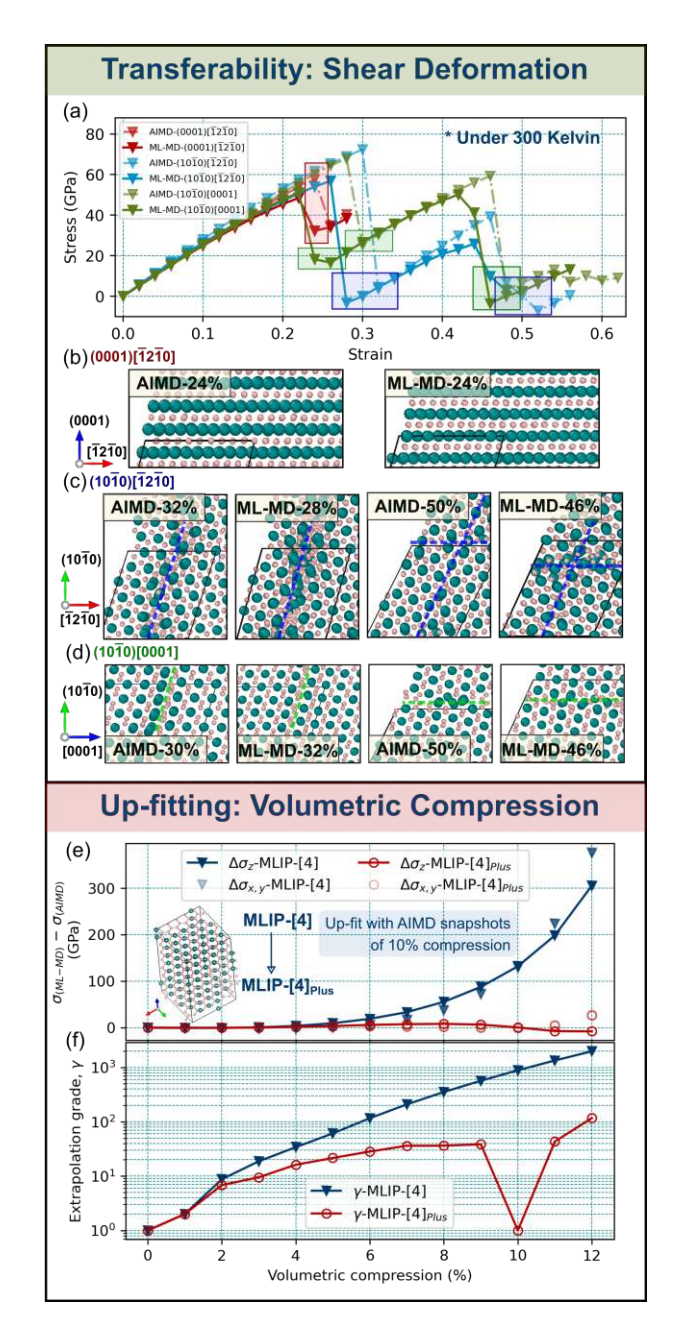


Fig. 8: Illustration of simulations to which the here-developed MLIP (MLIP-4) is transferable (a-d) or for which it requires up-fitting (e-f). (a) Comparison of AIMD (dash-dotted line) and ML-MD (solid line) stress/strain curves for TiB_2 subject to $(0001)[\overline{1210}]$, $(10\overline{10})[\overline{1210}]$, and $(10\overline{10})[0001]$ room-temperature atomic-scale shear deformation. (b, c, d) Representative snapshots at strain steps marked by shaded rectangles in (a). The dashed lines in (b, c, d) guide the eye for slip directions described in the text. (e) Differences in ML-MD and AIMD stresses $(\sigma_{(ML-MD)} - \sigma_{(AIMD)})$, resolved in the basal plane and [0001] direction ($\sigma_{x,y}$ and σ_z) of TiB₂ subject to room-temperature volumetric compression, plotted as a function of the compression percentage. (f) Blue and red data points indicate maximum extrapolation grades returned by MLIP-[4] and its up-fitted version, MLIP-[4] $_{Plus}$, during TiB₂ compression.

As shown in Fig. 8-e,f, compression-induced stresses along main crystallographic directions are indeed extremely large. In AIMD, they exceed 50 GPa for a 5% compression and reach $\approx 150 \,\mathrm{GPa}$ for a 10% compression. Our MLIP yields satisfactory agreement with AIMD for volumetric compression of 1–2\%, with stress tensor components differing from ab initio values by less than 1.83 GPa (9.57%) and γ indicating reliable extrapolation ($\gamma \leq 10 = \gamma_{\text{reliable}}$). A further increase in compression to 10%, however, causes increasing deviations from AIMD stresses and $\gamma \approx 10^2 - 10^3$.

We illustrate the effect of up-fitting by producing a new MLIP (MLIP-[4]_{Plus}) which learns from AIMD snapshots of 10% volumetrically-compressed TiB₂ (added to the LS of MLIP-[4]). This not only greatly improves accuracy for the 10% compression (stress differences are maximum 0.79 GPa (0.48%) and $\gamma < 2$) but also within the entire tested compression range (see red data points in Fig. 8-e,f).

Surface energies of TiB_2 .

Although our training set did not contain ideal surfaces, environments describing TiB₂'s fracture may facilitate reasonable predictions for energies of low-index surfaces. To test this hypothesis, we evaluate the energies of formation, $E_{\rm surf}$, of (0001), $(\overline{1210})$, and $(10\overline{10})$ surfaces, i.e. orthogonal to simulated tensile loading directions (Section 2–4).

The MLIP-predicted E_{surf} are consistent with equivalently produced ab initio values (Tab. 4). The differences are relatively small: 0.03 J m⁻² (1.40%) for $E_{\text{surf}}(0001)$, 0.04 J m^{-2} (1.68%) for $E_{\text{surf}}(\overline{1}2\overline{1}0)$, and 0.13 J m⁻² (5.75%) for $E_{\text{surf}}(10\overline{1}0)$, as underlined also by low extrapolation grades ($\gamma < \gamma_{\text{reliable}}$). ML-MS and DFT calculations of the present work indicate that the $TiB_2(\overline{1210})$ surface is energetically more stable than the basal plane. This is surprising, given that formation of $(\overline{1210})$ surfaces requires breaking strong, covalent B-B bonds. That the basal plane of TiB₂ is not the one with lowest energy has also been indicated by previous DFT tudies[94, 95]. Nevertheless, MLIP up-fitting on higher-accuracy DFT data would be needed to verify the relationship among TiB₂ surface energies.

Off-stoichiometric TiB₂ structures and other phases. Our MLIP was trained to snapshots of TiB₂ (AlB₂-type phase, P6/mmm) with a perfect stoichiometry (speaking of the entire supercell). Visualization of the training set (Fig. 3c), however, indicates presence of atomic environments with various Ti-to-B ratios as well as bond lengths and angles different from those in TiB₂. This may be useful for simulations of e.g. vacancy-containing TiB₂ structures commonly reported by synthesis [36] or other phases in the Ti-B phase diagram [96].

To investigate transferability to other phases, we use MS calculations to find the ground-state of known phases from the Ti-B phase diagram [70, 96]: Ti₂B (tetragonal, I4/mcm), Ti₃B₄ (orthorhombic, Immm), and TiB (orthorhombic Pnma)⁴. Additionally, we equilibrate the TiB₂ phase with Ti, B, or combined Ti and B vacancies: Ti₃₆B₇₁, Ti₃₅B₇₂, and Ti₃₅B₇₀. For all calculations, extrapolation grades $(\gamma \approx 10^2 - 10^4)$ are far beyond reliable extrapolation. In terms of total energies

⁴The supercell sizes are always ≈ 700 atoms, i.e. comparable to that used for TiB₂.

 (E_{tot}) , and lattice parameters (a, b, c), the largest deviation from ab initio values is exhibited by Ti_3B_4 (10% and 2.5% differences on E_{tot} and c, respectively).

Tab. 4: Transferability of the here-developed MLIP (MLIP-[4]) in molecular statics (MS) calculations of surface energies, $E_{\rm surf}$ (J m⁻²), for low-index surfaces of TiB₂. Our calculations consider stoichiometric TiB₂ surfaces, i.e. with 1:2 Ti-to-B ratio.

	Surface	$E_{\rm surf}$	Source
ML-MS	(0001)	3.80	This work
DFT	(0001)	3.80	This work
DFT	(0001)	4.50 – 4.72	Ref. [97]
DFT	(0001)	4.22 – 4.24	Ref. [94]
DFT	(0001)	4.14	Ref. [98]
DFT	(0001)	≈ 4.20	Ref. [95]
ML-MS	$(10\overline{1}0)$	3.98	This work
DFT	$(10\overline{1}0)$	4.12	This work
DFT	$(10\overline{1}0)$	≈ 4.10	Ref. [95]
ML-MS	$(\overline{1}2\overline{1}0)$	3.42	This work
DFT	$(\overline{1}2\overline{1}0)$	3.57	This work
DFT	$(\overline{1}2\overline{1}0)$	4.20 – 4.83	Ref. [94]
DFT	$(\overline{1}2\overline{1}0)$	≈ 4.02	Ref. [95]

Simulations of other stoichiometries and phases therefore require up-fitting (not necessarily due to poor accuracy but especially due to high uncertainty, $\gamma \gg$ γ_{reliable}). To illustrate the up-fitting effect, MLIP-[4] learns from additional ab initio snapshots: from 0 K equilibration of a 780-atom Ti₃B₄ supercell. Prior to up-fitting, equilibration of Ti₃B₄ yields $\gamma \geq 10^4$. Afterwards, $\gamma \leq 5 < \gamma_{\text{reliable}}$ and E_{tot} , a and c deviate from ab initio values by 4.18%, 0.07%, and 0.73%.

6 Viability of our training strategy for modelling tensile deformation in other ceramics

To illustrate general applicability of the here-proposed training strategy, we develop MLIPs for 5 other ceramic systems. Once more, we emphasize that the developed MLIPs are primarily targeted to simulations of uniaxial tensile loading at room temperature. The chosen materials are

hexagonal α -TaB₂ [63], which serves as example of changing the transition metal while keeping the same crystal structure, hexagonal ω -WB₂ [63] and γ -ReB₂[63], i.e., examples of changing the transition metal as well as the phase, cubic NaCl-type TiN [64], which serves as example of ceramic system with different non-metal species, different lattice symmetry, and bonding character that is less covalent but more ionic and metallic than TiB₂ and diborides in general, orthorhombic, nanolaminated Ti₂AlB₂ (a MAB phase [65]), which is example of ternary system with different crystal structure and mixture of ceramic-like and metallic-like bonding.

Training data generation, up-fitting, and validation follow steps carried out for TiB₂ in Sections 1–3. Again, the validation consists in (i) evaluating fitting and validation errors with respect to the training set and a meaningful validation set, (ii) comparing the predicted physical properties with equivalently calculated ab initio values, and (iii) monitoring the extrapolation grade during ML-MD simulations.

Fitting and validation errors of energies, forces, and stresses (RMSE < 3 meV atom $^{-1}$, < 0.15 eV Å⁻¹, and < 0.25 GPa, respectively) are similar to those evaluated for TiB₂ in Section 1 and close to the accuracy of the AIMD training set. Extrapolation grades for all configurations in the validation set are below the accurate extrapolation threshold ($\gamma < 2$).

Fig. 9 exemplifies validation of ML-MD tensile-stress/elongation curves against corresponding atomic-scale AIMD results. The intention is to demonstrate applicability of our training approach to different ceramic systems. Hence, we omit discussion of deformation and fracture mechanisms which, however, are consistent with AIMD results. The timeaveraged stresses recorded during ML-MD tensile tests differ from the corresponding AIMD values by 0-3.3 GPa, yielding statistical errors RMSE ≈ 2.0 GPa, $R^2 \approx 0.99$. The discrepancy is partly due to stochastic stress fluctuations, which may also onset fracture at slightly different strains in independent MD runs (compare ML-MD and AIMD results for TaB₂, ReB₂, and TiN in Fig. 9). Previous molecular dynamics tensiletesting investigations demonstrated that the statistical uncertainties on TiN elongation at fracture are comparable to the strain increment [90].

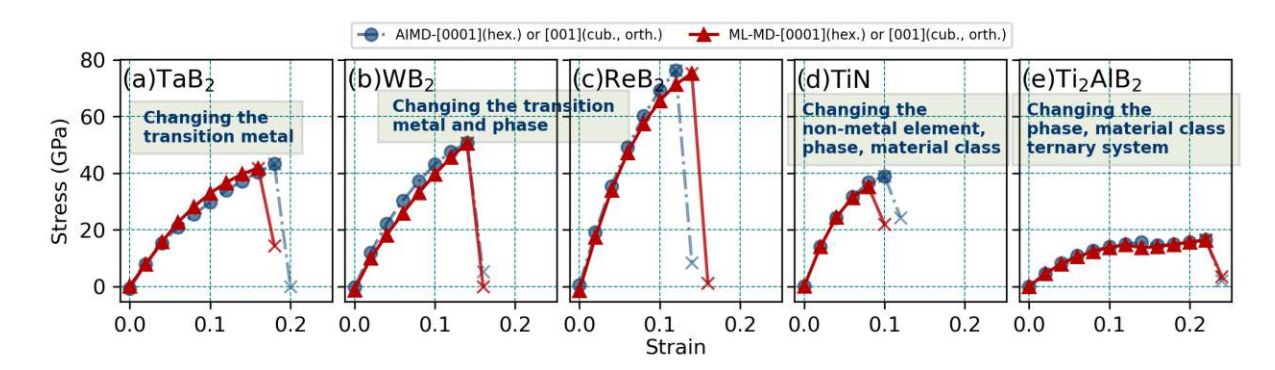


Fig. 9: Generality of our MLIP training strategy for ceramic materials, (a) α-TaB₂, (b) ω-WB₂, (c) γ-ReB₂, (d) NaCl-type TiN, and (e) the orthorhombic Ti₂AlB₂ MAB phase, as illustrated by stress/strain curves for room-temperature uniaxial tensile deformation. Specifically, the [0001] and the [001] loading directions are chosen as representative examples for hexagonal systems (TaB₂, WB₂, ReB₂) and for the cubic and the orthorhombic systems (TiN, Ti₂AlB₂), respectively. The supercell sizes and computational setup are equivalent to the atomic scale tensile tests for TiB₂, defined by the first bullet point in Section 3. Note that the stress values should not be over-interpreted, as they were obtained for atomic scale supercells (to make a fair comparison with ab initio data) and—in case of negligible size effects—are the ideal upper bounds attainable by a perfect single crystal.

The theoretical tensile strengths of TaB₂, WB₂, ReB₂, TiN, and Ti₂AlB₂ predicted by ML-MD are 40.3, 50.8, 76.2, 36.7 and 16.5 GPa, respectively. These values differ from those obtained via AIMD by maximum 8%. The corresponding ML-MD and AIMD tensile toughness values deviate by maximum 5%. Extrapolation grades during all ML-MD simulations indicate reliable extrapolation ($\gamma \leq 5 < \gamma_{\text{reliable}} \approx 10$) and remain of similar magnitude also during ML-MD tensile tests on supercells with S1-size (see second bullet point in Section 3).

The results in Fig. 9 suggest general applicability of our approach for development of MLIPs able to describe tensile deformation and fracture in hard ceramics. Specifically, our MLIPs correctly reproduce AIMD results of stress/strain curves and fracture mechanisms in different ceramic systems subject to tensile deformation. Extrapolation grades during

all ML-MD tensile tests (both atomic and nanoscale) are of similar magnitude as for TiB₂, hence indicating reliable extrapolation and realistic deformation and fracture processes.

7 Summary and Outlook

We proposed a strategy for the development of MLIPs specifically trained to description of deformation and fracture in tensile-loaded ceramic monocrystals. TiB₂ served as a model ceramic system. Training data generation, fitting, and validation procedure were performed within the moment tensor potential (MTP) formalism. MLIP-based molecular dynamics tensile-testing investigations have been carried out from the atomic scale ($\approx 10^3$ atoms) to the nanoscale ($\approx 10^4$ – 10^6 atoms). Furthermore, we discussed the MLIP's transferability to, e.g., description of TiB₂ subject to different loading conditions or different Ti-B phases, as well as the viability of the here-proposed training strategy for developing MLIPs of other ceramics.

Key findings are summarized below.

MLIP development:

MLIPs for simulations of tensile deformation until fracture can be trained following the scheme in Fig. 1, based on snapshots from finite-temperature AIMD simulations of sequentially elongated single-crystal models with sizes of $\approx 10^3$ atoms. An analogous training approach may be applicable to other loading conditions (e.g. shearing) and ceramics in different stoichiometries and crystalline phases (e.g. diborides, nitrides, MAB phases). The applicability of MLIPs to description of tensile deformation and Poisson's contraction at the nanoscale requires up-fitting. This is due to, e.g., nucleation of extended defects being hindered by the small size of AIMD supercells used for generation of training sets. We propose to generate additional ab initio data by room-temperature and elevated-temperature (1200 K) AIMD: imposing a large strain along one lattice vector, initializing atoms at ideal lattice sites, and equilibrating the supercell under fixed volume and shape. MLIPs fitted to room-temperature tensile dataset may be transferable to simulate other loading conditions; here we show examples of high-temperature tensile deformation and room-temperature shear deformation at the atomic scale. Contrarily, up-fitting is certainly required for simulations of volumetric compression, other phases and stoichiometries.

Predictions for TiB₂:

Our calculations indicate elastic isotropy of TiB₂'s basal plane at 300 and 1200 K. The directional dependence of mechanical properties in (initially) dislocation-free supercells qualitatively changes from the atomic to the nanoscale. However, all predicted properties rapidly saturate for supercell sizes increasing from $\approx 10^4$ to $\approx 10^6$ atoms. At 300 K, theoretical tensile strengths during [0001], [1010], and [1210] deformation reach 51–56 GPa. Nanoscale MD simulations provide insights into crack nucleation and growth mechanisms. Subject to [0001] tensile loading, Ti/B₂ layer delamination induces opening of nm-sized voids which rapidly coalesce, inducing formation of few-nm-size cracks inside the material. Fracture surfaces align predominantly with basal planes, {0001}, and first order pyramidal planes,

 $\{10\overline{1}1\}$. Considering deformation within the basal plane, $[10\overline{1}0]$ tensile test (i.e. loading in the direction of strong B-B bonds), most often induces crack deflection, formation of V-shaped defects, and fracture at $\{11\overline{2}2\}$ family of surfaces. Contrarily, the $[12\overline{10}]$ tensile deformation induces fracture at $\{10\overline{10}\}$ prismatic planes.

The example of TiB₂ together with additional ML-MD tensile tests done on other ceramics (TaB₂, WB₂, ReB₂, TiN, Ti₂AlB₂) indicate the viability of the here-proposed MLIP training strategy. Our approach may be extendable also to other MLIP formalisms. The predictions of nanoscale deformation and fracture in TiB₂ presented in this work may aid interpretation of future mechanical-testing experiments. Several previous studies have already demonstrated the importance of MD simulations for elucidating microscopy observations Refs. [99–101]. Follow-up work could focus on MLIP up-fitting for modelling more complex problems as, e.g., Mode-I loading of native flaws and nanosized cracks.

Bibliography

- F. Bianchini, A. Glielmo, J. Kermode und A. De Vita. Enabling QM-accurate simulation of dislocation motion in γ -Ni and α -Fe using a hybrid multiscale approach. Phys. Rev. Mater. 3.4 (2019), 043605.
- Y. Zhao. Understanding and design of metallic alloys guided by phase-field simulations. Npj Comput. Mater. 9.1 (2023), 94.
- G. Sivaraman, A. N. Krishnamoorthy, M. Baur, C. Holm, M. Stan, G. Csányi, C. Benmore und A. Vázquez-Mayagoitia. Machine-learned interatomic potentials by active learning: amorphous and liquid hafnium dioxide. Npj Comput. Mater. 6.1 (2020), 104.
- L. Fiedler, N. A. Modine, S. Schmerler, D. J. Vogel, G. A. Popoola, A. P. Thompson, S. Rajamanickam und A. Cangi. Predicting electronic structures at any length scale with machine learning. Npj Comput. Mater. 9.1 (2023), 115.
- S. M. Rassoulinejad-Mousavi und Y. Zhang. Interatomic potentials transferability for molecular simulations: A comparative study for platinum, gold and silver. Sci. Rep. 8.1 (2018), 2424.
- F. Bianchini, J. Kermode und A. De Vita. Modelling defects in Ni–Al with EAM and DFT calculations. Model. Simul. Mat. Sci. Eng. 24.4 (2016), 045012.
- L. Proville, D. Rodney und M.-C. Marinica. Quantum effect on thermally activated glide of dislocations. *Nat. Mater.* 11.10 (2012), 845–849.
- V. L. Deringer, M. A. Caro und G. Csányi. Machine learning interatomic potentials as emerging tools for materials science. Adv. Mater. 31.46 (2019), 1902765.
- Y. Zuo, C. Chen, X. Li, Z. Deng, Y. Chen, J. Behler, G. Csányi, A. V. Shapeev, A. P. Thompson, M. A. Wood u.a. Performance and cost assessment of machine learning interatomic potentials. J. Phys. Chem. A 124.4 (2020), 731–745.
- [10]R. Drautz. Atomic cluster expansion for accurate and transferable interatomic potentials. Phys. Rev. B 99.1 (2019), 014104.
- J. S. Smith, O. Isayev und A. E. Roitberg. ANI-1: an extensible neural network |11|potential with DFT accuracy at force field computational cost. Chem. Sci. 8.4 (2017), 3192-3203.

- A. V. Shapeev, E. V. Podryabinkin, K. Gubaev, F. Tasnádi und I. A. Abrikosov. Elinvar effect in β -Ti simulated by on-the-fly trained moment tensor potential. New J. Phys. 22.11 (2020), 113005.
- T. Nishiyama, A. Seko und I. Tanaka. Application of machine learning potentials to predict grain boundary properties in fcc elemental metals. Phys. Rev. Mater. 4.12 (2020), 123607.
- F. Deng, H. Wu, R. He, P. Yang und Z. Zhong. Large-scale atomistic simulation of dislocation core structure in face-centered cubic metal with Deep Potential method. Comput. Mater. Sci. 218 (2023), 111941.
- H. Mori und T. Ozaki. Neural network atomic potential to investigate the dislocation dynamics in bcc iron. Phys. Rev. Mater. 4.4 (2020), 040601.
- C. W. Rosenbrock, K. Gubaev, A. V. Shapeev, L. B. Pártay, N. Bernstein, G. |16| Csányi und G. L. Hart. Machine-learned interatomic potentials for alloys and alloy phase diagrams. Npj Comput. Mater. 7.1 (2021), 24.
- H. Zong, G. Pilania, X. Ding, G. J. Ackland und T. Lookman. Developing an interatomic potential for martensitic phase transformations in zirconium by machine learning. Npj Comput. Mater. 4.1 (2018), 48.
- X.-G. Li, C. Hu, C. Chen, Z. Deng, J. Luo und S. P. Ong. Quantum-accurate spectral neighbor analysis potential models for Ni-Mo binary alloys and fcc metals. Phys. Rev. B 98.9 (2018), 094104.
- F. Tasnádi, F. Bock, J. Tidholm, A. V. Shapeev und I. A. Abrikosov. Efficient prediction of elastic properties of Ti_{0.5}Al₀.5N at elevated temperature using machine learning interatomic potential. Thin Solid Films 737 (2021), 138927.
- [20] A. P. Thompson, L. P. Swiler, C. R. Trott, S. M. Foiles und G. J. Tucker. Spectral neighbor analysis method for automated generation of quantum-accurate interatomic potentials. J. Comput. Phys. 285 (2015), 316–330.
- J. Behler. Constructing high-dimensional neural network potentials: a tutorial review. Int. J. Quantum Chem. 115.16 (2015), 1032–1050.
- A. P. Bartók, M. C. Payne, R. Kondor und G. Csányi. Gaussian approximation potentials: The accuracy of quantum mechanics, without the electrons. Phys. Rev. Lett. 104.13 (2010), 136403.
- [23]A. V. Shapeev. Moment tensor potentials: A class of systematically improvable interatomic potentials. Multiscale Model. Simul. 14.3 (2016), 1153–1173.
- A. Seko, A. Togo und I. Tanaka. Group-theoretical high-order rotational inva-|24|riants for structural representations: Application to linearized machine learning interatomic potential. Phys. Rev. B 99.21 (2019), 214108.

- M. Qamar, M. Mrovec, Y. Lysogorskiy, A. Bochkarev und R. Drautz. Atomic cluster expansion for quantum-accurate large-scale simulations of carbon. J. Chem. Theory Comput. 19.15 (2023), 5151–5167.
- P. Rowe, G. Csányi, D. Alfe und A. Michaelides. Development of a machine |26|learning potential for graphene. Phys. Rev. B 97.5 (2018), 054303.
- D. A. Cohn, Z. Ghahramani und M. I. Jordan. Active learning with statistical [27]models. J. Artif. Intell. 4 (1996), 129–145.
- E. V. Podryabinkin und A. V. Shapeev. Active learning of linearly parametrized |28|interatomic potentials. Comput. Mater. Sci. 140 (2017), 171–180.
- [29] K. Gubaev, E. V. Podryabinkin und A. V. Shapeev. Machine learning of molecular properties: Locality and active learning. The Journal of chemical physics 148.24 (2018), 241727.
- [30] Y. Lysogorskiy, A. Bochkarev, M. Mrovec und R. Drautz. Active learning strategies for atomic cluster expansion models. Phys. Rev. Mater. 7.4 (2023), 043801.
- Y. Lysogorskiy, C. v. d. Oord, A. Bochkarev, S. Menon, M. Rinaldi, T. Hammerschmidt, M. Mrovec, A. Thompson, G. Csányi, C. Ortner u.a. Performant implementation of the atomic cluster expansion (PACE) and application to copper and silicon. *npj Comput. Mater.* 7.1 (2021), 1–12.
- [32]G. Luo. A review of automatic selection methods for machine learning algorithms and hyper-parameter values. Netw. Model. Anal. Health Inform. Bioinform. 5 (2016), 1-16.
- M. Salem, M. J. Cowan und G. Mpourmpakis. Predicting segregation energy in [33]single atom alloys using physics and machine learning. ACS omega 7.5 (2022), 4471-4481.
- J. Fang, M. Xie, X. He, J. Zhang, J. Hu, Y. Chen, Y. Yang und Q. Jin. Machine learning accelerates the materials discovery. Mater. Today Commun. (2022), 104900.
- F. Ribeiro und A. L. S. Gradvohl. Machine learning techniques applied to solar flares forecasting. Astron. Comput. 35 (2021), 100468.
- M. Magnuson, L. Hultman und H. Högberg. Review of transition-metal diboride [36]thin films. Vacuum 196 (2022), 110567.
- H. Holleck. Material selection for hard coatings. J. Vac. Sci. Technol. 4.6 (1986), |37|2661 - 2669.
- B. R. Golla, A. Mukhopadhyay, B. Basu und S. K. Thimmappa. Review on ultra-high temperature boride ceramics. Prog. Mater. Sci. 111 (2020), 100651.

- C. Wang, S. Akbar, W. Chen und V. Patton. Electrical properties of hightemperature oxides, borides, carbides, and nitrides. J. Mater. Sci. 30 (1995), 1627 - 1641.
- C. Sevik, J. Bekaert, M. Petrov und M. V. Milošević. High-temperature multigap superconductivity in two-dimensional metal borides. Phys. Rev. Mater. 6.2 (2022), 024803.
- [41]R. Wiedemann, H. Oettel und M. Jerenz. Structure of deposited and annealed TiB₂ layers. Surf. Coat. Technol. 97.1-3 (1997), 313–321.
- W. Hofmann und W. Jäniche. Die struktur von aluminiumborid AlB₂. Zeitschrift [42]für Physikalische Chemie 31.1 (1936), 214–222.
- J. Eorgan und N. Fern. Zirconium diboride coatings on tantalum. JOM 19.9 [43](1967), 6-11.
- J. T. Norton, H. Blumenthal und S. Sindeband. Structure of diborides of titanium, zirconium, columbium, tantalum and vanadium. JOM 1 (1949), 749–751.
- M. Mikula, B. Grančič, V. Buršíková, A. Csuba, M. Držík, Š. Kavecký, A. Plecenik [45]und P. Kúš. Mechanical properties of superhard TiB₂ coatings prepared by DC magnetron sputtering. Vacuum 82.2 (2007), 278–281.
- J. Geng, G. Liu, F. Wang, T. Hong, C. Xia, M. Wang, D. Chen, N. Ma und H. [46]Wang. Microstructural and mechanical anisotropy of extruded in-situ TiB₂/2024 composite plate. *Mater. Sci. Eng.* 687 (2017), 131–140.
- T. F. Zhang, B. Gan, S.-m. Park, Q. M. Wang und K. H. Kim. Influence of [47]negative bias voltage and deposition temperature on microstructure and properties of superhard TiB₂ coatings deposited by high power impulse magnetron sputtering. Surf. Coat. Technol. 253 (2014), 115–122.
- M. Mikula, B. Grančič, V. Buršíková, A. Csuba, M. Držík, Š. Kavecký, A. Plecenik und P. Kúš. Mechanical properties of superhard TiB₂ coatings prepared by DC magnetron sputtering. Vacuum 82.2 (2007), 278–281.
- C. Fuger, R. Hahn, A. Hirle, P. Kutrowatz, M. Weiss, A. Limbeck, O. Hunold, P. Polcik und H. Riedl. Revisiting the origins of super-hardness in TiB_{2+z} thin films-Impact of growth conditions and anisotropy. Surf. Coat. Technol. 446 (2022), 128806.
- [50]R. G. Munro. Material properties of titanium diboride. J. Res. Natl. Inst. Stan. 105.5 (2000), 709.
- Z. Chen, B. Paul, S. Majumdar, N. L. Okamoto, K. Kishida, H. Inui und S. |51|Otani. Room-temperature deformation of single crystals of ZrB₂ and TiB₂ with the hexagonal AlB₂ structure investigated by micropillar compression. Sci. Rep. 11.1 (2021), 14265.

- T. Zhang, S. Song, C. Xie, G. He, B. Xing, R. Li und Q. Zhen. Preparation of |52|highly-dense TiB₂ ceramic with excellent mechanical properties by spark plasma sintering using hexagonal TiB₂ plates. Mater. Res. Express 6.12 (2019), 125055.
- Y. Zhou, J. Wang, Z. Li, X. Zhan und J. Wang. First-Principles Investigation on the Chemical Bonding and Intrinsic Elastic Properties of Transition Metal Diborides TMB₂ (TM= Zr, Hf, Nb, Ta, and Y). Ultra-High Temperature Ceramics: Materials for Extreme Environment Applications (2014), 60–82.
- |54|F.-Z. Dai und Y. Zhou. Effects of transition metal (TM= Zr, Hf, Nb, Ta, Mo, W) elements on the shear properties of TMB₂s: A first-principles investigation. Comput. Mater. Sci. 117 (2016), 266–269.
- X. Zhang, X. Luo, J. Li, P. Hu und J. Han. The ideal strength of transition metal |55|diborides TMB₂ (TM= Ti, Zr, Hf): Plastic anisotropy and the role of prismatic slip. Scr. Mater. 62.8 (2010), 625–628.
- S. Attarian und S. Xiao. Development of a 2NN MEAM potential for TiB system and studies of the temperature dependence of the nanohardness of TiB₂. Comput. Mater. Sci. 201 (2022), 110875.
- [57]S. Attarian. Multiscale modeling of Ti/TiB composites. Diss. The University of Iowa, 2021.
- B. Timalsina. Development of Eam and Rf-MEAM Interatomic Potential for |58|Zirconium Diboride. Diss. Missouri State University, 2021.
- M. S. Daw, J. W. Lawson und C. W. Bauschlicher Jr. Interatomic potentials for zirconium diboride and hafnium diboride. Comput. Mater. Sci. 50.10 (2011), 2828–2835.
- G. Kresse und J. Furthmüller. Efficient iterative schemes for ab initio total-energy calculations using a plane-wave basis set. Phys. Rev. B 54.16 (1996), 11169.
- |61|G. Kresse und D. Joubert. From ultrasoft pseudopotentials to the projector augmented-wave method. Phys. Rev. B 59 (3 Jan. 1999), 1758–1775.
- J. P. Perdew, A. Ruzsinszky, G. I. Csonka, O. A. Vydrov, G. E. Scuseria, L. A. Constantin, X. Zhou und K. Burke. Restoring the density-gradient expansion for exchange in solids and surfaces. Phys. Rev. Lett. 100 (13 Apr. 2008), 136406.
- [63]T. Leiner, N. Koutná, J. Janovec, M. Zelený, P. H. Mayrhofer und D. Holec. On energetics of allotrope transformations in transition-metal diborides via plane-byplane shearing. *Vacuum* 215 (2023), 112329.
- |64|D. Sangiovanni, F. Tasnádi, L. Johnson, M. Odén und I. Abrikosov. Strength, transformation toughening, and fracture dynamics of rocksalt-structure $Ti_{1-x}Al_xN$ (0 x 0.75) alloys. Phys. Rev. Mater. 4.3 (2020), 033605.

- A. Carlsson, J. Rosen und M. Dahlqvist. Theoretical predictions of phase stability for orthorhombic and hexagonal ternary MAB phases. Phys. Chem. Chem. Phys. 24.18 (2022), 11249–11258.
- M. Parrinello und A. Rahman. Polymorphic transitions in single crystals: A new |66|molecular dynamics method. J. Appl. Phys. 52.12 (1981), 7182–7190.
- D. Sangiovanni, W. Mellor, T. Harrington, K. Kaufmann und K. Vecchio. Enhan-[67]cing plasticity in high-entropy refractory ceramics via tailoring valence electron concentration. *Mater. Des.* 209 (2021), 109932.
- N. Koutná, L. Löfler, D. Holec, Z. Chen, Z. Zhang, L. Hultman, P. H. Mayrhofer [68]und D. G. Sangiovanni. Atomistic mechanisms underlying plasticity and crack growth in ceramics: a case study of AlN/TiN superlattices. Acta Mater. 229 (2022), 117809.
- D. G. Sangiovanni, F. Tasnádi, T. Harrington, M. Odén, K. S. Vecchio und I. A. [69]Abrikosov. Temperature-dependent elastic properties of binary and multicomponent high-entropy refractory carbides. Mater. Des. 204 (2021), 109634.
- A. Jain, S. P. Ong, G. Hautier, W. Chen, W. D. Richards, S. Dacek, S. Cholia, D. Gunter, D. Skinner, G. Ceder u.a. Commentary: The Materials Project: A materials genome approach to accelerating materials innovation. APL Mater. 1.1 (2013), 011002.
- I. S. Novikov, K. Gubaev, E. V. Podryabinkin und A. V. Shapeev. The MLIP package: moment tensor potentials with MPI and active learning. Mach. learn.: sci. technol. 2.2 (2020), 025002.
- [72]R. Fletcher. Practical methods of optimization. John Wiley & Sons, 2013.
- L. C. Erhard, J. Rohrer, K. Albe und V. L. Deringer. A machine-learned interatomic potential for silica and its relation to empirical models. Npj Comput. Mater. 8.1 (2022), 90.
- A. P. Thompson, H. M. Aktulga, R. Berger, D. S. Bolintineanu, W. M. Brown, P. S. Crozier, P. J. in 't Veld, A. Kohlmeyer, S. G. Moore, T. D. Nguyen, R. Shan, M. J. Stevens, J. Tranchida, C. Trott und S. J. Plimpton. LAMMPS - a flexible simulation tool for particle-based materials modeling at the atomic, meso, and continuum scales. Comp. Phys. Comm. 271 (2022), 108171.
- A. Stukowski. Visualization and analysis of atomistic simulation data with OVITOthe Open Visualization Tool. Model. Simul. Mat. Sci. Eng. 18.1 (2009), 015012.
- |76|D. Chicco, M. J. Warrens und G. Jurman. The coefficient of determination Rsquared is more informative than SMAPE, MAE, MAPE, MSE and RMSE in regression analysis evaluation. Peer J Computer Science 7 (2021), e623.

- E. Podryabinkin, K. Garifullin, A. Shapeev und I. Novikov. MLIP-3: Active learning on atomic environments with Moment Tensor Potentials. arXiv preprint arXiv:2304.13144 (2023).
- H. Fan und J. A. El-Awady. Molecular dynamics simulations of orientation effects during tension, compression, and bending deformations of magnesium nanocrystals. J. Appl. Mech. 82.10 (2015), 101006.
- K. Nakano, T. Imura und S. Takeuchi. Hardness anisotropy of single crystals of IVa-diborides. Japanese Journal of Applied Physics 12.2 (1973), 186.
- M. Hodapp und A. Shapeev. In operando active learning of interatomic interaction [80]during large-scale simulations. Mach. learn.: sci. technol. 1.4 (2020), 045005.
- R. Freitas und Y. Cao. Machine-learning potentials for crystal defects. MRS Commun. 12.5 (2022), 510–520.
- P. Spoor, J. Maynard, M. Pan, D. Green, J. Hellmann und T. Tanaka. Elastic constants and crystal anisotropy of titanium diboride. Appl. Phys. Lett. 70.15 (1997), 1959–1961.
- G. M. Amulele und M. H. Manghnani. Compression studies of TiB₂ using synchrotron X-ray diffraction and ultrasonic techniques. J. Appl. Phys. 97.2 (2005), 023506.
- H. Xiang, Z. Feng, Z. Li und Y. Zhou. Temperature-dependence of structural and mechanical properties of TiB₂: A first principle investigation. J. Appl. Phys. 117.22 (2015).
- L. Chen, Y. Gu, Y. Qian, L. Shi, Z. Yang und J. Ma. A facile one-step route to [85]nanocrystalline TiB₂ powders. Mater. Res. Bull. 39.4-5 (2004), 609–613.
- M. Mukaida, T. Goto und T. Hirai. Preferred orientation of TiB₂ plates prepared by CVD of the $TiCl_{4+}B_2H_6$ system. J. Mater. Sci. 26 (1991), 6613–6617.
- E. Kelesoglu und C. Mitterer. Structure and properties of TiB₂ based coatings [87]prepared by unbalanced DC magnetron sputtering. Surf. Coat. Technol. 98.1-3 (1998), 1483-1489.
- B. Paul, N. L. Okamoto, M. Kusakari, Z. Chen, K. Kishida, H. Inui und S. Otani. |88| Plastic deformation of single crystals of CrB₂, TiB₂ and ZrB₂ with the hexagonal AlB₂ structure. Acta Mater. 211 (2021), 116857.
- H. Waldl, M. Tkadletz, A. Lechner, C. Czettl, M. Pohler und N. Schalk. Evolution of the fracture properties of arc evaporated $Ti_{1-x}Al_xN$ coatings with increasing Al content. Surface and Coatings Technology 444 (2022), 128690.
- D. G. Sangiovanni, A. Kraych, M. Mrovec, J. Salamania, M. Odén, F. Tasnádi und I. A. Abrikosov. Descriptor for slip-induced crack blunting in refractory ceramics. Physical Review Materials 7.10 (2023), 103601.

- Y. Jiao, L. Huang und L. Geng. Progress on discontinuously reinforced titanium matrix composites. J. Alloys Compd. 767 (2018), 1196–1215.
- S. Dub, S. Sichkar, V. Belous, G. Tolmacheva, P. Loboda, Y. I. Bogomol und [92]G. Kysla. Mechanical properties of single crystals of transition metals diborides TMB₂ (TM= Sc, Hf, Zr, Ti). Experiment and theory. J. Superhard Mater. 39 (2017), 308-318.
- J. Lei, S. Hu, C. L. Turner, K. Zeng, M. T. Yeung, J. Yan, R. B. Kaner und [93]S. H. Tolbert. Synthesis and high-pressure mechanical properties of superhard rhenium/tungsten diboride nanocrystals. ACS nano 13.9 (2019), 10036–10048.
- W. Sun, F. Dai, H. Xiang, J. Liu und Y. Zhou. General trends in surface stability and oxygen adsorption behavior of transition metal diborides (TMB₂). J. Mater. Sci. Technol. 35.4 (2019), 584–590.
- Q. Gan, H. Liu, S. Zhang, F. Wang, J. Cheng, X. Wang, S. Dong, Q. Tao, [95]Y. Chen und P. Zhu. Robust hydrophobic materials by surface modification in transition-metal diborides. ACS Appl. Mater. Interfaces 13.48 (2021), 58162–58169.
- J. Murray, P. Liao und K. Spear. The B-Ti (boron-titanium) system. Bull. alloy phase diagr. 7.6 (1986), 550–555.
- C. Guan und H. Zhu. Theoretical insights into the behaviors of sodium and [97]aluminum on the cathode titanium diboride surfaces. Comput. Mater. Sci. 211 (2022), 111535.
- [98]J. Clayton, W. Rubink, V. Ageh, D. Choudhuri, R. R. Chen, J. Du und T. Scharf. Deformation and Failure Mechanics of Boron Carbide–Titanium Diboride Composites at Multiple Scales. JOM 71 (2019), 2567–2575.
- N. Koutná, L. Löfler, D. Holec, Z. Chen, Z. Zhang, L. Hultman, P. H. Mayrhofer und D. G. Sangiovanni. Atomistic mechanisms underlying plasticity and crack growth in ceramics: a case study of AlN/TiN superlattices. Acta Mater. 229 (2022), 117809.
- J. Salamania, D. Sangiovanni, A. Kraych, K. C. Kwick, I. Schramm, L. Johnson, R. [100]Boyd, B. Bakhit, T. Hsu, M. Mrovec u.a. Elucidating dislocation core structures in titanium nitride through high-resolution imaging and atomistic simulations. Mater. Des. 224 (2022), 111327.
- [101]Z. Chen, Y. Zheng, L. Löfler, M. Bartosik, G. K. Nayak, O. Renk, D. Holec, P. H. Mayrhofer und Z. Zhang. Atomic insights on intermixing of nanoscale nitride multilayer triggered by nanoindentation. Acta Mater. 214 (2021), 117004.

Main Contribution II

Under Review in Acta Materialia, Elsevier

Shear-activated phase transformations of diborides via machine-learning potential molecular dynamics

Authors:

Shuyao Lin

David Holec Davide G. Sangiovanni Thomas Leiner Lars Hultman Paul H. Mayrhofer Nikola Koutná

Under Review, 2025



Shear-activated phase transformations of diborides via machinelearning potential molecular dynamics

Keywords: Machine learning interatomic potentials, molecular dynamics, diborides, shearing, phase transformation

Abstract

The layered character of transition metal diborides (TMB₂:s)—with three structure polymorphs representing different stackings of the metallic sublattice—evokes the possibility of activating phase-transformation plasticity via mechanical shear strain. This is critical to overcome the most severe limitation of TMB₂:s: their brittleness. To understand finite-temperature mechanical response of the α , ω , and γ polymorphs at the atomic scale, we train machine-learning interatomic potentials (MLIPs) for TMB₂:s, TM=(Ti, Ta, W, Re). Validation against ab initio data set supports the MLIPs' capability to predict structural and elastic properties, as well as shear-induced slipping and phase transformations. Nanoscale molecular dynamics simulations (> 10^4 atoms; $\approx 5^3$ nm³) allow evaluating theoretical shear strengths attainable in single-crystal TMB₂:s and their temperature evolution from 300 up to 1200 K. Quantitative structural analysis via angular and bond-order Steinhardt parameter descriptors shows that (0001)[1210] and $(0001)[10\overline{1}0]$ shearing activates transformations between the (energetically) metastable and the preferred phase of TiB₂, TaB₂, and WB₂. These transformations can be promoted by additional tensile or compressive strain along the [0001] axis. The preferred phase of ReB₂ shows negative thermal expansion and an unprecedented shear-induced plasticity mechanism: metallic/boron layer interpenetration and uniform lattice rotation.

Introduction

Renowned for their exceptional hardness [1, 2], high melting points [3], corrosion and erosion resistance, as well as excellent thermal and electrical conductivity [4], transition metal diborides (TMB₂:s) are crucial for various industrial applications requiring to withstand extreme conditions, such as high temperatures and/or severe mechanical loads [5, 6]. As most hard ceramics, TMB₂:s are severely limited by their brittleness. which may cause easy crack nucleation and/or propagation of pre-existed cracks. Thus, understanding mechanical response of diborides, in particular, loading conditions that facilitate plastic deformation, is of fundamental as well as of practical importance. Plasticity can be promoted in various ways, including alloying, nanostructural or superlattice design [7, 8]. Motivated by the striking structural similarity of diboride polymorphs, this work focuses on *intrinsic* plasticity mechanisms, namely, stress-activated transformation plasticity.

The possibility of transformation plasticity in TMB₂:s is evoked by their layered hexagonal structures—the α phase (space group (s.g.), P6/mmm), the ω and γ phase (s.g. P6₃/mmc) [9, 10]—representing different stackings of the TM sublattice, which may be interchangeable subject to mechanical loading. According to density functional theory (DFT) predictions [11], group 4–5 transition metals diborides energetically favor the α

phase, while those in group 6 favor the α and ω phase, and in group 7 favor the γ phase. There are, however, some inconsistencies in the literature regarding stable and metastable TMB_2 :s, such as WB_2 being quite sensitive to the synthesis conditions [7, 12–14] which may promote formation of phases far from the thermodynamic equilibrium. Other factors affecting the phase preference of TMB_2 :s are (i) the B sub/over-stoichiometry [15, 16] (often attributed to the presence of B vacancies [17, 18] or the B tissue phase along grain boundaries [19]), and (ii) the energetic proximity of some stackings (e.g., the α and ω stacking of TaB₂, or the ω and γ stacking of WB₂ [11]). Additional uncertainty on stable and metastable phases stems from the non-trivial distinction between the diboride phase polymorphs via X-ray diffraction or electron microscopy [20].

With only few experimental reports [12, 21], strain-activated phase transformations of TMB₂:s are a nearly untouched topic. Necessary investigations require fine control over the synthesis and micromechanical testing conditions as well as careful high-resolution transmission electron microscopy (HR-TEM) analysis. Atomistic simulations may guide these challenging experiments, offering access to properties of ideal single-crystals and well-defined loading conditions. While DFT studies indicated phase transformations in TMB₂:s [11, 22, 23], calculations based on molecular dynamics (MD) simulations at finite temperature have been rare due to the lack of reliable force fields [24–26] or their limitations in achieving quantum-level accuracy. Despite rapid advancement of machinelearning interatomic potentials [27, 28] (MLIPs) and their impressive capabilitiesincluding DFT-level of accuracy with up to 10^5 higher computational efficiency [29, 30, and systematic improveability via active learning [31]—MLIP training is non-trivial even for binary systems [32–34]. Only few MLIPs are available for ceramics [35, 36] and their applications beyond DFT length scales are sparse [37, 38]. The complex atomic interactions involved in phase transformations pose yet another obstacle [39–41].

Our study exploits machine-learning potential molecular dynamics (ML-MD) to reveal phase transformations of TMB₂:s subject to shear deformation. TiB₂, TaB₂, WB₂, and ReB₂ are chosen to exemplify group 4, 5, 6, and 7 TMB₂:s, energetically favoring the α phase (TiB₂, TaB₂), ω phase (WB₂), and γ phase (ReB₂). The MLIPs are trained in the moment tensor potential (MTP) formalism [42] and validated against relevant ab initio MD data, including the extrapolation grade (MV [43]) analysis. Subsequently, the α , γ , and ω phase are equilibrated at 300 K for each TMB₂, TM = (Ti, Ta, W, Re), using supercells with $\approx 15 \cdot 10^3$ atoms. Stress/strain curves derived from $(0001)[\overline{1}2\overline{1}0]$ shear simulations allow predicting (temperature-dependent) trends in the shear strengths and identifying diborides with shear-activated stacking changes. These changes are traced not only by visual inspection but also through quantitative analysis using angular and bond-order parameter descriptors of local atomic environments.

Our study showcases the capabilities of MLIPs in quantifying mechanical properties of structurally complex materials and predicting their structural evolution under experimentally relevant loading conditions. Key findings include $\omega \to \alpha$ transformation in TiB₂ and TaB_2 , $\alpha \to \omega$ transformation in WB₂, and anomalous behavior of ReB₂ exhibiting negative thermal expansion and homogeneous lattice rotation subject to shearing.

Methods

Ab initio molecular dynamics calculations

Finite-temperature Born-Oppenheimer ab initio molecular dynamics (ab initio MD) were carried out using VASP [44] together with the projector augmented wave (PAW) [45] method and the Perdew-Burke-Ernzerhof exchange-correlation functional revised for solids (PBEsol) [46]. The plane-wave cut-off energies of 300 eV and Γ -point sampling of the reciprocal space were employed.

Structural models of TMB₂s, TM=(Ti,Ta,W,Re), considered the α , γ , and ω polymorphs, i.e., were based on the AlB₂-type (P6/mmm), ReB₂-type (P6₃mmc), and WB₂-type (P6₃mmc) phase [11]. Their hexagonal unit cells were orthogonalized to satisfy following crystallographic relationships: $x \parallel [10\overline{1}0], y \parallel [\overline{1}2\overline{1}0], z \parallel [0001]$. All ab initio MD calculations were carried out in 720-atom supercells (240 TM+480 B), having dimensions of $\approx (1.5 \times 1.6 \times 2.6) \text{ nm}^3$. The supercells (3 for each TM) were equilibrated at desired temperature (300 K, in some cases also 1200 K) in 2 steps: during (i) a 10 ps isobaric-isothermal (NpT) simulation with Parrinello-Rahman barostat [47] and Langevin thermostat, and, subsequently, (ii) a 2-4 ps simulation with the canonical (NVT) ensemble based on Nosé-Hoover thermostat, using time-averaged lattice parameters from (i). Computational setup for shearing along the $(10\overline{1}0)[\overline{1}2\overline{1}0]$, $(0001)[\overline{1}2\overline{1}0]$, and $(10\overline{1}0)[0001]$ slip systems followed Refs. [48–50], in particular, using 2% strain increment and 2.7 ps relaxation at each strain. Stress tensor components were calculated by averaging data from the last 0.5 ps.

Room-temperature elastic constants, C_{ij} , were evaluated following Ref. [51], i.e., based on a second-order polynomial fit of stress/strain data from the [0001], $[10\overline{1}0]$, and $[\overline{1}2\overline{1}0]$ tensile simulations (used to derive C_{11} , C_{12} , C_{13} , C_{33}), and the $(0001)[\overline{1}2\overline{1}0]$, $(10\overline{1}0)[\overline{1}2\overline{1}0]$ and $(10\overline{1}0)[0001]$ shear simulations (used to derive C_{44}), considering strains between 0 and 4\%. This is consistent with our previous work [36], concerning C_{ij} of α -TiB₂.

Development and validation of machine-learning interatomic potentials (MLIPs)

We used the moment tensor potential (MTP) formalism, as implemented in the mlip-2 package [31]. Training data generation and training workflow involved multiple active learning loops, detailed in our previous work, see Ref. [36]-Fig.1. In short, each loop consisted of: (1) fitting a MLIP; (2) comparing the extrapolation grade, MV [43], against a learning set, LS; (3) expanding the training set by extrapolative $(MV \ge 2)$ configurations from the LS (using the MaxVol algorithm [43] via the select add command of mlip-2); (4) repeating from step (1) until accurate extrapolation (MV<2) is reached for all configuration in the LS. MLIPs were fitted based on 16g MTPs (referring to the highest degree of polynomial-like basis functions in the analytic description of the MTP [42]), using the Broyden-Fletcher-Goldfarb-Shanno method [52] with 1500 iterations, as well as weight of 1.0, 0.01 and 0.01 for total energy, stresses and forces in the loss functional. The cutoff radius of 5.5 Å was used, similar to other recent MLIP studies [53, 54] and motivated our previous tests for α -TiB₂ [36]. Validation set contained 20 % of all our ab initio MD data. The detailed validation strategy follows our previous



study [36]. Tab. S1 reports the detailed RMSE values for energy, forces, and stress of the final training set. Fig. S1 shows the direct validation against physical phenomena and statistical trends derived from our ab initio data for all here-studied materials, while Fig. S2 provides parity plots illustrating direct data comparison using TiB₂ as an example. Accuracy of our MLIPs is consistent with accuracy of the underlying ab initio training dataset and meets standards of previous MLIP benchmarking studies [55].

Molecular dynamics with MLIPs (ML-MD)

ML-MD calculations were performed with the LAMMPS code [56] interfaced with the mlip-2 package [31], which allows using MTP-type MLIPs (specified in the pair style command). Further, the active learning state file (state.als) was used to output the extrapolation grade, MV [43], during the simulations (note that our previous work uses γ instead of MV, which is not convenient here, as γ is one of the three investigated stackings).

To provide a fair comparison with our ab initio MD data, computational setup of equilibration, shear, and tensile tests at the atomic scale was always the most equivalent to the respective ab initio MD simulations, including evaluation of time-averaged stresses and elastic constants calculations. For more realistic simulations beyond ab initio length scales, we used supercells with 12,960 atoms and dimensions of about 5³ nm³. Prior to simulating shear deformation, the supercells were equilibrated for 5 ps at the targeted temperature using the isobaric-isothermal (NpT) ensemble, combining with the Nosé-Hoover thermostat with a 1 fs time step. The supercells were deformed at a constant strain rate $(0.5 \text{ m s}^{-1}, \text{ similar to typical values used in MD mechanical tests [57]})$.

Structural analysis and phase identification

The OVITO package [58] allowed visualizing MD trajectories and analyzing the volumetric strain distribution (using cut-off radius of \pm 0.1 Å). Due to structural complexity of the investigated diboride polymorphs, OVITO modifiers or other conventional tools of structure identification could not be employed. Instead, we used (i) angular distribution analysis, and (ii) Steinhardt bond-orientational order parameters [59]. We acknowledge that despite both provide a strong indication of the phase constitution, neither is completely unambiguous.

The bond analysis considered the nearest-neighbor B-B bonds within the 2 Å cutoff radius (selected from the $[a/\sqrt{3}, a]$ interval to encompass all the investigated TMB₂:s), in which each B was 3-coordinated. The angles $(120 \pm 5)^{\circ}$ served to classify B layers as "flat", where the range was chosen based on the standard deviation ($\approx 11^{\circ}$ for all TM elements) from room-temperature ab initio MD NVT equilibration. For "puckered" layers, a slightly different range of angles was used depending on the TM; e.g. $(106 \pm 6)^{\circ}$ for γ -ReB₂ or $(111 \pm 5)^{\circ}$ for ω -WB₂ (note that in case of partial overlap between the intervals used to classify "flat" and "puckered", each was expanded by 1°). Other angles were evaluated as "other".

Calculations of **Steinhardt parameters** were carried out using the PYSCAL package [60]. Specifically, the values were obtained by averaging the Voronoi-weighted Stein-

hardt parameters, more suitable to distinguish between complex crystal structures [60, 61]. For each atom (here we only analyze the B sublattice), PYSCAL allows calculating 10 Steinhardt parameters; q_3, q_4, \ldots, q_{12} . While the actual values (ranging from 0 to 0.6) did not allow straightforwardly distinguishing between the diboride polymorphs, their pairwise combinations $(q_i \text{ vs. } q_j, \text{ where } i, j \in [3, 12] \text{ and } i \neq j)$ did. Based on extensive testing, we selected the q_3 vs. q_4 plots to estimate the phase constitution in nanoscale supercells. Similar testing using Steinhardt parameters for the TM sublattice indicated less pronounced differences between the 3 polymorphs and the main text therefore only presents results for B layers.

Results and Discussion

1 Phase stability of TMB2:s (TM=Ti, Ta, W, Re) and proof-of-concept shear tests at ab initio length scales

First we predict room-temperature phase stability, structural parameters, and elastic constants of the model TMB₂:s (TM=Ti, Ta, W, Re) in the α , γ , and ω stacking. To support the hypothesis on strain-activated stacking changes, we present proof-of-concept shear tests at DFT-accessible length scales reveling $\omega \to \alpha$ transition in TiB₂. All predictions are obtained using the here-developed MLIPs (for details of the training and validation procedure, see the Methods) and shown consistent with analogical abinitio molecular dynamics (ab initio MD) simulations.

As depicted in Fig. 1a, the three polymorph structures differ not only by the stacking of the TM sublattice (α -AAAA, ω -ABBA, γ -ABAB), but also by the puckering of honeycomb-patterned B layers. Namely, all B layers are flat and puckered in the α and γ stacking, respectively, while they are periodically flat/puckered in the ω stacking. Room-temperature equilibration of the model TMB₂:s (TM=Ti, Ta, W, Re) in each polymorph structure shows that TiB_2 and TaB_2 energetically favor the α phase, WB_2 favors the ω phase, and ReB₂ favors the γ phase (Fig. 1b). This phase preference perfectly agrees with our room-temperature ab initio MD calculations, yielding 0.001-0.002 eV/at. and 0-0.004 Å difference from the corresponding MLIP-obtained potential energy and lattice parameter values, respectively. All properties are calculated as time averages. The same phase preference has been also indicated at 0 K by previous abinitio studies [11, 62, 63].

Depicted in Fig. 1b (room-temperature ML-MD results), ω -TiB₂ and γ -TiB₂ exhibit 0.31 and 0.61 eV/at. potential energy, E_P , difference from the preferred α -TiB₂, respectively. Therefore, these phases are energetically unfavorable (and experimentally unreported). TaB₂ exhibits the same E_P order, $\alpha < \omega < \gamma$, with smaller energetic differences from the α structure: 0.09 eV/at. (ω -TaB₂) and 0.20 eV/at. (γ -TaB₂). Experimental studies have shown formation of α -TaB₂ [7, 17] and, in one case, indicated presence of the (metastable) ω -TaB₂ [64]. WB₂ exhibits different order of potential energy, $\omega < \gamma < \alpha$, and even lower E_P differences between the three polymorphs than TaB₂: 0.02 eV/at. (γ -WB₂) and 0.14 eV/at. (α -WB₂). Despite only ω and α polymorphs have been reported [7, 12–14], the energetic proximity of the γ phase suggests that also γ -WB₂ could form. ReB₂ shows yet another order of energy, $\gamma < \omega < \alpha$, and increased

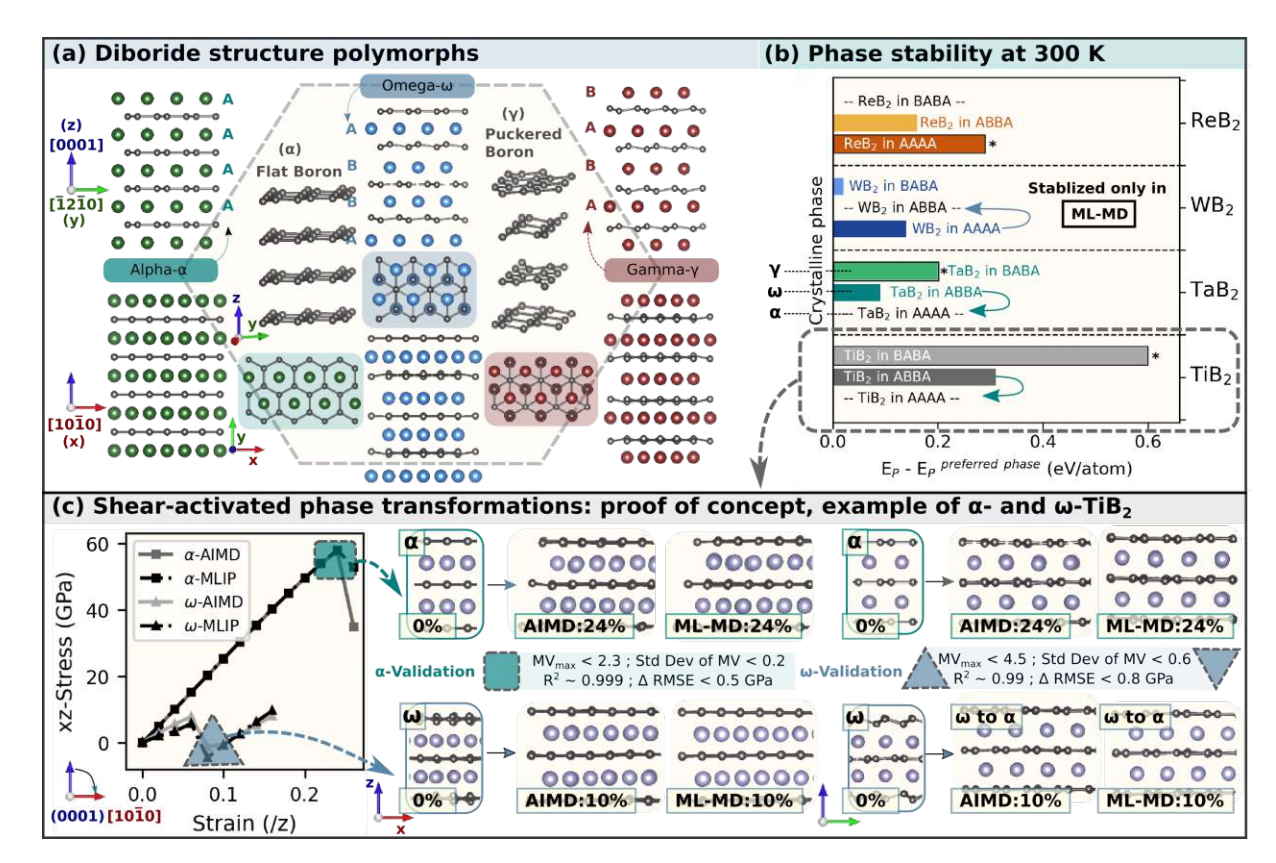


Fig. 1: Structure polymorphs of TMB2:s, their room-temperature stability for TM=(Ti, Ta, W, Re), and proof-of-concept shear tests showing $\omega \to \alpha$ transition in TiB₂. (a) Visualization of the α (AAAA stacking), ω (ABBA stacking), and γ (ABAB stacking) polymorphs in the ($\overline{1210}$) and (1010) plane view. The smaller-grey (larger-colored) spheres represent B (TM) atoms. (b) Potential energy, E_P , difference between each polymorph (α, ω, γ) and the lowest-energy (ground-state) polymorph from room-temperature ML-MD equlibration (720-atom supercells). The zero E_P difference shows that ${\rm TiB_2}$ and ${\rm TaB_2}$ favor the α phase, ${\rm WB_2}$ favors the ω phase, and ${\rm ReB_2}$ favors the γ phase. The results are consistent with ab initio MD data. Diborides that locally diverged from their ideal lattice sites during ab initio MD equilibration (but remained nearly perfect in ML-MD) are marked by star. (c) Proof-of-concept room-temperature shear simulations for α -TiB₂ and ω -TiB₂ (for technical details see the Methods), showing consistency between ab initio MD and ML-MD data in terms of stress and structure evolution; note the $\omega \to \alpha$ transformation in ω -TiB₂. The shear strain is applied along the $(0001)[10\overline{10}]$ slip system and the corresponding time-averaged stress tensor component (xz) is plotted in the left panel. Local structural snapshots are shown on the right, together with the R^2 error and the residual mean square error, RMSE, of MLIP-predicted stresses (compared with ab initio MD) and the MLIP's extrapolation grade during the simulation, indicating reliable extrapolation.

 E_P differences compared to TaB₂ and WB₂: 0.16 eV/at. (ω -ReB₂) and 0.29 eV/at. (α -ReB₂). Despite lack of experimental information for metastable diboride phases at ambient conditions—and this concerns not only ReB₂, but also other TMB₂:s—they may locally nucleate during micromechanical testing. Note that metastable ceramics with energetic differences from the preferred phase as high as 0.2 eV/at. have been realized experimentally [65, 66].

According to our ML-MD calculations, all the here-investigated TMB₂:s are mechanically and dynamically stable at 300 K. Mechanical stability [67] is deduced from elastic constants, C_{ij} , calculations (the values are given in Tab. 1). Finite-temperature dynamical stability is indicated by time-averaged atomic positions at ideal lattice sites,

at variance with (local) lattice distortions towards different polymorph structures being a sign of instability. We acknowledge that dynamical stability assessment is not completely unambiguous and may be sensitive to size effects and chosen simulation parameters. Besides equilibrating all diborides with ML-MD, we also set similar ab initio MD calculations (using the same 720-atom supercells). These suggest metastability/near-instability of α -ReB₂, γ -TaB₂, and γ -TiB₂ (marked by * in Fig. 1b), exhibiting (locally) more pronounced deviations from the ideal lattice sites. In previous 0 K DFT calculations, only α -WB₂ and α -ReB₂ presented dynamical instabilities [11, 68] which, according to our predictions, diminish or fully disappear with temperature (possibly also due to presence of anion vacancies, as suggested by Hahn et al. [20]).

Tab. 1 lists lattice parameters (a, c) and elastic properties (C_{ij}) and related observables, such as the Young's moduli) of the investigated TMB₂:s. Validation of MLIP-predicted values against those from analogical ab initio MD calculations reveals good quantitative agreement, with deviations of < 0.9% and < 8.0% in terms of lattice parameters and elastic constants, respectively. The MLIPs' reliability is further underpinned by consistency with other DFT and experimental values from literature. The exception is α -ReB₂ showing discrepancies even between DFT-calculated lattice and elastic constants [69, 70, with our room-temperature C_{ij} data falling in-between the range of DFT-predicted C_{ij} . This may further highlight the suggested (near-) instability of α -ReB₂ and, possibly, a stabilizing role of temperature.

Next, we take TiB₂—a well-known hard coating material [5, 83, 84]—as a model example for proof-of-concept simulations of (room-temperature) shear deformation. Recalling Fig. 1a, we intuitively expect that changes between the α , ω , and γ stacking can be mediated by tilting the $[0001]\parallel z$ axis (aligned with the typical growth direction [1]) towards the basal plane (xy), i.e., by shearing along the $(0001)[\overline{1}2\overline{1}0]$ or $(0001)[10\overline{1}0]$ slip system. As the basal plane of TMB₂:s is isotropic [9], we arbitrarily select the former (the latter is discussed in the upcoming sections). The corresponding stress/strain curves (Fig. 1c) reveal qualitatively different shear response of the preferred α -TiB₂ and the metastable ω -TiB₂. While the α stacking reaches the maximum shear stress (≈ 58 GPa) at 24% strain, the ω stacking exhibits its peak (7.9 GPa) significantly earlier, at 6% strain. In case of α -TiB₂, the stress drop after reaching the maximum (yield point) is associated with layer slipping and restoring nearly ideal α lattice sites. Contrarily, ω -TiB₂ undergoes a transformation towards the α phase (bottom row in Fig. 1c showing a magnification of the 720-atom TiB₂ supercell). As we simulate ideal shear, i.e. a volume-conserving transformation, the $\omega \to \alpha$ transformation results in α -TiB₂ with "incorrect" lattice parameters (of ω -TiB₂). Intuitively, loading conditions that allow volume relaxation are likely to lower the energetic costs of the transformation, as discussed later.

The stresses and strains withstood by single-crystal models during ab initio MD simulation (Fig. 1c) are typically one to two orders of magnitude larger than actual mechanical-test results due to absence of structural imperfections. What we emphasise, however, is the quantitative agreement between ab initio MD and ML-MD time-averaged data, and the fact that both capture the $\omega \to \alpha$ transformation. A comparison of ab initio MD and ML-MD predicted stresses during shear deformation of α -TiB₂ returns an R^2 of 0.999 and a residual mean square error (RMSE) of 0.5 GPa. The corresponding values recorded by shear simulations of ω -TiB₂ are 0.99 and 0.8 GPa. Analysis of

[Shear-activated transformations]

TMB_2	Method	T	a	c	C_{11}	C_{33}	C_{44}	C_{12}	C_{13}	Е	В	G	ν	Ref.
α -TiB ₂	ML-MD	300	3.04	3.22	588	409	261	85	98	554	236	246	0.113	This wor
	ab initio MD	300	3.03	3.23	588	430	252	79	111	547	244	243	0.126	This work
	Exp.	300	3.04	3.24	588	503	238	72	84	575	249	255	0.114	Ref. [71]
	Exp.	300	/	/	660	432	260	48	93	565	244	266	0.099	Ref. [72]
ω -TiB ₂	ML-MD	300	3.01	14.25	352	251	151	36	135	326	184	135	0.204	This wor
	$ab\ initio\ \mathrm{MD}$	300	3.01	14.27	326	239	127	52	116	285	162	118	0.207	This wor
	DFT	0	/	/	/	/	/	/	/	228	232	153	0.230^I	Ref. [73]
γ -TiB ₂	ML-MD	300	2.96	7.87	399	442	122	171	164	343	248	135	0.268	This wor
	DFT	0	3.03	7.16	492	426	62	75	83	322	210	130	0.244	II Ref.[11
α -TaB ₂	ML-MD	300	3.10	3.33	512	370	230	69	135	466	223	202	0.141	This wor
	$ab\ initio\ \mathrm{MD}$	300	3.09	3.33	510	392	252	72	125	486	221	214	0.134	This wor
	Exp.	300	3.09	3.24	/	/	/	/	/	551	228	/	/	Ref. [74
	Exp.	300	3.10	3.17^I	/	/	/	/	/	402	/	/	/	Ref. [75
	DFT	0	3.09	3.36	591	468	288	166	175	573^I	297^I	243^I	0.178^I	Ref. [76
ω -TaB ₂	ML-MD	300	3.05	14.60	646	373	212	113	181	520	285	217	0.196	This wor
	$ab\ initio\ \mathrm{MD}$	300	3.06	14.58	620	360	208	105	170	504	272	212	0.190	This wor
	DFT	0	3.05	14.64	/	/	/	/	/	/	293	237	0.181^I	Ref. [77
γ -TaB ₂	ML-MD	300	2.93	8.09	450	434	144	139	139	396	241	161	0.226	This wor
	DFT	0	3.04	7.58	544	571	114	129	109	432	261	176	0.225	$^{II}\mathrm{Ref.}[1]$
α -WB ₂	ML-MD	300	3.05	3.35	528	385	95	181	238	344	305	131	0.312	This wor
	$ab\ initio\ \mathrm{MD}$	300	3.02	3.37	531	383	72	195	232	316	305	119	0.327	This wor
	DFT	0	3.03	3.38	593	335	122	124	238	359^I	284^I	139^I	0.289^I	Ref. [78
	DFT	0	3.05	3.31	589	420	95	184	235	350	320	133	0.318	Ref. [79
ω -WB ₂	ML-MD	300	3.02	14.04	560	590	218	138	147	517	272	218	0.183	This wor
	$ab\ initio\ \mathrm{MD}$	300	3.02	14.06	552	597	230	120	172	522	278	220	0.187	This wor
	DFT	0	3.02	14.05	565	670	227	163	185	531^I	301^I	229^I	0.206^I	Ref. [78
	DFT	0	3.04	13.84	570	672	202	145	200	512	320	208	0.233	Ref. [79
	Exp.	300	2.99	13.91	/	/	/	/	/	504	349	200	0.259	Ref. [80
	Exp.	300	3.02	14.03	/	/	/	/	/	477	/	/	/	Ref. [16
γ -WB ₂	ML-MD	300	2.92	7.74	538	815	302	117	69	620	264	280	0.108	This wor
	$ab\ initio\ \mathrm{MD}$	300	2.94	7.73	525	817	320	115	69	623	260	283	0.101	This wo
	DFT	0	2.93	7.75	/	/	/	/	/	/	319	277	0.163^I	Ref. [77
	DFT	0	2.93	7.75	594	953	282	168	105	625	318	266	0.172	Ref. [62
α -ReB ₂	ML-MD	300	3.04	3.13	909	496	111	329	262	514	421	198	0.30	This wor
(Pressured)	DFT	0	2.58	2.97	1178	1042	210	414	409	829	650	321	0.29	Ref.[69
(Unpressured)	DFT	0	2.91	3.45	678	603	-18	214	173	Me	chanic	ally un	stable	Ref.[70]
ω -ReB ₂	ML-MD	300	2.98	13.87	579	654	223	247	262	535	371	212	0.260	This wor
	$ab\ initio\ \mathrm{MD}$	300	3.00	13.90	560	631	212	236	270	511	366	201	0.267	This wor
	DFT	0	2.98	14.10	/	/	/	/	/	/	335	197	0.254^I	Ref. [77
γ -ReB ₂	ML-MD	300	2.90	7.51	562	971	263	164	120	601	300	258	0.166	This wor
	$ab\ initio\ \mathrm{MD}$	300	2.92	7.50	586	960	267	175	139	608	311	259	0.174	This wo
	Exp.	300	/	/	674	1023	269	192	185	661	383	273	0.210	Ref. [81
	Exp.	300	2.90	7.48	/	/	/	/	/	/	360	/	/	Ref. [82
	DFT	0	2.88	7.41	668	1063	273	137	147	682	355	289	0.179	Ref. [79
												286	0.175^I	-

 $^{^{}I}$: Calculated based on the reference data; II : Original data from corresponding authors

Tab. 1: Room-temperature lattice parameters and elastic constants of the here-studied TMB2:s derived from ML-MD and reference ab initio MD simulations, compared with literature values (DFT, and experiments, shown as Exp.). Lattice parameters (a, c in Å) and elastic constants $(C_{ij}, \text{ in GPa}; \text{ for computational details see the Methods})$ at the temperature T (in K), presented together with the polycrystalline bulk modulus, B (in GPa), shear modulus, G (in GPa), Young's modulus, E (in GPa), and Poisson's ratio, ν .



the MLIP's extrapolation (quantified by the extrapolation grade, MV [43], the middle panel in Fig. 1c) shows close similarity of local atomic environments at each time step of the shear simulation with those in the training set. The low MV values indicate near-extrapolation, i.e., do not trigger further active learning (for in-depth discussion of MV and how it allows assessing reliability of ML-MD calculations, see our previous work [36]).

The same simulation setup as for TiB_2 is used to model room-temperature $(10\overline{1}0)[\overline{1}2\overline{1}0]$ shear deformation of TaB₂, WB₂, and ReB₂. Without over-stating the actual results, we highlight the consistency between ab initio MD and ML-MD data. The analysis of 9 shear tests (each producing 10,000–20,000 ML-MD configurations to be validated against ab initio MD data) yields acceptably low stress errors, $R^2=0.98-0.999$ and RMSE= 0-1.3 GPa. Furthermore, all shear-induced changes in stacking sequence predicted by abinitio MD ($\omega \to \alpha$ transition for TM=(Ti, Ta), $\alpha \to \omega$ transition TM=W; marked by arrows in Fig. 1b) are qualitatively reproduced in ML-MD runs. These preliminary calculations (Fig. 1 and Tab. 1) therefore support the reliability of our MLIPs and the possibility of shear-activated phase transformations in TMB_2 .

2 Shear strength and transformability of TMB₂:s at the nanoscale

The here-developed MLIPs are employed for more realistic shear simulations, where deformation is incremented at a lower rate in large (nanosized) supercells. These allow quantitative predictions of theoretical shear strength attainable in ideal single-crystal TMB₂:s (TM=Ti, Ta, W, Re) as well as atomic level understanding of shear-induced phase transformations (or/and nucleation of other defects), which may have been sizeconstrained in shear tests at ab initio length scales.

Based on our testing, a $\approx 15,000$ -atom supercell ($\approx 5^3$ nm³) is chosen to simulate room-temperature (0001)[1210] shear response of TMB₂:s (TM=Ti, Ta, W, Re) with the α , ω , and γ structure. Fig. 2a depicts stress/strain curves derived from shear tests for TiB₂ serving to evaluate the theoretical shear strength, $\sigma_{\rm max}$, of each structure polymorph (α, ω, γ) and the corresponding slip/transformation strain, $\varepsilon(\sigma_{\text{max}})$. In Fig. 2b we plot σ_{max} and $\varepsilon(\sigma_{\text{max}})$ values obtained for all TMB₂:s. Considering the most energetically favorable polymorph of each diboride (red-highlighted symbols in Fig. 2b), the order of shear strength is TiB₂ >TaB₂ >ReB₂ >WB₂, where TaB₂ and ReB₂ reach comparable σ_{max} . The same trend is predicted also for $\varepsilon(\sigma_{\text{max}})$.

TiB₂ exhibits the largest differences between shear response of the 3 polymorph structures (the largest shaded triangle in Fig. 2b). Namely, $\sigma_{\rm max}$ of the ω and γ phase decreases by > 70% (the corresponding $\varepsilon(\sigma_{\rm max})$ diminishes by about 50%) compared with the preferred α -TiB₂. TaB₂ mirrors the trend predicted for TiB₂, however, with smaller differences between $\sigma_{\rm max}$ and $\varepsilon(\sigma_{\rm max})$ of the 3 stackings. Recall that also the predicted stability order was the same, with smaller energetic differences in case of TM=Ta (Fig. 1b). WB₂ presents even smaller differences between shear response of the 3 stackings (Fig. 2b) which may further complicate their experimental identification. Specifically, $\sigma_{\rm max}$ of the preferred ω and the metastable α and γ phase nearly overlap, and are reached at essentially the same $\varepsilon(\sigma_{\text{max}})$ for ω and α (4% below $\varepsilon(\sigma_{\text{max}})$ of γ -WB₂). The ω and α polymorphs of ReB₂ yield nearly identical σ_{max} and $\varepsilon(\sigma_{\text{max}})$,

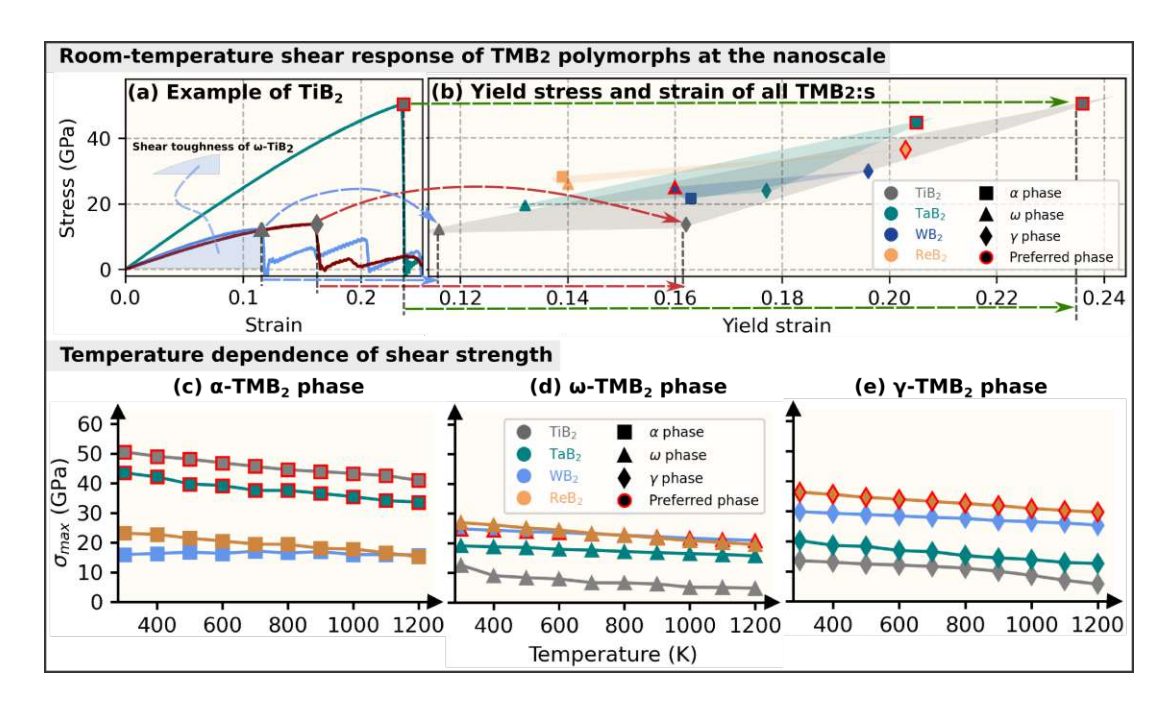


Fig. 2: Trends in room-temperature shear strength and slip/transformation strain of TMB₂:s (TM=Ti, Ta, W, Re) with the α , ω , and γ structure. The data is derived from ML-MD (0001)[$\overline{1210}$] shear simulations using $\approx 15,000$ -atom supercells. (a) Stress/strain curves for α -, ω -, and γ -TiB₂. The dashed arrow-headed lines mark the theoretical shear strength, $\sigma_{\rm max}$ (the maximum stress withstood during the shear test), and the corresponding shear strain, $\varepsilon(\sigma_{\rm max})$, also referred to as slip/transformation strain (corresponding to a stress release via slipping or some structural transformation). The blue-shaded region guides the eye for shear toughness (the energy density absorbed by the material until reaching $\sigma_{\rm max}$). (b) The $\sigma_{\rm max}$ and $\varepsilon(\sigma_{\rm max})$ values for all TMB₂:s (grey-TiB₂; turquoise-TaB₂; blue-WB₂; yellow-ReB₂). The square-, triangle, and diamond-shaped symbols denote the α , ω , and γ -stacking. The preferred phase is highlighted in red: α for TM=(Ti, Ta), ω for TM=W, and γ for TM=Re. Stress/strain curves for TM=(Ta, W, Re)—from which σ_{max} and $\varepsilon(\sigma_{\text{max}})$ values were derived, similarly to panel (a). Temperature dependence of σ_{max} for the here-studied TMB₂:s in the (c) α , (e) ω , and (d) γ structure, simulated in the same supercells (\$\approx 15,000\) atoms, equibrated at the respective temperature) as those used at room-temperature shear. Results for TM=(Ti, Ta, W, Re) are depicted in gray, teal, blue, and orange, respectively.

overshadowed by the preferred γ -ReB₂ which combines high shear strength and toughness (the integral below the stress/strain curve until $\varepsilon(\sigma_{\rm max})$). Additional investigations will be needed to verify dynamical stability of α -ReB₂ as well as γ -TiB₂, γ -TaB₂ (Section **1**).

Fig. 2(c-e) reveal the shear strength evolution of TMB₂:s with temperature, considering the 300 to 1200 K range (motivated by validation against ab initio MD data and relevant atomic environments in the training set). The most significant σ_{max} decrease, by $\approx 34.3\%$, is predicted for the α phase of ReB₂, followed by TiB₂ and TaB₂ with $\approx 20.0\%$. Notably, the shear strength of WB₂ appears nearly unaffected by temperature. This is demonstrated, for example, by a decrease in strength of the α phase of less than 1% at 1200 K. With the exception of WB₂, the rate at which σ_{max} diminishes upon temperature increase is quite similar among the studied diborides and is consistent with predictions for other ceramic materials [85].

Tab. 2 illustrates size effects in room-temperature shear response of TMB₂:s comparing data from nanoscale simulations with those at ab initio accessible scales. While $\sigma_{\rm max}$

<u> </u>	
<u>o</u>	
문	hub
0	edge
	nowk
<u>=</u>	our ki
	7
-	Ш

		≈1,00	00-atom su	percell (ab initio length scales)	pprox 15,000-atom supercell (beyond ab $initio$ length scales)				
	Phase	$\sigma_{\rm max}$	$\varepsilon(\sigma_{\max})$	Stress release mechanism	$\sigma_{ m max}$	$\varepsilon(\sigma_{\max})$	Stress release mechanism		
	$\underline{\alpha}$	50.0	22.9	Slip within α	50.2	23.4	Slip within α		
$\mathbf{Ti}\mathrm{B}_2$	ω	12.6	11.2	Transformation $\rightarrow \alpha$	12.3	11.6	Transformation $\rightarrow \alpha$		
	γ	14.6	16.3	Slip within γ	13.8	16.0	Slip within γ ; Local amorphous		
	$\underline{\alpha}$	44.5	20.6	Slip within α	44.8	20.7	Slip within α		
TaB_2	ω	19.9	12.8	Transformation $\rightarrow \alpha$	19.6	13.1	Transformation $\rightarrow \alpha$		
	γ	24.0	17.5	Slip within γ	24.1	17.1	Slip within γ ; Local amorphous		
	α	20.9	15.8	Slip within α	21.4	16.2	Local transformation $\rightarrow \omega$		
$\mathbf{W}\mathrm{B}_2$	$\underline{\omega}$	25.4	15.4	Slip within ω	25.0	16.1	Slip within ω		
	γ	30.1	19.6	Slip within γ	29.9	19.6	Slip within γ ; Local amorphous		
	α	26.9	12.8	Slip within α	28.6	14.0	Slip within α ; Local amorphous		
$\mathbf{Re}B_2$	ω	26.1	14.2	Local transformation $\rightarrow \gamma$	26.2	14.2	Local transformation $\rightarrow \gamma$		
	$\underline{\gamma}$	36.1	20.0	Slip within γ	36.4	20.2	Slip within γ ; Local amorphous		

Tab. 2: Size effects in room-temperature shear properties of TMB₂:s (TM=Ti, Ta, W, Re) derived from $(0001)[\overline{1}2\overline{1}0]$ ML-MD shear simulations. Shear strengths, σ_{\max} (in GPa), the corresponding slip/transformation strains, $\varepsilon(\sigma_{\max})$ (in %), and stress release mechanisms were evaluated using $\approx 1,000$ -atom and $\approx 15,000$ -atom supercells, respectively. The preferred phase of the respective TM is underlined: α for TM=(Ti, Ta), ω for TM=W, γ for TM=Re. Note that stress release mechanisms observed at the nanoscale have been simplified (omitting growth of certain defects) and their in-depth discussion is presented in Section 3.

and $\varepsilon(\sigma_{\rm max})$ show minor differences, structural changes associated with the shear stress drop are size-dependent. This is apparent through visual investigation of ML-MD videos from shear simulations, hinting at different extent of phase transformations. In Tab. 2, we summarize the observed stress release mechanisms, naming them as "slip" (leading to the recovery of nearly ideal lattice sites), "transformation" (local or full change of the stacking sequence), and "amorphization" (intermixing of some TM and B layers forming seemingly amorphous regions). Simulations with Å-scale supercells (left part of Tab. 2) reveal phase transformations in the (metastable) ω stacking of TiB₂, TaB₂, and ReB₂, while all other TMB₂ release shear stress by slip, fully restoring their ideal (initial) lattice sites.

At the nanoscale (right part of Tab. 2, the preferred α -TiB₂, α -TaB₂, ω -WB₂, and γ -ReB₂ also release shear stress via slipping, however, exhibit local relaxations beyond the ideal stacking sequences (γ -ReB₂ even locally amorphizes). Larger lattice distortions and local amorphization following lattice slip are observed also for the metastable γ stacking of TiB₂, TaB₂, WB₂, as well as the α stacking of ReB₂. Nucleation of additional defects accompanies also strain-activated phase transformations, predicted upon shearing the ω phase of TiB₂, TaB₂, and ReB₂. Additionally, a (local) $\alpha \to \omega$ phase transformation is revealed for WB₂ (Tab. 2), which has not been captured by supercells with Å-scale sizes. Note that these stress release mechanisms at the nanoscale have been simplified and their in-depth discussion is presented in the following section.

3 Structural analysis and specifics of each material system

Phase transformations at the nanoscale

To show the presence of a particular diboride polymorph beyond atomic length scales, we perform quantitative structural analysis via descriptors of local atomic environments. This includes evaluation of Steinhardt bond-orientational order parameters [59], q_i , based

on spherical harmonics and applicable to characterize crystals with arbitrary symmetry, liquids, or other complex structural motifs including defects [86, 87]. In our work, Steinhardt parameter calculations are complemented by angular analysis—based on the angular distribution within B layers—and visual inspection of ML-MD trajectories. For technical details see the Methods.

Fig. 3a shows fingerprints of each polymorph structure in the (a-1) angular and (a-2) Steinhardt parameter formalism. The B sublattice (first nearest-neighbor B atoms) in the α phase exhibits 120° angles, whereas the γ stacking is characterized by 111° angles. The ω stacking (alternating flat and puckered B sheets) equally represents both 120° and 111° angles. In terms of Steinhardt parameters, our testing reveals that the (presented) q_4 vs. q_6 plots provide the clearest distinction of the investigated diborides, consistently with previous studies using the same q_i combination for structure identification [88–91].

Fig. 3b-c illustrate the usage of the above descriptors, taking TiB₂ and WB₂ as examples. These two diborides are sheared starting either from (i) their energetically most favorable stackings, α -TiB₂ and ω -WB₂ (Fig. 3b), or from (ii) their metastable structure, ω -TiB₂ and α -WB₂ (Fig. 3c). For the corresponding stress/strain curves, please see Fig. 2a (TiB₂). Our structural analysis is performed for underformed structures and post-yielding. The diborides in which equilibration initiated from the ideal α (ω) lattice sites indeed closely resemble the α (ω) structure. This is shown by the close overlap between the actual and the reference q_4 vs. q_6 Steinhardt parameter pattern, where each B atom provides the shortest Euclidean distance, to the $[q_4, q_6]$ of the corresponding B in the ideal α and ω phase, respectively (quantified by the "similarity percentage" in the vertical bars-left side of the q_4 vs. q_6 plots). This result is underpinned also by the B-B bond angle distribution. Specifically, > 94% B-B angles in the α -TiB₂ and α -WB₂ are $\approx 120^{\circ}$, as expectable for the α phase, while both $\approx 111^{\circ}$ and $\approx 120^{\circ}$ angles are equally represented in the ω -TiB₂ and ω -WB₂.

Beyond the yield point, α -TiB₂ (Fig. 3b-1) and ω -WB₂ (Fig. 3b-2) restore their nearly ideal structure. In case of ω -WB₂, the small changes in the Steinhardt parameter pattern and the bond angle distribution may be indicative of local distortions and atomic displacements that are slightly more significant in relative comparison with α -TiB₂. Both the angular and Steinhardt parameter descriptors, however, clearly capture structural changes caused by shearing of the metastable ω -TiB₂ (Fig. 3c-1) and α -WB₂ (Fig. 3c-2). For the former, the corresponding Steinhardt parameters exhibit a close overlap with those of the ideal α -TiB₂ (with similarity above 80%, see the mostly blue vertical bar in Fig. 3c-1). This is also underpinned by the fact that > 93% of bond angles within the B network is 120°, as characteristic for the α structure. In case of α -WB₂, the opposite transition, $\alpha \to \omega$, occurs, however, not throughout the entire supercell (the percentage of ω structure is > 50% based on Steinhardt parameter descriptors). This is clear also from visual inspection of ML-MD videos and quantitatively supported by angular analysis (the right part of Fig. 3c-2), showing that $\approx 64\%$ of B layers remain flat (with 120° angles), whereas $\approx 34\%$ change to puckered (with 111° angles).

Bond angle distribution and Steinhardt parameter analysis is performed also for the other two material systems, TaB₂ and ReB₂. The results of TaB₂ (Fig. S6) resemble those for the above discussed TiB₂, which can be rationalized by the same energetic preference for the α , ω , and γ stacking (recall Fig. 1b). Unlike ω -TiB₂, ω -TaB₂ presents > 50% of flat layers already in equilibrium (at 300 K), suggesting that the ideal ω

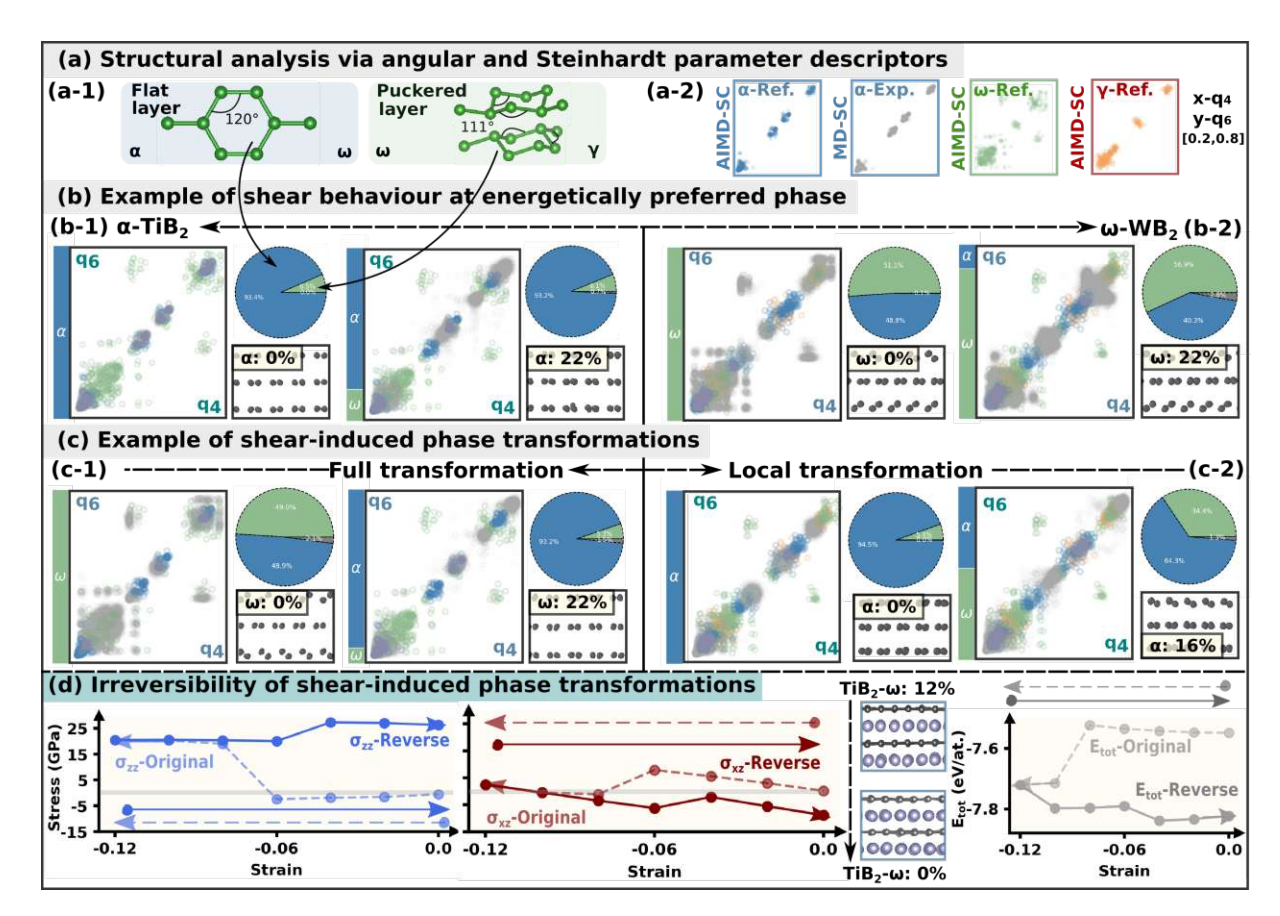


Fig. 3: Structural analysis of nano-sized supercells (here $\approx 5^3$ nm³) exemplified for TiB₂ and WB₂: both transforming to their energetically preferred phase upon shearing of the less favorable (ω resp. α) polymorph. (a) References for the α , ω and γ stackings (based on room-temperature equilibrated ab initio-scale supercells) using (a-1) angular descriptors (nearest-neighbor B-B atoms) and (a-2) Steinhardt parameters, namely, the q_4 vs. q_6 plots. The ranges of q_i s are always the same, (0.2, 0.8)). (b) Structural analysis of (b-1) α -TiB₂ and (b-2) ω WB₂ subject to room-temperature $(0001)[\overline{1210}]$ shear deformation, specifically, in equilibrium and after reaching the ultimate shear strength. (c) The same analysis of (c-1) ω -TiB₂ and (b-2) α WB₂. In all q_4 vs. q_6 plots, the grey points mark values for the investigated supercell, while the colored points mark the ideal reference structure, according to (a-2). The similarity with reference patterns is evaluated in the vertical bars, based on the shortest distance (in a Euclidean sense) between $[q_4, q_6]$ of each B atom and that of the corresponding B in the reference (ideal) stacking, indicating, e.g., that 20% of the B sublattice is the most similar to the α phase and 80% is the most similar to the ω phase. (d) Irreversibility of the phase transformation, exemplified by shear tests for ω -TiB₂, illustrated via the evolution of the σ_{xz} , σ_{zz} stress tensor component, and the E_{tot} (eV/at.), in which the original deformation is marked with dashed line, as the backward deformation with solid line.

stacking sequence is not perfectly replicated throughout the supercell. This may be interpreted as the $\omega \to \alpha$ transition in TaB₂ is possible already at very small strains, likely related to the relatively small energetic difference between the α and ω stacking. Applying the $(0001)[\overline{1}2\overline{1}0]$ shear strain induces the $\omega \to \alpha$ transition, consistently with atomic scale simulations (Section 5). Compared to TiB₂, however, there is a larger fraction of the B sublattice ($\approx 13\%$; in contrast with $\approx 2\%$ for TiB₂ in Fig. 3c-1) being neither perfectly flat nor puckered, but generally distorted.

Results for ReB₂ (Fig. S7) indicate structural changes in all phase polymorphs. Shearinduced plasticity is also observed in the preferred γ structure. These changes, however, do not necessarily include phase transformations, but rather local amorphization and nucleation of other defects, as discussed in the following sections. Shearing of α -ReB₂ leaves most of the layers flat (α -like), $\approx 7\%$ puckered, and $\approx 21\%$ distorted. For ω -ReB₂ and γ -ReB₂, the fraction of distorted B layers—after reaching the ultimate shear strength—increases to $\approx 27\%$ and $\approx 30\%$, respectively. With all B sheets initially puckered in γ -ReB₂, $\approx 22\%$ become flat subject to shearing. This is due to the onset of (local) amorphization.

As diboride ceramics are regarded as brittle, they typically fracture before yielding. Some yielding can be observed in compression, but upon bending or tension, yielding is rarely detected. [1]. In this study, periodic boundary conditions are applied during shearing; however, no fracture is observed, even upon increasing the shear strain to twice as large. Natural questions are (i) whether shearing far beyond the yield point (e.g., twice as large or even larger strains) can trigger phase transformation, and (ii) whether these phase transformations are reversible. In both cases, our simulations indicate against. Specifically, further strain increase leads to sequential slipping, as illustrated for TiB₂ (Fig. 3d), TaB₂ and WB₂. The reverse transformation—via the opposite (negative) ε_{xz} shear strain—would mean relaxing the stress component along the [0001] direction $(\sigma_{zz}$ stress), while, at the same time, increasing the potential energy, as we would transform towards the energetically less favorable stacking. What we observe when applying the opposite shear strain (Fig. 3d), however, is the total energy decrease (and σ_{zz} increase), as the energetically preferred stacking sequence resembles even closer to the ideal equilibrium structure (the only significantly non-zero stress is along [0001]).

Phase transformations under different shear or mixed tensile/compressive/shear conditions

Besides $(0001)[\overline{1210}]$ shear deformation, we additionally simulate (room-temperature) shearing along other low-index slip systems: $(0001)[10\overline{1}0]$ and $(\overline{1}2\overline{1}0)[10\overline{1}0]$. For small strain (linear elastic regime), the $(0001)[\overline{1}2\overline{1}0]$ and $(0001)[10\overline{1}0]$ shear response is essentially the same, due to elastic isotropy of the basal plane of hexagonal lattices. This extends even until the yield point. In particular, the predicted $(0001)[\overline{1210}]$ and $(0001)[10\overline{1}0]$ shear strengths are very similar (comparing the same TM elements and stacking sequences) and all deformation mechanisms as slipping and phase transformations remain qualitatively unchanged.

Due to differences in structural parameters of the 3 polymorphs structures, the fixed volume constraint in our shear simulations (simple shear [92]) may hinder the onset of phase transformations and/or limit them to a small region in the supercell. As shown in Tab. 1, these volumetric differences are mainly contributed by the $c \parallel [0001]$ lattice constant. Thus, shear-activated phase transformations may be further promoted when coupled with uniaxial (tensile/compressive) strain along the [0001] axis.

Imposing an initial uniaxial strain to simulation supercells allow us mimicking the effects of residual tensile/compressive stresses in diboride coatings subjected to mechanical load during shear deformation. For example, previous mechanical testing experiments demonstrated a monotonic increase in fracture toughness for nitride coatings with increasingly high residual compressive stresses [93]. Here, we select TiB₂ and WB₂ to

demonstrate the effect of uniaxial (tensile/compressive) strain on shear-mediated phase transformations.

Starting with TiB₂ (Fig. 4; the simulated structures are shown in Fig. 4a), we analyse the evolution of the σ_{xz} , σ_{xx} , σ_{yy} , and σ_{zz} stress tensor components during $(10\overline{1}0)[\overline{1}2\overline{1}0]$ shear deformation (σ_{xz} is the dominant stress tensor element). Compared with the rather low basal-plane stresses (Fig. 4b: $\sigma_{xx}=0$ –9.2 GPa, $\sigma_{yy}=0$ –2.2 GPa), the stress along the [0001] axis changes significantly. In particular, a gradual decrease down to ≈ -33 GPa (compressive stress) is observed for α -TiB₂, while an abrupt increase up to ≈ 19 GPa (tensile stress) is exhibited by ω -TiB₂ (Fig. 4c). Recall that the α -TiB₂ does not phase-transform but recovers nearly ideal α structure after slipping (Fig. 3b-1), as mirrored by the σ_{zz} stress component relaxing back to ≈ 0 GPa (Fig. 4c, green) and also by the potential energy, E_P , decrease towards the value of the ideal α -TiB₂ (Fig. 4d, green). Contrarily, the $\omega \to \alpha$ transition in ω -TiB₂ (recall Fig. 3c-1) increases σ_{zz} almost step-wise (Fig. 4c, blue), as the (transformed) ω -TiB₂ is under [0001] tension.

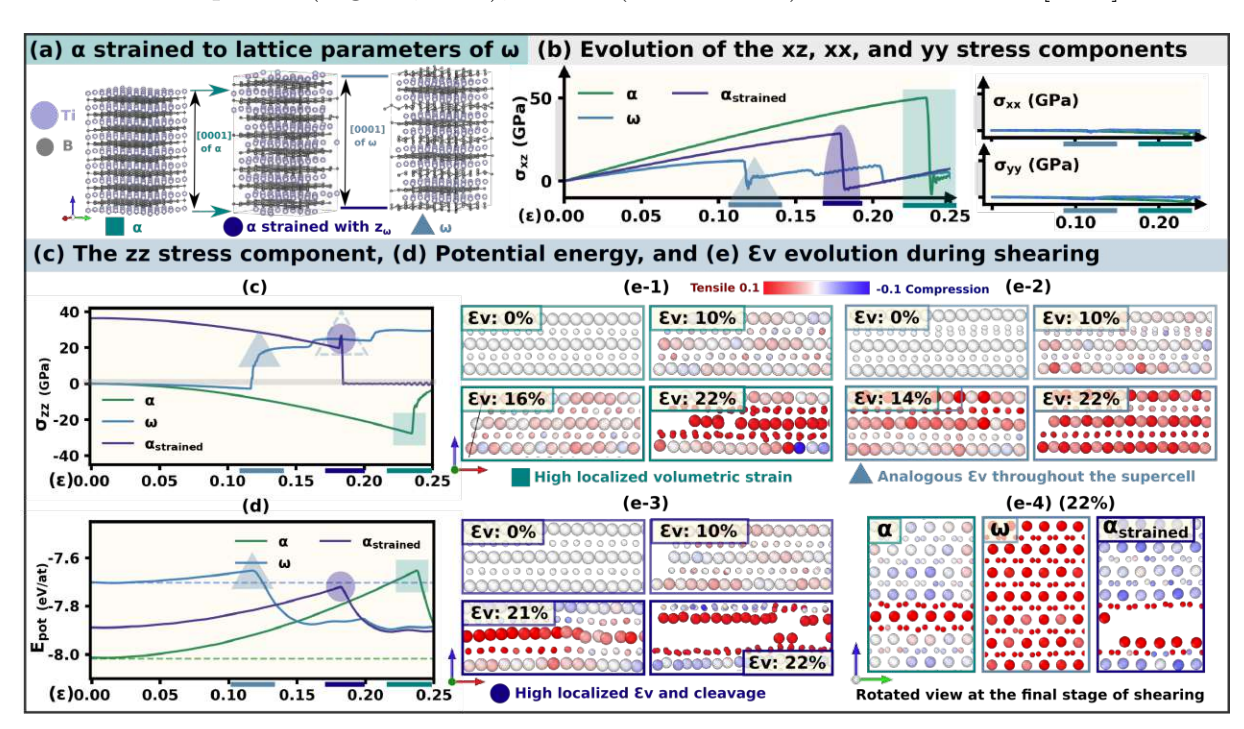


Fig. 4: The effect of uniaxial (tensile) strain on shear-activated transformations of TiB₂ at 300 K. (a) Visualization of the α , ω , [0001]-strained α , and γ phase of TiB₂. (b) Evolution of the σ_{xz} , σ_{xx} , σ_{yy} , and (c) σ_{zz} stress tensor components during (0001)[$\overline{1210}$] shearing at 300 K, correlated also with changes in (d) the potential energy, E_P. All data is derived from simulations with nano-sized supercells (here $\approx 5^3$ nm³). (e) Volumetric strain, ϵ_V , evolution at selected stages of shearing deformation.

Applying shear deformation to a pre-strained α -TiB₂—with all interlayer spacing equivalent to the ω stacking (Fig. 4a, middle)—decreases the shear strength (Fig. 4b) and, ultimately, nullifies the σ_{zz} strain. The E_P evolution is similar to the unstained α -TiB₂, only shifted towards higher values (compare green and purple lines in Fig. 4c). Importantly, the pre-strain does not suffice to activate the $\alpha \to \omega$ transition, which we suggest is very unlikely to be observed in experiments. Additional simulations (not shown) reveal that the shear strain activating the $\omega \to \alpha$ transition of ω -TiB₂ decreases if the supercell lattice parameter is imposed equal to that of the α polymorph.

Qualitatively, the same results are predicted also for TaB₂, underpinning its similarity with TiB_2 .

Fig. 4e depicts the volumetric strain, $\varepsilon_{\rm V}$, distribution in TiB₂ at key stages of shearing. Two qualitatively different scenarios are predicted. (i) $\varepsilon_{\rm V}$ remains essentially unchanged $(\varepsilon_{\rm V}\approx 0)$ and then highly localized in the layer undergoing the $(0001)[\overline{1210}]$ slip; the case of α -TiB₂ (Fig. 4e-1) and the strained α -TiB₂ (Fig. 4e-2). (ii) $\varepsilon_{\rm V}$ increases uniformly throughout the supercell until the phase transformation; the case of ω -TiB₂ (Fig. 4e-2). The difference in the $\varepsilon_{\rm V}$ distribution after the yield point is highlighted in Fig.4e-4, depicting also the (0001) cleavage observed upon shearing the pre-strained α -TiB₂. We suggest that despite TiB₂'s high [0001] tensile strength (53 GPa [36]), the combination of large shear and medium tensile strain promotes Ti/B layer cleavage (i.e., along the low-energy (0001) surface).

Fig. 5 depicts analysis of WB₂. This material energetically favors the ω stacking (recall Fig. 1), but can be equilibrated also in the α and γ structure. Similar to TiB₂, the basal plane of WB₂ exhibits a rather small stress increase (σ_{xx} =0-4.97 GPa, σ_{yy} =0-2.14 GPa) during shear deformation, irrespective of whether the initial stacking sequence is α , γ , or ω (Fig. 5b). Besides σ_{xz} (the main shear stress component), the only non-zero stress tensor element is again σ_{zz} , i.e. aligned with the [0001] direction. The energetically preferred ω -WB₂ behaves qualitatively similar as the energetically preferred α -TiB₂ $(\alpha\text{-TaB}_2)$. Specifically, shearing induces a gradual decrease of σ_{zz} (Fig. 5c, blue) which, following the lattice slip, relaxes back towards ≈ 0 GPa, mirrored by the potential energy decrease after slipping (Fig. 5d, blue).

Shearing of the metastable α -WB₂ mediates local $\alpha \to \omega$ transformation (see Fig. 3c-2). The corresponding σ_{zz} (Fig. 5c, green) indicates increasing compressive stress along the [0001] axis until reaching the ultimate shear strength. When α -WB₂ is pre-strained to match lattice parameters of the ω structure (schematically depicted in Fig. 5a), the shear strain necessary for the $\alpha \to \omega$ transformation decreases (and a larger fraction of the lattice transforms). Additional calculations reveal that similar conditions of residual strain are not sufficient to induce the $\gamma \to \omega$ transformation. Therefore, while we provide strong indications for observing the $\alpha \to \omega$ transformations in WB₂, $\omega \to \alpha$ or $\gamma \to \omega$ stacking changes are unlikely to occur. Recall that both the ω and α phase have been synthesized [7, 14], where the latter was B-substoichiometric [94]. In view of our predictions, achieving close-to-stoichiometric (1:2) W:B ratios may be a suitable route to promote transformation plasticity upon loading.

Volumetric strain analysis for WB₂ (Fig. 5e) reveals similar trends as those observed in TiB₂. Specifically, the preferred ω -WB₂ (Fig. 5e-2), showing no phase transformation, exhibits highly localized volumetric strain just within the layers that slip. The metastable α -WB₂, locally transforming to ω , exhibits high ε_V within the layers that transform (Fig. 5e-1). Contrarily, a nearly homogeneous volumetric strain distribution is predicted in the α -WB₂ initially strained to lattice parameter of the preferred ω -WB₂ and, consequently, the $\alpha \to \omega$ transition occurs throughout the entire lattice after yielding (Fig. 5e-3). A side view ($\overline{[12\overline{1}0]}$) of each structure's final configuration is presented in Fig. 5e-4 for TiB_2 .

Shear-mediated lattice rotation in ReB₂

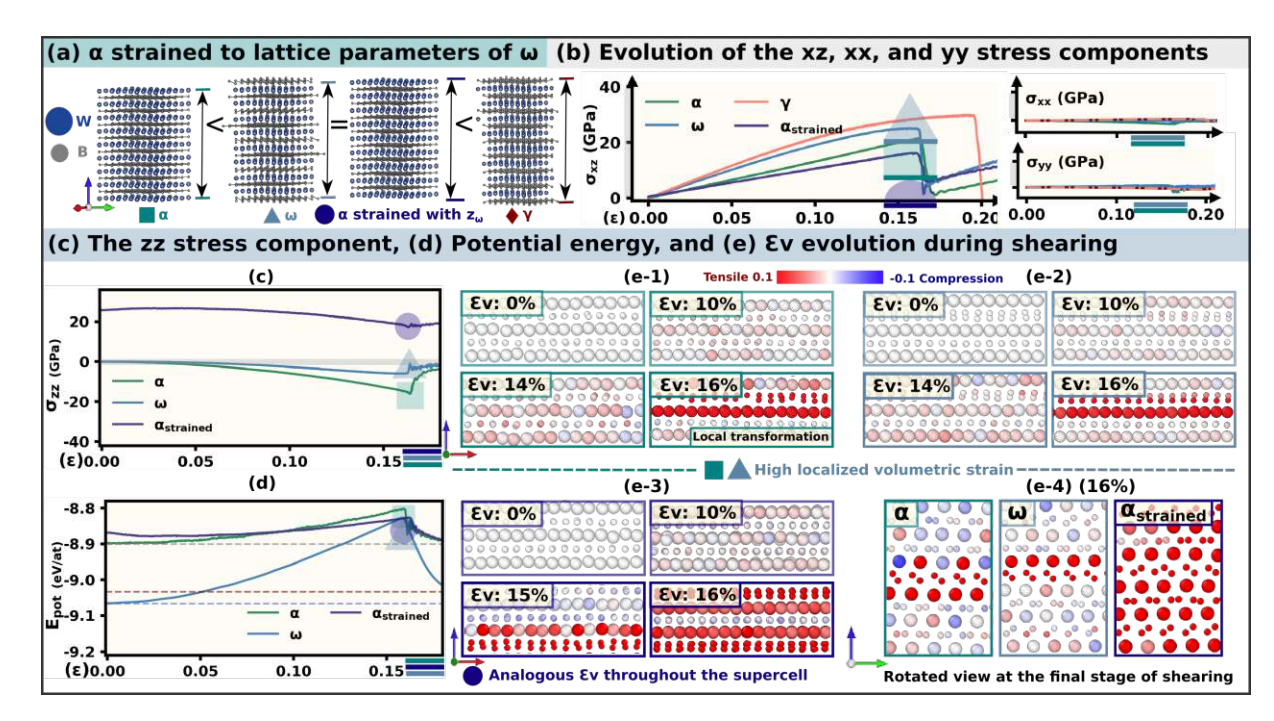


Fig. 5: The effect of uniaxial (tensile) strain on shear-activated transformations of WB₂ at 300 K. (a) Visualization of the α , ω , [0001]-strained α , and γ phase of TiB₂. (b) Evolution of the σ_{xz} , σ_{xx} , σ_{yy} , and (c) σ_{zz} stress tensor components during (0001)[$\overline{1210}$] shearing at 300 K, correlated also with changes in (d) the potential energy, E_P . All data is derived from simulations with nano-sized supercells (here $\approx 5^3$ nm³). (e) Volumetric strain, ϵ_V , evolution at selected stages of shearing deformation.

The mechanical behavior of ReB₂ appears anomalous in relation to what seen for other TMB₂:s. Our results indicate negative thermal expansion in the energetically favored gamma phase of ReB₂. The structure shrinks by $\approx 4.3\%$ with temperature increasing from 300 to 1200 K. The ω -ReB₂ exhibits, instead, anisotropic expansion/contraction upon heating to 1200 K. Its a(c) lattice parameters decrease (increase) by $\approx 2.2\% (\approx 14\%)$. This is at variance with TMB₂:s (TM=Ti, Ta, W) yielding a small (positive) thermal expansion, < 1.0% at 1200 K (slightly larger, 1.18% in a and 1.42% in c, in case of ω -TiB₂). The values are summarized and visualized for γ -WB₂ and γ -ReB₂ in (Fig. 6a).

Furthermore, despite γ is the preferred stacking of ReB₂, this diboride does not relieve stress during $(0001)[\overline{1}2\overline{1}0]$ slip. Instead, at the yield point, γ -ReB₂ undergoes intragrain rotation assisted by $(0001)[\overline{1}2\overline{1}0]$ and $(\overline{1}2\overline{1}0)[0001]$ slip, that is, both along and orthogonal to the basal plane. This is illustrated in (Fig. 6b), contrasting the volumetric strain distribution during shearing of the γ -WB₂ and γ -ReB₂. High volumetric strain is localized normal to the metal/boron sheets in the case of ReB₂ (Fig. 6b-2), showing their mutual shift along the [0001] axis, followed by interpenetration, and nearly homogeneous rotation of the lattice, in contrast with structural changes observed in γ -WB₂ (Fig. 6b-1) as well as other diborides. Simulations for various supercell sizes reveal that this effect is present already in $\approx 8,000$ -atom supercells, and also subject to shearing along the $(0001)[\overline{1}0\overline{1}0]$ slip system.

Shear-induced layer interpenetration and lattice rotation in γ -ReB₂ become even more apparent with increasing temperature, as we illustrate by shear tests at 1200 K. While more in-depth analysis would be necessary to understand this behavior, indications are

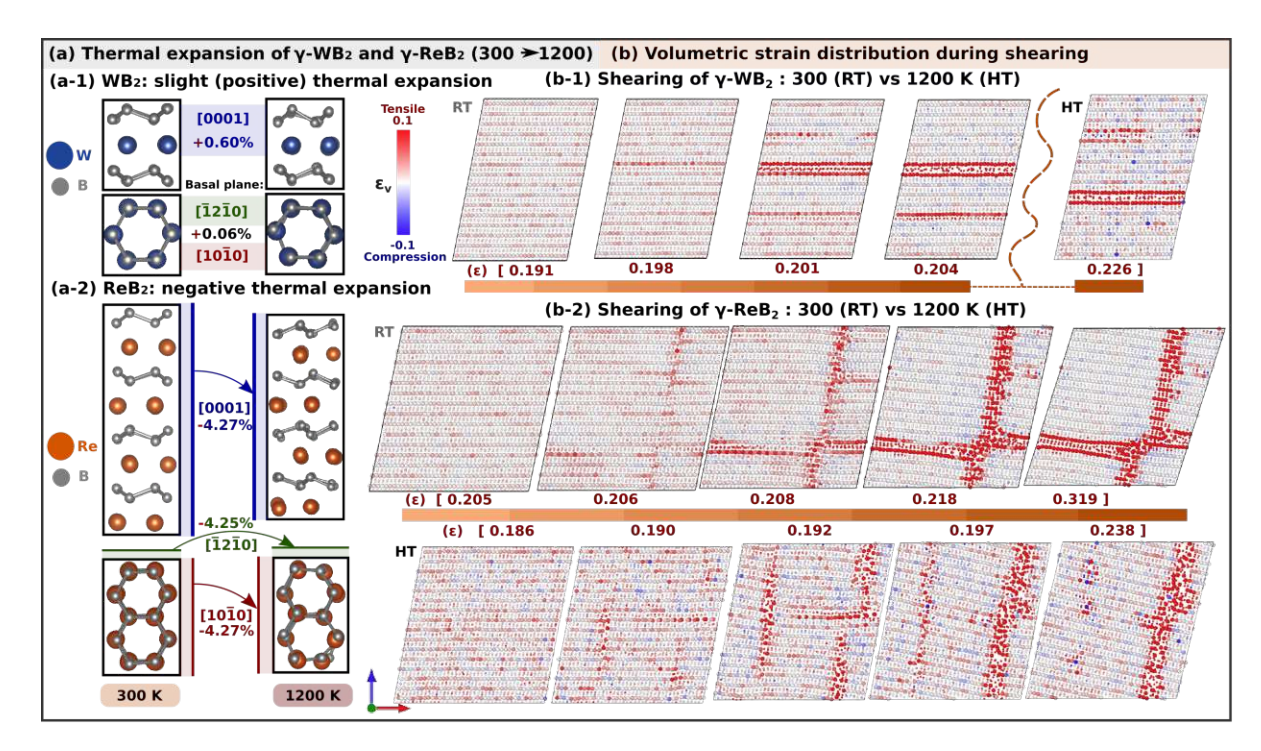


Fig. 6: Anomalous (negative) thermal expansion and shear response of γ -ReB₂, contrasted with γ -WB₂. (a) Changes in structural parameters of (a-1) γ -WB₂ and (a-2) γ -ReB₂ from 300 to 1200 K. (b) Volumetric strain evolution in (b-1) γ -WB₂ and (b-2) γ -ReB₂ subject to shear deformation along the $(0001)[\overline{1}2\overline{1}0]$ slip system at 300 K (RT) and 1200 K (HT).

given by the elastic constants. Specifically, the C_{33} is significantly larger than C_{11} for both γ -WB₂ and ReB₂ (Tab. 1). This disparity induces a diagonal distortion, causing elongation along the z-axis rather than the basal plane. This effect is particularly pronounced in γ -ReB₂, while an out-of-plane mismatch occurs (i.e., additional stresses along z-axis). Another factor may be that lattice rotation in combination with local amorphization allows readjusting the [0001] interplanar spacings which, as we know from the negative thermal expansion, decrease with temperature.

Discussion and design suggestions

Our ML-MD simulations revealed phase transformation in TiB₂ and TaB₂ ($\omega \to \alpha$ phase), as well as in WB₂ ($\alpha \to \omega$ phase), activated by shearing along the (0001)[1210] and $(0001)[10\overline{1}0]$ slip systems at room and higher temperatures. The activation shear strain ranged between 11 and 16.2%, further decreasing when combined with compressive (TiB₂ and TaB₂) or tensile (WB₂) strain along the [0001] axis. Such strain conditions may arise even prior to controlled mechanical tests during layer-by-layer deposition, via the superlattice architecture (template effect), or alloying. Our calculations indicate that TiB₂, TaB₂, and WB₂ exhibit similar thermal expansion coefficients over a wide temperature range, suggesting their compatibility for integrated structural applications.

Simulations in ideally stoichiometric single crystals allow isolating the intrinsic driving force for transformation plasticity. In practice, however, formation of diboride polymophs and transformations between them will be heavily influenced by synthesis-related factors e.g., off-stoichiometry, polycrystallinity, as well as deposition-induced artifacts [15, 17].

Follow-up modeling endeavors should therefore focus on addressing the impact of typical crystallographic defects, starting from the simplest and commonly reported case of B vacancies. Already training sets of our MLIPs contained atomic environments representative of stacking faults, voids, and other defects nucleating in the presence of mechanical strain, thus, provide a solid starting point for active learning on various vacancy-containing structures.

With both α and ω phases experimentally reported [7, 12, 13], WB₂ is a particularly interesting system and showing whether (near) ideal 1:2 W-to-B stoichiometry is crucial to control the predicted $\alpha \to \omega$ transition is an important step motivating future experiments. Another exciting research direction is transformation-induced superconductivity, motivated by recent findings for WB₂ (compression-induced superconductivity explained via nucleation of stacking faults and twins [12, 95]) and MoB₂ (with pressure-induced phase transition directly related to emergence of superconductivity [96]).

Conclusions

Shear-activated transformation plasticity of transition metal diborides was investigated via machine-learning potential molecular dynamics (ML-MD) simulations, pointing towards WB₂ as a particularly promising system that allows switching between the experimentally known α and ω polymorphs. Our approach—including quantitative structural analysis in nanoscale-sized supercells—allowed understanding stacking changes in TMB₂:s with atomic-scale resolution, under well-defined loading conditions (considering effects of additional uniaxial tensile/compressive strain), and excluding other defects that may nucleate depending on the synthesis conditions and complicate comparison of various TMB₂:s.

We choose TM=(Ti, Ta, W, Re) to represent group 4-7 transition metal diborides and trained four MLIPs using the MTP formalism and our previously proposed training and validation workflow [36]. Validation against finite-temperature ab initio molecular dynamics data together with extrapolation grade analyses supported the credibility of our MLIPs and their capability to predict shear-induced phase transformations. Considering all TMB₂:s in the α , ω , and γ polymorph structures, room-temperature ab initio MD and ML-MD equilibration showed that α is the preferred stacking for TM=(Ti, Ta), ω for TM=W, and γ for TM=Re. Besides mechanical stability of all TMB₂:s (derived from the calculated room-temperature elastic constants), also their dynamical stability was suggested. Only the cases of α -ReB₂, γ -TiB₂, and γ -TaB₂—exhibiting (local) relaxations beyond the ideal lattice sites—will require further dynamical stability verification.

Nanoscale room-temperature $(0001)[\overline{1}2\overline{1}0]$ shear simulations ($\approx 5^3$ nm³ samples) revealed that the order of theoretical shear strength—considering the energetically preferred polymorphs—is TiB₂ >TaB₂ >ReB₂ >WB₂. TiB₂ exhibited the vastest difference in shear strength of the polymorph structures, while WB₂ showed the highest similarity. According to structural analyses (via bond angle distribution and Steinhardt bondorientational order descriptors of local atomic environments), the energetically preferred polymorphs— α -TiB₂, α -TaB₂, and ω -WB₂—release the accumulated shear stress via (0001)[1210] slip, restoring nearly ideal lattice sites. For ReB₂, the preferred γ polymorph activated metal/boron layer interpenetration followed by homogeneous lattice rotation,

with other anomalous aspect being its negative thermal expansion. Shear-induced $\omega \to \alpha$ and $\alpha \to \omega$ transformation was shown for TM=(Ti, Ta) and TM=W, respectively. These transformations were promoted via additional compressive (for TM=(Ti, Ta)) or tensile (for TM=W) strain along the [0001] axis, decreasing the necessary transformation strain and increasing the fraction of the transformed lattice. Essentially the same shear strengths and stress release via slipping or phase transformations were predicted for shearing along the $(0001)[\overline{1}2\overline{1}0]$ and the $(0001)[10\overline{1}0]$ slip system.

Our work underscores the capability of MLIPs to predict transformation plasticity at scales accessible to electron microscopy and strain conditions locally resembling those during the growth or micromechanical testing. While observing the $\omega \to \alpha$ transformation in TiB₂ and TaB₂ may require very specific conditions (due to the energetic costs of the ω stacking), we suggest that $\alpha \to \omega$ transformations in WB₂ are accessible to experiment. Further, our findings suggest that the shear transformation plasticity in hard diborides can be tuned through the alloying of various TMB₂:s, indicating a potential avenue for future research.

Bibliography

- M. Magnuson, L. Hultman und H. Högberg. Review of transition-metal diboride thin films. Vacuum 196 (2022), 110567.
- H. Holleck. Material selection for hard coatings. J. Vac. Sci. Technol. 4.6 (1986), 2661 - 2669.
- C. Sevik, J. Bekaert, M. Petrov und M. V. Milošević. High-temperature multigap superconductivity in two-dimensional metal borides. Phys. Rev. Mater. 6.2 (2022), 024803.
- C. Wang, S. Akbar, W. Chen und V. Patton. Electrical properties of hightemperature oxides, borides, carbides, and nitrides. J. Mater. Sci. 30 (1995), 1627–1641.
- M. Mikula, B. Grančič, V. Buršíková, A. Csuba, M. Držík, Š. Kavecký, A. Plecenik und P. Kúš. Mechanical properties of superhard TiB₂ coatings prepared by DC magnetron sputtering. Vacuum 82.2 (2007), 278–281.
- J. Geng, G. Liu, F. Wang, T. Hong, C. Xia, M. Wang, D. Chen, N. Ma und H. Wang. Microstructural and mechanical anisotropy of extruded in-situ TiB₂/2024 composite plate. *Mater. Sci. Eng.* 687 (2017), 131–140.
- V. Moraes, C. Fuger, V. Paneta, D. Primetzhofer, P. Polcik, H. Bolvardi, M. Arndt, H. Riedl und P. Mayrhofer. Substoichiometry and tantalum dependent thermal stability of α -structured W-Ta-B thin films. Scr. Mater. 155 (2018), 5–10.
- R. Hahn, A. A. Tymoszuk, T. Wojcik, E. Ntemou, O. Hunold, P. Polcik, S. Kolozsvári, D. Primetzhofer, P. H. Mayrhofer und H. Riedl. Unraveling the superlattice effect for hexagonal transition metal diboride coatings. Scr. Mater. 235 (2023), 115599.
- X. Zhang, X. Luo, J. Li, P. Hu und J. Han. The ideal strength of transition metal diborides TMB₂ (TM= Ti, Zr, Hf): Plastic anisotropy and the role of prismatic slip. Scr. Mater. 62.8 (2010), 625–628.
- X. Xu, K. Fu, M. Yu, Z. Lu, X. Zhang, G. Liu und C. Tang. The thermodynamic, electronic and elastic properties of the early-transition-metal diborides with AlB₂type structure: A density functional theory study. J. Alloys Compd. 607 (2014), 198–206.

- T. Leiner, N. Koutná, J. Janovec, M. Zelený, P. H. Mayrhofer und D. Holec. On |11|energetics of allotrope transformations in transition-metal diborides via plane-byplane shearing. *Vacuum* 215 (2023), 112329.
- J. Lim, A. Hire, Y. Quan, J. Kim, S. Xie, S. Sinha, R. Kumar, D. Popov, C. Park, R. Hemley u.a. Creating superconductivity in WB₂ through pressure-induced metastable planar defects. Nat. Commun. 13.1 (2022), 7901.
- C. Wang, L. Song und Y. Xie. Mechanical and electrical characteristics of WB₂ synthesized at high pressure and high temperature. Materials 13.5 (2020), 1212.
- C. Jiang, Z. Pei, Y. Liu, J. Xiao, J. Gong und C. Sun. Preparation and characterization of superhard AlB₂-type WB₂ nanocomposite coatings. Phys. Status Solidi (A) 210.6 (2013), 1221–1227.
- C. Yeh und W. Kao. Preparation of TaB/TaB₂/mullite composites by combustion synthesis involving aluminothermic reduction of oxide precursors. J. Alloys Compd. 615 (2014), 734–739.
- T. Moscicki, J. Radziejewska, J. Hoffman, J. Chrzanowska, N. Levintant-Zayonts, D. Garbiec und Z. Szymanski. WB₂ to WB₃ phase change during reactive spark plasma sintering and pulsed laser ablation/deposition processes. Ceram. Int. 41.7 (2015), 8273-8281.
- |17|C. Hu, S. Lin, M. Podsednik, S. Mráz, T. Wojcik, A. Limbeck, N. Koutná und P. H. Mayrhofer. Influence of co-sputtering AlB₂ to TaB₂ on stoichiometry of non-reactively sputtered boride thin films. Mater. Res. Lett. 12.8 (2024), 561–570.
- M. Dahlqvist und J. Rosen. Impact of vacancies on structure, stability and properties of hexagonal transition metal diborides, MB₂ (M= Sc, Y, Ti, Zr, Hf, V, Nb, Ta, Cr, Mo, W, Mn, and Fe). Materialia 26 (2022), 101629.
- C. Fuger, R. Hahn, A. Hirle, T. Wojcik, P. Kutrowatz, F. Bohrn, O. Hunold, P. Polcik und H. Riedl. Tissue phase affected fracture toughness of nano-columnar TiB_{2+z} thin films. *Mater. Res. Lett.* 11.8 (2023), 613–622.
- R. Hahn, V. Moraes, A. Limbeck, P. Polcik, P. H. Mayrhofer und H. Euchner. Electron-configuration stabilized (W, Al) B₂ solid solutions. Acta Mater. 174 (2019), 398-405.
- B. Jiang, C. Chen, X. Wang, H. Wang, W. Wang, H. Ye und K. Du. Deformation induced twinning and phase transition in an interstitial intermetallic compound niobium boride. Acta Mater. 165 (2019), 459–470.
- [22]H.-Y. Zhang, F. Xi, Z.-Y. Zeng, X.-R. Chen und L.-C. Cai. First-Principles predictions of phase transition and mechanical properties of tungsten diboride under pressure. J. Phys. Chem. C 121.13 (2017), 7397–7403.

- F. Ling, K. Luo, L. Hao, Y. Gao, Z. Yuan, Q. Gao, Y. Zhang, Z. Zhao, J. He und D. Yu. Universal phase transitions of AlB₂-type transition-metal diborides. ACS omega 5.9 (2020), 4620–4625.
- J. A. Harrison, J. D. Schall, S. Maskey, P. T. Mikulski, M. T. Knippenberg |24|und B. H. Morrow. Review of force fields and intermolecular potentials used in atomistic computational materials research. Appl. Phys. Rev. 5.3 (2018).
- P.-L. Kang, C. Shang und Z.-P. Liu. Large-scale atomic simulation via machine learning potentials constructed by global potential energy surface exploration. Acc. Chem. Res. 53.10 (2020), 2119–2129.
- [26] M. H. Müser, S. V. Sukhomlinov und L. Pastewka. Interatomic potentials: Achievements and challenges. Adv. Phys.: X 8.1 (2023), 2093129.
- V. L. Deringer, M. A. Caro und G. Csányi. Machine learning interatomic potentials |27|as emerging tools for materials science. Adv. Mater. 31.46 (2019), 1902765.
- Y. Zuo, C. Chen, X. Li, Z. Deng, Y. Chen, J. Behler, G. Csányi, A. V. Shapeev, A. P. Thompson, M. A. Wood u.a. Performance and cost assessment of machine learning interatomic potentials. J. Phys. Chem. A 124.4 (2020), 731–745.
- [29]J. S. Smith, O. Isayev und A. E. Roitberg. ANI-1: an extensible neural network potential with DFT accuracy at force field computational cost. Chem. Sci. 8.4 (2017), 3192-3203.
- A. V. Shapeev, E. V. Podryabinkin, K. Gubaev, F. Tasnádi und I. A. Abrikosov. Elinvar effect in β -Ti simulated by on-the-fly trained moment tensor potential. New J. Phys. 22.11 (2020), 113005.
- I. S. Novikov, K. Gubaev, E. V. Podryabinkin und A. V. Shapeev. The MLIP package: moment tensor potentials with MPI and active learning. Mach. learn.: sci. technol. 2.2 (2020), 025002.
- |32|Y. Mishin. Machine-learning interatomic potentials for materials science. Acta Mater. 214 (2021), 116980.
- D. Dragoni, T. D. Daff, G. Csányi und N. Marzari. Achieving DFT accuracy with a machine-learning interatomic potential: Thermomechanics and defects in bcc ferromagnetic iron. Phys. Rev. Mater. 2.1 (2018), 013808.
- [34]T. Mueller, A. Hernandez und C. Wang. Machine learning for interatomic potential models. J. Chem. Phys. 152.5 (2020).
- M. Lashkarblooki, A. Z. Hezave, A. M. Al-Ajmi und S. Ayatollahi. Viscosity [35]prediction of ternary mixtures containing ILs using multi-layer perceptron artificial neural network. Fluid Ph. Equilibria. 326 (2012), 15–20.
- S. Lin, L. Casillas-Trujillo, F. Tasnádi, L. Hultman, P. H. Mayrhofer, D. G. Sangiovanni und N. Koutná. Machine-learning potentials for nanoscale simulations

- of tensile deformation and fracture in ceramics. npj Comput. Mater. 10.1 (2024), 67.
- L. Zhang, G. Csányi, E. van der Giessen und F. Maresca. Efficiency, accuracy, and transferability of machine learning potentials: Application to dislocations and cracks in iron. Acta Mater. 270 (2024), 119788.
- J. Behler. Perspective: Machine learning potentials for atomistic simulations. The Journal of chemical physics 145.17 (2016).
- C. Schran, F. L. Thiemann, P. Rowe, E. A. Müller, O. Marsalek und A. Michaelides. Machine learning potentials for complex aqueous systems made simple. Proc. Natl. Acad. Sci. 118.38 (2021), e2110077118.
- M. I. Mendelev und G. J. Ackland. Development of an interatomic potential for the simulation of phase transformations in zirconium. Philos. Mag. Lett. 87.5 (2007), 349-359.
- M. I. Mendeley, T. Underwood und G. Ackland. Development of an interatomic potential for the simulation of defects, plasticity, and phase transformations in titanium. J. Chem. Phys. 145.15 (2016).
- A. V. Shapeev. Moment tensor potentials: A class of systematically improvable [42]interatomic potentials. Multiscale Model. Simul. 14.3 (2016), 1153–1173.
- E. V. Podryabinkin und A. V. Shapeev. Active learning of linearly parametrized [43]interatomic potentials. Comput. Mater. Sci. 140 (2017), 171–180.
- G. Kresse und J. Furthmüller. Efficient iterative schemes for ab initio total-energy |44|calculations using a plane-wave basis set. Phys. Rev. B 54.16 (1996), 11169.
- G. Kresse und D. Joubert. From ultrasoft pseudopotentials to the projector augmented-wave method. Phys. Rev. B 59 (3 Jan. 1999), 1758–1775.
- J. P. Perdew, A. Ruzsinszky, G. I. Csonka, O. A. Vydrov, G. E. Scuseria, L. A. Constantin, X. Zhou und K. Burke. Restoring the density-gradient expansion for exchange in solids and surfaces. Phys. Rev. Lett. 100 (13 Apr. 2008), 136406.
- M. Parrinello und A. Rahman. Polymorphic transitions in single crystals: A new |47|molecular dynamics method. J. Appl. Phys. 52.12 (1981), 7182–7190.
- D. Sangiovanni, F. Tasnádi, L. Johnson, M. Odén und I. Abrikosov. Strength, transformation toughening, and fracture dynamics of rocksalt-structure $Ti_{1-x}Al_xN$ (0 x 0.75) alloys. Phys. Rev. Mater. 4.3 (2020), 033605.
- D. Sangiovanni, W. Mellor, T. Harrington, K. Kaufmann und K. Vecchio. Enhancing plasticity in high-entropy refractory ceramics via tailoring valence electron concentration. *Mater. Des.* 209 (2021), 109932.

- N. Koutná, L. Löfler, D. Holec, Z. Chen, Z. Zhang, L. Hultman, P. H. Mayrhofer und D. G. Sangiovanni. Atomistic mechanisms underlying plasticity and crack growth in ceramics: a case study of AlN/TiN superlattices. Acta Mater. 229 (2022), 117809.
- D. G. Sangiovanni, F. Tasnádi, T. Harrington, M. Odén, K. S. Vecchio und I. A. Abrikosov. Temperature-dependent elastic properties of binary and multicomponent high-entropy refractory carbides. Mater. Des. 204 (2021), 109634.
- |52|R. Fletcher. Practical methods of optimization. John Wiley & Sons, 2013.
- L. C. Erhard, J. Rohrer, K. Albe und V. L. Deringer. A machine-learned intera-|53|tomic potential for silica and its relation to empirical models. Npj Comput. Mater. 8.1 (2022), 90.
- |54|F. Tasnádi, F. Bock, J. Tidholm, A. V. Shapeev und I. A. Abrikosov. Efficient prediction of elastic properties of Ti_{0.5}Al_{0.5}N at elevated temperature using machine learning interatomic potential. Thin Solid Films 737 (2021), 138927.
- E. Podryabinkin, K. Garifullin, A. Shapeev und I. Novikov. MLIP-3: Active learning on atomic environments with Moment Tensor Potentials. arXiv preprint arXiv:2304.13144 (2023).
- A. P. Thompson, H. M. Aktulga, R. Berger, D. S. Bolintineanu, W. M. Brown, P. S. Crozier, P. J. in 't Veld, A. Kohlmeyer, S. G. Moore, T. D. Nguyen, R. Shan, M. J. Stevens, J. Tranchida, C. Trott und S. J. Plimpton. LAMMPS - a flexible simulation tool for particle-based materials modeling at the atomic, meso, and continuum scales. Comp. Phys. Comm. 271 (2022), 108171.
- Z. Chen, Y. Zheng, L. Löfler, M. Bartosik, G. K. Nayak, O. Renk, D. Holec, P. H. |57|Mayrhofer und Z. Zhang. Atomic insights on intermixing of nanoscale nitride multilayer triggered by nanoindentation. Acta Mater. 214 (2021), 117004.
- A. Stukowski. Visualization and analysis of atomistic simulation data with OVITO-|58|the Open Visualization Tool. Model. Simul. Mat. Sci. Eng. 18.1 (2009), 015012.
- P. J. Steinhardt, D. R. Nelson und M. Ronchetti. Bond-orientational order in liquids and glasses. Phys. Rev. B Condens. Matter 28.2 (1983), 784.
- |60|S. Menon, G. D. Leines und J. Rogal. pyscal: A python module for structural analysis of atomic environments. J. Open Source Softw. 4.43 (2019), 1824.
- [61]R. Tranås, O. M. Løvvik und K. Berland. Lattice Thermal Conductivity from First Principles and Active Learning with Gaussian Process Regression. arXiv preprint arXiv:2309.06786 (2023).
- [62]X.-Y. Cheng, X.-Q. Chen, D.-Z. Li und Y.-Y. Li. Computational materials discovery: the case of the W-B system. Acta Crystallogr. C 70.2 (2014), 85–103.

- W. J. Zhao und Y. X. Wang. Structural, mechanical, and electronic properties of TaB₂, TaB, IrB₂, and IrB: First-principle calculations. J. Solid State Chem. 182.10 (2009), 2880–2886.
- C. Fuger, V. Moraes, R. Hahn, H. Bolvardi, P. Polcik, H. Riedl und P. H. Mayrhofer. Influence of Tantalum on phase stability and mechanical properties of WB₂. MRS Communications 9.1 (2019), 375–380.
- J. Dai, X. Wu, Y. Song und R. Yang. Electronic structure mechanism of marten-[65]sitic phase transformation in binary titanium alloys. J. Appl. Phys. 112.12 (2012).
- W. Xing, X. Miao, F. Meng und R. Yu. Crystal structure of and displacive phase [66]transition in tungsten nitride WN. J. Alloys Compd. 722 (2017), 517–524.
- F. Mouhat und F.-X. Coudert. Necessary and sufficient elastic stability conditions [67]in various crystal systems. Phys. Rev. B Condens. Matter 90.22 (2014), 224104.
- M. Dahlqvist, U. Jansson und J. Rosen. Influence of boron vacancies on phase |68|stability, bonding and structure of MB₂ (M= Ti, Zr, Hf, V, Nb, Ta, Cr, Mo, W) with AlB2 type structure. J. Phys. Condens. Matter 27.43 (2015), 435702.
- Y. X. Wang, Z. X. Yan, W. Liu und G. L. Zhou. Novel high pressure structures and mechanical properties of rhenium diboride. J. Appl. Phys. 126.13 (2019).
- M.-M. Zhong, X.-Y. Kuang, Z.-H. Wang, P. Shao, L.-P. Ding und X.-F. Huang, Phase stability, physical properties, and hardness of transition-metal diborides MB₂ (M= Tc, W, Re, and Os): first-principles investigations. J. Phys. Chem. C 117.20 (2013), 10643–10652.
- G. M. Amulele und M. H. Manghnani. Compression studies of TiB₂ using syn-[71]chrotron x-ray diffraction and ultrasonic techniques. J. Appl. Phys. 97.2 (2005).
- P. Spoor, J. Maynard, M. Pan, D. Green, J. Hellmann und T. Tanaka. Elastic constants and crystal anisotropy of titanium diboride. Appl. Phys. Lett. 70.15 (1997), 1959-1961.
- V. Moraes, H. Riedl, C. Fuger, P. Polcik, H. Bolvardi, D. Holec und P. H. Mayrhofer. Ab initio inspired design of ternary boride thin films. Sci. Rep. 8.1 (2018), 9288.
- X. Zhang, G. E. Hilmas und W. G. Fahrenholtz. Synthesis, densification, and [74]mechanical properties of TaB₂. Mater. Lett. 62.27 (2008), 4251–4253.
- Z. Zhang, H. Liang, H. Chen, L. Ding, M. Song und J. Wang. Physical properties of high-temperature sintered TaB₂ under high pressure. Ceram. Int. 47.7 (2021), 9061-9067.
- Y. Zhou, H. Xiang, Z. Feng und Z. Li. General trends in electronic structure, stability, chemical bonding and mechanical properties of ultrahigh temperature

- ceramics TMB₂ (TM= transition metal). J. Mater. Sci. Technol. 31.3 (2015), 285-294.
- N. Wang, Z. Fu, D. Legut, B. Wei, T. C. Germann und R. Zhang. Designing ultrastrong 5d transition metal diborides with excellent stability for harsh service environments. Phys. Chem. Chem. Phys. 21.29 (2019), 16095–16107.
- P. Li, L. Ma, M. Peng, B. Shu und Y. Duan. Elastic anisotropies and thermal conductivities of WB₂ diborides in different crystal structures: A first-principles calculation. J. Alloys Compd. 747 (2018), 905–915.
- X. Hao, Y. Xu, Z. Wu, D. Zhou, X. Liu, X. Cao und J. Meng. Low-compressibility and hard materials ReB₂ and WB₂: Prediction from first-principles study. Phys. Rev. B 74.22 (2006), 224112.
- S. Yin, D. He, C. Xu, W. Wang, H. Wang, L. Li, L. Zhang, F. Liu, P. Liu, Z. Wang u.a. Hardness and elastic moduli of high pressure synthesized MoB₂ and WB₂ compacts. *High Press. Res.* 33.2 (2013), 409–417.
- J. Levine, J. Betts, J. Garrett, S. Guo, J. Eng, A. Migliori und R. Kaner. Full elastic tensor of a crystal of the superhard compound ReB₂. Acta Mater. 58.5 (2010), 1530-1535.
- H.-Y. Chung, M. B. Weinberger, J. B. Levine, A. Kavner, J.-M. Yang, S. H. [82]Tolbert und R. B. Kaner. Synthesis of ultra-incompressible superhard rhenium diboride at ambient pressure. Science 316.5823 (2007), 436–439.
- [83]W. Hofmann und W. Jäniche. Die struktur von aluminiumborid AlB₂. Zeitschrift für Physikalische Chemie 31.1 (1936), 214–222.
- |84|J. Eorgan und N. Fern. Zirconium diboride coatings on tantalum. JOM 19.9 (1967), 6-11.
- D. G. Sangiovanni, A. Kraych, M. Mrovec, J. Salamania, M. Odén, F. Tasnádi und I. A. Abrikosov. Descriptor for slip-induced crack blunting in refractory ceramics. Physical Review Materials 7.10 (2023), 103601.
- J. Haeberle, M. Sperl und P. Born. Distinguishing noisy crystalline structures using bond orientational order parameters. Eur. Phys. J. E 42 (2019), 1–7.
- K. Z. Takahashi, T. Aoyagi u.a. Searching local order parameters to classify [87]water structures of ice Ih, Ic, and liquid. J. Chem. Phys. 154.16 (2021).
- M. Chaudhuri, E. Allahyarov, H. Löwen, S. Egelhaaf und D. Weitz. Triple junction at the triple point resolved on the individual particle level. Phys. Rev. Lett. 119.12 (2017), 128001.
- H. Eslami, P. Sedaghat und F. Müller-Plathe. Local bond order parameters for [89]accurate determination of crystal structures in two and three dimensions. Phys. Chem. Chem. Phys. 20.42 (2018), 27059–27068.

- G. Kim, B. Na, G. Kim, H. Cho, S. Kang, H. S. Lee, S. Choi, H. Kim, S. Lee und Y. Kim. Benchmark of machine learning force fields for semiconductor simulations: datasets, metrics, and comparative analysis. Adv. Neural Inf. Process. Syst. 36 (2024).
- T.-Q. Yu, P.-Y. Chen, M. Chen, A. Samanta, E. Vanden-Eijnden und M. Tuckerman. Order-parameter-aided temperature-accelerated sampling for the exploration of crystal polymorphism and solid-liquid phase transitions. J. Chem. Phys. 140.21 (2014).
- [92]M. Destrade, J. G. Murphy und G. Saccomandi. Simple shear is not so simple. Int. J. Non-Linear Mech. 47.2 (2012), 210–214.
- Z. Zhang, A. Ghasemi, N. Koutná, Z. Xu, T. Grünstäudl, K. Song, D. Holec, Y. He, P. H. Mayrhofer und M. Bartosik. Correlating point defects with mechanical properties in nanocrystalline TiN thin films. Mater. Des. 207 (2021), 109844.
- C. Fuger, R. Hahn, L. Zauner, T. Wojcik, M. Weiss, A. Limbeck, O. Hunold, P. Polcik und H. Riedl. Anisotropic super-hardness of hexagonal WB₂ $\pm z$ thin films. Mater. Res. Lett. 10.2 (2022), 70–77.
- R. Heid, B. Renker, H. Schober, P. Adelmann, D. Ernst und K.-P. Bohnen. Lattice dynamics and electron-phonon coupling in transition-metal diborides. Phys. Rev. B 67.18 (2003), 180510.
- P. Dee, J. Kim, A. Hire, J. Lim, L. Fanfarillo, S. Sinha, J. Hamlin, R. Hennig, P. Hirschfeld und G. Stewart. Diboride compounds doped with transition metals: A route to superconductivity through structure stabilization as well as defects. Phys. Rev. B 109.10 (2024), 104520.

Main Contribution III

Under Review in Acta Materialia, Elsevier

Machine-learning potentials predict orientation- and mode-dependent fracture in refractory diborides

Authors:

Shuyao Lin

Zhuo Chen Rebecca Janknecht Zaoli Zhang Lars Hultman Paul H. Mayrhofer Nikola Koutná Davide G. Sangiovanni

Under Review, 2025



Machine-learning potentials predict orientation- and mode-dependent fracture in refractory diborides

Keywords: Transition metal diborides; Machine-Learning interatomic potentials; Fracture toughness: Molecular statics

Abstract

Fracture toughness $(K_{\rm Ic})$ and fracture strength $(\sigma_{\rm f})$ are key criteria in the selection and design of reliable ceramics. However, their experimental characterization remains challenging—especially for ceramic thin films, where size and interfacial effects hinder accurate and reproducible measurements. Here, machine-learning interatomic potentials (MLIPs) trained on ab initio datasets of single crystal models deformed up to fracture are used to characterize transgranular cleavage in pre-cracked ceramic diboride TMB_2 (TM = Ti, Zr, Hf) lattices through stress intensity factor (K)-controlled loading. Mode-I simulations performed across distinct crack geometries show that fracture is primarily driven by straight crack extension along the original plane. The corresponding macroscale fracture-initiation properties ($K_{\rm Ic} \approx 1.7-2.9 \text{ MPa} \cdot \sqrt{\rm m}, \ \sigma_{\rm f} \approx 1.6-2.4 \text{ GPa}$) are extrapolated using established scaling laws. Considering TiB₂ as a representative system, additional simulations explore loading conditions ranging from pure Mode-I (opening) to Mode-II (sliding). TiB₂ models containing prismatic cracks exhibit their lowest fracture resistance under mixed-mode conditions, where the crack deflects onto pyramidal planes—as confirmed by nanoindentation tests on TiB₂(0001) thin films. This study establishes K-controlled, MLIP-based simulations as predictive tools for orientationand mode-dependent fracture in ceramics. The approach is readily extendable to finite temperatures for evaluating fracture behavior under conditions relevant to refractory applications.

Introduction

Fracture mechanics roots in Griffith's work during the 1920s [1]. Griffith recognized that hard yet brittle materials, such as glass, fracture at stresses far below their theoretical strength due to microstructural imperfections. These flaws act as stress concentrators that facilitate crack initiation. He also demonstrated that crack propagation occurs when the elastic strain energy released during crack extension exceeds the energy required to form new crack surfaces.

Three decades later, Irwin [2] extended Griffith's energy-based criterion by incorporating dissipative, non-linear processes such as plastic deformation in metals. He introduced the concept of stress intensity factor, K, to quantify near-tip stress field in linear elastic materials. Irwin also classified fracture into three distinct modes – Mode I (opening), Mode II (sliding), and Mode III (tearing) – each governed by a corresponding critical stress intensity factor: $K_{\rm Ic}$, $K_{\rm IIc}$, and $K_{\rm IIIc}$.

The critical stress intensity factor $K_{\rm Ic}$ is recognized as the practically most significant. The term $K_{\rm Ic}$ is often referred to as the material's fracture toughness, since fracture in solids generally initiates at structural flaws under tension. The $K_{\rm Ic}$ is a property

measured through standardized tests (see, e.g., Refs. [3–7]), which involve introducing a crack into a sample and applying a controlled load or displacement to determine the conditions leading to fracture. However, the reproducibility of $K_{\rm Ic}$ measurements depends strongly on microstructural features, including crystallographic defect density [8-14].

Traditional fracture toughness tests are limited in resolving nanoscale mechanisms responsible for fracture initiation. These limitations become especially pronounced in thin-film materials, where small dimensions and substrate effects complicate measu-[15]. Thus, advancing the fundamental understanding of fracture requires complementing mechanical tests with state-of-the-art in-situ imaging |16, 17|. In this context, atomistic simulations play a vital role by providing direct insights into fracture initiation mechanisms and enabling accurate characterization of fracture properties at atomic scale.

Machine-learning interatomic potentials (MLIPs) can offer detailed atomic-scale understanding of materials' fracture initiation and accurate evaluation of fracture properties. Although the reliability of MLIP-based simulations depends on the quality of the underlying ab initio training data [18–22], MLIPs are systematically improvable force fields [23, 24] [25-27] that can achieve accuracy comparable to density functional theory (DFT), but with up to five orders of magnitude greater computational efficiency. We have recently proposed an MLIP training workflow and a validation standard [28] aimed at reproducing the elastic and plastic properties of bulk ceramic lattices – specifically, systems free of extended crystallographic defects in their unstrained state – as predicted by ab initio molecular dynamics (AIMD). Using MLIP-based molecular dynamics simulations, we investigated how theoretical strength varies with supercell size, as well as the anisotropy of slip and fracture behavior under tensile and shear loading at both room and elevated temperatures. The training and validation strategy presented in Refs. [28–30] lay the foundations to this work.

Here, we use MLIPs in K-controlled-loading simulations to investigate the mechanical properties and fracture paths in defective (pre-cracked) Group-IV transition-metal diborides, TMB₂:s (TM=Ti, Zr, Hf). As most ceramics, TMB₂:s are prone to fracture without yielding, but exhibit ultra-high thermal stability [31], exceptionally high hardness [32], corrosion resistance, and excellent thermal and electrical conductivity [33]. Unlike other hard ceramic protective coatings (e.g. nitrides and carbides) for which the fracture properties have been characterized relatively thoroughly [34–39], information on the toughness and strength available in the literature for TMB₂:s is sparse [40-42]. An experimental characterization of the fracture resistance of diboride films is further complicated by largely varying degrees of stoichiometry (TMB_{1,53-2,72}) which, together with a typically high density of crystallographic defects [43, 44], constitutes an additional hurdle to understanding the structure/property relationship in this class of materials [45]. The limitations of the experiments provide further motivation to use MLIPs to characterize fracture initiation in diboride systems.

Methods

Ab initio calculations

Finite-temperature Born-Oppenheimer ab initio molecular dynamics (AIMD) calculations were carried out using VASP [46] together with the projector augmented wave (PAW) [47] method and the Perdew-Burke-Ernzerhof exchange-correlation functional revised for solids (PBEsol) [48]. The plane-wave cut-off energies of 300 eV and Γ -point sampling of the reciprocal space were employed.

Structural models of TMB₂:s, TM=(Ti, Zr, Hf) were based on the α polymorph, adopting AlB₂-type (P6/mmm) phase [49, 50]. The hexagonal unit cells were orthogonalized using the following crystallographic orientations: $x \parallel |1010|, y \parallel |1210|, z \parallel |0001|$. All AIMD calculations were conducted using 720-atom supercells (240 TM+480 B) with dimensions of $\approx (1.5 \times 1.6 \times 2.6)$ nm³. The supercells were equilibrated at target temperature (300 K and 1200 K) through a two-step process: (i) a 10 ps isobaric-isothermal (NpT) equilibration simulation using the Parrinello-Rahman barostat [51] and the Langevin thermostat; (ii) a 2-4 ps simulation with the canonical (NVT) ensemble based on Nosé-Hoover thermostat, imposing the time-averaged lattice parameters obtained from the equilibration stage (i).

Room-temperature elastic constants, C_{ij} , were determined following Ref. [52], i.e., obtained from a second-order polynomial fit of stress/strain data from the [0001], $[10\overline{1}0]$, and $[\overline{1}2\overline{1}0]$ tensile simulations (used to derive C_{11} , C_{12} , C_{13} , C_{33}), and the $(0001)[\overline{1}2\overline{1}0]$. $(10\overline{1}0)[\overline{1}2\overline{1}0]$ and $(10\overline{1}0)[0001]$ shear simulations (used to derive C_{44}). Strains ranging from 0 to 4\% were considered. Stress tensor components were calculated by averaging data over the final 0.5 ps of each simulation. Zero Kelvin elastic constants were also calculated using the stress-strain method, with the same energy convergence criteria as the AIMD simulations but smaller strain (< 1%). The methodology is consistent with our previous work [28] on α -TiB₂. The surface energies were calculated at zero Kelvin using 60-atom TMB₂ supercells $(3 \times 3 \times 1 \text{ k-mesh} \text{ and cut-off energy of } 300 \text{ eV})$ together with a 12 Å vacuum layer.

Molecular statics/dynamics with MLIPs (ML-MS/MD)

ML-MS calculations were conducted using the LAMMPS code [53] interfaced with the mlip-2 package [27] enabling the usage of MTP-type MLIPs. Active learning has been performed using the concept of extrapolation grade, MV [54], which also served to assess the reliability during MD simulations with the trained MLIPs. For MLIP validation purposes, we performed MD simulations of uniaxial deformation and calculated elastic constants. Computational setup for equilibration and tensile tests at the atomic scale was designed to closely match the corresponding AIMD simulations. For zero-Kelvin elastic constant validation, to minimize variables and maintain accuracy, we conducted MD calculations at 10 K instead of using MS simulations. The zero-Kelvin surface energies were validated using ML-MS with 12 Å vacuum, the same as in DFT calculations.

K-controlled MS simulations were utilized to evaluate the effective resistance to brittle cleavage, using cracked-plate models of sizes reaching $\approx 10^6$ atoms (A =



 $L^2 \approx 250^2 \text{nm}^2$, where A is the plate area and L is the lateral size). Theory and methods followed Refs. [55–58]. We employed square TMB₂ plates (with area of L^2) with all the possible geometries for both Mode-I and Mode-II loadings, i.e., $(0001)[10\overline{1}0]$ $(Nr.1), (0001)[\bar{1}210] (Nr.2), (1210)[1010] (Nr.3), (\bar{1}210)[0001] (Nr.4), (1010)[0001] (Nr.5),$ (1010) [1210] (Nr.6). The supercells were periodic along the crack-front direction with thickness of approximately 0.5 nm.

Atoms in the frame region centered at the crack tip are incrementally displaced by applying increasing values of the stress intensity factors K_I , K_{II} , and K_{mix} , using a step size of 0.02 MPa \sqrt{m} . For mixed-mode loading, the components are calculated as follows:

$$K_{\text{mix}} = \sqrt{K_I^2 + K_{II}^2},$$
 (1.a)

$$K_I = K_{\text{mix}} \cdot \frac{a}{\sqrt{a^2 + b^2}},\tag{1.b}$$

$$K_{II} = K_{\text{mix}} \cdot \frac{b}{\sqrt{a^2 + b^2}},\tag{1.c}$$

where a and b represent the prescribed Mode-I and Mode-II percentages, such that a + b = 100.

All, except frame atoms, were relaxed with the conjugate-gradient algorithm at each K increment, with tolerances set to 10^{-14} for the relative change in energy and 10^{-14} eV/Å for forces. The simulations were carried out with atomically sharp cracks (deleting half monolayer), where interactions between atoms on opposite sides of the crack plane were screened over ≈ 1 nm. Additionally, the cracked plates are constructed with an equal number of atomic layers above and below the crack plane.

The **Griffith fracture toughness**, K_{Ic}^{G} , was derived from [59]:

$$K_{\rm Ic}^{\rm G} = \left[2E_{\rm surf}^{\rm unrel} \,\Lambda_{22}^{-1}\right]^{1/2},$$
 (5.2)

where E^{unrel}_{surf} represents the unrelaxed surface energy and $\overline{\Lambda}$ is the Stroh energy tensor, calculated from the elastic tensor.

Experimental methods

A TiB_{2.04} coating with near 1:2 stoichiometry and approximately 2 μ m thickness was provided for analysis. The coating was deposited using an in-house DC balanced magnetron sputtering system, employing a 6-inch, powder-metallurgically produced TiB₂/C (99/1 wt.%) target (>99.6% purity). The complete deposition procedure is detailed in Ref. [45]. Nanoindentation tests were performed using an CSIRO UMIS indenter equipped with a cube-corner diamond tip to induce controlled cracking. A total of 17 indents were applied at peak loads (F_m) ranging from 50 to 450 mN. The tests followed a force-controlled loading-unloading cycle. A cross-sectional TEM lamella was extracted from a radial crack tip using a Thermo Scientific Scios 2 DualBeam FIB-SEM system. Following a conventional FIB milling and lift-out procedure as presented in Ref. [60], an 8 μ m thick tungsten protection layer was deposited over the region of

interest to prevent milling damage. Initially, a 2 μ m thick cross-sectional lamella was prepared, which was then refined by sequential ion milling steps to approximately 100 nm. Final cleaning steps at 2 kV and 27 pA, followed by Ar ion milling at 0.5 kV using a Gatan PIPS II system, further reduced the thickness to <75 nm, allowing high-resolution TEM analysis.

The cross-sectional transmission electron microscopy (TEM) specimens were prepared using an FEI Quanta 200 3D DBFIB. A 200 kV field emission TEM (JEOL 2100F) equipped with an image-side spherical aberration (C_S) -corrector was used in the highresolution TEM (HRTEM) study, demonstrating a resolution of 1.2 Å at 200 kV. The aberration coefficient was set close to zero, under which the HRTEM images were taken under slightly over-focus conditions (close to the Scherzer defocus). A CCD Orius camera is used to record HRTEM images, where image sizes are 2048 pixels × 1336 pixels. The strain fields in TiB_2 were calculated based on the C_S -corrected HRTEM images by the geometric phase analysis (GPA) method. According to the GPA algorithm, the displacement fields can be obtained by selecting two non-collinear Bragg vectors in the power spectrum generated from a HRTEM image.

Results and discussion

1 MLIP validation and theoretical strengths of defect-free crystals

Tab. 1: MLIP validation. Comparison between ML-MS and DFT results for diboride lattice constants (a, c), elastic constants (C_{ij}) , polycrystalline moduli (Young's modulus, E, bulk modulus, B, shear modulus. G), and relaxed surface energies E_{surf} on (0001), (10 $\overline{10}$), and ($\overline{12}\overline{10}$) lattice planes. Literature DFT values are also included.

$\overline{\text{TMB}_2}$	Lattice	Elastic constants (GPa)							Surface energy (J/m ²)			Reference			
	a	c	C_{11}	C_{33}	C_{44}	C_{12}	C_{13}	E	B	G	(0001)	$(10\overline{1}0)$	$(\overline{1}2\overline{1}0)$		
${ m TiB}_2$	3.027	3.213	654	464	259	76	115	580	263	256	3.80	3.98	3.42	This work (DFT)	
	3.030	3.204	636	441	272	61	92	576	242	261	3.80	4.12	3.57	This work (ML-MS)	
	3.029	3.219	656	461	259	65	98	582^{I}	253^{I}	261^{I}	/	/	/	Ref. [61]	
	/	/	660	464	255	60	96	583^{I}	250	258	4.20^{II}	4.10^{II}	/	Ref. [62]	
	3.029	3.219	/	/	/	/	/	/	/	/	4.21	4.19	/	Ref. [63]	
ZrB_2	3.180	3.545	539	422	270	52	109	523	226	235	3.86	4.54	3.83	This work (DFT)	
	3.167	3.531	551	427	248	54	118	517	234	228	3.61	4.38	3.57	This work (ML-MS)	
	3.168	3.536	555	436	254	62	119	524	238	231	/	/	/	Ref. [61]	
	/	/	539	420	238	60	116	502^{I}	231	218	3.85^{II}	4.45^{II}	/	Ref. [62]	
	3.168	3.536	/	/	/	/	/	/	/	/	3.91	4.33	/	Ref. [64]	
HfB ₂	3.149	3.480	602	432	309	57	105	580	238	266	3.88	4.53	4.07	This work (DFT)	
	3.127	3.473	604	473	271	70	137	565	263	248	3.53	4.51	3.83	This work (ML-MS)	
	3.165	3.512	584	457	257	98	135	544	253	238	/	/	/	Ref. [61]	
	/	/	588	448	248	89	138	533^I	260	227	3.80^{II}	4.35^{II}	/	Ref. [62]	
	3.163	3.515	602	452	258	78	137	550	260	239	/	/	/	Ref. [65]	

^I: Calculated based on the reference data.

Our MLIPs, based on the moment tensor potential (MTP) framework [27], are trained on ab initio molecular dynamics (AIMD) data for transition metal diborides subjected to deformation up to fracture, as well as configurations under extreme loading conditions. All Group-IV diborides (TiB₂, ZrB₂, HfB₂) crystallize in the hexagonal α/AlB_2 -type phase [50]. Training and validation errors, quantified by the residual mean square error (RMSE), remain below 8 meV/atom for energies, 0.24 eV/Å for forces, and 0.6 GPa for

 $^{^{}II} \colon \mathbf{Value}$ extracted from a figure.

stresses. Before applying these MLIPs to simulations of defective diboride crystals under load, their reliability is demonstrated through direct comparison with DFT results and AIMD-based tensile tests.

Tab. 1 presents the results obtained by MLIP-based molecular statics simulations and DFT calculations from this and previous studies. Although our MLIPs are trained mainly on AIMD data collected at finite temperature, they reproduce 0 K DFT lattice parameters (a, c), elastic constants (C_{ij}) , and surface energies (E_{surf}) satisfactorily well. Note that static DFT and AIMD calculations of this work are carried out using the same accuracy parameters (see the Methods). The deviations in lattice parameters are below 0.7%, while the C_{11} , C_{33} , and C_{44} elastic constants, as well as the polycrystalline bulk (B), shear (G) and Young's moduli (E) differ by less than 10% from the corresponding DFT values. For $C_{i\neq j}$ elastic constants, the deviations are generally below 20%. With regard to surface energies, the differences between MLIP and static DFT values are lower than 6.5%.

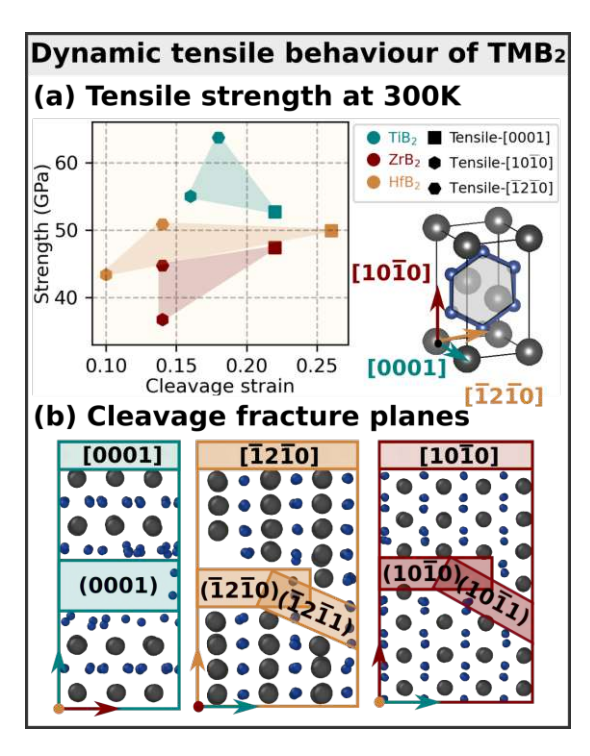


Fig. 1: Uniaxial tensile simulations at 300 K using MLIP-based molecular dynamics (ML-MD). (a) Maximum stress (theoretical tensile strength) sustained by TMB₂:s, (TM=Ti, Zr, Hf) during uniaxial tensile deformation along [0001] (square), $[10\overline{1}0]$ (vertical hexagon), and $[\overline{1}2\overline{1}0]$ (horizontal hexagon) directions. (b) Cleavage fracture after reaching the maximum stress point, with plane identification. The image on the right in (a) shows a diboride hexagonal lattice structure in the α -phase, including orthogonal crystal axes. The shadowed boron hexagonal layer is aligned with the basal plane.

In addition to reproducing elastic properties, our MLIPs describe materials' behaviors under stress conditions that induce structural instabilities. Specifically, the potentials were trained on AIMD data of supercells subjected to uniaxial tension up to cleavage and to shear strain up to activation of lattice slip at finite temperatures, together with configurations under extreme loading conditions. Thus, the training sets encompass diborides under tensile strain along various crystallographic directions and shear deformation along distinct slip systems. Training and extensive validation of the TiB₂-MLIP

is detailed in Refs. [28, 29]. Importantly, the ability of the MLIP to model tensile and shear deformation in large single-crystal supercells – beyond the feasible size limits of DFT calculations – has been assessed using the concept of the extrapolation grade $(\gamma [54])$, which is commonly employed in active learning to identify extrapolative atomic environments. More precisely, γ quantifies the similarity between local atomic environments that emerge during nanoscale simulations and those represented in the training set. A high extrapolation grade indicates significant deviation from the training data and corresponds to greater uncertainty in the predicted energies and forces.

Since the newly trained MLIPs for HfB₂ and ZrB₂ follow the same training protocol previously established for TiB₂, |28, 29| we do not repeat all validation steps here. Overall, the results obtained using our force fields closely reproduce the properties of the underlying AIMD training configurations. These include cleavage mechanisms on various low-index planes, which are particularly relevant for the crack propagation simulations presented in this study.

We begin by analyzing the results of MLIP-based molecular dynamics (MLIP-MD) simulations performed on small ($\sim 10^3$ atoms), initially defect-free, single-crystal diboride supercells subjected to tensile strain at room temperature. While these simulations are primarily intended to capture temperature-dependent elastic responses (e.g., Ref. [52]) and ideal fracture properties – such as the theoretical strength and intrinsic toughness of a perfect crystal (e.g., Ref. [66]) – they also allow for the rapid identification and clear visualization of energetically preferred fracture planes. In addition, they can signal whether the crystal has an inherent tendency to undergo stress-induced lattice transformations, which may enhance toughness and delay fracture initiation. [66, 67]. As shown in our earlier studies on TiB₂ [28], the crack orientation observed under uniform tensile strain of pristine lattices remain qualitatively unchanged with increasing supercell size, despite the appearance of lattice distortions in larger systems. This supports the use of small, computationally efficient models to explore the intrinsic fracture extension planes of ideal crystals in different loading orientations.

Fig. 1 summarizes the theoretical tensile strength and the corresponding fracture strain of diborides elongated parallel to [0001], $[10\overline{1}0]$, $[\overline{1}2\overline{1}0]$ crystallographic directions. The results reveal a pronounced anisotropy in the mechanical response: while the *elastic* response of hexagonal lattices is isotropic within the basal plane, the tensile strength and fracture strain vary significantly with loading orientation. Among the studied materials, TiB₂ consistently exhibits the highest theoretical strength, followed by HfB₂ and ZrB₂ (Fig. 1-(b)). All systems withstand the largest strain along the [0001] axis.

As shown in Fig. 1-(b), fracture occurs through brittle cleavage along basal, prismatic, or pyramidal planes, depending on the direction of applied tension. While the active cleavage plane changes with orientation, the fracture mechanisms remain consistent across the three diborides. Interestingly, in some cases the fracture planes are not orthogonal to the loading axis, but instead align with first-order pyramidal planes such as (1011). This result is somewhat unexpected, but could be explained based on energetic arguments (differences in surface energies) or shear stress accumulation during tension.

Fracture along first-order pyramidal planes of hexagonal crystals has been predicted in theoretical studies based on surface energy, interplanar spacing, and elastic modulus.

For example, previous analyses identified these planes as energetically favorable cleavage paths under specific stress orientations – particularly in hcp titanium and magnesium [68]. Experimental studies further support this view, having observed crack propagation along (1011)-type planes in single-crystal Ti and Mg [69, 70]. Our MLIP-MD simulations are consistent with these findings: in addition to fracture along low-index cleavage planes, we observe skewed crack paths that align with first-order pyramidal planes. This suggests that crystallographic anisotropy in AlB₂-type diborides can promote cleavage along inclined planes, even under nominally uniaxial tension.

Although these results provide valuable insight into the intrinsic fracture behavior of ideal, defect-free crystals, they should be interpreted with caution. The small size of the simulation cells and the absence of native extended defects – common in sputterdeposited diborides – limit the reliability of the predicted crack paths. A more physically representative description of fracture initiation is offered by nanoscale simulations based on K-controlled loading of defective lattices (see below).

2 Mode-I loading of TMB₂:s

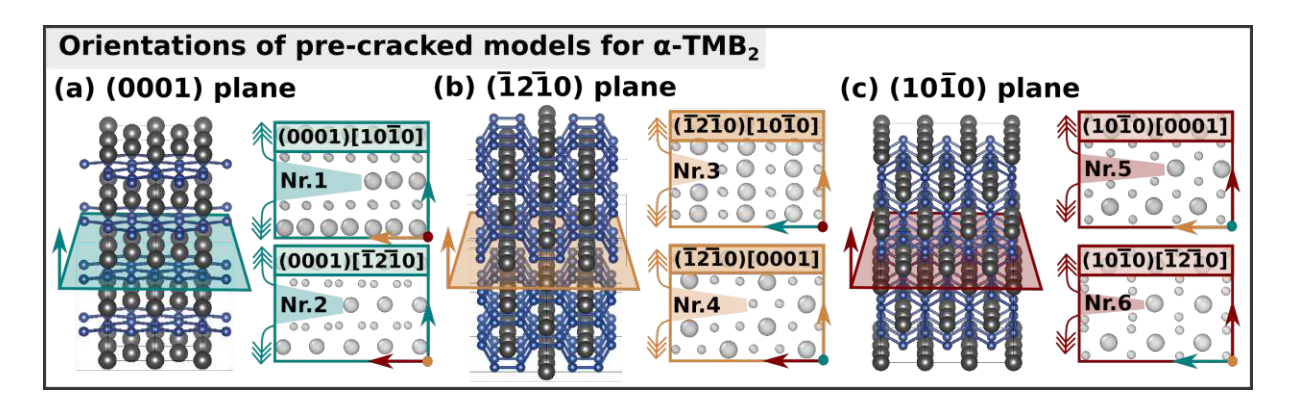


Fig. 2: Cracked-plate lattice geometries of hexagonal α -structured diborides considered in this work. (a) (0001) crack surface with $[10\overline{1}0]$ (Nr.1) and $[\overline{1}2\overline{1}0]$ (Nr.2) crack-front directions. (b) $(\overline{1}2\overline{1}0)$ crack surface with $[10\overline{1}0]$ (Nr.3) and [0001] (Nr.4) crack-front directions. (c) $(10\overline{1}0)$ crack surface with [0001] (Nr.5) and $[\overline{1}2\overline{1}0]$ (Nr.6) crack-front directions.

The mechanical properties of diborides are calculated via K-controlled loading (molecular statics at 0 K) of lattice models containing an atomically sharp crack (cracked-plate models). In these simulations, the stress-intensity factor K_I is incrementally increased to identify the conditions corresponding to the onset of crack extension [56, 58]. Calculations are repeated for varying plate areas A, enabling extrapolation of the fracture-initiation toughness and fracture-initiation strength to the macroscale limit using established scaling relations [58]. Here, both properties are extracted from the tensile stress versus stress-intensity curve at the value of K_I corresponding to the rupture of the first chemical bond at the crack tip.

To systematically investigate fracture behavior in hexagonal α -structured TMB₂, we consider six low-index crack configurations, denoted as (hklm)[h'k'l'm'], where the first set indicates the crack plane and the second the crack-front direction (Fig. 2). Among these, the $(\overline{1210})[10\overline{10}]$ and $(10\overline{10})[\overline{1210}]$ orientations (Nr.3 and Nr.6), in which fracture initiates perpendicular to (0001) basal plane, are particularly relevant for comparison

with experiments. This is because the [0001] direction corresponds to the typical growth orientation of TMB₂ thin films, making these geometries representative of loading conditions encountered in experimental toughness assessments (e.g., by nanoindentation).

Fig. 3 illustrates the evolution of volumetric strain and bond-breaking events during Mode-I loading for each crack geometry, showing atomic configurations at increasing K_I : before crack extension, at the onset of propagation, and well beyond it. In all cases, stress concentrates at the crack tip as K_I approaches the critical value K_{Ic} , triggering fracture. On the (0001) plane (Fig. 3a,b), cracks initiate via rupture of TM-B bonds, while on the $(1\bar{2}10)$ and $(10\bar{1}0)$ planes (Fig. 3c-f), fracture begins with B-B bond breaking. Most commonly, fracture initiation is marked by the breaking of a single bond, although multiple bond ruptures are observed in some cases, as in model Nr.3. In certain configurations, crack advance is delayed by crack trapping – a phenomenon arising from the discreteness of atomic bonding, which can locally stabilize the crack tip over a finite loading interval before mechanical instability sets in [71].

Following crack initiation, the crack propagation behavior varies by geometry. Some cracks extend smoothly along the original cleavage plane (e.g., Nr.1, Nr.3, Nr.4), while others follow more complex trajectories, such as zigzag growth (Nr.2, Nr.5) or oblique deflection across crystallographic planes (Nr.6). These patterns underscore the importance of lattice anisotropy and local bonding topology in guiding fracture evolution, as discussed in detail below.

Fig. 4 compares the extrapolated fracture toughness K_{Ic}^{∞} (Fig. 4a) and maximum fracture strength σ_{\max}^{∞} (Fig. 4b) for Group-IV TMB₂ systems across all six geometries. These values are obtained through inverse polynomial extrapolation to infinite plate area, following the procedure in Ref. [58]. HfB₂ generally exhibits the highest K_{Ic}^{∞} , near 2.8 MPa· \sqrt{m} , except in geometry Nr.3, where TiB₂ shows a higher toughness (2.24) vs. 2.01 MPa· \sqrt{m}). ZrB₂ typically shows the lowest values (1.8 MPa· \sqrt{m}), except in Nr.1, where it marginally exceeds TiB₂. Maximum strengths σ_{\max}^{∞} are comparable across materials (2.0 GPa), with the exception of geometry Nr.4, where TiB₂ sustains higher stress prior to fracturing. Importantly, while toughness and strength vary with plate size – a fundamental reason for performing K-controlled simulations, which require sufficiently large plate areas to avoid biasing crack-tip phenomena – the underlying fracture mechanisms remain qualitatively unchanged for a given crack geometry across all materials (Fig. 4c). This size invariance supports the validity of using the fracture properties of finite-size models to extrapolate macroscale fracture properties.

It is instructive to compare the extrapolated toughness values obtained from atomistic simulations (K_{Ic}^{∞}) with the corresponding Griffith-model estimates (K_{Ic}^{G}) , as the ratio $K_{Ic}^{\infty}/K_{Ic}^{G}$ provides a meaningful metric of intrinsic brittleness or plasticity-mediated toughening. Griffith predictions are derived from unrelaxed surface energies and zero-Kelvin elastic constants (Tab. 1) [57, 58, 72]. A ratio near unity reflects ideally brittle behavior, while significantly higher values indicate enhanced toughness due to plastic deformation at the crack tip. For instance, ratios approaching three have been reported for high-Al-content $Ti_{1-x}Al_xN$ [58], where atomistic simulations reveal crack-tip plasticity. In contrast, the near one-to-one correspondence observed here for TMB₂ (Tab. 2) reflects their intrinsically brittle nature, consistent with other brittle ceramics such as TiN(001), where $K_{Ic}^{\infty} \approx K_{Ic}^{G}$ and no plasticity is observed for atomically sharp cracks [58]. Nevertheless, deviations between K_{Ic}^{∞} and K_{Ic}^{G} – typically within 0.5–20%, but reaching

up to 30% for HfB₂ geometries Nr.1 and Nr.2 – underscore the limitations of the Griffith model. Such differences may arise not only from atomistic-scale phenomena like lattice trapping, bond discreteness, and local stress localization [57], but also from crack path deflection, as observed in TiN(111) reorienting onto lower-energy (001) planes (Fig. 8a in Ref. [58]). Unlike Griffith's assumption of linear elasticity and straight-through propagation along the initial cleavage plane, K-controlled atomistic simulations resolve these non-ideal behaviors directly, making them essential for accurate predictions of fracture in brittle ceramics.

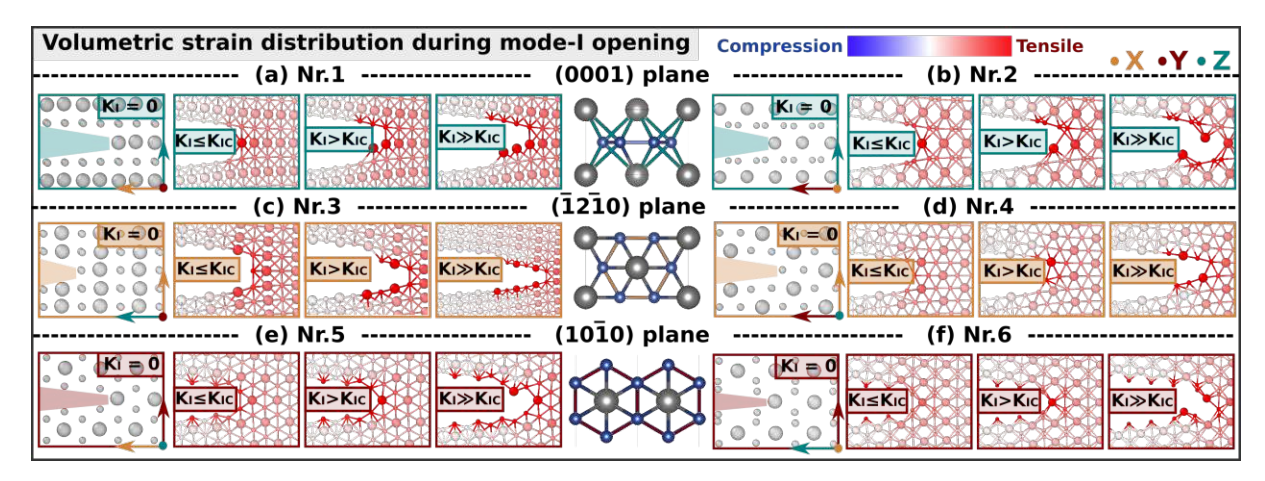


Fig. 3: Bond breakage and volumetric strain distribution in cracked plate models subjected to Mode-I loading as a function of the stress intensity factor. Atomic configurations just before, shortly after, and well above K_{Ic} for different crack geometries: (a, b) (0001), (c, d) ($\overline{1210}$), and (e, f) $(10\overline{1}0)$ planes. The simulation snapshots illustrate volumetric strain distributions in blue/red color scale.

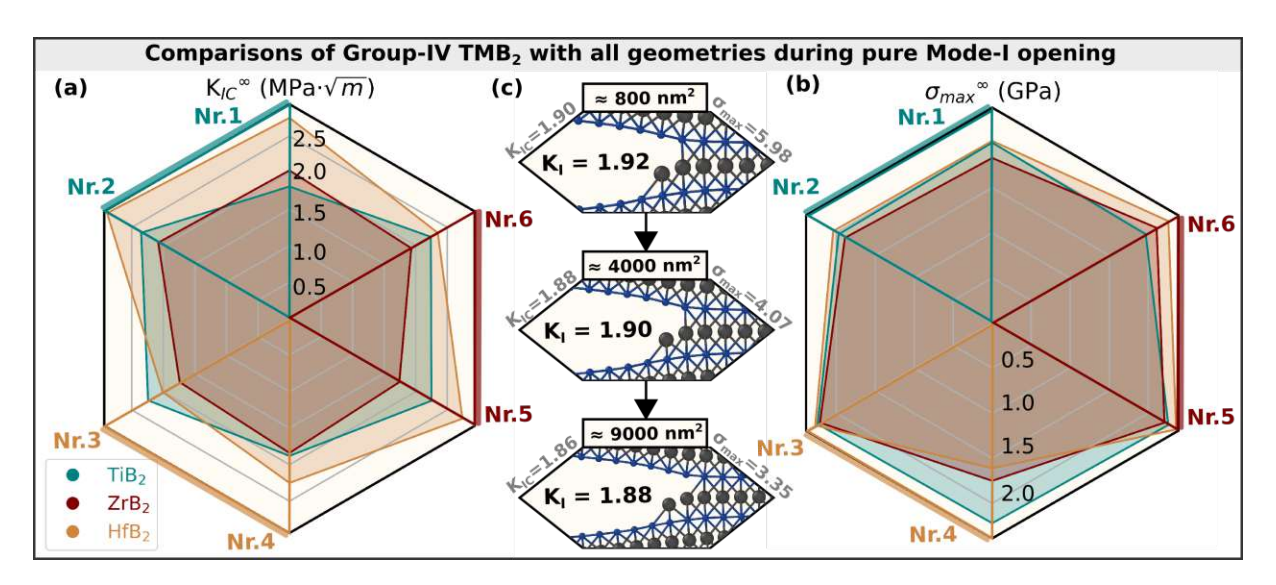


Fig. 4: Comparison of extrapolated Mode-I fracture toughness K_{Ic}^{∞} (a) and fracture strength σ_{\max}^{∞} (b) for TiB₂ (teal), ZrB₂ (orange), and HfB₂ (red), across all six crack geometries. The geometry indices Nr.1-Nr.6 are also colored in teal-orange-red, consistent with Fig. 2. Note that all crack geometries are modeled for all three materials. (c) Illustration of the influence of the plate area on the calculated fracture toughness (case of TiB₂ with crack geometry Nr.1). Note that the fracture mechanism remains qualitatively unchanged with increasing size of the supercell.

Tab. 2: Macroscale Mode-I fracture initiation toughness (K_{Ic}^{∞}) , Griffith fracture toughness (K_{Ic}^{G}) and fracture strengths (σ_{max}^{∞}). The K_{Ic}^{∞} , σ_{max}^{∞} , and their standard deviations are extrapolated at the infinite size limit by fitting the K_{Ic} and σ_{max} values calculated for finite plate areas (see constitutive scaling laws established in Ref. [58]). The K_{Ic}^{G} is derived from the unrelaxed surface energy (E_{surf}^{unrel}) and elastic tensor computed by ML-MS.

Geometry		${ m TiB}_2$			ZrB_2		HfB ₂			
	$K_{Ic}^{\infty} (MPa \cdot \sqrt{m})$	$K_{Ic}^G (MPa \cdot \sqrt{m})$	σ_{max}^{∞} (GPa)	$K_{Ic}^{\infty} (MPa \cdot \sqrt{m})$	$K_{Ic}^G (MPa \cdot \sqrt{m})$	σ_{max}^{∞} (GPa)	$K_{Ic}^{\infty} (MPa \cdot \sqrt{m})$	$K_{Ic}^G (MPa \cdot \sqrt{m})$	σ_{max}^{∞} (GPa)	
$(0001)[10\overline{10}] (Nr.1)$	1.81 ± 0.03	2.02	2.00 ± 0.77	2.03 ± 0.04	1.86	1.83 ± 0.65	2.75 ± 0.02	1.93	2.02 ± 0.64	
$(0001)[\overline{1}2\overline{1}0] (Nr.2)$	2.35 ± 0.03	2.20	1.97 ± 0.49	2.08 ± 0.02	1.98	1.89 ± 0.22	2.89 ± 0.02	2.05	2.04 ± 0.31	
(0001)	E_{surf}^{unrel} : 4.02 (J/m ²)			E_{i}	urrel: 3.68 (J/m ²)		E_{surf}^{unrel} : 3.61 (J/m ²)			
$\overline{(12\overline{10})[10\overline{10}]}$ (Nr.3)	2.24 ± 0.02	2.37	2.24 ± 0.63	1.74 ± 0.02	2.18	2.21 ± 0.68	2.01 ± 0.02	2.20	2.27 ± 0.61	
$(\overline{1}2\overline{1}0)[0001]$ (Nr.4)	1.88 ± 0.02	2.29	2.22 ± 0.67	1.84 ± 0.02	2.15	1.75 ± 0.29	2.25 ± 0.05	2.18	1.61 ± 0.54	
$(\bar{1}2\bar{1}0)$	E_s^u	$_{urf}^{inrel}$: 4.36 (J/m ²)		E_{i}	urrel: 4.33 (J/m ²)		E_{surf}^{unrel} : 4.07 (J/m ²)			
$(10\overline{1}0)[0001]$ (Nr.5)	2.25 ± 0.02	2.24	2.26 ± 0.69	1.74 ± 0.02	2.04	2.21 ± 0.68	2.74 ± 0.03	2.22	2.36 ± 0.47	
$(10\overline{1}0)[\overline{1}2\overline{1}0] (Nr.6)$	2.24 ± 0.02	2.16	1.97 ± 0.60	1.93 ± 0.02	2.01	2.11 ± 0.33	2.25 ± 0.02	2.20	2.26 ± 0.34	
$(10\overline{1}0)$	E_s^u	urrel: 3.88 (J/m ²)		E_{ε}	unrel: 3.81 (J/m ²)		E_{surf}^{unrel} : 4.15 (J/m ²)			

Fig. 5 compares post-initiation fracture behavior in TiB₂, ZrB₂, and HfB₂ for three representative geometries under Mode-I loading: (0001)[1010] (Nr.1), (1210)[1010] (Nr.3), and (1010)[1120] (Nr.6). Each subpanel displays the atomic configuration at the onset of crack propagation (K_{Ic}) and the resulting fracture morphology (crack wake) at $K_I \gg K_{Ic}$. In all cases, fracture initiates through rupture of TM-B or B-B bonds (Fig. 3), but the subsequent crack paths vary by material and geometry.

In diborides with native cracks on the (0001) and (1210) surfaces, Mode-I loading results in crack propagation that remains confined to the original cleavage plane (see Fig. 5a and Fig. 5b). The surface energy differences reported in Tab. 1 offer a plausible explanation for this behavior. Across all diboride systems, the ML-MS surface energies of the (0001) and (1210) planes are similar to each other and consistently lower than that of the (1010) surface. As a result, there is no strong energetic driving force to redirect the crack away from its initial orientation in these configurations.

More surprising material-specific behaviors emerge in Fig. 5c, where native cracks are positioned on the (1010) planes – identified as the highest-energy cleavage planes among those considered (Tab. 1). In ZrB₂ and HfB₂ (Fig. 5c-2 and c-3), these cracks readily deflect onto inclined (1101) planes during Mode-I loading. The phenomenon is reminiscent of what is observed in TiN, where cracks on high-energy (111) surfaces extend onto lower-energy (001) planes (see Fig. 8a in Ref. [58]). Although surface energies for firstorder pyramidal (1101) planes are not available, the observed deflections suggest that these planes are energetically more favorable than (1010) in ZrB₂ and HfB₂. Additional support comes from tensile simulations on small defect-free cells (Fig. 1c), which show oblique fracture paths – indicating an intrinsic tendency for crack redirection onto inclined planes that are presumably lower in energy. By contrast, in TiB₂ (Fig. 5c-1), the crack propagates stably along the (1010) plane without deviation. This suggests that any potential energetic advantage associated with switching to a pyramidal plane is not sufficient to activate deflection – possibly due to competing crystallographic or mechanical constraints that favor continuation along the original cleavage plane.

In summary, although energetic arguments provide valuable guidance for interpreting fracture patterns, the examples shown in Fig. 5c highlight the inherent complexity of fracture phenomena. These cases illustrate how cleavage energetics and crystallographic constraints interact in a material-specific manner and underscore the need for direct atomistic simulations to fully resolve the evolution of crack paths.

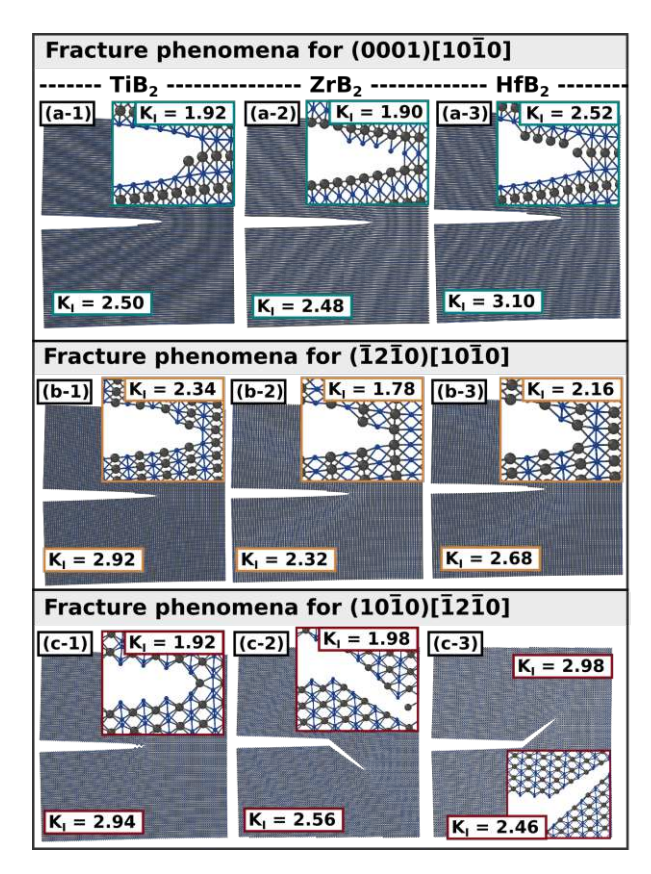


Fig. 5: Fracture mechanisms in Group-IV TMB₂ compounds following crack initiation $(K_I \gtrsim K_{Ic})$. Simulation snapshots are shown for one representative example per crack geometry: (a) (0001)[1010] $(Nr. 1), (b) (\overline{1210})[10\overline{10}] (Nr. 3), and (c) (10\overline{10})[\overline{1210}] (Nr. 6).$ Each panel compares TiB_2 (*-1), ZrB_2 (*-2), and HfB₂ (*-3) under pure Mode-I loading (the stress intensities K_I are expressed in MPa· \sqrt{m}). Each subpanel illustrates crack extension due to stress intensities well above K_{Ic} ($K_I \gtrsim K_{Ic} + 0.5 \text{ MPa}\sqrt{\text{m}}$), whereas the insets show magnifications of atomic configurations immediately after reaching K_{Ic} . Cracks are seen to either propagate along the initial plane or deflect depending on material and orientation. TM atoms (Ti, Zr, Hf) are depicted in dark gray; B atoms in light blue. The selected plate models have an area of $L^2 = 30 \text{ nm} \times 30 \text{ nm} = 900 \text{ nm}^2$

To assess the relevance of our simulation results, we now compare them with experimental measurements of fracture toughness for TiB₂, ZrB₂, and HfB₂. Reported values range between 1.8-6.8 MPa $\cdot \sqrt{m}$ for TiB₂ [73-75], 2.2-5.0 MPa $\cdot \sqrt{m}$ for ZrB₂ [40, 41, 76], and $2.8-7.2 \text{ MPa} \cdot \sqrt{\text{m}}$ for HfB₂ [77, 78]. The calculated toughness values fall within these experimental ranges (see Fig. 4 and Tab. 2), but direct comparison is complicated by the broad scatter in reported data. This variability arises from differences in sample preparation, microstructural characteristics (e.g., porosity, grain boundary density and grain sizes, and residual stresses), and the specific mechanical testing methods used. Furthermore, many experimental configurations involve mixed-mode loading – typically a combination of Mode-I and Mode-II – rather than ideal Mode-I conditions [79]. The role of mixed-mode effects is examined in the following section.

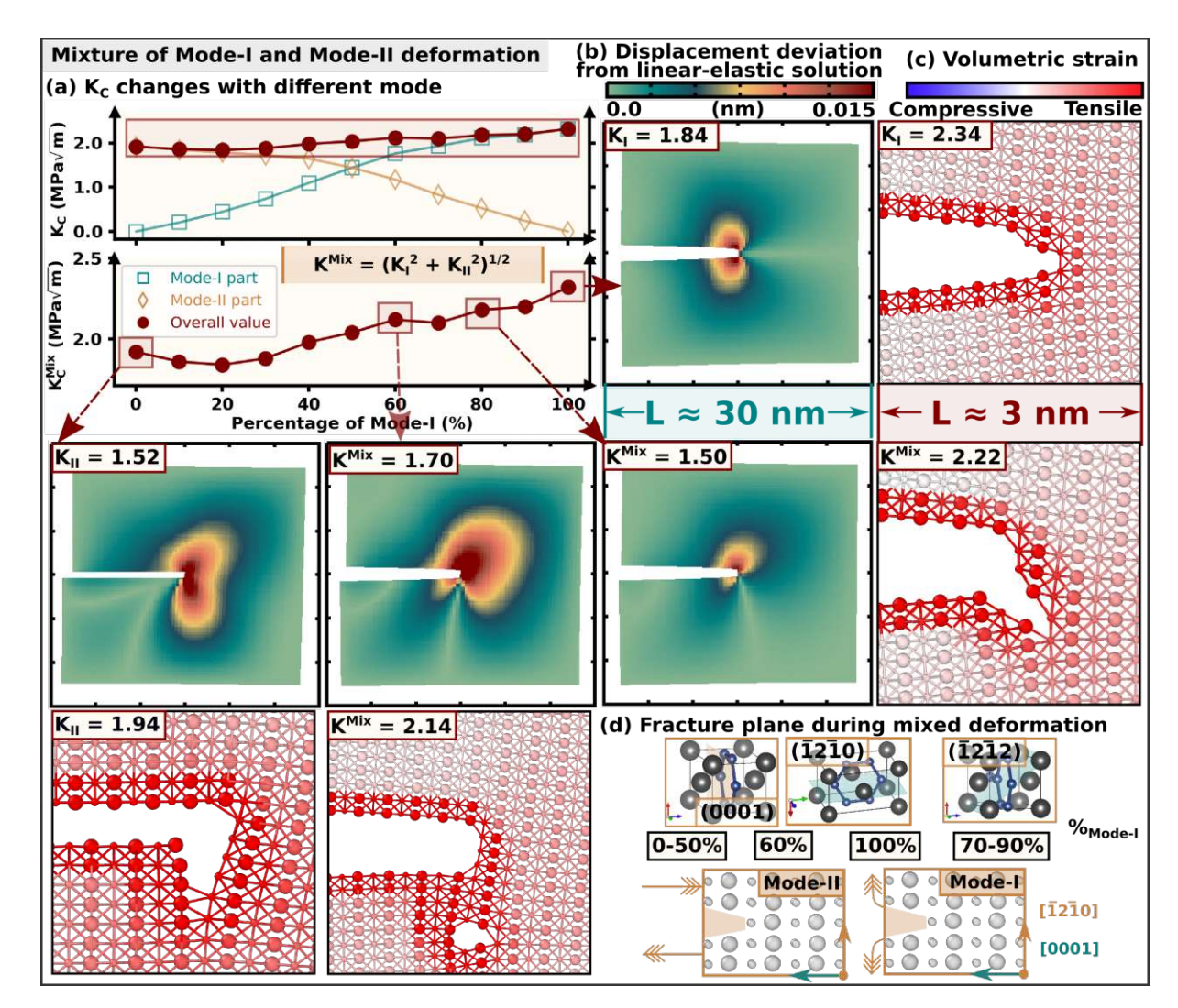


Fig. 6: Fracture mechanisms under mixed Mode-I/Mode-II loading, as exemplified by TiB₂ in the $(\bar{1}2\bar{1}0)[10\bar{1}0]$ (Nr. 3) crack geometry. (a) Critical stress intensity values K_c (red) as a function of Mode-I contribution, decomposed into K_I (teal) and K_{II} (orange) components. (b) Maps of atomic displacement deviations from the corresponding linear-elastic solutions at a stress intensity $K^{\text{mix}} \approx K_c - 0.02 \text{ MPa}\sqrt{\text{m}}$, visualizing the effect of mixed-mode loading on lattice distortion. (c) Volumetric strain patterns near the crack tip under pure Mode-I and mixed-mode conditions, showing fracture behavior at $K^{\text{mix}} \approx K_c + 0.02 \text{ MPa}\sqrt{\text{m}}$. (d) Summary of fracture mechanisms as a function of Mode-I content: from basal cleavage under pure Mode-II, to (0001) and ($\bar{1}2\bar{1}2$) plane fracture under mixed loading, to fully prismatic cleavage under pure Mode-I. Crystallographic directions [0001], [10 $\bar{1}0$], and [$\bar{1}2\bar{1}0$] are color-coded for reference. The stress intensity factors in (b) and (c), are expressed in MPa· $\sqrt{\text{m}}$.

3 Mixed Mode-I and Mode-II loading: example of TiB₂

Achieving a purely Mode-I fracture in mechanical testing experiments is uncommon due to material heterogeneity, sample geometry, or the specific loading configuration [80–82]. Even minor misalignments, combined with microstructural features such as grain boundaries or phase interfaces, can introduce shear components that promote mixed-mode fracture [83–85]. In this section, we examine mixed Mode-I and Mode-II crack opening, using TiB_2 as a representative system. Two crack geometries are considered for the main discussion: $(\overline{1210})[10\overline{10}]$ (Nr. 3) and $(10\overline{10})[\overline{1210}]$ (Nr. 6). Additionally, results

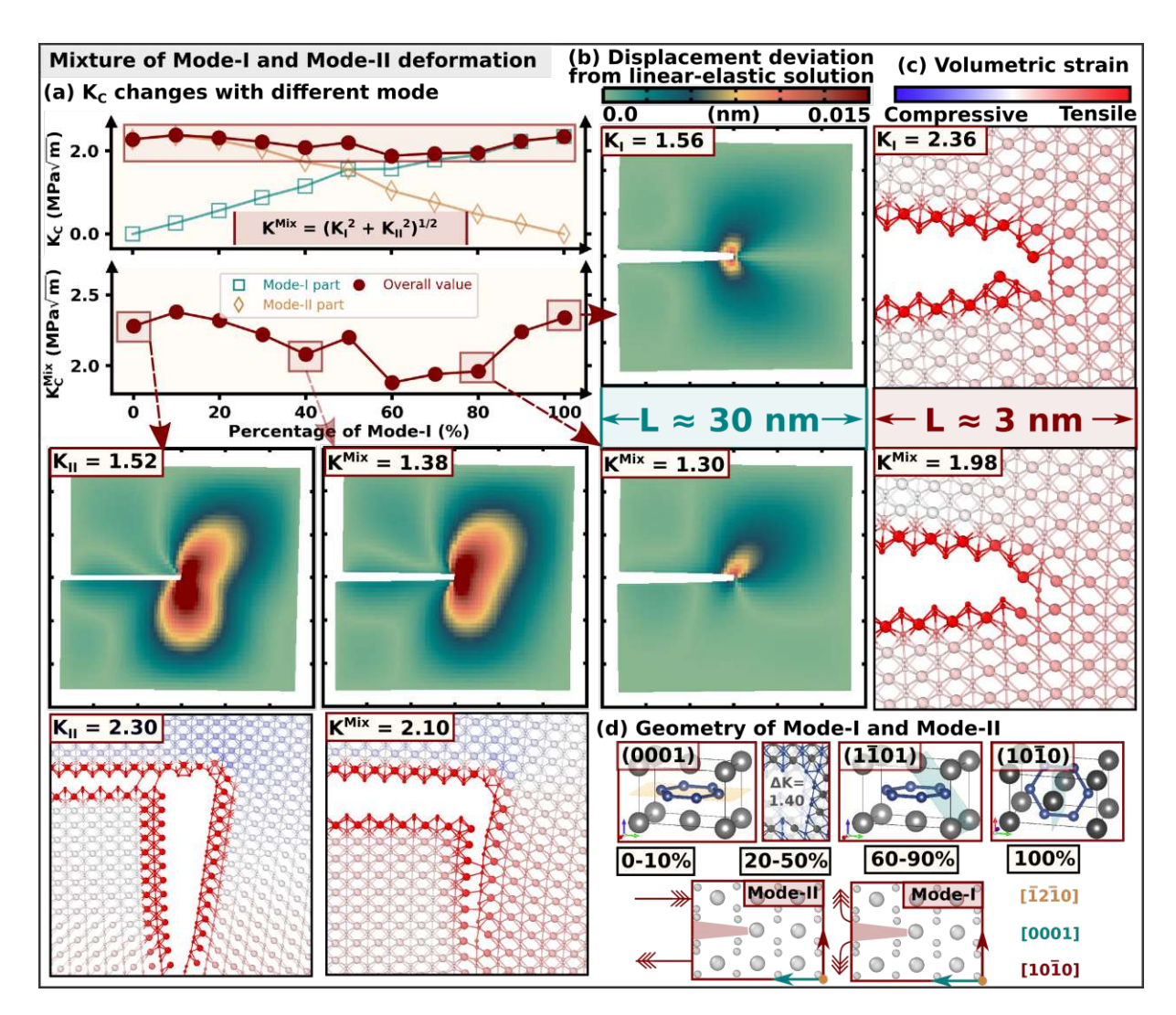


Fig. 7: Fracture mechanisms under mixed Mode-I/Mode-II loading, as exemplified by TiB₂ in the $(10\overline{1}0)[\overline{1}2\overline{1}0]$ (Nr.6) crack geometry. (a) Critical stress intensity values K_c (red) as a function of Mode-I contribution, decomposed into K_I (teal) and K_{II} (orange) components. (b) Maps of atomic displacement deviations from the corresponding linear-elastic solutions at a stress intensity $K^{\text{mix}} \approx K_c - 0.02 \text{ MPa}\sqrt{\text{m}}$, visualizing the effect of mixed-mode loading on lattice distortion. (c) Volumetric strain patterns near the crack tip under pure Mode-I and mixed-mode conditions, showing fracture behavior at $K^{\text{mix}} \approx K_c + 0.02 \text{ MPa}\sqrt{\text{m}}$. (d) Summary of fracture paths as a function of Mode-I content demonstrating four different mechanisms and three distinct fracture planes with varying ratios. Note that fracture at 20-50% Mode-I loading initiates with lattice slip along the basal plane. Crystallographic directions [0001], [10 $\overline{1}$ 0], and [$\overline{1}2\overline{1}$ 0] are color-coded for reference. The stress intensity factors in (b) and (c), are expressed in MPa· $\sqrt{\text{m}}$.

for mixed loading obtained for the $(10\overline{1}0)[0001]$ (Nr. 5) and $(1\overline{2}10)[0001]$ (Nr. 4) cracked plate models are briefly described below.

Fracture under mixed Mode-I and Mode-II loading can be described using energy-based criteria that account for the full crack-tip stress field. A well-known example is the strain energy density criterion by Sih and MacDonald [86], which evaluates the angular distribution of energy around the crack tip to predict both initiation and propagation direction. While rigorous, this approach requires evaluating the spatial dependence of stresses near the tip and is therefore complex to apply. Here, we adopt

a common approximation in linear elastic fracture mechanics, taking the total driving force for crack growth as $K^{\rm mix}=\sqrt{K_I^2+K_{II}^2}$ (see, e.g., Eq. 15 in Ref. [87] and Eq. 7a in Ref. [88]). That is, K^{mix} is the norm of a vector with orthogonal components K_I and K_{II} . This definition provides a practical estimate of the overall stress intensity and enables consistent comparisons across different mixed-mode loading cases.

To analyze the influence of mixed Mode-I/Mode-II loading on fracture mechanisms in TiB_2 , we begin with simulations using the $(\overline{1}2\overline{1}0)[10\overline{1}0]$ cracked-plate model (Nr. 3). In this configuration, the relative contribution of Mode-I is varied in increments of 10% from pure Mode-II (0%) to pure Mode-I (100%) (Fig. 6a). At each step, the corresponding components K_I and K_{II} are computed according to Eqs. (1.a)–(1.c) (see **Methods** section), while K^{mix} is incremented in steps of 0.02 MPa· $\sqrt{\text{m}}$.

Fig. 6a shows that the critical stress-intensity value for fracture initiation K_c^{mix} (hereafter abbreviated as K_c) generally increases with higher Mode-I contributions, rising from $K_{IIc} = 1.92 \text{ MPa} \cdot \sqrt{\text{m}}$ for pure Mode-II to $K_{Ic} = 2.22 \text{ MPa} \cdot \sqrt{\text{m}}$ for pure Mode-I. Interestingly, a slight drop in K_c is observed near the 20% Mode-I / 80% Mode-II ratio, where the toughness reaches a local minimum of 1.84 MPa $\cdot\sqrt{m}$. This suggests that the (1210)[1010] crack geometry in TiB₂ is most susceptible to fracture under predominantly shear-dominated loading conditions with a modest tensile component. Fig. 6b displays the deviation in atomic displacements from the linear-elastic solution (see Ref. [56] for technical details) at load levels near K_c , capturing the evolution of the stress field. Distinct fracture responses emerge depending on the balance between shear and tensile loading.

As shown in Figs. 6c and 6d, crack propagation transitions through four different mechanisms depending on the mode ratio. Under pure Mode-I loading, the crack propagates predominantly along the original $(\overline{1210})$ fracture plane. As the Mode-I fraction decreases to intermediate levels, deflection occurs onto either the $(\bar{1}2\bar{1}2)$ or (0001) planes. In particular, at 70% Mode-I content, the crack path shifts entirely to the $(\overline{1212})$ plane, marking a transition that begins with the activation of pyramidal slip and subsequently evolves into full oblique fracture. At 60% Mode-I, the crack initially extends along the (0001) plane before redirecting to $(\overline{1210})$. For Mode-I fractions below 50% – including the pure Mode-II case – the structure consistently fractures along the basal (0001) plane. This behavior closely resembles the crack growth mechanism observed in the (1210)|0001| (Nr. 4) loading geometry.

The $(10\overline{1}0)[\overline{1}2\overline{1}0]$ (Nr. 6) deformation behavior (Fig. 7a) exhibits a more intricate trend in K_c^{mix} , including a minimum of 1.88 MPa· $\sqrt{\text{m}}$ at 60% Mode-I. The toughness values for pure Mode-I and Mode-II are relatively similar- $K_{Ic} = 1.72 \text{ MPa} \cdot \sqrt{\text{m}}$ and $K_{IIc} = 1.94 \text{ MPa} \cdot \sqrt{\text{m}}$, respectively. Fig. 7b, showing the displacement deviation from the linear-elastic solution, highlights the evolving crack-tip stress fields. Combined with Figs. 7c and 7d, these results reveal distinct fracture mechanisms as the loading mode varies.

Under pure Mode-I loading, the native (1010) crack extends in a zigzag fashion along mirrored diagonal facets, maintaining an overall horizontal trajectory. Between 90% and 60% Mode-I, crack growth transitions to the $(1\overline{1}01)$ plane-consistent with the first-order pyramidal slip system and the preferred cleavage path in ZrB₂ and HfB₂ (see Fig. 5c). As the Mode-I fraction decreases further, between 50% and 10%, fracture begins with

basal-plane slip followed by crack opening along the (0001) surface. A similar basal-slip mechanism has been observed in simple-shear simulations of single-crystal TMB₂ (TM = Ti, Ta, W, Re) lattice models [29]. From 10% Mode-I down to pure Mode-II, the crack opens directly along the (0001) surface, without preceding slip.

The evolution observed in the $(10\overline{1}0)[0001]$ (Nr. 5) configuration follows a more straightforward pattern. From pure Mode-I down to 90% Mode-I, fracture proceeds along the $(10\overline{10})$ plane, though in a straight rather than zigzag path. At 80-70% Mode-I, the crack shifts to the $(11\overline{20})$ plane, and for all lower Mode-I ratios – including pure Mode-II – fracture occurs through the $(1\overline{1}00)$ plane. These transitions suggest the activation of prismatic slip after reaching K_c .

The fracture toughness values for the $(\overline{1}2\overline{1}0)[10\overline{1}0]$ and $(10\overline{1}0)[\overline{1}2\overline{1}0]$ configurations show only minor differences between K_{Ic} and K_{IIc} . As seen in Fig. 6 and Fig. 7, all four toughness values—corresponding to pure Mode-I and Mode-II loading for both geometries-cluster around 2 MPa $\cdot \sqrt{m}$, indicating a consistent resistance to fracture regardless of loading mode or crack orientation. While this suggests similar macroscopic toughness under tension and shear, the underlying mechanisms differ markedly and confirm the strongly brittle nature of TiB_2 .

Under pure Mode-II loading, one would expect slip to initiate along the original crack plane—as seen in other hard ceramics. For instance, in TiN, atomistic simulations reveal that a (110)[010] crack under pure Mode-II activates slip along the $\{110\}\langle110\rangle$ system, which lies within the original crack surface [57]. In contrast, TiB₂ shows no such response. Rather than slipping, TiB₂ cracks along the orthogonal (0001) basal plane. This highlights TiB₂'s low propensity for shear-induced plasticity—even Mode-II loading is accommodated through brittle cleavage.

4 Experimental testing and verification of fracture simulations

To support the results of our atomistic simulations, we perform cube-corner nanoindentation experiments on TiB₂ thin films with near 1:2 Ti-to-B stoichiometry. The film's microstructure before and after indentation is characterized using high-resolution transmission electron microscopy (HRTEM). The as-deposited samples exhibit [0001] orientation (Fig. 8a), consistent with the typical growth direction of TMB₂ thin films.

Cube-corner indentation is known to generate a combination of Mode-I (opening) and Mode-II (shearing) stresses [89]. Post-mortem HRTEM analysis of the [0001]-oriented TiB₂ films reveals that cracks initiate from the indentation site along a prismatic plane and subsequently deflect onto an inclined plane at approximately 40° (Fig. 8b). This oblique fracture trajectory suggests that crack propagation occurs under mixed-mode loading conditions. To interpret this behavior, we compare the experimental observations with our ML-MS simulations of defective lattices containing native prismatic cracks – that is, orthogonal to the basal plane – shown in Figs. 6 and 7.

As illustrated in Fig. 5b-1 and Fig. 5c-1, cracks in TiB₂ loaded under pure Mode-I conditions propagate straight along the original prismatic plane-a response inconsistent with crack deflection observed in the experimental test. In contrast, simulations under mixed Mode-I/Mode-II loading (Figs. 6 and 7) reveal crack redirection toward inclined pyramidal planes, especially when the Mode-I contribution lies between 60% and 90%

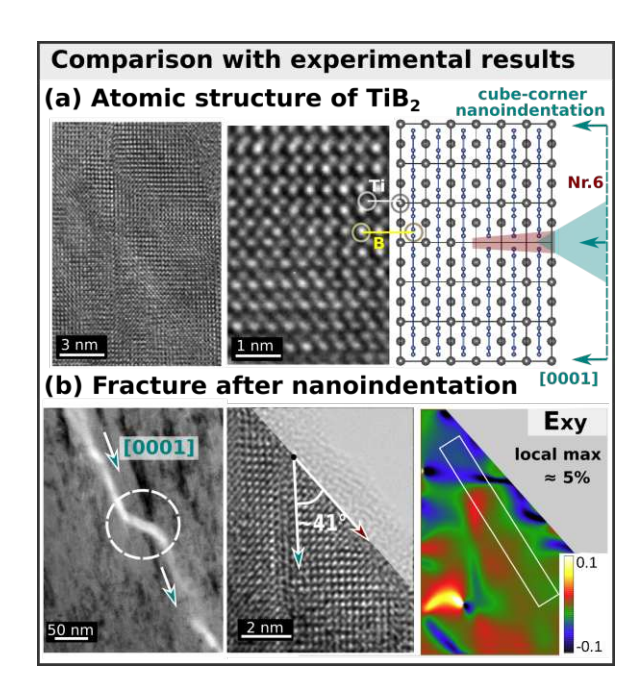


Fig. 8: Comparison of simulation and experimental results for TiB₂. (a) Atomic structure of TiB₂ thin film from HRTEM prior to nanoindentation, compared with the atomistic model used for pre-crack simulations, with the [0001] direction indicated. The brighter pattern represents two nearest-neighbor B atoms merging together, while the relatively darker pattern corresponds to Ti atoms. The contrast reversal of brightness is caused by the thicker TEM sample. (b) HRTEM pattern after cube-corner nanoindentation, showing angle changes during fracture. The average shear strain, E_{xy} , is highlighted using the geometric phase analysis (GPA) pattern.

(see Figs. 6d and 7d). In particular, simulations of $(10\overline{10})[\overline{1210}]$ cracked-plate models under < 40\% Mode-II loading component show diagonal crack propagation along the (1101) plane-closely matching the experimental deflection angle and aligning with the relatively low energetic cost of pyramidal slip in AlB₂-type materials [90, 91].

Additionally, geometric phase analysis (GPA) of the post-morten microstructure reveals a local maximum shear strain of approximately 5% near the crack tip, consistent with a mixed-mode fracture mechanism involving Mode-II contribution. Taken together, these findings suggest that the experimentally observed crack deflection originates from mixed-mode loading during nanoindentation and reinforce the relevance of our atomistic simulations for predicting and interpreting fracture patterns in brittle ceramics.

The fracture toughness measured for the same TiB₂ sample by microcantilever bending yielded a value of 3.08 MPa $\cdot\sqrt{m}$ [45], approximately 40% higher than both the extrapolated K_{Ic}^{∞} and the Griffith-based estimate K_{Ic}^{G} . This difference likely arises from several factors. First, the experimental measurement reflects the response of a columnar polycrystalline matrix, where microstructural features such as grain boundaries and local residual stresses (up to ≈ 3 GPa compressive residual stress in this series of TiB₂ sample [92]) can enhance resistance to crack propagation – effects that are not captured in our idealized atomistic models. Second, the geometry of a notched microcantilever – with notch widths on the order of tens of nanometers [45] – differs significantly from the atomically sharp cracks modeled in simulations. Prior atomistic work on TiN(001) - a similarly brittle ceramic - showed that fracture toughness increases with notch width and saturates at a value roughly 20% above the atomically sharp case, once the

notch spans just a few atomic layers [57]. This suggests that toughness values obtained from finite-width experimental notches are inherently higher than those predicted for atomically sharp cracks.

A further contribution to the discrepancy may stem from how fracture initiation is defined in our simulations. To ensure consistency across all crack geometries and materials, we identify fracture onset with the rupture of the first chemical bond at the crack tip. While this criterion is unambiguous and reproducible, it neglects lattice trapping—where the atomic lattice imposes an energy barrier to crack propagation and other atomistic effects that can locally stabilize the crack front and delay its advance. As a result, the extrapolated K_{Ic}^{∞} values may modestly underestimate the effective macroscopic toughness, particularly for configurations prone to such trapping phenomena.

Looking ahead, a key challenge for MLIP-based atomistic modeling is to incorporate simplified but representative features of real microstructures. These may include common point defects such as boron or metal vacancies [43, 44], extended planar defects like anti-phase boundaries [93, 94], or amorphous-like B-rich columns [95]. However, introducing defects arbitrarily based on stoichiometry is not sufficient. To enable meaningful comparison with experimental data, one must first identify which defect types and distributions are relevant for the adopted synthesis conditions, and then construct ad hoc atomistic models that reflect those microstructural features. As emphasized in Ref. [56], these models must be built with care to avoid unphysical artifacts. For example, placing a native dislocation too close to the crack plane can significantly alter the strain field near the crack tip, biasing the computed toughness and limiting the generality of the results. Ultimately, by combining process-aware defect modeling with rigorous K-controlled simulations, it may become possible to quantitatively link intrinsic fracture properties to those measured in structurally complex, real-world TiB₂-based ceramics.

Conclusion

To investigate the intrinsic fracture properties of Group-IV transition metal diborides $(TMB_2, TM = Ti, Zr, Hf)$, we performed K-controlled molecular statics simulations on pre-cracked lattice models using machine-learning interatomic potentials (MLIPs). The potentials were validated following a protocol analogous to our previous work [28], ensuring that surface energies, elastic constants, and theoretical tensile strengths reproduce static DFT and finite-temperature AIMD results.

Our analysis focused on six low-index atomically sharp crack geometries under pure Mode-I loading: $(0001)[10\overline{1}0]$, $(0001)[\overline{1}2\overline{1}0]$, $(\overline{1}2\overline{1}0)[10\overline{1}0]$, $(\overline{1}2\overline{1}0)[0001]$, $(10\overline{1}0)[0001]$, and $(10\overline{1}0)[\overline{1}2\overline{1}0]$, where (hklm) denotes the crack surface and [h'k'l'm'] the crack line or crack front direction. The macroscale fracture toughness K_{Ic}^{∞} and fracture strength σ_{\max}^{∞} were obtained by extrapolating results from different plate sizes. While all diboride systems exhibit similar fracture strengths ($\approx 2.0 \text{ MPa} \cdot \sqrt{\text{m}}$), the toughness ranked as: $HfB_2 \approx 2.7 MPa \cdot \sqrt{m} > TiB_2 \approx 2.3 MPa \cdot \sqrt{m} > ZrB_2 \approx 1.8 MPa \cdot \sqrt{m}$, with minor deviations in two geometries. The predicted values fall within the ranges reported experimentally: 1.8-6.8 MPa· \sqrt{m} for TiB₂ [73-75], 2.2-5.0 MPa· \sqrt{m} for ZrB₂ [40, 41, 76, and 2.8–7.2 MPa $\cdot\sqrt{m}$ for HfB₂ [77, 78]. Deviations from experimental values can be attributed to the absence of microstructural features in simulations (e.g., grain boundaries, residual stress), wider notches used in experiments [45], and our strict definition of fracture onset – based on the first bond rupture – which overlooks effects like lattice trapping that can delay crack advance.

We further explored the influence of mixed Mode-I/Mode-II loading on fracture resistance K_c and crack path evolution in TiB₂, focusing on the $(\overline{1}2\overline{1}0)[10\overline{1}0]$ and $(10\overline{10})[\overline{12}\overline{10}]$ geometries. Simulations showed that mixed-mode loading can significantly alter fracture trajectories and reduce K_c . In particular, K_c minima emerged under specific shear/tensile combinations, with cracks deflecting toward inclined pyramidal planes. This behavior was confirmed experimentally by cube-corner nanoindentation on [0001]-oriented TiB₂ thin films, which exhibited oblique crack propagation at $\approx 40^{\circ}$. Geometric phase analysis revealed local shear strain of $\approx 5\%$, consistent with mixedmode loading and supporting our atomistic predictions.

Taken together, these results demonstrate that K-controlled ML-MS simulations offer a predictive, atomistically detailed framework for evaluating fracture properties in brittle ceramics. By resolving how loading mode, crystallographic orientation, and local structure influence crack evolution, our approach provides both quantitative and mechanistic insight. Although finite-temperature effects were not explicitly modeled, the agreement between ML-MD and AIMD in prior validation supports future extensions of this framework to dynamic and environment-sensitive fracture phenomena. This paves the way toward systematic prediction of fracture-related descriptors and mechanisms in complex ceramic systems.

Bibliography

- A. A. Griffith. VI. The phenomena of rupture and flow in solids. Proc R Soc Lond A Math Phys Sci 221.582-593 (1921), 163–198.
- G. R. Irwin. Analysis of stresses and strains near the end of a crack traversing a plate. Journal of Applied Mechanics 24.3 (Juni 2021), 361–364. ISSN: 0021-8936.
- T. Nose und T. FUJII. Evaluation of fracture toughness for ceramic materials by a single-edge-precracked-beam method. J. Am. Ceram. Soc. 71.5 (1988), 328–333.
- T. L. Anderson, M. Dawes und H. McHenry. Elastic-plastic fracture toughness tests with single-edge notched bend specimens. ASTM International, 1985.
- E. M. Shaji, S. R. Kalidindi, R. D. Doherty und A. S. Sedmak. Plane strain fracture toughness of MP35N in aged and unaged conditions measured using modified CT specimens. *Mater. Sci. Eng. A* 340.1-2 (2003), 163–169.
- J. Underwood, S. Freiman, F. Baratta u.a. A review of chevron-notched fracture specimens. Chevron-notched Specimens, Testing and Stress Analysis: A Symposium. Bd. 855. ASTM International. 1984, 5.
- R. Kolhe, C.-Y. Hui und A. T. Zehnder. Effects of finite notch width on the fracture of chevron-notched specimens. Int. J. Fract. 94 (1998), 189–198.
- B. Gludovatz, S. Wurster, A. Hoffmann und R. Pippan. Fracture toughness of polycrystalline tungsten alloys. Int. J. Refract. Met. Hard Mater. 28.6 (2010), 674 - 678.
- M. E. Launey und R. O. Ritchie. On the fracture toughness of advanced materials. Adv. Mater. 21.20 (2009), 2103–2110.
- X. Zeng und A. Hartmaier. Modeling size effects on fracture toughness by dislocation dynamics. Acta Mater. 58.1 (2010), 301–310.
- J. J. Möller und E. Bitzek. Fracture toughness and bond trapping of grain boundary cracks. Acta Mater. 73 (2014), 1–11.
- T. Shimokawa, M. Tanaka, K. Kinoshita und K. Higashida. Roles of grain boundaries in improving fracture toughness of ultrafine-grained metals. Phys. Rev. B Condens. Matter 83.21 (2011), 214113.
- S. Samborski und T. Sadowski. Dynamic fracture toughness of porous ceramics. J. Am. Ceram. Soc. 93.11 (2010), 3607–3609.

- H.-J. Kleebe, G. Pezzotti und G. Ziegler. Microstructure and fracture toughness of Si₃N₄ ceramics: combined roles of grain morphology and secondary phase chemistry. J. Am. Ceram. Soc. 82.7 (1999), 1857–1867.
- Z. Zhang, A. Ghasemi, N. Koutná, Z. Xu, T. Grünstäudl, K. Song, D. Holec, Y. He, P. H. Mayrhofer und M. Bartosik. Correlating point defects with mechanical properties in nanocrystalline TiN thin films. Mater. Des. 207 (2021), 109844.
- L. Ma, A.-L. Fauchille, M. R. Chandler, P. Dowey, K. G. Taylor, J. Mecklenburgh und P. D. Lee. In-situ synchrotron characterisation of fracture initiation and propagation in shales during indentation. Energy 215 (2021), 119161.
- K. Fadenberger, I. E. Gunduz, C. Tsotsos, M. Kokonou, S. Gravani, S. Brands-[17]tetter, A. Bergamaschi, B. Schmitt, P. H. Mayrhofer, C. C. Doumanidis u.a. In situ observation of rapid reactions in nanoscale Ni–Al multilayer foils using synchrotron radiation. Appl. Phys. Lett. 97.14 (2010).
- Y. Mishin. Machine-learning interatomic potentials for materials science. Acta Mater. 214 (2021), 116980.
- D. Dragoni, T. D. Daff, G. Csányi und N. Marzari. Achieving DFT accuracy with a machine-learning interatomic potential: Thermomechanics and defects in bcc ferromagnetic iron. Phys. Rev. Mater. 2.1 (2018), 013808.
- T. Mueller, A. Hernandez und C. Wang. Machine learning for interatomic potential |20|models. J. Chem. Phys. 152.5 (2020).
- L. Zhang, G. Csányi, E. van der Giessen und F. Maresca. Efficiency, accuracy, and transferability of machine learning potentials: Application to dislocations and cracks in iron. Acta Mater. 270 (2024), 119788.
- J. Behler. Perspective: Machine learning potentials for atomistic simulations. The Journal of chemical physics 145.17 (2016).
- |23|V. L. Deringer, M. A. Caro und G. Csányi. Machine learning interatomic potentials as emerging tools for materials science. Adv. Mater. 31.46 (2019), 1902765.
- Y. Zuo, C. Chen, X. Li, Z. Deng, Y. Chen, J. Behler, G. Csányi, A. V. Shapeev, A. P. Thompson, M. A. Wood u.a. Performance and cost assessment of machine learning interatomic potentials. J. Phys. Chem. A 124.4 (2020), 731–745.
- [25]J. S. Smith, O. Isayev und A. E. Roitberg. ANI-1: an extensible neural network potential with DFT accuracy at force field computational cost. Chem. Sci. 8.4 (2017), 3192-3203.
- A. V. Shapeev, E. V. Podryabinkin, K. Gubaev, F. Tasnádi und I. A. Abrikosov. |26|Elinvar effect in β -Ti simulated by on-the-fly trained moment tensor potential. New J. Phys. 22.11 (2020), 113005.

- I. S. Novikov, K. Gubaev, E. V. Podryabinkin und A. V. Shapeev. The MLIP package: moment tensor potentials with MPI and active learning. Mach. learn.: sci. technol. 2.2 (2020), 025002.
- S. Lin, L. Casillas-Trujillo, F. Tasnádi, L. Hultman, P. H. Mayrhofer, D. G. Sangiovanni und N. Koutná. Machine-learning potentials for nanoscale simulations of tensile deformation and fracture in ceramics. npj Comput. Mater. 10.1 (2024), 67.
- [29]S. Lin, D. Holec, D. Sangiovanni, T. Leiner, L. Hultman, P. Mayrhofer und N. Koutná. Shear-activated phase transformations of diborides via machine-learning potential molecular dynamics. Preprint 10.21203/rs.3.rs-5327540/v1 (2024).
- N. Koutná, S. Lin, L. Hultman, D. G. Sangiovanni und P. H. Mayrhofer. Machinelearning potentials for structurally and chemically complex MAB phases: strain hardening and ripplocation-mediated plasticity. Preprint dx.doi.org/10.2139/ssrn.5187025 (2025).
- C. Sevik, J. Bekaert, M. Petrov und M. V. Milošević. High-temperature multigap superconductivity in two-dimensional metal borides. Phys. Rev. Mater. 6.2 (2022), 024803.
- H. Holleck. Material selection for hard coatings. J. Vac. Sci. Technol. 4.6 (1986), 2661-2669.
- C. Wang, S. Akbar, W. Chen und V. Patton. Electrical properties of hightemperature oxides, borides, carbides, and nitrides. J. Mater. Sci. 30 (1995), 1627 - 1641.
- H. Waldl, M. Tkadletz, A. Lechner, C. Czettl, M. Pohler und N. Schalk. Evolution of the fracture properties of arc evaporated $Ti_{1-x}Al_xN$ coatings with increasing Al content. Surface and Coatings Technology 444 (2022), 128690.
- Y. Moritz, C. Kainz, M. Tkadletz, C. Czettl, M. Pohler und N. Schalk. Mi-|35|crostructure and mechanical properties of arc evaporated Ti (Al, Si) N coatings. Surf. Coat. Technol. 421 (2021), 127461.
- R. Daniel, M. Meindlhumer, W. Baumegger, J. Zalesak, B. Sartory, M. Burghammer, C. Mitterer und J. Keckes. Grain boundary design of thin films: using tilted brittle interfaces for multiple crack deflection toughening. Acta Mater. 122 (2017), 130-137.
- T. Csanádi, M. Vojtko, Z. Dankházi, M. J. Reece und J. Dusza. Small scale [37]fracture and strength of high-entropy carbide grains during microcantilever bending experiments. J. Eur. Ceram. Soc. 40.14 (2020), 4774–4782.
- J. Tatami, M. Katayama, M. Ohnishi, T. Yahagi, T. Takahashi, T. Horiuchi, |38|M. Yokouchi, K. Yasuda, D. K. Kim, T. Wakihara u.a. Local fracture toughness of Si₃N₄ ceramics measured using single-edge notched microcantilever beam specimens. J. Am. Ceram. Soc. 98.3 (2015), 965–971.

- J. P. Best, J. Zechner, J. M. Wheeler, R. Schoeppner, M. Morstein und J. Michler. Small-scale fracture toughness of ceramic thin films: the effects of specimen geometry, ion beam notching and high temperature on chromium nitride toughness evaluation. *Phil. Mag.* 96.32-34 (2016), 3552–3569.
- F. Monteverde, S. Guicciardi und A. Bellosi. Advances in microstructure and mechanical properties of zirconium diboride based ceramics. Mater. Sci. Eng. A 346.1-2 (2003), 310–319.
- |41|T. Csanádi, A. Azizpour, M. Vojtko und W. G. Fahrenholtz. The effect of crystal anisotropy on fracture toughness and strength of ZrB₂ microcantilevers. J. Am. Ceram. Soc. 107.3 (2024), 1669–1681.
- M. Vidiš, T. Fiantok, M. Gocník, P. Švec Jr, Š. Nagy, M. Truchly, V. Izai, T. Roch, L. Satrapinskyy, V. Śroba u.a. Hardness and fracture toughness enhancement in transition metal diboride multilayer films with structural variations. Materialia 34 (2024), 102070.
- C. Hu, S. Lin, M. Podsednik, S. Mráz, T. Wojcik, A. Limbeck, N. Koutná und P. H. Mayrhofer. Influence of co-sputtering AlB₂ to TaB₂ on stoichiometry of non-reactively sputtered boride thin films. Mater. Res. Lett. 12.8 (2024), 561–570.
- T. Glechner, H. Oemer, T. Wojcik, M. Weiss, A. Limbeck, J. Ramm, P. Polcik und H. Riedl. Influence of Si on the oxidation behavior of TM-Si-B2az coatings (TM= Ti, Cr, Hf, Ta, W). urf. Coat. Technol. 434 (2022), 128178.
- C. Fuger, R. Hahn, A. Hirle, T. Wojcik, P. Kutrowatz, F. Bohrn, O. Hunold, |45|P. Polcik und H. Riedl. Tissue phase affected fracture toughness of nano-columnar TiB_{2+z} thin films. *Mater. Res. Lett.* 11.8 (2023), 613–622.
- [46]G. Kresse und J. Furthmüller. Efficient iterative schemes for ab initio total-energy calculations using a plane-wave basis set. Phys. Rev. B 54.16 (1996), 11169.
- G. Kresse und D. Joubert. From ultrasoft pseudopotentials to the projector |47|augmented-wave method. *Phys. Rev. B* 59 (3 Jan. 1999), 1758–1775.
- J. P. Perdew, A. Ruzsinszky, G. I. Csonka, O. A. Vydrov, G. E. Scuseria, L. A. Constantin, X. Zhou und K. Burke. Restoring the density-gradient expansion for exchange in solids and surfaces. Phys. Rev. Lett. 100 (13 Apr. 2008), 136406.
- T. Leiner, N. Koutná, J. Janovec, M. Zeleny, P. H. Mayrhofer und D. Holec. On [49]energetics of allotrope transformations in transition-metal diborides via plane-byplane shearing. Vacuum 215 (2023), 112329.
- C. Hu, S. Mráz, P. J. Pöllmann, T. Wojcik, M. Podsednik, B. Hajas, A. Limbeck, N. Koutná, J. M. Schneider und P. H. Mayrhofer. Microstructure, mechanical properties, thermal decomposition and oxidation sequences of crystalline AlB₂ thin films. Mater. Des. 250 (2025), 113584.

- M. Parrinello und A. Rahman. Polymorphic transitions in single crystals: A new molecular dynamics method. J. Appl. Phys. 52.12 (1981), 7182–7190.
- D. G. Sangiovanni, F. Tasnádi, T. Harrington, M. Odén, K. S. Vecchio und I. A. Abrikosov. Temperature-dependent elastic properties of binary and multicomponent high-entropy refractory carbides. Mater. Des. 204 (2021), 109634.
- A. P. Thompson, H. M. Aktulga, R. Berger, D. S. Bolintineanu, W. M. Brown, P. S. Crozier, P. J. in 't Veld, A. Kohlmeyer, S. G. Moore, T. D. Nguyen, R. Shan, M. J. Stevens, J. Tranchida, C. Trott und S. J. Plimpton. LAMMPS - a flexible simulation tool for particle-based materials modeling at the atomic, meso, and continuum scales. Comp. Phys. Comm. 271 (2022), 108171.
- E. V. Podryabinkin und A. V. Shapeev. Active learning of linearly parametrized [54]interatomic potentials. Comput. Mater. Sci. 140 (2017), 171–180.
- P. Andric und W. Curtin. New theory for Mode I crack-tip dislocation emission. [55]J. Mech. Phys. Solids 106 (2017), 315–337.
- P. Andric und W. A. Curtin. Atomistic modeling of fracture. Model. Simul. Mat. Sci. Eng. 27.1 (2018), 013001.
- D. G. Sangiovanni, A. Kraych, M. Mrovec, J. Salamania, M. Odén, F. Tasnádi [57]und I. A. Abrikosov. Descriptor for slip-induced crack blunting in refractory ceramics. Physical Review Materials 7.10 (2023), 103601.
- D. G. Sangiovanni, A. Kjellén, F. Trybel, L. Johnson, M. Odén, F. Tasnádi und I. Abrikosov. Controlled polymorphic competition—a path to tough and hard ceramics. Acta Materialia 294 (2025), 121121.
- |59|T. T. C. Ting. Anisotropic Elasticity: Theory and Applications. Oxford University Press, Apr. 1996. ISBN: 9780195074475.
- M. Schaffer, B. Schaffer und Q. Ramasse. Sample preparation for atomic-resolution STEM at low voltages by FIB. Ultramicroscopy 114 (2012), 62–71.
- Y. Zhou, H. Xiang, Z. Feng und Z. Li. General trends in electronic structure, stability, chemical bonding and mechanical properties of ultrahigh temperature ceramics TMB₂ (TM= transition metal). J. Mater. Sci. Technol. 31.3 (2015), 285 - 294.
- [62]Q. Gan, H. Liu, S. Zhang, F. Wang, J. Cheng, X. Wang, S. Dong, Q. Tao, Y. Chen und P. Zhu. Robust hydrophobic materials by surface modification in transition-metal diborides. ACS Appl. Mater. Interfaces 13.48 (2021), 58162–58169.
- W. Sun, H. Xiang, F.-Z. Dai, J. Liu und Y. Zhou. Anisotropic surface stability |63|of TiB₂: A theoretical explanation for the easy grain coarsening. J. Mater. Res. 32.14 (2017), 2755–2763.

- W. Sun, J. Liu, H. Xiang und Y. Zhou. A theoretical investigation on the anisotropic surface stability and oxygen adsorption behavior of ZrB₂. J. Am. Ceram. Soc. 99.12 (2016), 4113–4120.
- T. Yang, X. Han, W. Li, X. Chen und P. Liu. First-principles calculations on the |65|interfacial stability and bonding properties of HfN (111)/HfB₂ (0001) interface. Vacuum 207 (2023), 111678.
- D. G. Sangiovanni, K. Kaufmann und K. Vecchio. Valence electron concentration [66]as key parameter to control the fracture resistance of refractory high-entropy carbides. Science Advances 9.37 (2023), eadi2960.
- [67]N. Koutná, L. Löfler, D. Holec, Z. Chen, Z. Zhang, L. Hultman, P. H. Mayrhofer und D. G. Sangiovanni. Atomistic mechanisms underlying plasticity and crack growth in ceramics: a case study of AlN/TiN superlattices. Acta Mater. 229 (2022), 117809.
- [68]V. Paidar und J. Capek. Anisotropy of fracture in hexagonal metals. Int. J. Fract. 225 (2020), 123–127.
- V. Kaushik, R. Narasimhan und R. K. Mishra. Experimental study of fracture behavior of magnesium single crystals. Mater. Sci. amp; Enq. A 590 (2014), 174-185.
- Y. Mine, S. Ando und K. Takashima. Fatigue Crack Propagation in Titanium Single Crystals. Key Eng. Mater. 145-149 (1998), 721-726.
- R. Thomson, C. Hsieh und V. Rana. Lattice Trapping of Fracture Cracks. J. Appl. Phys. 42.8 (1971), 3154–3160.
- P. Andric und W. A. Curtin. Atomistic modeling of fracture. *Model. Simul. Mater.* Sci. Eng. 27.1 (2019), 013001.
- M. K. Ferber, P. F. Becher und C. B. Finch. Effect of microstructure on the properties of TiB₂ ceramics. J. Am. Ceram. Soc. 66.1 (1983), C-2.
- S. Bhaumik, C. Divakar, A. K. Singh und G. Upadhyaya. Synthesis and sintering of TiB₂ and TiB₂-TiC composite under high pressure. Mater. Sci. Enq. A 279.1-2 (2000), 275-281.
- W. Wang, Z. Fu, H. Wang und R. Yuan. Influence of hot pressing sintering |75|temperature and time on microstructure and mechanical properties of TiB₂ ceramics. J. Eur. Ceram. Soc. 22.7 (2002), 1045–1049.
- J. J. Swab, J. Jarman, W. Fahrenholtz und J. Watts. Mechanical properties of ZrB₂ ceramics determined by two laboratories. Int. J. Appl. Ceram. Technol. 20.5 (2023), 3097-3103.

- K. Li, Z. Huang, J. Yuan, X. Li, Z. Wang, M. Hu, T. Wang, X. Hu, Y. Li und X. Zhang. Synthesis and growth mechanism of highly crystalized multi-branched HfB₂ microrods with self-toughening effect. Mater. Des. 244 (2024), 113196.
- Z. Wang, X. Liu, B. Xu und Z. Wu. Fabrication and properties of HfB₂ ceramics based on micron and submicron HfB₂ powders synthesized via carbo/borothermal reduction of HfO₂ with B₄C and carbon. Int. J. Refract. Met. Hard Mater. 51 (2015), 130-136.
- |79|T. Maccagno und J. Knott. Brittle fracture under mixed modes I and II loading. Int. J. Fract. 29 (1985), R49–R57.
- J. Royer. Study of pure and mixed-mode fracture of a brittle material. Exp. Mech. 28 (1988), 382–387.
- M. De Moura, R. Campilho und J. Gonçalves. Pure mode II fracture characterization of composite bonded joints. Int. J. Solids Struct. 46.6 (2009), 1589–1595.
- R. Jalayer, B. Saboori und M. R. Ayatollahi. A novel test specimen for mixed mode I/II/III fracture study in brittle materials. Fatigue Fract. Eng. Mater. Struct. 46.5 (2023), 1908–1920.
- V. Rizov. Mixed-mode I/II fracture study of polymer composites using Single [83]Edge Notched Bend specimens. Comput. Mater. Sci. 77 (2013), 1–6.
- A. Braham, W. Buttlar und F. Ni. Laboratory mixed-mode cracking of asphalt [84]concrete using the single-edge notch beam. Road Mater. Pavement Des. 11.4 (2010), 947-968.
- R. Margevicius, J. Riedle und P. Gumbsch. Fracture toughness of polycrystalline [85]tungsten under mode I and mixed mode I/II loading. Mater. Sci. Eng. A 270.2 (1999), 197-209.
- G. Sih und B. MacDonald. Fracture mechanics applied to engineering problems strain energy density fracture criterion. Engineering Fracture Mechanics 6.2 (1974), 361 - 386.
- Y. Zou, B. Derreberry und M. Farooq. Through-wall failure of a main steam bypass line socket weld and the flaw evaluation methodology. International Journal of Pressure Vessels and Piping 216 (2025), 105531.
- [88]J. Predan, V. Močilnik und N. Gubeljak. Stress intensity factors for circumferential semi-elliptical surface cracks in a hollow cylinder subjected to pure torsion. Engineering Fracture Mechanics 105 (2013), 152–168.
- I. Gupta, C. Sondergeld und C. Rai. Fracture toughness in shales using nanoindentation. J. Pet. Sci. Eng. 191 (2020), 107222.

- B. Hunter, X.-X. Yu, N. De Leon, C. Weinberger, W. Fahrenholtz, G. Hilmas, M. L. Weaver und G. B. Thompson. Investigations into the slip behavior of zirconium diboride. J. Mater. Res. 31.18 (2016), 2749–2756.
- C. Fuger, R. Hahn, L. Zauner, T. Wojcik, M. Weiss, A. Limbeck, O. Hunold, P. Polcik und H. Riedl. Anisotropic super-hardness of hexagonal $WB_2\pm z$ thin films. Mater. Res. Lett. 10.2 (2022), 70–77.
- A. Hirle, P. Dörflinger, C. Fuger, C. Gutschka, T. Wojcik, M. Podsednik, A. Limbeck, S. Kolozsvári, P. Polcik, C. Jerg u.a. Mechanical properties of DCMS and HiPIMS deposited Ti1-xMoxB2±z coatings. Surf. Coat. Technol. 497 (2025), 131750.
- J. Palisaitis, M. Dahlqvist, L. Hultman, I. Petrov, J. Rosen und P. O. Persson. [93]On the nature of planar defects in transition metal diboride line compounds. Materialia 24 (2022), 101478.
- J. Palisaitis, M. Dahlqvist, A. J. Hall, J. Thörnberg, I. Persson, N. Nedfors, L. Hultman, J. E. Greene, I. Petrov, J. Rosen u.a. Where is the unpaired transition metal in substoichiometric diboride line compounds? Acta Mater. 204 (2021), 116510.
- J. Thörnberg, J. Palisaitis, N. Hellgren, F. F. Klimashin, N. Ghafoor, I. Zhirkov, C. Azina, J.-L. Battaglia, A. Kusiak, M. A. Sortica u.a. Microstructure and materials properties of understoichiometric TiB_x thin films grown by HiPIMS. Surf. Coat. Technol. 404 (2020), 126537.

Chapter 6

Summary and outlook

Recent studies underscore machine learning interatomic potential (MLIP) as a promising bridge to combine the accuracy of ab initio methods with the computational efficiency of molecular dynamics, as empirical interatomic potentials are often material-specific and have limited applicability. Despite the advantages of MLIPs, a systematic training strategy for case-specific applications remains underdeveloped. In this thesis, I employed ab initio molecular dynamics (AIMD) calculations to evaluate the ideal mechanical properties of transition metal diborides (TMB₂) and developed MLIPs within the moment tensor potential (MTP) framework, using AIMD results as the training set to enable further nanoscale modeling. Further, TMB₂ are promising superhard materials; however, their brittleness under deformation and the mechanisms behind metastable phase formation during synthesis remain open questions – well-suited for atomistic modeling to provide atomic-scale insights and guidance for experimental efforts. The thesis further overviews the fundamental concepts of first-principles calculation, which forms the foundation of computational physics and is central to the "ab initio" approach.

The core chapter of this thesis presents my contributions to the field, as supported by 3 key publications. Additionally, the other studies I (co-)authored indicate that my scientific work was not strictly limited to MLIP development and transition metal diborides. Instead, it also encompasses static calculations of defective structures in Ta-Al-B compounds and high-entropy carbide alloys using density functional theory, complemented by collaborative experimental work, to validate and predict the change of stability and structural parameters while considering the effects of imperfect stoichiometry. Key outcomes of my doctoral research include: (i) developing a robust and transferable MLIP training strategy for case-specific ceramic simulations, achieving high validation accuracy across diverse loading scenarios; (ii) confirming the exceptional mechanical properties and high-temperature stability of TMB₂, reinforcing its potential for demanding applications; (iii) predicting phase transformations that may occur among three typical structural polymorphs of TMB₂ under ambient deformation conditions, offering insights into phase-transition mechanisms in ceramics; (iv) simulating Mode-I crack opening, which provides a realistic method for obtaining K_{Ic} values in complex ceramics through ML-MD via here-developed MLIP training strategy.

Future work could focus particularly on further structural design of this material, such as creating superlattices or alloying, to achieve optimal stability, mitigate brittleness, and prevent phase transformations that are shown to significantly reduce mechanical properties, especially for TiB₂ with highest phase-dependence of shear strength, as WB₂ exhibits the lowest. Experimental validation of the fracture mechanisms could also provide critical insights, bridging computational predictions with practical applications.





SHUYAO LIN

Email: shuyao.lin@tuwien.ac.at; ORCID: 0000-0003-4979-4174 Google Scholar: Shuyao Lin

 Computational materials researcher specializing in machine learning potentials for multi-scale modeling and designing structures to achieve optimal properties.

EXPERTISE FIELDS

- Machine learning potentials training for finite-temperature modelling
- Molecular dynamics simulation for deformation behavior of ceramics
- Quantum-mechanical properties calculations of high-entropy alloys and defective ceramics
- Quantum-transport properties calculations of semiconductors

EDUCATION

o Ph.D. in Materials Science | Faculty of Materials Science & Technology

2022-2025

Technische Universität Wien (AT), Linköping University (SE)

- Topic: Machine learning approach for high-temperature diboride materials under extreme loads.
- Keywords: Machine learning interatomic potentials training, molecular dynamics simulation, finite-temperature deformation behaviour modelling.
- o Master of Science | Faculty of Materials Science

2020-2022

Technische Universität Darmstadt (DE), Aalto University (FI)

- Thesis: First-principles calculation of thermal transport properties driven by ferroelectrics phase transition.
- Keywords: First-principles calculation, thermoelectric transport properties simulation.
- Bachelor of Engineering | Faculty of Materials Science & Engineering

2016-2020

University of Science and Technology Beijing (CN)

• Thesis: Dynamics of photocatalysis in complex water systems.

Professional Experience

• Guest researcher | Centre for Predictive Modelling Guided by Prof. J. Kermode in University of Warwick (UK). Responsibilities: methods investigation.

Full-time · 04.2025-07.2025

- o Doctoral researcher and university assistant | Group for thin film materials Full-time · 09.2022-08.2025 Guided by Dr. N. Koutná and Prof. P. Mayrhofer in TU Wien (AT), Dr. D. Sangiovanni in Linköping University (SE) Responsibilities: supervise students; support experimental studies; help with teaching and exams.
- Research and teaching assistant | Group for theory of magnetic matrials Part-time · 04.2021-06.2022 Guided by Prof. H. Zhang in TU Darmstadt (DE), and Dr. A. Karttunen in Aalto University (FI). Responsibilities: advise students; data evaluations; help with exams.
- Internship | Group for bio-inspired materials and interfacial science Guided by Prof. S. Wang in Chinese Academy of Sciences (CN). Responsibilities: sample preparation and characterization; data analysis.

Part-time · 09.2019-02.2020

• Research assistant | Group for development of photocatalytic materials Part-time · 11.2017-06.2020 Guided by Prof. W. Cao in University of Science and Technology Beijing (CN).

Responsibilities: advise students; sample preparation and characterization; perform sample testing and evaluation.



TU Sibliothek, Your knowledge hub

SCIENTIFIC EXPERIENCE

Research visits in collaborating groups

Prof. Lars Hultman's group, Linköping University

SE, 2022 & 2023 & 2024 & 2025

Prof. Matous Mrovec's group, Ruhr-Universität Bochum

DE, 2023

Prof. David Holec's group, Montanuniversität Leoben

AT, 2023

Prof. Pavel Souček's group, Masaryk University

CZ, 2023

o Peer review contributions at international journals

npj. Computational Materials (Springer); Digital Discovery (RSC); Physical Chemistry Chemical Physics (RSC); Vacuum (Elsevier); Surfaces and Interfaces (Elsevier); Surface & Coatings Technology (Elsevier); Applied Energy Materials (ACS)

SELECTED PUBLICATIONS (in total 6 first-author and 7 co-author papers, 250+ citations)

o MLIP combined MD - Ceramics - Deformation

- S.Lin, L.Casillas-Trujillo, F.Tasnádi, L.Hultman, P.H.Mayrhofer, D.G.Sangiovanni, N.Koutná. Machine-learning potentials for nanoscale simulations of tensile deformation and fracture in ceramics. *npj. Computational Materials*, 10, 67, 2024.
- S.Lin, D.Holec, D.G.Sangiovanni, T.Leiner, L.Hultman, P.H.Mayrhofer, N.Koutná. Shear-activated phase transformations of diborides via machine-learning potential molecular dynamics *Under Review in Acta Materialia*
- S.Lin, Z.Chen, R.Janknecht, Z.Zhang, L.Hultman, P.H.Mayrhofer, N.Koutná, D.G.Sangiovanni. Machine-learning potentials predict orientation- and mode-dependent fracture in refractory diborides *Under Review in Acta Materialia*
- N.Koutná, S.Lin, L.Hultman, D.G.Sangiovanni, P.H.Mayrhofer. Machine-learning potentials for structurally
 and chemically complex MAB phases: strain hardening and ripplocation-mediated plasticity
 Accepted in Materials & Design

o DFT - Semiconductor - Anharmonicity

- S.Lin, C.Shen, H.Zhang. Electric-field-tunable thermal conductivity in anti-ferroelectric materials. *Materials Today Physics*, 32, 100998, 2023.
- **S.Lin**, J.Yue, W.Ren, C.Shen, H.Zhang. Strong anharmonicity and medium-temperature thermoelectric efficiency in antiperovskite Ca₃XN (X = P, As, Sb, Bi) compounds. *Journal of Materials Chemistry A*, 12 (30), 19567-19579, 2024.

Experimental collaboration

- T.Stasiak, S.Debnárová, S.Lin, N.Koutná, Z.Czigány, K.Balázsi, V.Buršíková, P.Vašina, P.Souček. Synthesis and characterization of ceramic high entropy carbide thin films from the Cr-Hf-Mo-Ta-W refractory metal system. Surface and Coatings Technology, 485, 130839, 2024.
- C.Hu, S.Lin, M.Podsednik, S.Mráz, T.Wojcik, A.Limbeck, N.Koutná, P.H.Mayrhofer. Influence of co-sputtering AlB₂ to TaB₂ on stoichiometry of non-reactively sputtered boride thin films.
 Materials Research Letters, 12(8), 561-570, 2024.

PERSONAL GRANTS AND FELLOWSHIPS

o Forschungsforderprogramm "Internationale Kommunikation"

AT, 2025

Awarded by Österreichische Forschungsgemeinschaft (Austrian Research Association). 3-month abroad visiting

o Added Value Student Activities (AVSA) grant

DE & FI, 2020-2022

Awarded by European Institute of Innovation & Technology, Raw Materials.

Amount:€13,500, 2-year master

Sibliothek, Your knowledge hub

SCHOLARSHIPS AND AWARDS

o Graduate Student Award - Finalist

USA, 2025

Awarded by the Advanced Surface Engineering Division (ASED) of American Vacuum Society (AVS)

 \circ Stipendium für kurzfristige wissenschaftliche Arbeiten im Ausland

AT & UK, 2025

Awarded by Technische Universität Wien

o Förderungen für Konferenzteilnahmen

AT, 2025, 2024, 2023, 2022

Awarded by Technische Universität Wien, multiple times.

 Förderungen für Auslandsbeziehungen Awarded by Technische Universität Wien. AT & SE, 2023

o Outstanding Undergraduate Graduation Thesis of Beijing

CN, 2020

Awarded by Beijing Municipal Education Commission

(CO-)SUPERVISION

PhD project of Priyanshu Sorout in TU Wien, AT

06.2025-05.2029

"Predictive modeling of defect evolution in multicomponent ceramics"

BSc project of Vincent Bossert in TU Wien, AT

05.2025-10.2025

"Stability of stacking faults in TMB_2 systems with machine learning interatomic potentials"

BSc project of Franziskus Baumgartner in TU Wien, AT

03.2025-08.2025

"Effect of vacancies on α -TiB₂-based superlattices via *ab initio* molecular dynamics calculations"

CONFERENCES AND PRESENTATIONS

Fulfilling the Multiscale Promise in Materials: Getting Information out of the Atomistic Scale

GAP/(M)ACE Developers & Users Meeting

DE, 2024

International Conference on Metallurgical Coatings and Thin Films

USA, 2024 & 2025

DPG-Frühjahrstagung of the Condensed Matter Section (SKM)

DE, 2023 & 2024

European Congress and Exhibition on Advanced Materials and Processes

DE,2023

International Workshop on Computational Physics and Materials Science: Total Energy and Force Methods

IT, 2023

TECHNICAL AND LANGUAGE SKILLS

Coding & Operating: Python, R, Linux, LaTex, Fortran Matlab, C++ **Modeling**: VASP, Lammps, Alamode, Phonopy, ShengBTE, Amset, Boltztrap, etc.

Analysis & Post-processing: Ovito, VESTA, VMD, ASE, Pyscal, Quippy, etc.

Language: English (C1), German (B2), French (A2), Mandarin (Native)

REFERENCES

o **Asst.Prof. Nikola Koutná** nikola.koutna@tuwien.ac.at

• Assoc.Prof. Davide G. Sangiovanni davide.sangiovanni@liu.se

 Univ.Prof. Paul H. Mayrhofer paul.mayrhofer@tuwien.ac.at supervisor of Ph.D thesis TU Wien, AT co-supervisor of Ph.D thesis Linköping University, SE co-supervisor of Ph.D thesis TU Wien, AT



Place: Vienna Date: 16.July 2025

I hereby declare that all the details provided above are true and accurate to the best of my knowledge.